THE UNIVERSITY *of* EDINBURGH

Dark Matter and Galaxies: using Gravitational Lensing to Map their Relative Distributions

Lars Koens

Doctor of Philosophy
The University of Edinburgh
August 2014

Abstract

Cosmological constraints from galaxy surveys are as accurate as our understanding of the relative distributions of dark matter and galaxies, known as galaxy bias. Weak gravitational lensing is a powerful probe of galaxy bias, since the distortion in the shapes of distant galaxies, called shear, is directly related to the dark matter distribution, which can be compared to the galaxy field. I look at the galaxy clustering amplitude relative to the dark matter field, quantified by the galaxy bias b, as well as the cross-correlation coefficient r, which tells us how correlated the positions of galaxies are with the dark matter.

In this thesis I present several techniques to constrain galaxy bias through weak lensing, using both numerical simulations and observational data. The most commonly used method, using aperture statistics, is shown to be subject to serious systematics in the presence of noisy data and scale- and time dependence in the galaxy bias. A local comparison technique is introduced, where the foreground distribution is used to predict the shear in the background, to which it is compared. The technique is tested with simulations, concluding that it requires high quality data. A model fitting approach is proposed, based on the McDonald (2006) galaxy bias model. The two parameters of this model, a large scale bias, b_1, and a parameter, b_2, that quantifies the scale dependence of the bias, are insufficient in the presence of stochasticity. Therefore, $\mathcal{R}$ is introduced as an additional parameter to take this into account.

I present galaxy bias constraints for two spectroscopic galaxy samples: the Baryon Oscillations Spectroscopic Survey (BOSS) and the WiggleZ Dark Energy Survey (WiggleZ), applying the traditional aperture method and the model fitting approach to the Red Sequence Cluster Lensing Survey (RCSLenS). Both techniques strongly suggest that galaxies trace mass, but in a complicated way, with differences in scale- and time dependence between the samples considered. The WiggleZ galaxy bias is found to be around $b \sim 1.2$, depending on redshift

and scale, and has a low cross-correlation coefficient of $r \sim 0.5$ at small scales. The BOSS samples have higher bias with scale dependence around $b \sim 2.0$ and show no sign of stochasticity, finding r to be close enough to unity to be explained within a deterministic scenario. The observations are in line with previous galaxy bias measurements from lensing data.

The thesis incorporates work on the X-ray Luminosity Function (XLF) of galaxy clusters, measured from the Wide Angle ROSAT Pointed Survey (WARPS). Evolution is quantified with a likelihood analysis and I conclude that it is driven by a decreasing number density of high luminosity clusters with redshift, while the bulk of the cluster population remains nearly unchanged out to redshift $z \sim 1.1$, as expected in a low density Universe.

I conclude by investigating the impact of my galaxy bias measurements from BOSS and WiggleZ on the growth rate of structure, as extracted from Redshift Space Distortions (RSD). The imperfect correlation between the galaxy and matter field, as quantified by $\mathcal{R}$ and b_2, leads to an underestimation of the true growth rate under the assumption of a linear bias. Therefore, in order to constrain galaxy bias and gravity simultaneously, future cosmological redshift surveys require high quality lensing data.

Declaration

I declare that this thesis was composed by myself, that the work contained herein is my own except where explicitly stated otherwise in the text, and that this work has not been submitted for any other degree or professional qualification except as specified.

Parts of this work have been published in Koens et al. (2013).

(*Lars Koens, August 2014*)

Acknowledgements

First of all, I would like to thank my supervisors Catherine Heymans and Fergus Simpson for their consistent support, encouragement, patience, and incredible wisdom. Special thanks also to Chris Blake for his support and guidance during my time in Melbourne, and giving access to the WiggleZ and BOSS surveys.

I would like to thank the many people who have adviced me over the course of this thesis, in particular Alan Heavens, John Peacock, Bejamin Joachimi, Andy Taylor, Nic Ross, Patrick Simon, Felipe Marin, Peder Norberg, and Sylvain de la Torre. I would like to thank Christopher Bonnett for making available his lensing codes, as well as introducing me to the world of measuring correlation functions with Martin Kilbinger's Athena software. Major thanks to Bob Mann and Martin Kilbinger, for interesting discussions during the viva and spotting many typos. I acknowledge Joachim Harnois-Deraps and Ludo van Waerbeke for providing simulations, from which mock data was constructed for this thesis. I am indebted to the RCSLenS team led by Hendrik Hildebrandt, who generously gave access to the data analysed in chapter 4. Chapter 6 was done in collaboration with the wonderful WARPS team, and I am particularly grateful to Ben Maughan and Steve Phillipps for all their support. The WARPS survey is based on archival ROSAT data, made publicly available by NASA. This thesis was funded by the European Research Council under the EC FP7 grant number 240185.

Special thanks go to Luuk and Marion, Gwenda and Ingrid. I would also like to thank Pete and Caitlin for their musical and artistic support, Peter for his persistent optimism; and finally, I thank Demelza, for her love.

Contents

List of Figures

List of Tables

Chapter 1

The Structure of the Universe

Knowledge of the Universe has improved markedly over the last decennia. Observations of the microwave background radiation, large-scale structure, and distant supernovae indicate the existence of dark matter and dark energy. Understanding the nature of dark energy, the unknown cause of accelerated expansion, is expected to reveal fundamental physics, for example in the form of higher dimensions or a new law of gravity.

This thesis is concerned with the cosmological information contained in the large-scale distribution of galaxies. The complexity of galaxy formation and interactions results in an uncertain relationship with the total matter distribution, of which dark matter is the dominant component, driving the evolution of cosmological structures. The relationship between galaxies and dark matter is called galaxy bias. In this thesis I explore its properties with observations of gravitational light deflection over cosmological distances.

1.1 The Standard Model

Einstein's cosmological constant and de Sitter's non-static Universe inspired astronomers in the 1920s to probe the distance-redshift relation of galaxies. A number of searches for this relation were performed with some degree of success and it is now known as the Hubble law: a positive correlation between the distance of a galaxy and the velocity with which it recedes from us.

The observations seemed to imply that the Universe had a beginning in time and space (Lemaître, 1931). This idea, later deemed the Big Bang, was highly controversial; it was thought that time and space had always existed. There was a tremendous effort towards solving Einstein's equations in such a way that the Universe did not have a beginning, while at the same time explaining the observed distance-redshift relation. Famous example are the oscillatory Universe and the steady-state model. Likewise, a theory was popular among some in which light loses energy through interactions, also causing a positive correlation between distance and velocity (tired light, proposed by Zwicky, 1929). Although such theories are now refuted, the distance-redshift relation remains a key tool in cosmology.

An observational consequence of the big bang is the relic radiation that fills all space, the Cosmic Microwave Background (CMB) radiation. The idea of a Big Bang remained controversial even with observational confirmation of the CMB in 1964; the radiation was argued to be stellar in origin, mainly by supporters of the then still popular steady-state model. More accurate measurements in the 1970s confirmed the CMB's extreme degree of isotropy, hence it was the perfect candidate for the predicted relic radiation. The Big Bang model was established.

The distance-redshift relation together with the detection of the CMB provide the most important evidence for the inflationary (see Section 1.1.1) Big Bang model. Supernovae Type Ia are currently popular sources to probe the distance-redshift relation. For a homogeneous group of objects, one can plot the distance of each object against the speed at which it recedes from us. The resulting plot is known as a Hubble diagram, after Edwin Hubble who used galaxies to find indications of a linear relationship between distance and velocity, suggesting that the Universe is expanding. In today's context the supernova Hubble diagrams are interpreted as evidence for accelerated expansion (Perlmutter et al., 1999; Riess et al., 1998), which can be understood as follows. If the expansion of the Universe is accelerating, the expansion was more slowly in the past than it is today. This increases the light travel time and distance of high redshift supernovae, so that they appear dimmer. Hence, the observed relative distance between nearby and distant supernovae provided evidence for accelerated expansion. The observed nonlinear relation is necessary, but not sufficient; a few decades earlier, with CMB observations in their earliest stages, these observations would have been welcomed by supporters of the steady-state model, which also predicts accelerated expansion (Sandage, 1962).

The progress of cosmology in the past century has culminated into a concordance, or standard model. Its parameters are constrained with increasing accuracy, but the model requires the introduction of a dark sector, including dark matter and dark energy, whose physical origins remain largely unknown. In the next sections I describe the standard model, introducing essential cosmological concepts that will be used throughout the thesis.

1.1.1 The Friedmann Universe

As the Universe expands the proper distance between objects with no peculiar velocity increases according to the evolution of the scale factor $R(t)$, while the comoving distance is defined to remain constant. This allows us to write the Hubble law as

$$H = \frac{\dot{R}}{R}, \tag{1.1}$$

where H is the Hubble parameter (or constant in the sense of constant in space but not in time). The evolution of the Hubble parameter depends on the properties of space, the theory of gravity, and the components that make up the energy density.

Gravity in the standard model is described by General Relativity (Einstein, 1916). Its famous field equations encode how the gravitational field results from the distribution of mass or energy through the curvature of spacetime. This also applies to the Universe as a whole; the density of the Universe is directly linked to its global geometry.

The cosmological principle states that the Universe is isotropic and homogeneous and holds for the smoothed out structure of the Universe on large scales. The metric consistent with the cosmological principle is the Robertson-Walker metric, which simply multiplies static space with the time dependent scale factor. In polar coordinates the Robertson-Walker metric can be written as

$$ds^2 = c^2dt^2 - a^2(t)\left[dw^2 + f_K(w)^2(d\theta^2 + \sin^2\theta d\phi^2)\right], \tag{1.2}$$

where we have introduced the comoving radial distance w, the polar angle θ and the azimuthal angle ϕ, the normalised scale factor $a(t) = R(t)/R_0$, where $R_0 = R(t = 0)$, and $f_K(w)$ is the comoving angular diameter distance, which

depends on curvature

$$f_K(w) = \begin{cases} k^{-1/2}\sin(k^{1/2}w) & (k>0) \quad \text{spherical} \\ w & (k=0) \quad \text{flat} \\ (-k)^{-1/2}\sinh\left((-k)^{1/2}w\right) & (k<0) \quad \text{hyperbolic.} \end{cases} \tag{1.3}$$

The redshift is defined as the shift of spectral lines $z \equiv \nu_{\rm e}/\nu_{\rm r} - 1$, where $\nu_{\rm e}$ and $\nu_{\rm r}$ are the frequencies at the time of emission and reception, respectively. Since photons travel over null geodesics of zero proper time, we find their equation of motion by setting $ds = 0$, and $f_K = 0$ in (1.2), so that in a Universe described by the Robertson-Walker metric

$$w = \int_{t_e}^{t_r} \frac{cdt}{R(t)}. \tag{1.4}$$

The integral runs from the emission time $t_{\rm e}$ to the reception time $t_{\rm r}$ of the photon. Equation (1.4) shows that the time delay of events in the distant Universe are proportional to the expansion of space, since $dt_{\rm e}/dt_{\rm r} = R(t_{\rm e})/R(t_{\rm r})$. This relates the observable redshift directly to the scale factor

$$a(t) = \frac{1}{1+z}. \tag{1.5}$$

Redshifts of galaxies as high as $z = 8.6$ have been confirmed (Lehnert et al., 2010), which, according to (1.5) is light emitted when the Universe was only $\sim 10\%$ of its current size (and $\sim 0.1\%$ of its current volume).

Equation (1.4) can also be used to calculate the maximum distance particles could have travelled in a given time frame, denoted the particle horizon. Setting the lower integration limit to $t = t_{\rm Planck}$ then the particle horizon at time t can be found by integrating out to t, which defines causally connected regions of space.

The Friedmann equations govern the dynamics of the expansion and are based on the Robertson-Walker metric (1.2), Einstein's theory of gravity and, for Equation (1.7), conservation of energy. They can be written as

$$\dot{R}^2 - \frac{8\pi G}{3}\rho R^2 - \frac{\Lambda c^2}{3} = -kc^2 \tag{1.6}$$

$$\ddot{R} = -\frac{4\pi G R}{3c^2}(\rho c^2 + 3p) + \frac{\Lambda c^2}{3}. \tag{1.7}$$

(Friedmann, 1922). In the standard model, the observed accelerated expansion is

attributed to the cosmological constant Λ. It was introduced by Einstein in his field equations as the curvature of empty space. To understand how the different contributions to the energy density behave as space expands, we require their equation of state parameter $\mathrm{w}_i = p/(\rho_i c^2)$, which is $\mathrm{w}_m \approx 0$ for matter, $\mathrm{w}_r = 1/3$ for radiation and $\mathrm{w}_\Lambda = -1$ for Λ.

From the Friedmann Equation (1.7) solutions for single component universes can be derived as

$$\rho_i \propto a^{-3(1+\mathrm{w}_i)}, \tag{1.8}$$

where w_i is the equation of state parameter of component i. This tells us that in multicomponent universes there will be eras that are dominated by one of the components, starting with the one that has the highest equation of state parameter, radiation, followed by matter, and finally the cosmological constant will dominate the energy budget (provided there are no unknown components with even lower equation of state parameters).

With the dimensionless density parameters

$$\Omega_i \equiv \frac{8\pi G\rho_{i,0}}{3H_0^2}, \qquad \Omega_\Lambda \equiv \frac{\Lambda}{3H_0^2}, \qquad \Omega_k \equiv -\frac{k}{H_0^2}. \tag{1.9}$$

we can write the first Friedmann equation as

$$H^2(a) = H_0^2\left(\Omega_\Lambda + \Omega_m a^{-3} + \Omega_r a^{-4} + \Omega_k a^{-2}\right), \tag{1.10}$$

where H_0 is the present day value of the Hubble parameter $H_0 = 67.4 \pm 1.4$ (Planck Collaboration et al., 2013c). From Equations (1.4), (1.5) and (1.10) we find the comoving distance w as a function of redshift z

$$w(z) = \frac{c}{H_0}\int \left(\Omega_\Lambda + \Omega_m(1+z)^3 + \Omega_r(1+z)^4 + \Omega_k(1+z)^2\right)^{-\frac{1}{2}} dz. \tag{1.11}$$

To conclude, the distance-redshift relation is sensitive to the density parameters and is as such fundamental to observational cosmology.

Inflation

The Friedmann equations relate the density contributions to the expansion of space and its geometry. There are, however, a number of problems with the

model presented so far, which are related to the initial conditions, when the Universe was very hot and dense. The most important are the horizon- and the flatness problems.

The particle horizon at the redshift of the CMB $z_{\rm CMB} \sim 1100$, which is the distance light could have travelled since Planck time $t = t_{\rm Planck}$ (the smallest time interval measurable), implies regions of causal connection of only about 1 degree on the sky. This is the horizon problem, expressed by John Peacock as going to an African jungle to find out that people eat haggis there.

Yet another problem is that present day flatness requires extreme fine tuning. If in the early stages the density parameter Ω deviated slightly from 1, it would do so to a much greater degree at present times. How then, is it possible that the current density is very close to $\Omega = 1$, and not some extreme value?

Homogeneity of the CMB and the flat space time geometry that the size of hot and cold spots infer (see also Section 1.2.1) means that the CMB is strongly in favour of an initial state of accelerated expansion, known as inflation (Guth, 1981; Sato, 1981). A period of inflation results in an increased size of causally connected regions, hence solving the horizon problem if inflation endures long enough. It also solves the flatness problem because Ω will be driven towards 1 regardless of its initial value.

Standard Model of Particle Physics

Finally, the concordance model incorporates the Standard Model of particle physics to explain the interaction of particles on the very small scales, such as scattering processes in the early Universe, which accounts for the last scattering surface and hence the CMB. Particle physics also explains the abundance of chemical elements in the Universe. Dark matter, however, is not described by particle physics and may suggest that we need to go beyond the Standard Model, despite its recent success with observational confirmation of the Higgs field (Chatrchyan et al., 2012).

1.1.2 Structure Formation in ΛCDM

This section summarises our current understanding of the growth of density fluctuations in the Universe, from the smooth CMB anisotropies to the highly

non-Gaussian density fields at low redshifts.

Zwicky showed that, under the assumption of hydrostatic equilibrium, the amount of matter in clusters of galaxies, as inferred from their luminosities, is too low to explain the high velocity dispersion of galaxies (Zwicky, 1933, 1937). Hence, there has to be extra mass (or at least a deeper gravitational potential) in clusters in order to prevent them from falling apart. It is also required to keep stars and gas in galaxies together. As with dark energy, the physical origin of dark matter is uncertain. However, like dark energy, discussed in Section 1.1.3, observations rule out many scenarios and the currently popular candidate for dark matter is the Weakly Interacting Massive Particle (WIMP). WIMPs are cold, meaning they move about at non-relativistic speeds, are collisionless and cannot lose energy through electromagnetic radiation. The type of dark matter plays a vital role in how structure forms. If cold dark matter is dominant, then structure forms hierarchically (larger structures form by accreting smaller structures), consistent with observations of clusters of galaxies (e.g. the last chapter of this thesis on the X-ray Luminosity Function of galaxy clusters).

Evolution of the (Local) Matter Contrast

The matter contrast can be described by the fractional overdensity function

$$\delta(\mathbf{x}) = \frac{\rho(\mathbf{x}) - \bar{\rho}}{\bar{\rho}}, \tag{1.12}$$

where ρ is the density and $\bar{\rho}$ is the average density. Note that $\overline{\delta(x)} = 0$ and $\delta(x) \geq -1$ for all x. Perturbation modes are a combination of adiabatic and isocurvature modes. Inflation predicts initial fluctuations to be purely adiabatic and is consistent with the latest CMB measurements from the Planck satellite (Planck Collaboration et al., 2013c). Isocurvature contributions result from an uneven distribution of the different components of the total density field.

Within the particle horizon the fractional overdensity grows to linear order ($\delta \ll 1$) according to

$$\ddot{\delta} + 2H\dot{\delta} - 4\pi G\rho_m\delta = 0, \tag{1.13}$$

which can be derived from general relativity. This relation between perturbation growth and the expansion of space is important for observational cosmology, as it shows that probes of density changes are sensitive to dark energy, see Section

1.2. A solution can be found by separating the fractional overdensity in a growing and decaying mode $\delta(x,t) = A(x)D(t) + A'(x)D'(t)$

$$\ddot{D} + 2H(z)\dot{D} - \frac{3}{2}\Omega_{m,0}H_0^2(1+z)^3 D = 0. \tag{1.14}$$

For a flat Universe a solution can be written as (Peebles, 1980)

$$D(z) = \frac{H(z)}{H_0}\int_z^\infty \frac{dz'(1+z')}{H^3(z')}\left[\int_0^\infty \frac{dz'(1+z')}{H^3(z')}\right]^{-1} \tag{1.15}$$

The horizon grows with time, so that large fluctuations will at some time t_{enter} cover causally connected regions. Such fluctuations do not grow until matter domination (the time in the Universe when the global equation of state changes to w $\approx$ 0). This particular time (corresponding to a redshift of roughly $z \sim 3 \times 10^3$) is called matter-radiation equality and leaves an imprint in the present day clustering pattern of galaxies. In the radiation dominated era the expansion rate is too high for cosmological structures to form.

With dark matter contributing a significant portion to the energy density, the time frame that coincides with our observational capacity is not quite dominated by the cosmological constant yet. Ω_m contributes to late time structure growth, while Ω_Λ hinders growth (until it dominates and structure formation comes to a halt). This yields an integral that cannot be solved analytically, Equation (1.15), but has the following fitting formula

$$g(a) = \frac{5}{2}\Omega_m(a)\left[\Omega_m^{4/7}(a) - \Omega_\Lambda(a) + \left(1+\frac{1}{2}\Omega_m(a)\right)\left(1+\frac{1}{70}\Omega_\Lambda\right)\right]^{-1} \tag{1.16}$$

(Carroll et al., 1992), which is often referred to as the growth function and provides an approximation to the growing mode solution, so that

$$\delta(a) = \delta(0)a\frac{g(a)}{g(a_0)}, \tag{1.17}$$

provided $\delta \ll 1$.

The Power Spectrum

Inflation predicts the primordial density field to be a scale-invariant Gaussian random field (Zel'dovich, 1970). Its statistical properties are fully described by

the power spectrum

$$P(\mathbf{k}) = \langle |\delta(\mathbf{k})|^2 \rangle, \tag{1.18}$$

where $\delta(\mathbf{k})$ is the Fourier transform of $\delta(\mathbf{x})$. Since structure formation can be cast in terms of the functional form of the power spectrum $P(k, z)$, it is a topic of much theoretical investigation and used throughout all fields of cosmology.

It is common to express the power spectrum in its dimensionless form

$$\Delta^2(k) = \frac{4\pi k^3 P(k)}{(2\pi)^3}. \tag{1.19}$$

The scale-invariant power spectrum can be shown to obey $P(k) \propto k$ (or $\Delta^2(k) \propto k^4$). This can be seen by first writing the power spectrum as a featureless power law $\langle |\delta(\mathbf{k})|^2 \rangle \propto k^n$, where n is the spectral index. In this form there is no preferred length scale, as expected in the early Universe. The spectral index n quantifies how much large- versus small-scale power there is. For too large n there will be too much inhomogeneity on large scales, while too small n results in too much mass being converted into primordial black holes. These arguments lead to $n \approx 1$ (Zeldovich, 1972) and CMB observations agree with this prediction (e.g. Planck Collaboration et al., 2013a).

The Poisson equation relates the gravitational potential $\delta\Phi$ to the density field

$$\nabla^2 \Phi = 4\pi G \rho \delta, \tag{1.20}$$

so that, upon taking the Fourier transform, we have

$$\Phi_k = -4\pi G \rho \delta_k k^{-2}. \tag{1.21}$$

Hence, $\delta_k \propto k^2 \Phi_k$, from which it follows that $P_\delta \propto k^4 P_\Phi$. If $n = 1$, then $P_\Phi \propto k^{-3}$, and Δ^2_Φ is a constant. This means that, for $n = 1$, the Universe is equally smooth or wrinkled, regardless of scale.

Structure growth increases the amplitude of the fluctuations and boosts power at all scales. However, since small fluctuations do not grow in the radiation dominated era (depending on the time they enter the growing horizon and the redshift of matter-radiation equality), there is a turnover in the power spectrum at higher k modes (small wave lengths). Additionally, at early times the particles travel at relativistic velocities, so that free streaming damps small-scale

fluctuations. The overall modification to the initial power spectrum that arises from radiation pressure and damping is encoded in the Transfer function T, so that

$$P(k, z) = T^2(k, z)P(k, z_{\rm ref}), \tag{1.22}$$

where $z_{\rm ref}$ corresponds to the time of initial conditions, before structure growth. Since hot dark matter (HDM) is relativistic, while cold dark matter (CDM) is not, CDM perturbations can start growing at earlier times than HDM perturbations. Only the very large HDM perturbations are prevented from being erased by free streaming. The suppression of baryon fluctuation growth due to free streaming is called Silk damping. Baryon perturbations oscillate from a battle between radiation pressure and gravity, causing modulations in the transfer function. Clearly, the Transfer function is different for the type of matter considered and the generally accepted model is one with CDM, radiation, neutrinos, and baryons.

The oscillations in the baryon fluid prior to recombination are referred to as Baryon Acoustic Oscillations (BAO), see also Section 1.2.4. Through gravity BAO also affect dark matter. This process has left an observable imprint in the clustering pattern of galaxies today (Eisenstein et al., 2005). The study of BAO in the distribution of galaxies is one example of how the Fourier transform of the power spectrum, the autocorrelation function, can be preferential in describing cosmological density fields. The autocorrelation function is commonly referred to as just the correlation function and is defined as

$$\xi(\mathbf{r}) \equiv \langle \delta(\mathbf{x})\delta(\mathbf{x}+\mathbf{r}) \rangle. \tag{1.23}$$

Its relation to an isotropic power spectrum in three dimensions is

$$\xi(r) = \frac{V}{(2\pi)^3} \int P(k) \frac{\sin(kr)}{kr} 4\pi k^2 {\rm d}k, \tag{1.24}$$

where V is the normalisation volume. While BAO are detected in the correlation function as a bump (with some width) around a characteristic r, it forms oscillations in the power spectrum. In reality the bump is smeared out by various processes, washing out the oscillations in the power spectrum and hampering detection.

The normalisation of the power spectrum is quantified by σ_8, defined as the root

mean square matter density variation within spheres of radius $R = 8h^{-1}\text{Mpc}$

$$\sigma_R^2 = \int_0^\infty \frac{3}{k(kR)^3} \left[\sin(kR) + kR\cos(kR)\right] \Delta^2(k) dk. \tag{1.25}$$

Recently the value of σ_8 has been determined to high accuracy by Planck Collaboration et al. (2013c), who quote $\sigma_8 = 0.8344 \pm 0.027$.

Non-linear Structure Formation

The linear transfer function does not properly take into account the collapse of small scale fluctuations and growth from accretion, which become important when the field departs from its Gaussian birth. The rare high density peaks are important to model, because they turn into the observable, albeit biased, galaxy groups and clusters.

The modelling of the growth of non-linear densities is much more complicated, but can be studied with N-body simulations. In this approach particles in a box act as matter in the Universe. For each particle the equation of motion is solved to find the positions and velocities after incrementing the time by a small amount. This process starts at some high redshift (when the power spectrum was approximately linear) and continued until the field has evolved to a desired redshift.

Fitting formulae have been invented for the non-linear power spectrum from such N-body simulations and provide the current approach to modelling the power spectrum (Harnois-Déraps et al., 2014; Peacock and Dodds, 1996; Smith et al., 2003; Takahashi et al., 2012). A disadvantage of N-body simulations is the large computation time, while it is often required to know the dependence of the power spectrum on the various cosmological parameters. In this respect it is worth mentioning the Coyote emulator (Heitmann et al., 2010), which takes a limited amount of high precision N-body simulations to predict the power spectrum for a set of cosmological parameters. Although physically motivated, in the end the models are judged by how well they fit the simulations.

The construction of N-body simulations is a challenging subject. Each particle represents a collection of much less massive particles and collisions have to be prevented by softening the $1/r^2$ law of gravity. With more particles the softening length can be reduced and smaller scales are more accurately modelled. On small

scales there are resolution problems as well as increased physical complexity due to galaxy formation and feedback processes. There is an ongoing attempt to accurately combine large dark matter simulations with hydrodynamic simulations that include baryons (e.g. Wiersma et al., 2009). The problem with just dark matter simulations is that it is impossible to accurately model the very small scales, whereas with hydrodynamic simulations the box size is too small to account for large density modes that may affect galaxy formation (e.g. Kereš et al., 2012).

1.1.3 Dark Energy

The standard ΛCDM model is compatible with the vast majority of astronomical data. The few parameters involved are measured with high consistency over a wide range of cosmological probes (Weinberg et al., 2013).

The physical mechanism for the accelerated expansion, which in ΛCDM cosmology is Λ, is generically referred to as dark energy. From the perspective of General Relativity Λ is simply a free parameter that describes astronomical data very well. However, Λ imposes a fundamental problem, which is often referred to as the 'cosmological constant problem' (Weinberg, 1989); the density as calculated from the zeropoint energy of a vacuum is, according to Planck scales (or electroweak scales), approximately 120 (or 60) orders of magnitude larger compared to what Λ implies. This extreme discrepancy is one of the main problems in physics and has resulted in a plethora of dark energy scenarios, of which the most important are summarised here, but for a review see Yoo and Watanabe (2012).

Quintessence

Quintessence replaces Λ by the energy density of a field ϕ with potential $V(\phi)$. The potential requires fine tuning in order to explain late time acceleration. The introduction of a scalar field makes the dark energy density time dependent, and can therefore be constrained with observations of an evolving dark energy equation of state, e.g. $\mathrm{w} = \mathrm{w}_0 + \mathrm{w}_1(1 - a)$.

There are two main problems with Quintessence: (1) until a physical explanation of the potential is provided it remains arbitrary, and (2) it does not explain $\Lambda = 0$. However, it forms a possibility and deserves observational assessment. There is

as yet no evidence that suggests a dynamical form of dark energy.

Alternative Geometries

Dark energy may be a manifestation of modified geometry with respect to the Robertson-Walker metric (1.2) in such a way that we live in an underdense region. For example, the symmetry properties of the cosmological principle can be replaced by spherical symmetry around us. This is the Tolman-Bondi-Lemaitre Universe. What appears to be accelerated expansion is explained as the gravitational attraction of matter away from us. This requires the observer to be at a special place, that is, the centre of a huge spherical structure. Not only does this model violate the Copernican principle, it also involves fine-tuning.

Claims of inhomogeneity as an explanation for the apparent acceleration of the Universe are frequent in astrophysics, because it is a relatively simple way of saving the laws of physics without the need for Λ. For example, there were claims of a 'dark flow' (Kashlinsky et al., 2008) of galaxy clusters towards a specific position on the sky, based on CMB data. This is refuted with the latest Planck results. Generally, such claims come and go in the literature. A more recent example is the discovery of a large structure, claimed to be in conflict with the cosmological principle (Clowes et al., 2013).

The Multiverse

The existence of carbon-based life on Earth was reason for Hoyle et al. 1953 to predict an excited state of the carbon nucleus such that it resonates with the energy level of three alpha particles. Without this resonant state, the reaction rate of heavy elements would be too slow in order for there to be sufficient elements for life to evolve. This was not the first time that the presence of life on Earth had astronomical implications. In the 19th century biologists provided a lower limit on the age of the Universe, since for life to have evolved up to human beings requires a certain amount of time, which was greater than the age of the Earth as predicted by Lord Kelvin from the cooling time (since Earth's radioactivity was not taken into account).

The idea that the existence of observers influences the global properties of the Universe is called the anthropic principle, and, combined with the idea of

a multiverse, solves fine tuning and coincidence problems. If there are 10^{100} universes, than it is no surprise that we find ourselves in one with exactly the right natural constants. With no empirical evidence, the multiverse remains a hypothesis, although perhaps the same applies to the idea of one universe.

Modified Gravity

The observed accelerated expansion may also be a manifestation of beyond-Einstein gravity. Such theories are designed to be indistinguishable from General Relativity on astrophysical scales, but differ on cosmological scales. To construct a modified gravity theory is a difficult task, given the success of General Relativity in the solar system, as well as the observed orbital decay of the binary pulsar PSR B1913+16, and the precession of Mercury's orbit, see for example Weinberg et al. (2013). Here we describe a tiny fraction of the numerous ways of modifying general relativity. For a review of modified gravity scenarios see Clifton et al. (2012).

Braneworld theories avoid the need of a cosmological constant by adding an extra dimension to account for accelerated expansion (Dvali et al., 2000; Klein, 1926; Randall and Sundrum, 1999). Branes are extended objects of higher dimension than strings, which themselves are the hypothetical fundamental objects that through vibrations can account for the variety of particles in the Universe. The open strings have their endpoints attached to branes (these are the standard model particles like fermions and bosons), whereas gravitation acts by means of closed strings, which can move freely in the higher-dimensional spacetime. The complexity of string theory makes it difficult for observational cosmology to find useful constraints. Consequently, an active field of research is the translation of string theory to observables, and vice versa (e.g. Wands, 2006).

An important class of theories is $f(R)$ gravity, where f is some function of the Ricci scalar R. An important consequence is an effectively time and scale dependent gravitational constant $G(t)$. Although it is not straightforward to invent functions for $f(R)$ that satisfy solar system constraints, there is a broad class of theories available, some of which are indistinguishable from general relativity but lack similar motivation. A common approach is to Taylor expand the functions $f(R) = c_0 + c_1 R + c_2 R^2 + ...$, such that in general relativity with cosmological constant we have $c_0 = \Lambda$ and $c_1 = 1$, and for $f(R)$ we have nonzero c_2

(e.g. Berry and Gair, 2011). From this perspective it seems that Λ is the simplest form of $f(R)$ gravity (apart from general relativity itself without a cosmological constant).

Tensor-Vector-Scalar gravity (TeVeS Bekenstein, 2004) is yet another theory and is the relativistic generalisation of Modified Newtonian Dynamics (MOND Milgrom, 1983). The strongest evidence for dark matter, the bullet cluster, refutes the simplest forms of TeVeS convincingly (Markevitch et al., 2004). This is a merging system in which the collisionless dark matter is only gravitationally affected by the merger, while the X-ray gas interacts via pressure and gravity. This results in an offset between the X-ray contours observed from space with Chandra and the mass contours from gravitational lensing. Perhaps even stronger evidence against TeVeS comes from small scales; Seifert (2007) showed that in a universe described by TeVeS stars can only exist for about 2 weeks.

1.2 Cosmological Probes

Observational cosmology is hampered by cosmic variance (the fact that we have only one observable Universe), hence the experiment cannot be repeated (without resorting to N-body simulations). Fortunately, the Universe is large and varied enough, and our minds creative enough, to tackle its physics from various angles. The cosmological probes that have made an important impact are briefly summarised here to paint the picture of where we are in our current understanding.

1.2.1 CMB Anisotropies

CMB anisotropies had long been predicted from the idea that the structures that we see today are the result of fluctuations at earlier times. The fluctuations have to be present in the density field at the redshift of last scattering, and therefore present in the map of the CMB temperature. This is the idea of gravitational instability. As well as balloon-borne instruments, such as BOOMERanG (Lange et al., 2001), the three satellites COBE (Cosmic Background Explorer) (Smoot et al., 1992), WMAP (Wilkinson Microwave Anisotropy Probe) (Spergel et al., 2003) and Planck (Planck Collaboration et al., 2013c) have been key in establishing the standard model of cosmology.

The average temperature of the CMB is $\langle T \rangle = 2.73$ K and the fluctuations $\delta T/T$ are defined with respect to this

$$\frac{\delta T}{T} = \frac{T - \langle T \rangle}{\langle T \rangle}. \tag{1.26}$$

The isotropy of the CMB is reflected in the root mean square temperature fluctuations as $\langle (\delta T/T)^2 \rangle^{1/2} \sim 10^{-5}$. Edinburgh's Blackford Hill would be too high a mountain on an equally isotropic Earth (even the Netherlands do not possess acceptable geography).

The CMB temperature map consists of primary and secondary anisotropies. The primary anisotropies are directly related to the density fluctuations of the Universe at the time of recombination, when the photons for the first time free streamed in a slightly anisotropic density field, while the secondary anisotropies are the result of the scattering of photons as they travel through the Universe.

Primary Anisotropies

When the photons free stream out of the last-scattering shell they are gravitationally red- and blueshifted, depending on the density fluctuations, causing the primary anisotropies. The density fluctuations also affect the time of recombination; a higher local density means that it is less redshifted, since, locally, recombination occurs later. The last important effect arises from the nonzero velocity field, causing Doppler shifts in temperature and frequency.

The Fourier transform of the temperature correlation function gives the ensemble average power C_ℓ. Figure 1.1 shows the quantity $\ell(\ell+1)C_\ell/2\pi$ from Planck which would be constant in the case of a scale-invariant spectrum.

The peaks in C_ℓ in Figure 1.1 are the result of acoustic waves in the photon-baryon fluid at the time of last-scattering, as discussed in 1.1.2. The positions as well as their heights depend on the cosmological model. The position of the first peak, when combined with a measure of the Hubble constant, is in very good agreement with a flat Universe. The second peak is at a harmonic position of the first peak and its height relative to the first and third (and fifth ...) is sensitive to the amount of baryons in the oscillating fluid. Baryons also affect the positions of the peaks, as well as how C_ℓ decreases at high multipoles. Overall the amount of baryons indicated by the CMB is quite large, but in good agreement with

predictions from Big Bang nucleosynthesis. Some of the constrained parameters by Planck are given in Table 1.1.

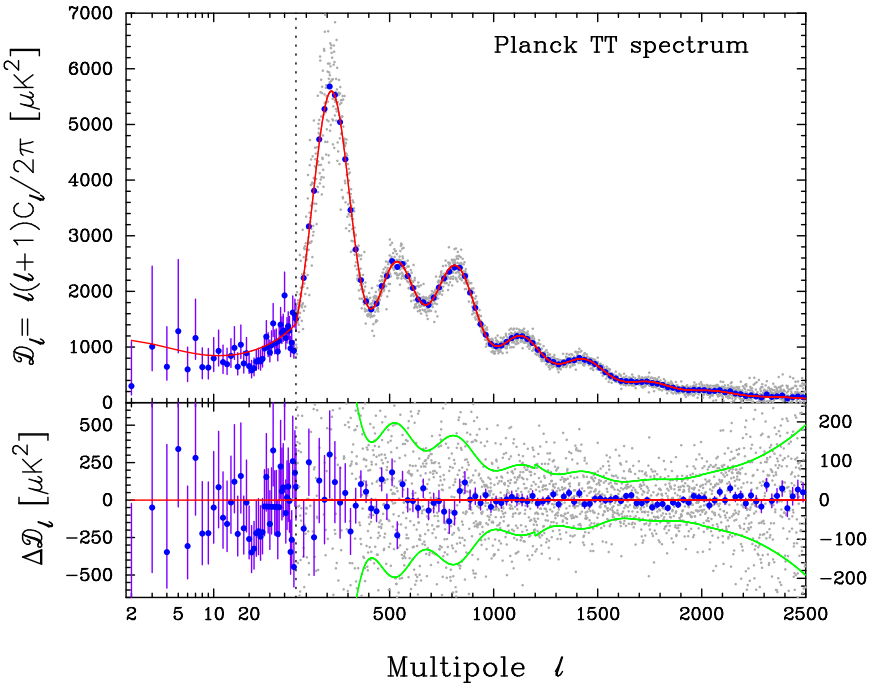

Figure 1.1 *Planck's temperature power spectrum taken from Planck Collaboration et al. (2013c). The blue points are the temperature multipoles binned in $\Delta\ell = 31$, while the grey points represent the power spectrum multipole by multipole. The red line is the best-fit ΛCDM prediction. Residuals with respect to the best fit ΛCDM model are shown in the lower panel. The green line describes the $\pm 1\sigma$ region of the model.*

Secondary Anisotropies

CMB photons are scattered along the line of sight, causing what are called secondary anisotropies. The most important are the Integrated Sachs-Wolfe effect (Sachs and Wolfe, 1967) and the Sunyaev-Zeldovich effect (Zeldovich and Sunyaev, 1969).

In an evolving universe with either nonzero Λ or non-unity Ω the gravitational potential changes along the path of the photon, causing a change in redshift. At the time of last scattering the radiation density is high enough to affect the expansion and contribute to the Integrated Sachs-Wolfe effect. More importantly, at late times, $z \lesssim 2$ the Universe becomes dominated by Λ and enters a phase of accelerated expansion, changing the gravitational potential along the photon

Table 1.1 *Cosmological parameters from Planck*

$\Omega_b h^2$	$\Omega_c h^2$	Ω_Λ	H_0 [km Mpc^{-1} s^{-1}]
0.02217 ± 0.00033	0.11805 ± 0.0031	0.693 ± 0.019	67.9 ± 1.5

(Planck Collaboration et al., 2013a) The temperature anisotropies map measured by Planck is in good agreement with a spatially flat 6 parameter ΛCDM model. The baryon density $\Omega_b h^2$ and dark matter density $\Omega_c h^2$ are both part of this model, while the Hubble constant H_0 and the normalisation of the power spectrum σ_8 are derived quantities. Only Planck data (temperature and lensing) were used for the values quoted here.

trajectories, and hence their temperatures. Nonlinear structure formation also affects the gravitational redshifting of the photons, and is often referred to as the Rees-Sciama effect (Rees and Sciama, 1968).

The Sunyaev-Zeldovich effect is a scattering of low energy photons (most abundantly the CMB photons) with hot electrons trapped in the potential wells of galaxy clusters. The CMB photons travelling through the clusters interact via Compton scattering with the hot electrons to see their spectrum distorted. At frequencies of ~ 150 GHz the Sunyaev-Zeldovich effect imprints a clear signature in the spectrum of the CMB. Although a distortion, the effect provides a redshift independent sensitivity to the detection of galaxy clusters, only limited by cluster mass (which is redshift dependent). An all-sky survey based on Planck data has provided a unique statistically complete sample of galaxy clusters Planck Collaboration et al. (2013b), of which a subsample has already been used for cosmological parameter estimation (Planck Collaboration et al., 2013d), finding inconsistent results with CMB-only constraints.

1.2.2 Supernovae Type Ia

Supernovae type Ia (SNe Ia) explosions are a particular physical event in which a carbon-oxygen white dwarf accretes mass from a companion star to ignite again and in some cases cause a supernova explosion. Although this is a stellar event, the light intensity over time (light curve), is conveniently related to luminosity, and hence provides a measure of the luminosity distance when calibrated against local SNe Ia. SNe Ia can be used as calibrated standard candles and have led to the discovery that the expansion of space is accelerating (Perlmutter et al., 1999; Riess et al., 1998), although, prior to these results, Efstathiou et al. (1990) proposed $\Lambda \neq 0$ from the APM galaxy survey by measuring the power spectrum,

and Jackson and Dodgson (1997) used compact radio sources as standard rulers to show nonzero Λ was favoured.

The luminosity distance for a flat Universe is given by

$$\begin{aligned} d_{\mathrm{L}} &= \sqrt{\frac{L}{4\pi f}} \\ &= (1+z)\int_0^z \frac{dz'}{H(z')}, \end{aligned} \tag{1.27}$$

where f is the observed flux. The evolution of the Hubble parameter is given by the Friedmann equation, as described in Section 1.1.1. In the case of dark energy with a varying equation of state $\mathrm{w}(z)$ the Friedmann equation can be written as

$$H(z)^2 = H_0^2\left[\Omega_k(1+z)^2 + \Omega_m(1+z)^3 + \Omega_v e^{3\int_0^z \frac{1+\mathrm{w}(z')}{1+z'}dz'}\right], \tag{1.28}$$

where Ω_v is the dark energy density. Constraining the dark energy equation of state parameter from d_{L} requires high accuracy measurements and solid understanding of the intrinsic scatter in the SNe Ia population.

Claims of accelerated expansion from SNe Ia need careful consideration of systematics. Dust in the host galaxy can result in dimming of the supernova. Since the properties of galaxies evolve with redshift, this needs to be taken into account (Branch et al., 1996). Evolution of the supernova properties, e.g. due to metallicity, have to be examined, but results so far are consistent with no difference in light curves between high redshift and low redshift samples (e.g. Aldering et al., 2000). Gravitational lensing also affects the luminosities, but can be accounted for by studying the galaxy distributions (Jönsson et al., 2006). And finally, K-correction causes some scatter in the population due to uncertainties from instrumentation (Kim et al., 1996).

1.2.3 X-Ray Galaxy Clusters

Galaxy clusters trace the rare high density peaks of the matter field. Their growth over cosmic time and distribution in space is sensitive to cosmological parameters (e.g. Borgani and Guzzo, 2001).

The very massive, relaxed clusters are large enough to be representative (in some respects) to the global properties of the Universe. This idea has been applied to

the baryon fraction (Sasaki, 1996) and has led to the first independent detection of accelerated expansion (Allen et al., 2002) after the famous SNe Ia results. The baryon fraction was derived from X-ray spectroscopy, luminosity, and lensing observations of the mass profile. False cosmological assumptions would lead to artificial redshift dependence of the baryon fraction, allowing for cosmological parameter constraints.

The X-ray Luminosity Function (XLF) can be translated to the halo mass function, the comoving volume density of objects as a function of mass $dN/dVdM$, where N is the number of objects, V the comoving volume and M the mass. The number of massive clusters compared to low mass clusters evolves with redshift and is sensitive to the details of hierarchical structure formation. Additionally, the comoving volume element dV is sensitive to $H(z)$, which carries dependence on Ω_m and Ω_Λ.

The evolution of the mass function can be probed with galaxy redshift surveys, see Section 1.2.4, and from the X-ray Luminosity Function (XLF). X-ray cluster surveys probe high redshifts, have high statistical completeness, and do not suffer from uncertainties that arise from identifying galaxies that belong to the cluster. However, the relation between luminosity and mass of a sample of clusters exhibits an intrinsic scatter, which reflects the various non-gravitational contributions to the energy budget, such as mergers, cooling flows and contamination from galaxies with an active galactic nucleus (AGN). This scatter results in a bias when relating mass to luminosity (flux-limited samples have a relatively large fraction of high L/M clusters), and is important to understand for cosmological studies (Maughan et al., 2007).

Mantz et al. (2008) constrain dark energy from the XLF along with a mass relation that has been calibrated with hydrodynamical simulations. It is the first such study and with the new X-ray observatory eROSITA (Merloni et al., 2012) it is expected that XLF studies will remain important for studying the growth of structure.

1.2.4 Galaxy Redshift Surveys

Galaxy surveys aim to map the large scale structure and constrain cosmological parameters by simultaneously measuring distances and the evolving distribution of matter. The density of galaxies is thought to be a function of the matter

density and with knowledge of this relation, called galaxy bias (see Chapter 2), the distribution of galaxies is one of the most powerful probes of gravity.

On large scales, galaxy bias is assumed to be a simple linear mapping from matter to galaxies. One of the main aims of this thesis is to critically assess this by looking at the distribution of galaxies of the Baryon Oscillations Spectroscopic Survey (BOSS) and the WiggleZ Dark Energy survey, relative to what is expected from lensing, see Section 1.2.5.

The bias is dependent on galaxy type, although mainly through correlation with galaxy mass, which galaxy bias depends mainly on (e.g. Norberg et al., 2002). Luminous Red Galaxies (LRGs) are passive elliptical galaxies which sit more towards the centre of density peaks and are more strongly clustered than dark matter, while blue emission line galaxies (BEGs) are star forming galaxies and are less strongly clustered. It can be argued that LRGs are more suitable for BAO work, because of the high bias, while blue galaxies are better tracers for linear clustering and Redshift Space Distortions (see below).

Apart from galaxy bias, galaxy surveys require accurate theoretical predictions of the non-linear power spectrum. Non-linear clustering is also important for the modelling of Redshift Space Distortions, the Baryon Acoustic Oscillations peak, and higher order statistics. An alternative approach to tackling the complexity of non-linearities has been proposed by Simpson et al. (2011). They have invented a clipping technique in which high density peaks are discarded to obtain a clipped power spectrum that is in shape remarkably similar to the linear power spectrum. It is expected that this approach, which can in principle be incorporated into other cosmological probes, will provide a strong alternative to measuring the dark energy equation of state parameter.

The wealth of data produced by galaxy surveys reveals the 'cosmic web', or better 'cosmic sponge'[1], of clusters and filaments and can be analysed in many ways; the most important for dark energy are summarised here. The probes discussed in this and the previous section are included in the science goals of EUCLID (Laureijs et al., 2011).

[1] As mentioned in a talk by Fergus Simpson, Melbourne, 2012

Redshift Space Distortions

The clustering of galaxies in redshift space is different from real space due to peculiar motions (Kaiser, 1987), induced in two ways: (1) galaxy motions within galaxy clusters and (2) the growth of structure. This produces a measurable anisotropic effect of which an example is shown in Figure 1.2, taken from Samushia et al. (2013), which shows the two-dimensional correlation function of galaxies from BOSS, showing a different clustering pattern parallel to the line of sight, $r_\parallel$, compared to the perpendicular separation $r_\perp$.

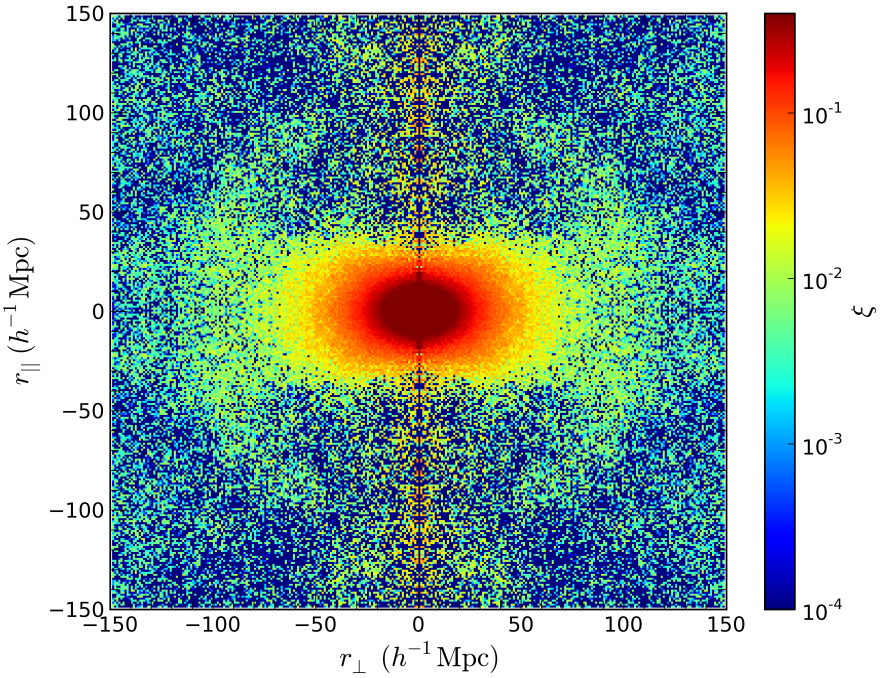

Figure 1.2 *The clustering of galaxies from BOSS along and perpendicular to the line of sight, taken from Samushia et al. (2013). This pattern visualises the contribution to velocities from the growth of structure, affecting the redshift inferred separations along the line of sight.*

This apparent anisotropy can be modelled, allowing for constraints on the growth rate

$$f = \frac{d\ln D}{d\ln a}, \tag{1.29}$$

where D is the growth factor, eq. (1.15). To good approximation

$$f = {\Omega_m}^\gamma, \tag{1.30}$$

with γ depending on the theory of gravity Linder (2005), e.g. $\gamma \simeq 6/11$ for general relativity. Hence, in the matter dominated era $f = 1$. This section derives the

Kaiser formula and summarises the main results so far.

Consider a distant region in space which covers a small angle on the sky, such that radial distortions are all on the same axis. The relation between the linear displacement field $\boldsymbol{x}$ and the velocity field $\boldsymbol{u}$ of dark matter is

$$\begin{aligned}
\boldsymbol{u} &= \frac{d\boldsymbol{x}}{dt} && (1.31)\\
&= \frac{a}{a}\frac{\boldsymbol{x}}{\boldsymbol{x}}\frac{da}{da}\frac{d\boldsymbol{x}}{dt} && (1.32)\\
&= \left(\frac{da}{dt}\frac{1}{a}\right)\left(\frac{a}{\boldsymbol{x}}\frac{d\boldsymbol{x}}{da}\right)\boldsymbol{x} && (1.33)\\
&= \left(\frac{da}{dt}\frac{1}{a}\right)\left(\frac{d\mathrm{ln}\boldsymbol{x}}{d\mathrm{ln}a}\right)\boldsymbol{x} && (1.34)\\
&= Hf\boldsymbol{x}, && (1.35)
\end{aligned}$$

where we used the Zeldovich approximation to relate the amplitude of the displacement field to the density perturbation.

The apparent distance to the region in space as inferred by the cosmological redshifts is

$$\boldsymbol{r}_{\mathrm{app}} = \boldsymbol{r} + (\hat{r}\cdot\boldsymbol{u}/H)\hat{r} \tag{1.36}$$

The direction of $\boldsymbol{r}$ is $\hat{r}$ and the direction of $\boldsymbol{u}$ is $\hat{k}$. If we define $\mu \equiv \hat{k}\cdot\hat{r}$, we have

$$\boldsymbol{r}_{\mathrm{app}} = \boldsymbol{r} + (\mu u/H)\hat{r}, \tag{1.37}$$

When a plane wave disturbance runs at some angle to the line of sight, it will produce a displacement field $\boldsymbol{x}$ in the direction of the wave $\boldsymbol{k}$. The apparent displacement is

$$\begin{aligned}
\boldsymbol{x}_{\mathrm{app}} &= \boldsymbol{x} + (\hat{r}\cdot\boldsymbol{u}/H)\hat{r} && (1.38)\\
&= \boldsymbol{x} + (\hat{r}fx\hat{k})\hat{r} && (1.39)\\
&= \boldsymbol{x} + (f\mu x)\hat{r}. && (1.40)
\end{aligned}$$

To find the component of this along $\hat{k}$ we multiply the second term by $\hat{k}\cdot\hat{k} = 1$

$$\boldsymbol{x}_{\rm app} = x\hat{k} + [f\mu x(\hat{k}\cdot\hat{k})]\hat{r} \tag{1.41}$$
$$= (x)\hat{k} + (f\mu^2 x)\hat{k} \tag{1.42}$$
$$= x(1+f\mu^2)\hat{k} \tag{1.43}$$

In the Zeldovich approximation the apparent density perturbation due to this mode is directly proportional to the amplitude of the apparent displacement (along $\hat{k}$). Using C as the constant of proportionality, we can write for the fractional overdensity in redshift space (^{s}) and real space (^{r})

$$\delta^s = C \times x_{\rm app} \tag{1.44}$$
$$= C \times x(1+f\mu^2) \tag{1.45}$$
$$= \delta^r(1+f\mu^2). \tag{1.46}$$

When taking into account the galaxy bias (for more details see Section 2.2), the RSD effect can be written in terms of the power spectrum of galaxies in redshift space P^s_{gg}, which is known as the Kaiser formula

$$P^s_{gg}(k) = b^2 P^r_{mm}(1+f\mu^2/b)^2. \tag{1.47}$$

That is, the growth rate f is measured by looking at the difference between the clustering along and perpendicular to the line of sight; in an isotropic Universe and no growth of structure they should be the same.

The formalism works only for large physical scales. At non-linear scales there are two issues. Firstly, the growth equation is non valid. With decreasing physical scale, the growth of structure becomes more dominated by complex physics. Secondly, at small scales the peculiar velocity contribution to the redshift is due to motions within groups and clusters. This is called the Fingers of God effect, since all structures seem to be pointed towards the observer when redshifts are converted to distances, based on the Hubble flow.

Baryon Acoustic Oscillations

Baryon Acoustic Oscillations (BAO) are statistical standard rulers; the geometry of space is probed by looking at a preferred scale in the correlation function or power spectrum. The idea to use this for cosmology was already noted by Shanks

et al. (1987) for the clustering of quasars (a type of distant galaxy with energetic AGN). They noted that if a feature exists in the correlation function of quasars and this can be detected at both low and high redshift, then it is possible to study the expansion of space.

In the case of BAO the preferred clustering scale is the result of sound waves in the early Universe. The idea to use this as a cosmological probe was proposed by Cooray et al. (2001) and Blake and Glazebrook (2003). Shortly after, it was put into practice with its first detection (Eisenstein et al., 2005). Earlier datasets contained some hints but were thought to be too weak to provide evidence of BAO (Eisenstein et al., 1998; Meiksin et al., 1999).

The BAO probe is related to the Alcock Packzinsky (AP) test (Alcock and Paczynski, 1979): for isotropic objects the comoving transverse distance equals the comoving radial distance. This distance, say L, can be written from the transverse dimension as $L = \Delta\theta \times (1+z)d_A(z)$ and from the radial dimension as $L = \Delta z \times c/H(z)$. Therefore, $\Delta z/\Delta\theta = (1+z)d_A(z)H(z)/c$ can be observed as a function of redshift. It was noted by Ballinger et al. (1996) that the AP test can also be applied to the (isotropic) clustering of galaxies.

The AP test does not require L to be known a priori, in which case the test is relative. BAO, however, can be thought of as an absolute AP test, because the preferred clustering scale (L) is known from the sound horizon $\sim$ 150Mpc, constrained by the CMB. This scale will be visible as the BAO peak in the correlation function. Matter-radiation equality and possible inflationary imprints can also provide an absolute AP test. However, by measuring the BAO peak at different (effective) redshifts, the BAO peak can also provide a relative AP test.

To measure the correlation function an input (fiducial) cosmology is required to convert redshifts to distances. The input cosmology also affects the location of the BAO peak. By using the constraints from the CMB and accurate modelling of the power spectrum, the 'dilation' from the input cosmology can be calculated. Eisenstein et al. (2005) proposed to use d_V, the average distance of galaxies in a sphere, which gives equal weight to the transverse and radial dilation. Averaging over all directions gives the quantity d_V

$$d_V(z) = \left[(1+z)^2 d_A(z)^2 \frac{cz}{H(z)}\right]^{1/3} \tag{1.48}$$

which contains $d_A(z)^2$ to represent the two directions on the sky, and $H(z)^{-1}$ from

the direction along the line of sight. d_V provides a robust distance scale against uncertainties in the cosmological model, since d_A and H cancel approximately at redshifts where the BAO is measured, so that the volume remains close to constant. The dilation coefficient α quantifies the distortion in the distance-redshift relation with respect to the fiducial value and is defined as

$$\alpha = \frac{d_{V,\mathrm{fid}}(z)}{d_V(z)}, \tag{1.49}$$

where $d_{V,\mathrm{fid}}$ uses the input cosmological model. With knowledge of the standard ruler scale, a χ^2 fit is performed to find α, which effectively shifts the measured BAO peak to the a priori known position and provides knowledge of d_A^2/H at an effective redshift given by the sample of galaxies.

BAO are one of the most promising tools for discovering the nature of dark energy. A scale dependent bias would shift the BAO peak and for some extreme scenarios, non-local galaxy formation can cause BAO-like wiggles in the power spectrum (Coles and Erdogdu, 2007). Also, d_V is only accurate for high b, since if β is large, see Section 1.2.4, then predominantly longitudinal modes are measured, so H rather than d_V.

1.2.5 Galaxy Imaging Surveys

The presence of the large scale structure distorts the null geodesics over which photons travel. This causes distortions in the shapes of distant galaxies (Gunn, 1967; Kristian and Sachs, 1966), probed with Galaxy Imaging Surveys. Lensing arcs and multiple images can appear around foreground galaxy clusters, in which case the regime of lensing is defined to be strong. The effect is, however, weak for the vast majority of galaxies.

Lensing studies the deformation in shapes of galaxies relative to the shapes before lensing. The lensing signal is contaminated by galaxies that feel each others gravitational field, so that they become intrinsically aligned (e.g. Heymans et al., 2004). This means that the galaxies are not entirely randomly distributed over the sky. This contamination can be suppressed by removing close galaxy pairs.

Weak Gravitational Lensing (WGL) is a probe of dark energy through the growth of perturbations and geometry of the Universe, see Equations 1.13 and 1.28. In this section the weak gravitational lensing formalism is briefly introduced. For

an excellent review see Hoekstra and Jain (2008). In Section 2.3 it will be shown how WGL and galaxy clustering can be used to measure galaxy bias parameters as a function of scale.

For reasons of practicality I have sketched the geometry of a lensing system, see Figure 1.3. It shows the relation between apparent position $\boldsymbol{\theta}$ and the position in the source plane $\boldsymbol{\beta}$, that is

$$\boldsymbol{\beta} = \boldsymbol{\theta} - \boldsymbol{\alpha}, \tag{1.50}$$

which is often called the reduced lensing equation. The apparent angular shift is α, related to the deflection angle $\widehat{\alpha}$ by $\alpha = \widehat{\alpha}(D_\mathrm{s} - D_\mathrm{d})/D_\mathrm{s}$.

Consider a light ray passing within distance ξ of a point mass M. According to general relativity, the path of the light ray will be deflected by an angle $\widehat{\alpha} = \frac{4GM}{c^2\xi}$, provided ξ is much larger than the Schwarzschild radius of the lens. If the gravitational field of a mass distribution $\rho(\boldsymbol{r})$ is weak, the field equations may be linearised, and the total deflection angle is approximated by the sum of a series of lens planes. Another approximation in gravitational lensing is the Born approximation: since the path of the deflected light ray near the lensing mass is only slightly curved on the scale of the gradient of the mass distribution, the light path is approximated as radial.

The lens distribution of galaxies is divided in cells of volume $\mathrm{d}V = \mathrm{d}m/\rho(\boldsymbol{r})$, where $\mathrm{d}m$ is assumed to act as a point mass. According to the Born approximation, a light ray propagating along the z-axis at $(\boldsymbol{\xi}, z)$, which passes through $\mathrm{d}V$, located at $(\boldsymbol{\xi'}, z')$, has impact parameter $\boldsymbol{\xi} - \boldsymbol{\xi'}$. Summing up each deflection gives the total deflection angle

$$\begin{aligned}\widehat{\alpha}(\boldsymbol{\xi}) &= 4\frac{G}{c^2}\sum \mathrm{d}m(\boldsymbol{\xi'}, z')\frac{\boldsymbol{\xi} - \boldsymbol{\xi'}}{|\boldsymbol{\xi} - \boldsymbol{\xi'}|^2} \\ &= 4\frac{G}{c^2}\int \mathrm{d}^2\xi' \int \mathrm{d}z'\rho(\boldsymbol{\xi'}, z')\frac{\boldsymbol{\xi} - \boldsymbol{\xi'}}{|\boldsymbol{\xi} - \boldsymbol{\xi'}|^2}\end{aligned} \tag{1.51}$$

The surface mass density over the plane of the lens distribution is defined to be $\Sigma(\xi) \equiv \int \mathrm{d}z\rho(\boldsymbol{\xi}, z)$, such that the deflection angle can be rewritten as

$$\widehat{\alpha}(\boldsymbol{\xi}) = 4\frac{G}{c^2}\int \mathrm{d}^2\xi'\,\Sigma(\boldsymbol{\xi'})\frac{\boldsymbol{\xi} - \boldsymbol{\xi'}}{|\boldsymbol{\xi} - \boldsymbol{\xi'}|^2} \tag{1.52}$$

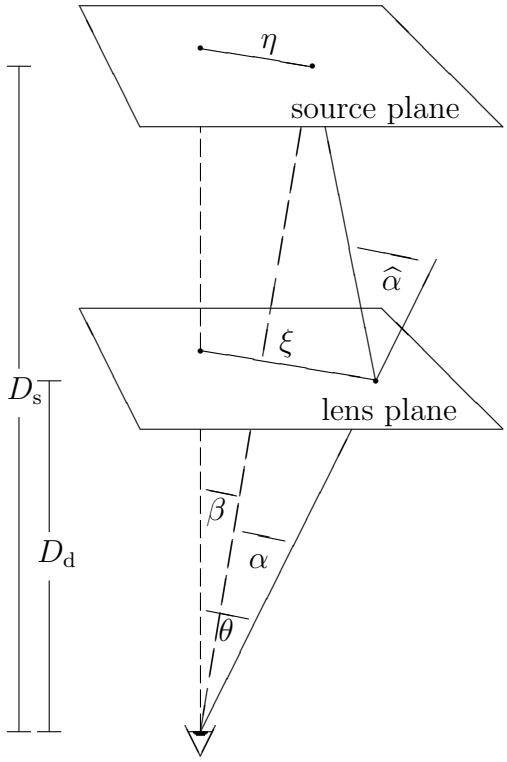

Figure 1.3 *A schematic of a lensed source. The two dimensional position of the source at distance D_s is represented by η. The impact parameter ξ is defined in the lens plane at distance D_d. A source at angle β will appear at angle $\theta = \beta + \alpha$. Since the distances need to be inferred from the angles and transverse physical sizes on a static Euclidean spatial background, it is natural to use angular diameter distances ($D_d = \xi/\theta$ and $D_s = \eta/\theta$).*

The surface mass density (Σ_{cr}) which yields multiple solutions to the lens equation for fixed β, and thus corresponds to an Einstein ring or multiple images will now be derived. Consider first the case of a circularly shaped lens with constant Σ. In this special case, the deflection angle at impact radius r is $\widehat{\alpha} = 4\pi\Sigma r/c^2$, similar to the point mass case with $M \to \Sigma\pi r^2$, and $\xi \to r$. In order to see an Einstein ring, we require $\alpha = \theta$. Since $\alpha = \widehat{\alpha} D_{\rm s}/(D_{\rm s} - D_{\rm d})$ and $r = \theta D_{\rm d}$, the above can be summarised as

$$\theta = \alpha = \frac{D_{\rm s} - D_{\rm d}}{D_{\rm s}} \frac{4G\Sigma_{\rm cr}\pi\theta D_{\rm d}}{c^2}$$

$$\Rightarrow$$

$$\Sigma_{\rm cr} = \frac{D_{\rm s}}{D_{\rm d}(D_{\rm s} - D_{\rm d})} \frac{c^2}{4\pi G} \tag{1.53}$$

Therefore we have

$$\alpha(\theta) = \frac{\Sigma}{\Sigma_{\rm cr}}\theta. \tag{1.54}$$

The ratio $\Sigma/\Sigma_{\rm cr}$ is the *convergence*, henceforth denoted κ. It distinguishes between strong lensing ($\kappa \geq 1$) and weak lensing ($\kappa \ll 1$).

$$\kappa(\boldsymbol{\theta}) \equiv \frac{\Sigma(\boldsymbol{\theta} D_{\rm d})}{\Sigma_{\rm cr}} \tag{1.55}$$

The scaled deflection angle α in terms of κ is given by

$$\boldsymbol{\alpha}(\boldsymbol{\theta}) = \frac{1}{\pi}\int {\rm d}^2\theta' \kappa(\boldsymbol{\theta}) \frac{\boldsymbol{\theta} - \boldsymbol{\theta'}}{|\boldsymbol{\theta} - \boldsymbol{\theta'}|^2} \tag{1.56}$$

Since κ is defined as a dimensionless surface mass density, it can be related via a Poisson equation to a gravitational potential, which is the *lensing potential* ψ, related to the deflection angle as $\boldsymbol{\alpha} = \nabla_\theta \psi$. Integrating (1.56) and using the identity $\nabla \ln \boldsymbol{a} = \boldsymbol{a}/|\boldsymbol{a}|^2$ we have

$$\psi(\boldsymbol{\theta}) = \frac{1}{\pi}\int {\rm d}^2\theta' \kappa(\boldsymbol{\theta'}) \ln|\boldsymbol{\theta} - \boldsymbol{\theta'}|, \tag{1.57}$$

such that the Poisson equation is

$$\nabla^2_\theta \psi(\boldsymbol{\theta}) = 2\kappa(\boldsymbol{\theta}) = \nabla_\theta \alpha(\boldsymbol{\theta}). \tag{1.58}$$

Convergence is sensitive to the isotropic focussing of light rays by the lens. Therefore, gravitational lensing can increase the size with which a galaxy appears on the sky. Together with Liouville's theorem of conservation of phase-space density for the photons emitted by the source, the surface brightness of the source will be conserved under lensing. This results in source magnification, quantified as the ratio of image area over source area: $\mu = \partial\theta^2/\partial^2\beta$. Shear is the term given to anisotropic focussing of light rays by the lens, and is responsible for changing the shape of the image as well as magnification. It is common to describe both phenomena by considering the 2×2 matrix of the lens map, termed

the magnification matrix. It turns out to have convenient symmetric properties.

$$\begin{aligned} A_{ij} &\equiv \frac{\partial \beta^i}{\partial \theta^j} \\ &= \delta_{ij} - \frac{\partial \alpha^i}{\partial \theta^j} \\ &= \delta_{ij} - \frac{\partial^2 \psi}{\partial \theta^i \partial \theta^j} \end{aligned} \tag{1.59}$$

The components of A can be decomposed into the observables convergence and the components of the complex shear, $\gamma = \gamma_1 + \mathrm{i}\gamma_2 = |\gamma| e^{2i\phi}$, where ϕ is the orientation.

$$\begin{aligned} \kappa &= \frac{1}{2}(\psi_{11} + \psi_{22}) \\ \gamma_1 &= \frac{1}{2}(\psi_{11} - \psi_{22}) = \gamma \cos(2\phi) \\ \gamma_2 &= \psi_{12} = \psi_{21} = \gamma \sin(2\phi), \end{aligned} \tag{1.60}$$

where

$$\psi_{ij} = \frac{\delta^2 \psi}{\delta \phi^i \delta \phi^j}. \tag{1.61}$$

Using (1.58) and (1.60) the magnification matrix in terms of κ and γ is

$$A = \begin{pmatrix} 1 - \kappa - \gamma_1 & -\gamma_2 \\ -\gamma_2 & 1 - \kappa + \gamma_1 \end{pmatrix}. \tag{1.62}$$

This allows the magnification parameter to be written as the inverse of A's determinant

$$\mu = \frac{1}{\det(A)} = \frac{1}{(1-\kappa)^2 - \gamma^2}. \tag{1.63}$$

The observations of image distortions suffer from the degeneracy of ellipticity, shear, and convergence, for which reason it is common to define the observable *reduced shear* as

$$g(\boldsymbol{\theta}) \equiv \frac{\gamma(\boldsymbol{\theta})}{1 - \kappa(\boldsymbol{\theta})}, \tag{1.64}$$

in terms of which A is

$$A = (1 - \kappa) \begin{pmatrix} 1 - g_1 & -g_2 \\ -g_2 & 1 + g_1 \end{pmatrix}. \tag{1.65}$$

In principle, this shows that for $\kappa = 1$ the source would be infinitely magnified. Substantial magnification has frequently been observed, but the approximation of

geometrical-optics fails in this critical case (Ohanian 1983), preventing the source from being infinitely magnified.

Weak Lensing

When considering the density field of the large scale structure, the lensing mass is described by a density function which extends from the source to the observer. The deflection of the light ray will accordingly be a function of radial distance w and the angle $\boldsymbol{\theta}$ at which it propagates.

General relativity provides the relation between the deflection angle and the gradient of the gravitational potential perpendicular to the light path.

$$\widehat{\alpha} = \frac{2}{c^2} \int \nabla_{\perp} \Phi \mathrm{d}z \tag{1.66}$$

The desired distance and angle information in Equation (1.66) will be derived from the difference in light propagation in unperturbed and perturbed Minkowski space. Consider the propagation equation of a pair of light rays, one fiducial and one at comoving seperation $\boldsymbol{x}$ travelling at an angle $\boldsymbol{\theta}$, in Minkowski space

$$\frac{\mathrm{d}^2 \boldsymbol{x}}{\mathrm{d}w^2} = \begin{cases} -K\boldsymbol{x} & \text{unperturbed space} \\ -\frac{2}{c^2}\nabla_{\perp}\Phi & \text{perturbed space} \end{cases} \tag{1.67}$$

Lensing requires that the rays at the location of the observer intersect, that is $w = 0$ corresponds to $\boldsymbol{x} = \mathbf{0}$, such that $\frac{\mathrm{d}\boldsymbol{x}}{\mathrm{d}w} = \boldsymbol{\theta}$. The solutions to Equation (1.67) are therefore

$$\boldsymbol{x} = \begin{cases} f_K(w)\boldsymbol{\theta} & \text{unperturbed space} \\ f_K(w)\boldsymbol{\theta} - \frac{2}{c^2}\int_0^w \mathrm{d}w' f_K(w-w')\nabla_{\perp}\Phi\left(\boldsymbol{x}, w'\right) & \text{perturbed space} \end{cases} \tag{1.68}$$

Since $f_K(w)\boldsymbol{\alpha} = \boldsymbol{x}_{\text{unperturbed}} - \boldsymbol{x}_{\text{perturbed}}$, the deflection angle angle is

$$\boldsymbol{\alpha} = \frac{2}{c^2}\int_0^w \mathrm{d}w' \frac{f_K(w-w')}{f_K(w)} \nabla_{\perp}\Phi\left(\boldsymbol{x}, w'\right) \tag{1.69}$$

Using (1.58) and noting that $\partial\theta = (f_K)^{-1}\partial x$, the effective convergence is

$$\kappa_{\rm eff} = \frac{1}{c^2}\int_0^w \mathrm{d}w' \frac{f_K(w-w')f_K(w')}{f_K(w)}\nabla_x^2\Phi\left(\boldsymbol{x}, w'\right) \tag{1.70}$$

Note that the effective convergence is a 3 dimensional function of θ_1, θ_2, and w. The projected version, which depends only on $\boldsymbol{\theta}$, is the 2D convergence $\bar{\kappa}_{\rm eff}$, and is related to $\kappa_{\rm eff}$ through

$$\bar{\kappa}_{\rm eff} = \int_0^\infty \mathrm{d}w' n(w')\kappa_{\rm eff}, \tag{1.71}$$

where $n(w)$ is the normalised source distribution and ∞ the horizon distance. It is useful to define the weighting function $g(w)$, which measures the lensing efficiency of a lens at distance w

$$g(w) = \int_w^\infty \mathrm{d}w' n(w')\frac{f_K(w'-w)}{f_K(w')} \tag{1.72}$$

Hence, the 2D effective convergence is given by

$$\bar{\kappa}_{\rm eff} = \frac{3H_0^2\Omega_m}{2c^2}\int_0^\infty \mathrm{d}w\, g(w)f_K(w)\frac{\delta\left(f_K(w)\boldsymbol{\theta}, w\right)}{a(w)} \tag{1.73}$$

where we have used the Poisson equation $\nabla_x^2\Phi = 3H_0^2\Omega_m\delta/2a$. The effective convergence power spectrum P_κ is the Fourier transform of the 2D correlation function of $\bar{\kappa}_{\rm eff}$. It is related to the matter power spectrum

$$P_\kappa(\ell) = \frac{9}{4}\left(\frac{H_0}{c}\right)^4\Omega_m^2\int_0^\infty \mathrm{d}w\frac{g^2(w)}{a^2(w)}P_\delta\left(\frac{\ell}{f_K(w)}; w\right), \tag{1.74}$$

(Bartelmann and Schneider, 1999). We can also derive the shear power spectrum P_γ. The Fourier transform pairs of Equation (1.60) are

$$\hat{\kappa}(k) = -\frac{1}{2}\left(k_1^2 + k_2^2\right)\hat{\psi}(k) \tag{1.75}$$

$$\hat{\gamma_1}(k) = -\frac{1}{2}\left(k_1^2 - k_2^2\right)\hat{\psi}(k) \tag{1.76}$$

$$\hat{\gamma_2}(k) = -k_1k_2\hat{\psi}(k) \tag{1.77}$$

We can define

$$\hat{\gamma}(k) = \lambda(k)\hat{\kappa}(k), \tag{1.78}$$

where $\lambda(k) = \lambda_1(k) + \mathrm{i}\lambda_2(k)$, with

$$\lambda_1(k) = \frac{k_1^2 - k_2^2}{k_1^2 + k_2^2} \tag{1.79}$$

$$\lambda_2(k) = \frac{2k_1k_2}{k_1^2 + k_2^2}. \tag{1.80}$$

The correlation function of the shear field is

$$\langle \gamma(\boldsymbol{x})\gamma^*(\boldsymbol{x}+\boldsymbol{\theta})\rangle = \frac{1}{(2\pi)^4}\int \mathrm{d}^2k\hat{\gamma}(\boldsymbol{k})e^{-i\,\boldsymbol{x}\cdot\boldsymbol{k}}\int \mathrm{d}^2k'\hat{\gamma}^*(\boldsymbol{k'})e^{i\,(\boldsymbol{x}-\boldsymbol{\theta})\cdot\boldsymbol{k}'}. \tag{1.81}$$

Noting that $\langle\hat{\kappa}(\boldsymbol{k})\hat{\kappa}^*(\boldsymbol{k})\rangle = (2\pi)^2\delta_D(\boldsymbol{k}-\boldsymbol{k}')P_\kappa(k)$, and using Equation (1.78), we have

$$\langle\gamma\gamma^*\rangle_\theta = \frac{1}{(2\pi)^2}\int \mathrm{d}^2k\lambda(\boldsymbol{k})\lambda^*(\boldsymbol{k})P_\kappa(k)e^{i\,\boldsymbol{\theta}\cdot\boldsymbol{k}}. \tag{1.82}$$

In the reference frame, $\boldsymbol{\theta} = (\theta, 0)$, we let α be the angle between $\boldsymbol{k}$ and $\boldsymbol{\theta}$, so that $\lambda = e^{2\,i\,\alpha}$ and $d^2k = k\,dk\,d\alpha$, giving

$$\langle\gamma\gamma^*\rangle_\theta = \frac{1}{(2\pi)^2}\int \mathrm{d}k\,kP_\kappa(k)\int \mathrm{d}\alpha e^{i\,\theta k\cos\alpha}. \tag{1.83}$$

Bessel functions of the first kind can be defined as

$$J_n(x) = \frac{1}{2\pi\,i^n}\int_0^{2\pi}\mathrm{d}\alpha e^{i\,x\cos\alpha}e^{i\,n\,\alpha}, \tag{1.84}$$

so that

$$\langle\gamma\gamma^*\rangle_\theta = \frac{1}{2\pi}\int \mathrm{d}k\,k\,P_\kappa J_0(k\theta), \tag{1.85}$$

Taking the Fourier transform of P_κ, we obtain the convergence correlation function

$$\langle\kappa\kappa^*\rangle_\theta = \frac{1}{(2\pi)^2}\int \mathrm{d}^2kP_\kappa(k)e^{i\,\boldsymbol{k}\cdot\boldsymbol{\theta}} \tag{1.86}$$

$$= \frac{1}{2\pi}\int \mathrm{d}k\,k\,P_\kappa(k)J_0(k\theta). \tag{1.87}$$

Comparing to the shear correlation function, we find $\langle\gamma\gamma^*\rangle_\theta = \langle\kappa\kappa^*\rangle_\theta$, hence

$$P_\kappa = P_\gamma. \tag{1.88}$$

Referring the shears to tangential axes and at 45° to the radius, with respect to each galaxy pair, we can use rotations $\gamma \to \gamma' = \gamma e^{-2i\psi} = -\gamma_t - i\gamma_\times$ to

define correlation functions with tangential and cross components, ξ_{tt} and $\xi_{\times\times}$ respectively: $\xi_{\pm}(\theta) = \xi_{tt} \pm \xi_{\times\times}$. This pair of correlations is related to the matter fluctuations through the convergence power spectrum

$$\xi_{+}(\theta) = \int_0^\infty \frac{d\ell}{2\pi} \ell P_\kappa(\ell) J_0(\ell\theta),$$
$$\xi_{-}(\theta) = \int_0^\infty \frac{d\ell}{2\pi} \ell P_\kappa(\ell) J_4(\ell\theta). \tag{1.89}$$

These correlation functions provide powerful tools to estimate P_κ and estimate cosmological parameters, since

$$P_\kappa(\ell) = \int_0^\infty \mathrm{d}\theta\theta\xi_{\pm}(\theta) J_{0,4}, \tag{1.90}$$

with the caveat that $\xi_{\pm}$ are in general only known for a limited range of angular separations, leading to errors in the estimations of $P_\kappa(\ell)$. This can be partly evaded by parameterising $P_\kappa(\ell)$ in band-powers.

In this thesis two galaxy imaging surveys are discussed: the Canada France Hawaii Telescope Lensing Survey (CFHTLenS) in Chapter 3 and the Red Sequence Cluster Lensing Survey (RCSLenS) in Chapter 4. RCSLenS has overlap with BOSS and WiggleZ, allowing us to study the galaxy bias of these spectroscopic samples.

E and B modes and the Aperture Mass Statistic

The tangential shear γ_t and cross shear $\gamma_\times$ with respect to the position on the sky $\boldsymbol{\theta}$ are given by

$$\gamma_t(\boldsymbol{\theta}') = -\mathrm{Re}\left(\gamma(\boldsymbol{\theta}')\mathrm{e}^{-2\mathrm{i}\phi}\right) \tag{1.91}$$
$$\gamma_\times(\boldsymbol{\theta}') = -\mathrm{Im}\left(\gamma(\boldsymbol{\theta}')\mathrm{e}^{-2\mathrm{i}\phi}\right), \tag{1.92}$$

where γ is the complex shear, ϕ determines the orientation of the shear $\boldsymbol{\vartheta} = \boldsymbol{\theta}' - \boldsymbol{\theta}$, so that, using the complex notation, $\vartheta_1 + \mathrm{i}\vartheta_2 = |\boldsymbol{\vartheta}|\mathrm{e}^{\mathrm{i}\phi}$. The ellipticity correlation functions $\xi_\pm$ can be written in terms of γ_t and $\gamma_\times$ as follows

$$\xi_{\pm}(\theta) = \langle\gamma_t(\theta+\theta')\gamma_t(\theta')\rangle \pm \langle\gamma_\times(\theta+\theta')\gamma_\times(\theta')\rangle. \tag{1.93}$$

In the presence of distortions not associated with lensing, shear correlations are produced that do not correspond to the projected density field κ. The distortions in the measurement can be characterised via E/B decomposition. To first order, lensing only produces E-modes, while B-modes arise from higher order lensing effects (Schneider et al., 2002b) and systematics, see Figure 1.4. The aperture mass is defined as (Kaiser, 1995; Schneider, 1996)

$$M_{ap}(\theta_{ap}, \boldsymbol{\theta}) = \frac{1}{\theta_{ap}^2} \int \mathrm{d}^2\boldsymbol{\theta}' U\left(\frac{|\boldsymbol{\theta}' - \boldsymbol{\theta}|}{\theta_{ap}}\right) \kappa(\boldsymbol{\theta}'). \tag{1.94}$$

The function U is a compensated filter function, so $\int \mathrm{d}x\, x\, U(x) = 0$, and is constant on concentric curves. This filtering makes the statistic insensitive to the underlying constant sheet mass of the lens, while remaining sensitive to the variations in the density field, which are responsible for the shear. Hence, it removes any constant contribution to the convergence. The aperture mass can be measured from the shear

$$M_{ap/\times}(\theta_{ap}, \boldsymbol{\theta}) = \frac{1}{\theta_{ap}^2} \int \mathrm{d}^2\boldsymbol{\theta}' Q\left(\frac{|\boldsymbol{\theta}' - \boldsymbol{\theta}|}{\theta_{ap}}\right) \gamma_{t/\times}(\boldsymbol{\theta}'), \tag{1.95}$$

where the filter function Q is related to U as follows

$$Q(x) = \frac{2}{x^2} \int_0^x \mathrm{d}y\, y\, U(y) - U(x). \tag{1.96}$$

The E/B-mode separation follows from decomposing the shear into the cross and tangential components at each point in the field. Note that M_{ap} only considers the tangential component of the shear, that is, the E-mode, while the quantity $\langle M_\times \rangle$ is sensitive to $\gamma_\times$, so should be consistent with zero across all filter scales θ_{ap}, in the absence of systematics.

Combination of Peculiar Velocities and Lensing

The metric of a perturbed Robertson-Walker spacetime involves two potentials; the Newtonian potential Ψ and the curvature potential Φ.

$$ds^2 = (1 + 2\Psi)dt^2 - a^2(t)(1 - 2\Phi)dx^2. \tag{1.97}$$

According to general relativity peculiar velocities are induced by Φ, whereas massless particles travel as much through space as through time, so respond

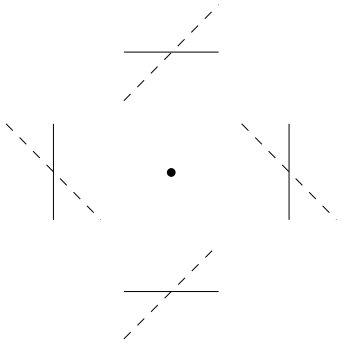

Figure 1.4 *The solid lines show the E-mode, around a lens at the position of the black dot, while the dashed lines represent the B-mode.*

equally to both Φ and Ψ. Although weak lensing and Redshift Space Distortions (RSD) are both sensitive to gravity, they probe the Robertson-Walker metric differently, providing strong constraints when combined (e.g. Cai and Bernstein, 2012; Simpson et al., 2013). Facilitating the accurate combination of RSD and WGL is the long-term vision for the use of the results and analysis in this thesis.

The methods above can and have been applied to different wavelengths and types of object. For example, lensing of the CMB photons is a secondary anisotropy effect and has been used to detect nonzero Λ (Sherwin et al., 2011). Also, galaxy clusters are subject to peculiar motions and give rise to Redshift Space Distortions (Kashlinsky et al., 2008), and Baryon Acoustic Oscillations can be measured from the Lyman-alpha forest (McDonald and Eisenstein, 2007).

Chapter 2

Galaxy Bias

Galaxy bias describes the statistical relation between the distribution of galaxies and dark matter as illustrated in Figure 2.1. Knowledge of this relation sheds light on galaxy formation and evolution. Its main interest for this thesis, however, comes from cosmology, where constraints from galaxy surveys are limited by our understanding of how galaxies trace mass. This chapter provides an overview of the theoretical and observational status of galaxy bias.

2.1 Introduction

Kaiser (1984) proposed the idea of enhanced galaxy formation in dense environments to explain the higher correlation function of galaxy clusters relative to that of the galaxies. He argued that galaxy clusters, and possibly all galaxies, are biased tracers of the total matter distribution. The resulting high peak bias model could in principle reconcile the low density of the Coma cluster (measured from the mass-to-light ratio first by Zwicky 1933) with an Einstein-de Sitter universe ($\Omega_m = \Omega = 1$), which became strongly favoured when inflation was introduced to explain fundamental shortcomings of the standard model, see Section 1.1.1.

If galaxy clusters only collapse at the rare high density peaks, then this causes galaxy cluster bias. This idea was generalised to galaxies by Davis et al. (1985) and Bardeen et al. (1986), such that there exists a critical density ρ_c that acts as a threshold for galaxy formation. If galaxy formation were a simple process, its link to galaxy bias is simply through the parameter ρ_c and could be constrained from

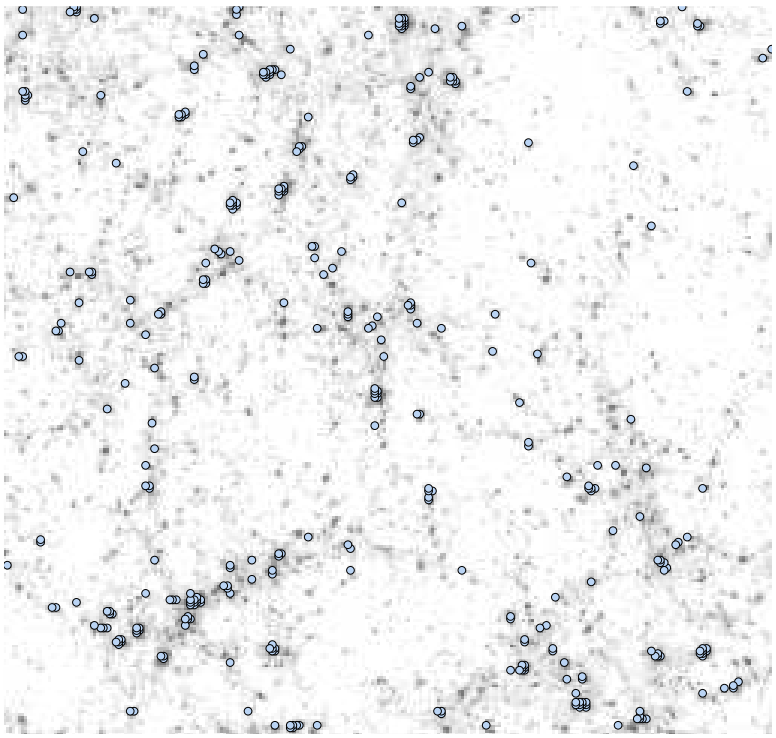

Figure 2.1 *Galaxies are biased tracers of the matter distribution. This map shows in grey the dark matter field which the galaxies, represented by the circles, trace in a discrete manner. Cosmological information derived from the dynamics of the dark matter distribution is limited by how well we understand how galaxies sample it. For this Figure I used a Clone simulation (Harnois-Déraps et al., 2012) and performed a Poisson sampling to obtain galaxy positions.*

galaxy bias measurements. Unfortunately, galaxy formation is a process that involves hidden factors, such as random variations in the underlying density field as well as the geometry of the background structure. Dekel and Lahav (1999) show that higher order statistics are required to disentangle all the physical mechanisms of galaxy formation. In this investigation, however, we limit ourselves to 1-point and 2-point statistics to focus on the cosmological implications of a stochastic, non-linear galaxy bias.

2.1.1 Definitions of Galaxy Bias

The difference between the distribution of galaxies and dark matter can be studied with the (co)variances of the fractional overdensities δ of galaxies and dark matter

$\delta_W(x) \equiv \rho(x)/\bar{\rho} - 1$, smoothed with some window

$$\delta_W(x) = \int d^3x' \delta(x') W(x - x'). \tag{2.1}$$

For convenience the filter subscript is henceforth dropped ($\delta = \delta_W$). Deterministic galaxy bias is the case where the density contrast of galaxies δ_g is some function of the density contrast of matter δ_m

$$\delta_g = f(\delta_m). \tag{2.2}$$

The function f is unknown and it has become common to use an expansion of the form

$$\delta_g = \sum_i^\infty \frac{b_i}{i!} \delta_m^i, \tag{2.3}$$

(Fry and Gaztanaga, 1993). If the galaxy overdensity at some position $\boldsymbol{x_1}$ is affected by the density at another position $\boldsymbol{x_2}$, the bias is said to be non-local, and the coefficients b_i would carry spatial dependence. Therefore, Equation (2.3) is known as the local bias expansion and recent studies (e.g. Chan et al., 2012; Pollack et al., 2012) criticise its use.

To first order the relation is linear, with only b_1 as the relevant parameter $\delta_g = b_1 \delta_m$. This linear model has been used throughout the decades, but provides an incomplete description of the complex relation between the galaxy overdensity δ_g and matter overdensity δ_m.

At small scales the linear bias relation breaks down due to nonlinear structure formation; at intermediate scales various mechanisms such as non-local bias will cause deviations from this relation; at large scales it should be fairly accurate, although primordial non-gaussianity could cause non-linear behaviour at the largest scales $k < 0.001$ Mpc h^{-1} (Desjacques et al., 2011). Despite all this, the linear bias model has been used extensively, in particular the derived relations

$$\xi_g(s) = b_1^2 \xi_m(s), \tag{2.4}$$

and

$$P_g(k) = b_1^2 P_m(k), \tag{2.5}$$

where $\xi(s)$ is the 2-point correlation function and s the comoving separation, $P(k)$ is the power spectrum as a function of wavenumber k, and subscripts g and m denote galaxies and dark matter, respectively.

A simplified non-linear local bias model can be obtained by writing Equation 2.3 to second order

$$\delta_g = b_0 + b_1\delta_m + \frac{b_2}{2}\delta_m^2, \tag{2.6}$$

where b_2 governs scale-dependence and can be constrained from higher order statistics (Frieman and Gaztanaga, 1994; Fry and Gaztanaga, 1993), with some observational success (Gaztañaga et al., 2005; Verde et al., 2002).

How well would the model in Equation (2.6) perform in the case there is a non-zero third order term b_3, taking Equation (2.3) up to third order? Analysing such a galaxy sample, assuming $b_3 = 0$, would result in a large measure for b_2. This is illustrated by taking the millennium output at redshift $z = 0$, and construct a galaxy catalogue by applying (2.3) to the dark matter field averaged over boxes with smoothing length $R = 2\text{Mpc/h}$, and $b_1 = 0.7, b_2 = 0.1\times10^{-1}, b_3 = 0.1\times10^{-2}$, and $b_{i>3} = 0$, then the best-fit value for b_2 is $\simeq 0.6$ (as a result of b_3 blowing up extreme density peaks of the highly non-Gaussian field).

Furthermore, the bias relation is expected to have a stochastic component. Stochasticity arises from random processes in the formation of galaxies such that there exists a scatter in the relation between the number of galaxies formed and the local density. It has become common to group together all scale-dependence into b_2. However, in the presence of stochasticity, the model becomes inaccurate. Without resorting to higher order terms, we can model stochasticity with the density contrast of a smoothed field of Gaussian noise ϵ multiplied by a stochasticity parameter c, that is

$$\delta_g = f(\delta_m) + c\epsilon. \tag{2.7}$$

If we neglect stochasticity in our galaxy bias model and fit (2.6) to a galaxy field which has a stochastic component, the parameter b_2 will be insensitive to the noise.

A single bias parameter is clearly insufficient for describing the relative distributions of dark matter and galaxies. This also applies to the galaxy bias in terms of ξ and P, Equations (2.4) and (2.5), where higher order terms affect the average linear bias but also cause the galaxies and dark matter to be less correlated. We therefore need to introduce the cross-correlation coefficient r in a similar way as the linear galaxy bias parameter. We follow Dekel and Lahav (1999) to define

galaxy bias parameters, giving us the two central equations of this thesis

$$b(R) \equiv \sqrt{\frac{\langle \delta_g^2 \rangle}{\langle \delta_m^2 \rangle}}, \tag{2.8}$$

$$r(R) \equiv \frac{\langle \delta_g \delta_m \rangle}{\sqrt{\langle \delta_g^2 \rangle \langle \delta_m^2 \rangle}}, \tag{2.9}$$

where R is the smoothing scale, which precise definition depends on the window used, see Equation (2.1), for example, R can be the width of a Gaussian filter, or the length of the box that is averaged over. Theoretically, these equations are preferred; observationally, they are unattractive, because a measurement of the dark matter field is required for the comparison. Chapter 5 discusses the possibility of measuring these quantities from weak lensing and galaxy clustering, using mass reconstruction techniques.

The bias parameter $b(R)$ encodes how strongly clustered the galaxies are with respect to the dark matter and depends primarily on the mass of the tracer population (in the sense that clustering signals of massive objects are stronger, see Norberg et al., 2002). The cross-correlation coefficient $r(R)$ is sensitive to how correlated the positions of the galaxies and dark matter are. It is sensitive to non-linear bias and stochasticity. According to the Cauchy-Schwarz inequality $r(R)$ is bounded between anti-correlation (galaxies sit preferentially in dark matter voids) and perfect correlation (galaxies trace the dark matter exactly) $-1 < r(R) < 1$. The case $r(R) = 0$ corresponds to the case where the galaxy field has no correlation with the dark matter field.

The effect of nonzero b_2 on the cross-correlation coefficient can be calculated by substituting Equation (2.6) in Equation (2.9), finding that $r(R)$ is decreased with nonzero b_2.

$$r(R) = \frac{\langle \delta_m [b_0 + b_1 \delta_m + \frac{1}{2} b_2 \delta_m^2] \rangle}{\sqrt{\sigma^2 \langle [b_0 + b_1 \delta_m + \frac{1}{2} b_2 \delta_m^2]^2 \rangle}} \tag{2.10}$$

$$= \frac{b_1 \sigma^2 + \frac{1}{2} b_2 \sigma^3}{\sqrt{\sigma^2 \langle (b_0 + \frac{1}{2} b_2 \delta_m^2)^2 + 2 b_0 b_1 \delta_m + b_1^2 \delta_m^2 + b_1 b_2 \delta_m^3 \rangle}} \tag{2.11}$$

where for clarity we have substituted $\langle \delta_m^i \rangle$ as σ^i, noting that $\langle \delta_m^1 \rangle \sigma^1 = 0$.

Note that $\langle \delta_g \rangle = b_0 + b_2 \sigma^2 / 2 = 0$, so we can substitute $b_0 = -b_2 \sigma^2 / 2$. In the

Gaussian approximation we can set $\sigma^3 = 0$. Hence,

$$r(R) = \frac{b_1\sigma^2}{\sqrt{\sigma^2[\frac{1}{2}b_2^2(\sigma^2)^2 + b_1^2\sigma^2]}} \tag{2.12}$$

$$= \frac{1}{\sqrt{1 + \frac{1}{2}(b_2/b_1)^2\sigma^2}} \tag{2.13}$$

The fact that galaxies are discrete tracers of a smooth density field could also be interpreted as galaxy bias. To study this in more detail, I have done the following. First, particles are randomly sampled from a Clone dark matter simulation (Harnois-Déraps et al., 2012, for more details see also Chapter 3) and treated as galaxies (yielding $b(R) = r(R) = 1$). Next, the number of galaxies is reduced and the galaxy bias parameters $b(R)$ and $r(R)$ are calculated for different smoothing lengths for 4 galaxy samples. The results are shown in Figure 2.2. We find that with fewer galaxies the galaxy bias parameters deviate more from the input $b(R) = r(R) = 1$.

The behaviour of $r(R)$ in the presence of shot noise is shown in Figure 2.2. The sampling is such that the likelihood of finding n galaxies at position x scales with the dark matter density $\rho \propto 1 + \delta_m(x)$, so that with increased sampling and for larger smoothing scales the galaxy field is less biased. In the presence of shot noise the bias $b(R)$ is increased, while $r(R)$ is decreased. With fewer galaxies, the smooth dark matter distribution is transformed into a spiky galaxy distribution. Therefore, at small scales these regions appear strongly clustered relative to the smooth dark matter distribution in the presence of shot noise. The spikes disappear with increasing smoothing length R, hence the behaviour of $b(R)$. The curves for $r(R)$ can be understood by noting that under-sampling effectively adds uncorrelated noise to δ_g, decreasing $r(R)$ at smaller scales. Shot noise effects are also described in Guzik and Seljak (2001) for $r(k)$.

Galaxy bias parameters b and r are often defined in terms of observationally more attractive clustering statistics. A popular definition of bias in real space is with the use of 2-point correlation functions $\xi(s) = \langle\delta(x)\delta(x+s)\rangle$ (Peebles, 1980)

$$b(s) \equiv \sqrt{\frac{\xi_g}{\xi_m}}, \tag{2.14}$$

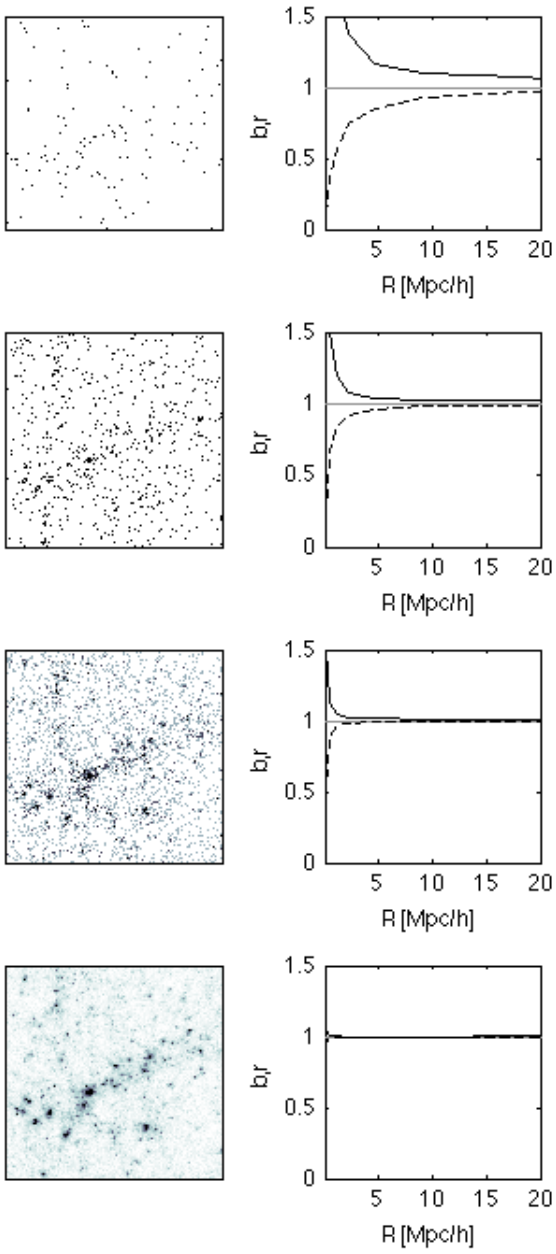

Figure 2.2 *The effect of shot noise on the galaxy bias parameters $b(R)$ (solid line) and $r(R)$ (dashed line) for a clone realisation at $z = 0.344$. The left panels show the sampling with a finite number of test particles of the dark matter field (zoomed in on 57 Mpc^2, noting that the bias parameters correspond to the total field of 147 Mpc^2). The number of galaxies was increased by a factor of 5 with every next lower panel. The right panels show the galaxy bias parameters, calculated by comparing the noisy fields with the smooth dark matter distribution.*

$$r(s) \equiv \frac{\xi_{gm}}{\sqrt{\xi_g \xi_m}}, \tag{2.15}$$

where the auto- and cross-correlations ξ are measured as a function of separation s. It is worthy of remark that $r(s)$ is not bounded like $r(R)$, since the Cauchy-Schwarz inequality does not apply to correlation functions. In the presence of shot noise, the correlation functions are unbiased, albeit noisy, estimates of the true clustering. Hence, $r(s) = 1$ is recovered within errors, but some data points will have $r(s) > 1$. Furthermore, complex r can arise when either ξ_g or ξ_m is negative, and perfect correlation leads to $r(s) = -1$ on the very large scales where the 2-point correlation functions are negative. To show the properties of $r(s)$, I have created 2 samples, A and B, containing objects that were randomly sampled from the same distribution (a clone dark matter field at $z = 0.344$). Sample A consists of 10^5 objects, while B was constructed from the same distribution, but has only 10^4 objects. Figure 2.3 shows the behaviour of $r(s)$. Error bars reflect Poisson uncertainties and the cross data point represents a complex number, so one of the two autocorrelation functions is negative, and one is positive.

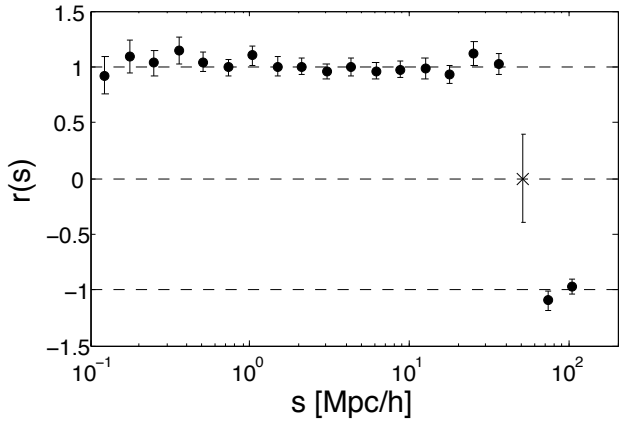

Figure 2.3 *The cross-correlation coefficient $r(s)$, Equation (2.15), between a sample of 10^5 and a sample of 10^4 objects, both sampled from the same dark matter distribution (a clone realisation at $z = 0.344$). The cross is a complex data point. The two negative data points at large scales are the result of all correlation functions being negative.*

We can also define bias parameters in wavenumber k-space

$$b(k) \equiv \sqrt{\frac{P_g}{P_m}}, \tag{2.16}$$

$$r(k) \equiv \frac{P_{gm}}{\sqrt{P_g P_m}}, \tag{2.17}$$

where P_g is the power spectrum of galaxies, P_m the matter power spectrum,

and P_{gm} the galaxy-matter cross power spectrum, all measured as a function of wavenumber k. Although in principle $-1 < r(k) < 1$, values of $r(k) > 1$ have been reported (e.g. Guzik and Seljak, 2001) as a result of applying a shot noise correction to P_g with incorrect assumptions about how galaxies populate dark matter haloes (not simply Poissonian). However, this shot noise correction forces $r = 1$ over a slightly larger range of scales.

To summarise, there are many different models to relate galaxy distributions to the underlying dark matter, e.g. Equations (2.3) and (2.7). We have many observables to study this, e.g. Equations (2.8)-(2.9), (2.14)-(2.17). It is important to distinguish between them, since they are sensitive to galaxy bias properties in different ways. From here on we will use b and r to discuss general properties of these estimators, but use R, s, and k as arguments of the galaxy bias parameters when referring to a specific estimator.

2.1.2 Galaxy bias as a function of type, time, and scale

It has long been known that different types of galaxies cluster differently on the sky (Davis and Geller, 1976). One of the major steps forward in this field was by Norberg et al. (2002) who showed that the dependence of galaxy type with bias is due to the correlation of galaxy type with halo mass. That is, mass is the discriminator. The more massive haloes, such as those hosting red ellipticals, have a higher correlation function, while less massive haloes, such as those hosting blue emission line galaxies, trace the lower density modes. Both galaxy types will be examined in Chapter 4.

Tegmark and Peebles (1998) provide the first predictions of the redshift dependence of galaxy bias. Their simple model is based on how gravity tends to correlate galaxies and mass over time, which for the cross-correlation coefficient r implies $r(t - \mathrm{d}t) \leq r(t) \leq 1$. Similarly, galaxy bias b is driven towards unity. Apart from the gravity driven evolution of galaxy bias, there are more complex contributions to the time-dependence, most notably galaxy mergers and ongoing galaxy formation (e.g. Simon, 2005). Observations confirm this prediction and recently, Lindsay et al. (2014) have shown that the bias evolves strongly for radio galaxies, with $b \sim 10$ at $z \sim 1.55$ and $b \sim 2$ at $z = 0.3$.

Selection effects may be degenerate with estimations of the redshift dependence of galaxy bias; more massive galaxies are more biased, but also brighter and

therefore detectable out to higher redshift. Accurate knowledge of the survey selection function is required when studying time-dependence of galaxy bias (e.g. Nuza et al., 2013).

Although it is safe to assume $r = 1$ at large physical scales, the rate at which r approaches 1 may be slowed down as a result of considering the distributions of single galaxy types. In the multiple tracer approach to Redshift Space Distortions one obtains $\beta_a = f/b_a$ and $\beta_b = f/b_b$ from 2 tracers, a and b, so that one obtains the growth rate f free from bias (Blake et al., 2013; McDonald and Seljak, 2009). For these studies it may be of interest to study the trade off with the cross-correlation coefficient, which may be better behaved for the combined sample, including as many density tracers as possible.

2.1.3 Galaxy Bias from Skewness

Galaxy bias measurements need to somehow compare the galaxy field to the dark matter field. Weak gravitational lensing as well as redshift space distortions are direct probes of dark matter and how to use them to extract galaxy bias information is explained in the next sections. Alternatively, one can look at 2- and 3-point statistics, which we review in this section.

Higher order statistics are sensitive to non-Gaussian features, which can arise through several mechanisms. For the local universe the dominant contribution comes from gravity, which skews the overdensities, since $\delta \geq -1$, although this is degenerate with galaxy bias, which, if galaxies are biased tracers, also contributes to skewness.

Gravitational instability leaves a specific signature in higher-order statistics by collapsing structures along the shortest-axis (creating sheets and filaments), which can be separated from the effects of galaxy bias, since bias preserves the overall shape of structures. If galaxies are more biased tracers, then current observations support a more Gaussian dark matter field, while an unbiased galaxy field would imply that observations are in support of a non-Gaussian dark matter field.

The bispectrum of galaxies can be written in such as way that the two contributions to skewness are separated. Verde et al. (2002) performed a likelihood fitting to show that the galaxies of the 2dF Galaxy Redshift Survey are unbiased within confidence limits, based on about half the total sample of

$\sim 250,000$ redshifts.

Recently, it has been shown (e.g. Chan et al., 2012; Manera and Gaztañaga, 2011; Pollack et al., 2012) that the 2-point bias parameters are, in general, different from what is found with 3-point statistics, when analysed with the second order bias model in Equation (2.6), most notably the linear term b_1. This is perhaps not surprising, since the quadratic bias expansion, Equation 2.6, could be an incomplete description of the true, unknown, function f as in $\delta_g = f[\delta_m]$. This is the result of non-local bias and/or non-negligible higher order terms. Non-local bias can be caused by all sorts of processes, most notably dependence of galaxy formation on the tidal field, time-dependence of the bias, velocity bias, stochasticity, and non-Gaussianity, e.g. Chan et al. (2012); Matsubara (1995). It was shown by Chan et al. (2012) that an initial state of a local bias evolves into a non-local bias, and the bias is more likely to be non-local at late times than at early times.

2.2 Redshift Space Distortions and Galaxy Bias

The cosmological density field is in a dynamic state: smaller structures are accelerated towards denser environment and away from voids. The galaxy field is also subject to gravitational flows, since they trace the dark matter field. When converting their redshifts to distances, a clustering isotropy arises. The effect is called Redshift Space Distortions (RSD), introduced in Section 1.2.4. Before the discovery of dark energy, the theory of gravity was assumed to be known, hence the uncertainty on the growth rate was solely through Ω_m. Therefore, the original goal of redshift space distortions was to measure bias parameters and Ω_m, instead of constraining modified gravity theories. In the following sections it will be shown how the measured growth rate is affected by different assumptions for galaxy bias. In particular, we analyse the following question:

What growth rate do we measure under the assumption of a linear bias when the true bias is non-linear and stochastic?

In Section 1.2.4 the Kaiser formula was derived in the assumption that galaxies are perfect tracers of the mass. Here it is shown how to fold in b and r into the Kaiser formula. Traditionally, the galaxy bias is assumed to be linear and deterministic, such that $\delta^{\rm light} = b\delta^{\rm mass} = \delta^{\rm mass} + (b-1)\delta^{\rm mass}$, so that the first term

is affected by peculiar velocities and the second is assumed to be some additional clustering pattern due to the bias. Applying this to Equation (1.46) of Section 1.2.4, we find

$$\begin{aligned}
\delta_s^l &= \delta_r^m(1+f\mu^2) + (b-1)\delta_r^m && (2.18)\\
&= \delta_r^m + \delta_r^m f\mu^2 + b\delta_r^m - \delta_r^m && (2.19)\\
&= \delta_r^m f\mu^2 + b\delta_r^m && (2.20)\\
&= \delta_r^m(b+f\mu^2) && (2.21)\\
&= \frac{\delta_r^m}{b}(1+f/b\mu^2) && (2.22)\\
&= \delta_r^l(1+\beta\mu^2), && (2.23)
\end{aligned}$$

where the subscripts r and s are real and redshift space, respectively, and the superscripts l and m denote luminous matter and dark matter, respectively. Note that (2.21) can be written as

$$\delta_s^l = \delta_r^l + \delta_r^m f\mu^2 \tag{2.24}$$

so that the auto-term of the luminous matter density $\langle\delta_s^l\delta_s^l\rangle$ is sensitive to the real space cross term $\langle\delta_r^l\delta_r^m\rangle$. That is,

$$\begin{aligned}
\langle\delta_s^l\delta_s^l\rangle &= \langle(\delta_r^l + \delta_r^m f\mu^2)(\delta_r^l + \delta_r^m f\mu^2)\rangle && (2.25)\\
&= \langle\delta_r^l\delta_r^l + 2\delta_r^l\delta_r^m f\mu^2 + \delta_r^m\delta_r^m f^2\mu^4\rangle && (2.26)\\
&= \langle\delta_r^l\delta_r^l\rangle + 2\langle\delta_r^l\delta_r^m\rangle f\mu^2 + \langle\delta_r^m\delta_r^m\rangle f^2\mu^4. && (2.27)
\end{aligned}$$

With the definitions of $b(R)$ and $r(R)$ as in Equations (2.8) and (2.9) (where $\delta_g = \delta_r^l$ and $\delta_m = \delta_r^m$) as well as $\beta = f/b$, we have

$$\begin{aligned}
\langle\delta_s^l\delta_s^l\rangle &= \langle\delta_r^l\delta_r^l\rangle\left(1 + 2\beta\mu^2 r + \beta^2\mu^4\right) && (2.28)\\
&= b^2\langle\delta_r^m\delta_r^m\rangle\left(1 + 2r\beta\mu^2 + \beta^2\mu^4\right) && (2.29)
\end{aligned}$$

So we obtain for the Kaiser formula with cross-correlation coefficient

$$P_g^s(k,\mu) = b(k)^2 P_m^r(k)\left(1 + 2r(k)\beta\mu^2 + \beta^2\mu^4\right) \tag{2.30}$$

This is the result of Pen (1998). In case $r = 1$ the above satisfies the Kaiser formula. This is easily shown by rewriting (2.30)

$$P_g^s(k,\mu) = b^2 P_m^r(k)\left(1+\beta\mu^2\right)^2 - b^2 P_m^r(k) 2\beta\mu^2(1-r). \tag{2.31}$$

The measured redshift space galaxy power spectrum is related to the matter power spectrum, the galaxy bias parameters b and r, and the growth rate f. To extract the individual parameters, it is common to expand the galaxy redshift power spectrum with Legendre polynomials (e.g. Baldauf et al., 2010; Pen, 1998)

$$P_s^g(k) = P_r^g(k)[\alpha_0(\beta) + \alpha_2(\beta)L_2(\mu) + \alpha_4(\beta)L_4(\mu)], \tag{2.32}$$

which has terms dependent and independent on the angle μ. It can be shown (Pen, 1998) that the coefficients are given by

$$\alpha_0(\beta) = 1 + \frac{2}{3}r\beta + \frac{1}{5}\beta^2; \tag{2.33}$$

$$\alpha_2(\beta) = \frac{4}{3}r\beta + \frac{4}{7}\beta^2; \tag{2.34}$$

$$\alpha_4(\beta) = \frac{8}{35}\beta^2. \tag{2.35}$$

by writing out Equation (2.32):

$$P_s(k) = P_r(k)\Bigg[\left(1+\frac{2}{3}r\beta+\frac{1}{5}\beta^2\right) \tag{2.36}$$

$$+\left(\frac{4}{3}r\beta+\frac{4}{7}\beta^2\right)\left(\frac{1}{2}\left(3\mu^2-1\right)\right) \tag{2.37}$$

$$+\left(\frac{8}{35}\beta^2\right)\left(\frac{1}{8}\left(35\mu^4-30\mu^2+3\right)\right)\Bigg], \tag{2.38}$$

and combining $\beta^i\mu^j$ terms for clarity:

$$= P_r(k)\Bigg[1+\left(\frac{2}{3}r-\frac{2}{3}r\right)\beta \tag{2.39}$$

$$+\left(\frac{1}{5}-\frac{2}{7}+\frac{3}{35}\right)\beta^2 + 2r\beta\mu^2 \tag{2.40}$$

$$+\left(\frac{6}{7}r-\frac{6}{7}r\right)\beta^2\mu^2+\beta^2\mu^4\Bigg] \tag{2.41}$$

$$= P_r(k)\left[1+2r\beta\mu^2+\beta^2\mu^4\right] \tag{2.42}$$

Therefore, the parameters β and r can be solved for by measuring α_2 and α_4 separately. So far, the only RSD analysis to focus on $r(k)$ is the WiggleZ survey (Blake et al., 2011), although the growth rate was fixed to some value, instead of fitting β and r simultaneously. The result is an r consistent with 1, although errors are large ($\Delta r \sim 0.2 - 0.4$).

There are many complications that need to be accounted for in RSD analyses. Dense environments contribute uncorrelated galaxy motions at small scales where, in addition, the linear prediction of the matter power spectrum breaks down. There are several ways to model this: (1) convolution of the Kaiser formula with a function that describes the random motions (Hatton and Cole, 1998), (2) perturbation theory with the addition of a damping term (Scoccimarro, 2004), and (3) fitting formulae motivated by N-body simulations, such as Smith et al. (2003). Furthermore, RSD analyses from wide surveys need to take the wide angle effect into account when μ between galaxies becomes non-negligible, which contribution is degenerate with β and r (e.g. Yoo and Seljak, 2013).

The RSD formalism above is one of the most powerful probes of galaxy bias. Unfortunately, the mystery that we call dark energy has shifted focus to constraining gravity, while the observational status of galaxy bias remains poor.

2.2.1 Measured versus True Growth Rate

Section 2.2 outlined the dependence of the observed redshift space galaxy power spectrum on β and r. Dekel and Lahav (1999) argue that the quantities of interest for RSD are the average b and r over the range of scales used for the growth rate measurement. Although this is true, it should be noted that in reality the non-linearity of b and r will have some effect: the smaller scales contribute more constraining power than the larger scales, hence the measurement may be dominated by regions where b and r deviate significantly from their averaged counterparts.

Consider the scenario that the true bias is linear and deterministic, $b = b_0$. If $b_0 \neq 1$, the measured growth rate in the assumption of $b_0 = 1$ differs from the true growth rate. Equating the two Kaiser formulae for redshift space distortions,

where the first assumes $b = 1$ and the second $b = b_0$, we find

$$P^s_{gg,\mathrm{m}}(f_\mathrm{m}, b = 1) = P^s_{gg,\mathrm{t}}(f_t, b = b_0) \tag{2.43}$$

$$P_{\delta\delta}(1 + f_\mathrm{m}\mu^2)^2 = b_0^2 P_{\delta\delta}(1 + \frac{f_\mathrm{t}\mu^2}{b_0})^2 \tag{2.44}$$

$$f_\mathrm{m} = \frac{b_0 - 1}{\mu^2} + f_\mathrm{t}, \tag{2.45}$$

where f_m and f_t are the measured and true growth rate, respectively. The average value for μ^2 is found by integrating over all possible angles between wave vectors. Using spherical coordinates, we find

$$\langle\mu^2\rangle = \frac{\int\int \cos^2(\theta)\sin(\theta)\mathrm{d}\phi\mathrm{d}\theta}{\int\int \sin(\theta)\mathrm{d}\phi\mathrm{d}\theta} \tag{2.46}$$

$$= \frac{-\int \cos^2(\theta)\mathrm{dcos}(\theta)}{\int \sin(\theta)\mathrm{d}\theta} \tag{2.47}$$

$$= \frac{\left[-\frac{1}{3}\cos^3(\theta)\right]_0^{\pi/2}}{\left[-\cos(\theta)\right]_0^{\pi/2}} \tag{2.48}$$

$$= \frac{1}{3}. \tag{2.49}$$

If $b_0 > 1$ in the real Universe, the measured growth rate is an overestimation of the true growth factor ($f_m < f_t$), because structure seems more evolved than it really is. For example, if $f_\mathrm{m} = 0.6$ and the true bias is $b_0 = 1.2$, $f_\mathrm{t} = 0.55$.

With a scale-dependent bias the relation $f_m(b) = f$ will also depend on scale. Consider the case that the measurements assume scale independence, $b = b_0$, and the reality is scale-dependence, $b = b(k)$. This gives

$$f_\mathrm{m} = [b(k) - b_0]/\mu^2 + f \tag{2.50}$$

For example, consider $b(k) = b_0(k/k_0)^\alpha$. Note that $k = \sqrt{k_\parallel^2 + k_\perp^2}$ and $\mu = k/k_\parallel$. In terms of $k_\parallel$ and $k_\perp$ we can write

$$f_m = (b_0 - 1)\frac{k_\parallel^2(k_\perp^2 + k_\parallel^2)^{(\alpha-1)/2}}{(k_{\parallel,0}^2 + k_{\perp,0}^2)^{\alpha/2}} + f. \tag{2.51}$$

Instead of the $1/\langle\mu\rangle^2$ factor in Equation (2.45), we have a more complicated factor that depends on the details of $b(k)$.

The growth rate is also affected by a low cross-correlation coefficient. For

simplicity consider $b = 1$. Then equate (as above for scale-dependence) the measured and true galaxy power spectra:

$$1 + 2f^m\mu^2 + (f^m)^2\mu^4 = 1 + 2rf^{\rm true}\mu^2 + (f^{\rm true})^2\mu^4 \tag{2.52}$$

$$f^m = \frac{\sqrt{1 + 2rf^{\rm true}\mu^2 + (f^{\rm true})^2\mu^4} - 1}{\mu^2} \tag{2.53}$$

If we assume a true growth factor of $f^{\rm true} = 0.69$ we can plot Equation 2.53 as a function of r, see Figure 2.4, showing that growth rate measurements neglecting r entirely only provide lower bounds. Also, in the extreme case, the cross-

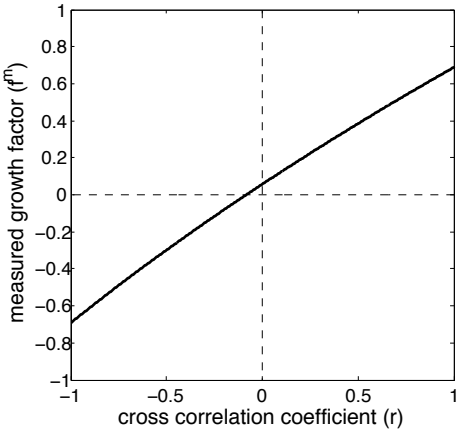

Figure 2.4 *The growth rate measured assuming $r = 1$ as a function of the true underlying cross-correlation coefficient. For this curve the true growth rate was set to $f^{true} = 0.69$, b is neglected, and r was assumed constant over the RSD k-range considered. μ was set to $\langle\mu\rangle \approx 0.65$.*

correlation coefficient swops the sign of the growth rate. This makes sense, since the galaxies trace the expanding voids where the density decreases, while the dark matter structure is still growing at a positive rate. Although this is very hypothetical and unrealistic, it does show that knowledge of r is required to good accuracy.

The growth rate is very sensitive to the theory of gravity, parameterised with γ, see Equation (1.30). Therefore, small systematic effects can lead to large errors. It is easy to show that the relative difference in γ is $\log(f_t)/\log(f_m) - 1$. The relative difference in growth factor is

$$\frac{f_t}{f_m} - 1 = \frac{f_t\mu^2}{\sqrt{1 + 2rf_t\mu^2 + f_t^2\mu^4}} - 1 \tag{2.54}$$

Perhaps more realistically, the cross-correlation is on average around $\langle r\rangle = 0.99$,

which would give a measured growth factor of 0.6841 in Figure 2.4. Although this is not a huge difference (0.9%) it means a 2.2% error in γ.

2.2.2 χ^2 Tests

To study the discrepancy between measured and true growth as a result of galaxy bias in more detail, this section fits a model with simple bias assumptions to mock data with galaxy bias. The model, shown in Figure 2.5, is a power spectrum as a function of angle μ and wavenumber k. We can construct a mock measurement by applying galaxy bias parameters. A comparison between the model and the mock data will reveal the sensitivity of cosmological parameter constraints to galaxy bias. This is done by fitting a Kaiser model with linear bias to mock data with nonlinear stochastic bias.

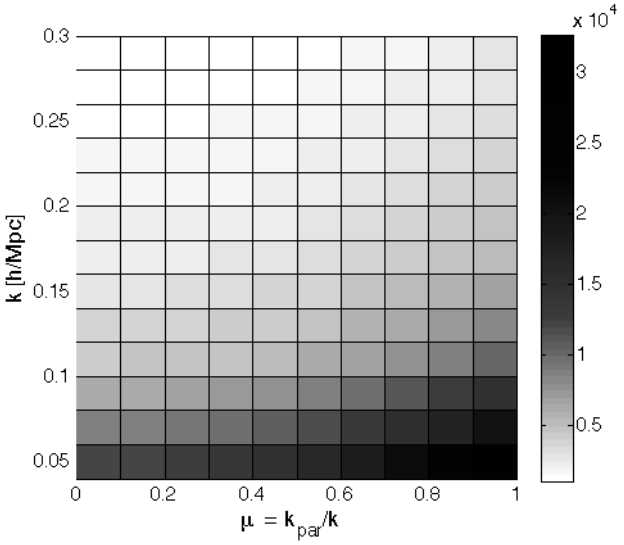

Figure 2.5 *The galaxy power spectrum as predicted by the Kaiser formula as a function of angle μ and wavenumber k and for a growth rate of $f = 0.69$.*

The χ^2 statistic is minimised by changing model parameters. In our case it is given by

$$\chi^2(f, b^{\rm lin}) = \sum_{i=1}^{n}\sum_{j=1}^{m} \frac{\left[M(\mu_i, k_j) - F(\mu_i, k_j)\right]^2}{E^2}, \tag{2.55}$$

where M is the model, F is the input fiducial model (including the toy galaxy bias models), f is the growth rate, $b^{\rm lin}$ is the linear bias, and the errors E (on F)

were calculated from (Tegmark, 1997)

$$\frac{\delta P}{P} = \frac{1}{\sqrt{m}} \left(1 + \frac{1}{nP} \right), \tag{2.56}$$

where $P = P(k) = P(\sqrt{k_\perp^2 + k_\parallel^2})$, n is the number density. The number of Fourier modes m can be calculated from the density of states in $k-$space, $\rho_k = V/(2\pi)^3$, where V is the surveyed volume, so that $m = \rho_k \times 2\pi k_\perp \times \delta k_\perp \times \delta k_\parallel$. To calculate the errors, a WiggleZ-like survey set up was adopted, which measured redshifts of 2.4×10^5 galaxies out to $z \sim 1$ over ~ 1000 square degrees (Drinkwater et al., 2010). By comparing the confidence regions obtained with Equation (2.55), we can reveal how sensitive the growth rate is to incorrect assumptions on galaxy bias.

The power spectrum is modelled with and without galaxy bias as follows. CAMB (Lewis and Bridle, 2002; Seljak and Zaldarriaga, 1996) is an advanced and widely used code for calculating the matter power spectrum from the growth of structure, transfer function, and non-linear physics, applied to Gaussian initial conditions. This was used with $[\Omega_m, \Omega_\Lambda] = [0.3, 0.7]$. The galaxy bias functions are toy models, since no direct observations currently exist on scales probed by RSD. The model M and fiducial model F are obtained from Equation (2.30), where for M we use $b(k) = b^{lin}$ and $r(k) = 1$. An example of M is shown in Figure 2.5.

The following toy models for $b(k)$ and $r(k)$ were adopted, which provide realistic behaviour of the galaxy bias parameters at the scales probed by RSD

$$b(k) = b_1 + b_2\, k^2 \tag{2.57}$$

$$r(k) = 1 - r_1 \sqrt{k}, \tag{2.58}$$

noting that k is in $\mathrm{Mpc}^{-1}\ h$, so that b_2 and r_1 are not dimensionless. Three galaxy bias scenarios of interest are summarised in Table 2.1, showing what values are used for b_1, b_2, and r_1 in Equations (2.57) and (2.58). The (S1) case has a scale-dependent bias $b(k)$ and $r = 1$, (S2) has $b =$constant and r varies with scale, and for (S3) both b and r are scale-dependent. Note that in principle scenario (S1) and (S2) are unrealistic; non-linear galaxy bias affects both bias parameters, but serves to separate out the effects of b and r. With scenario (S3) an answer to the main question of this section is obtained: What growth rate do we measure in the assumption of a linear bias when the true bias is non-linear and stochastic?

Table 2.1 *Scenarios for F*

	b	r
S1	$b_1 = 0.9, b_2 = 0.2$	$r_1 = 0.0$
S2	$b_1 = 0.9, b_2 = 0.0$	$r_1 = 0.1$
S3	$b_1 = 0.9, b_2 = 0.2$	$r_1 = 0.1$

Figure 2.6 shows the measured growth rate when the data analysis assumes a linear bias (both b_2 and r_1 are zero), while the true galaxy bias is given by the scenarios in Table 2.1. From left to right the panels correspond to (S1), (S2), and (S3). Contours show the 1σ and 2σ confidence levels. The dot is the best fit value of the linear bias analysis, while the cross is at the true growth rate. The position of the cross in the b_0 direction is the average bias on the scales probed. For (S1) and (S3) the average bias is $\langle b(k) \rangle = 0.935$. S2 adopts a linear bias, so $\langle b(k) \rangle$ is simply $b_1 = 0.9$.

The left panel in Figure 2.6 corresponds to the (S1) scenario, showing that a nonlinear bias has an effect on the shape of the redshift galaxy power spectrum and, hence, the growth rate and best fit linear bias are slightly biased compared to the fiducial model. Figure 2.7 plots the measured growth rate as a function of b_2. The data analysis assumes $b_2 = 0$. It was obtained by performing the χ^2 procedure for a range of b_2 values. Note that the change is only modest for realistic values of b_2, reflecting what was noted by Dekel and Lahav (1999): an amplitude difference between P_g^s and P_g^r is more important than a change in shape as a result of b_2.

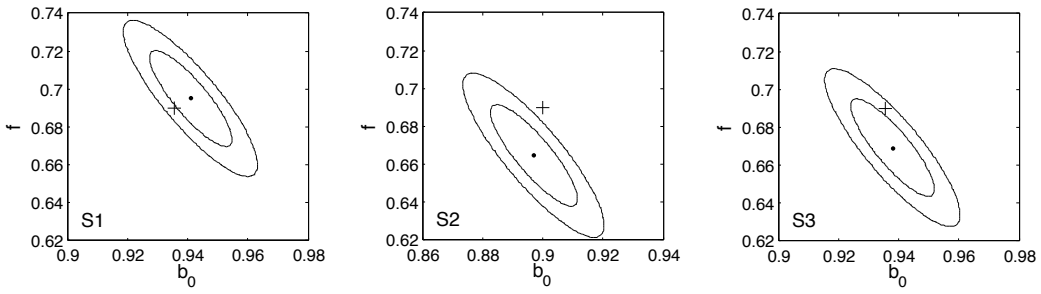

Figure 2.6 *The measured growth rate in the assumption of a linear bias when the true underlying galaxy bias is given by the scenarios S1-S3 in Table 2.1. The contours show the 1σ and 2σ confidence levels, the dot is the best fit value, while the cross shows the true growth rate and average galaxy bias b.*

The effect of a scale-dependent cross-correlation coefficient is investigated with the (S2) case, shown in the middle panel of Figure 2.6. The toy $r(k)$ model,

Equation (2.58), ensures that r rises to 1 with decreasing k. (S2) has $r_1 = 0.1$, resulting in $r > 0.92$ across the scales probed. Despite the fact that r is close to unity, the measured growth rate is significantly underestimated. As yet there are no observational studies that investigate the scale-dependence of the cross-correlation coefficient at the scales probed by RSD. This is the subject of our analysis in Chapter 4.

Finally, the case (S3) is discussed, in which the fiducial model has both galaxy bias parameters varying with scale. To be consistent, Equations (2.57) and (2.58) were used with the same choice of parameter values ($[b_1, b_2, r_1] = [0.9, 0.2, 0.1]$). The right panel of Figure 2.6 shows the expected parameter constraints, showing that the discrepancy is less striking compared to the individual effects. This can be explained from (S1) and (S2) working in opposite directions.

To conclude, growth rate measurements are very sensitive to how galaxies trace mass. Therefore, it may come as a surprise that recent studies (e.g. Beutler et al., 2013; Blake et al., 2011; de la Torre et al., 2013), assuming $b = b^{\rm lin}$, are in such good agreement with ΛCDM, noting that with the Planck results the RSD analyses seem to slightly underestimate the growth rate (Chuang et al., 2013). This section shows that it is possible that ignorance about b and r cancels out, explaining the impressive growth rate results, while having inaccurate knowledge about how galaxies trace the dark matter distribution.

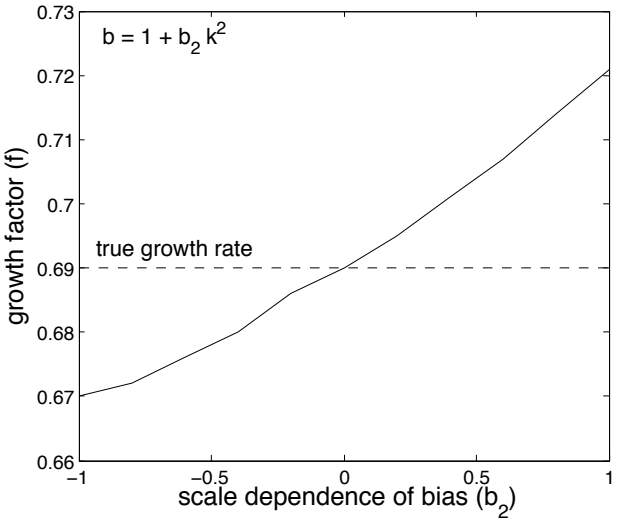

Figure 2.7 *The solid line shows the measured growth rate f as a function of b_2 as in $b(k) = 1 + b_2 k^2$, obtained by fitting the biased galaxy power spectrum to a linearly biased galaxy power spectrum, over a range of b_2 values.*

2.3 Galaxy bias from Weak Lensing

Weak Gravitational Lensing (WGL) is one of the most promising tools at our disposal for directly probing the dark matter. The observed shear pattern is a measure of both the geometry of the Universe and the growth of structure. Through the evolution of the matter power spectrum, WGL provides a unique tool to constrain dark energy (e.g. Hoekstra and Jain, 2008). Additionally, WGL can be employed to study how galaxies trace the dark matter, greatly increasing their value for cosmological parameter estimation (Schneider et al., 1998).

An exciting lensing tool is the construction of cosmological dark matter maps from shear measurments (Massey et al., 2007; Van Waerbeke et al., 2013). For the purpose of measuring galaxy bias the dark matter maps are required to be accurate representations of the true dark matter distribution. However, simulations show that the translation from shear to density induces inaccuracies (e.g. Jullo et al., 2014), which hampers the extraction of galaxy bias as a function of smoothing lengths [$b(R)$ and $r(R)$] from WGL. A promising solution is presented in Chapter 5.

So far, we have introduced several definitions of galaxy bias as a result of the variety of ways to describe density fields. This section focuses on auto- and cross-correlation functions of source ellipticities and lens positions, their dependence on galaxy bias parameters, and how to extract them. The resulting galaxy bias parameters will behave similar to $b(s)$ and $r(s)$ in Equations (2.14) and (2.15), due to the use of correlation functions. In this section yet another definition is introduced and it remains, up until this date, the only set of bias parameters measured by cosmic shear, galaxy-galaxy lensing, and galaxy clustering (Bonnett, 2012; Hoekstra et al., 2002; Jullo et al., 2012; Simon et al., 2007). In all studies the galaxy bias parameters deviated from a simple linear model and the cross-correlation coefficient was found to reach values as low as $r \sim 0.5$, implying significant offsets between galaxies and dark matter.

2.3.1 Raw Estimators

This section follows on from Section 1.2.5, where WGL was first introduced. It is convenient to define the *lensing kernel* W as

$$W(w) = \frac{3\Omega_m H_0^2 f_K(w)}{2c^2 a(w)} \int_w^\infty \mathrm{d}w' p_b(w') \frac{f_K(w'-w)}{f_K(w')}, \tag{2.59}$$

(e.g. Simon et al., 2007) which is essentially $g(w)$ of Equation (1.72) times the comoving angular diameter distance $f_K(w)$, and factors from Poisson's equation. For a given $p_b(w)$, the distribution of sources in comoving distance w, the lensing kernel defines the foreground distribution of lenses that the source distribution would be most sensitive to.

In Section 1.2.5 it was shown that in the weak lensing limit the convergence and shear are a projection of the three-dimensional density contrast δ_m

$$\kappa(\boldsymbol{\theta}) = \int_0^\infty \mathrm{d}w W(w) \delta_m \left(f_K(w)\boldsymbol{\theta}, w\right) \tag{2.60}$$

$$\gamma(\boldsymbol{\theta}) = -\frac{1}{\pi} \int_0^\infty \mathrm{d}^2\boldsymbol{\theta}' \kappa(\boldsymbol{\theta}' - \boldsymbol{\theta}) \frac{1}{(\theta_1' - i\theta_2')^2} \tag{2.61}$$

Similar to the convergence, the projected three dimensional galaxy contrast is defined as

$$\delta n(\boldsymbol{\theta}) = \int_0^\infty \mathrm{d}w\, p_f(w) \delta_g(f_K(w)\boldsymbol{\theta}, w), \tag{2.62}$$

where $p_f(w)$ is the distribution of foreground galaxies as a function of comoving distance w. For galaxy bias measurements, it would be ideal to have $p_f(w) = W(w)$, because this means that the lensing and clustering correlation functions probe the same redshift, reducing the cosmological correction. The more the effective redshift deviates from half that of the source distribution, the more scale-dependent the cosmological correction becomes, since redshift and scale-dependence of the bias parameters are correlated. In practice the ideal source lens geometry is difficult to achieve, since the redshift distributions of source and lens galaxies are determined by survey design. Altering the redshift distributions implies a reduction in the number density, increasing shot noise.

The correlations of ellipticities and galaxy number density contrast can be measured and related to the projected matter power spectrum P_κ, the projected galaxy-matter cross power spectrum $P_{\kappa n}$, and the projected galaxy power

spectrum P_n:

$$4\pi^2\delta_{\rm D}(\boldsymbol{\ell}+\boldsymbol{\ell'})P_\kappa(|\boldsymbol{\ell}|) = \langle\tilde{\kappa}(\boldsymbol{\ell})\tilde{\kappa}(\boldsymbol{\ell'})\rangle \tag{2.63}$$

$$4\pi^2\delta_{\rm D}(\boldsymbol{\ell}+\boldsymbol{\ell'})P_{\kappa n}(|\boldsymbol{\ell}|) = \langle\tilde{\kappa}(\boldsymbol{\ell})\delta\tilde{n}(\boldsymbol{\ell'})\rangle \tag{2.64}$$

$$4\pi^2\delta_{\rm D}(\boldsymbol{\ell}+\boldsymbol{\ell'})P_n(|\boldsymbol{\ell}|) = \langle\tilde{\kappa}(\boldsymbol{\ell})\delta\tilde{n}(\boldsymbol{\ell'})\rangle, \tag{2.65}$$

where the tilde denotes the Fourier transform. Therefore, the power spectra are found from Equations (2.60) and (2.62)

$$P_\kappa(\ell) = \int_0^\infty {\rm d}w \left(\frac{W(w)}{f_K(w)}\right)^2 P_m\left(\frac{\ell}{f_K(w)}; w\right), \tag{2.66}$$

$$P_{\kappa n}(\ell) = \int_0^\infty {\rm d}w \frac{W(w)p_f(w)}{\left(f_K(w)\right)^2}(brP_m)\left(\frac{\ell}{f_K(w)}; w\right), \tag{2.67}$$

$$P_n(\ell) = \int_0^\infty dw \left(\frac{p_f(w)}{f_K(w)}\right)^2 (b^2P_m)\left(\frac{\ell}{f_K(w)}, w\right), \tag{2.68}$$

(e.g. Simon et al., 2007) where the power spectrum bias definitions of Equations (2.16) and (2.17) were applied to relate P_m to the cross P_{gm} and galaxy P_g power spectra.

The power spectra in Equations (2.66), (2.67), and (2.68) are related to the correlation functions of ellipticities $\xi_\pm$, of positions and ellipticites γ_t, and of the positions $\omega(\theta)$ as follows

$$\omega(\theta) = \langle\delta n(\theta+\theta')\delta n(\theta')\rangle \tag{2.69}$$

$$= \int_0^\infty \frac{{\rm d}\ell\,\ell}{2\pi} P_n(\ell)J_0(\ell\theta) \tag{2.70}$$

$$\langle\gamma_t\rangle(\theta) = \langle\delta n(\theta+\theta')\gamma_t(\theta')\rangle \tag{2.71}$$

$$= \int_0^\infty \frac{{\rm d}\ell\,\ell}{2\pi} P_{\kappa n}(\ell)J_2(\ell\theta) \tag{2.72}$$

$$\xi_\pm(\theta) = \langle\gamma_t(\theta+\theta')\gamma_t(\theta')\rangle \pm \langle\gamma_\times(\theta+\theta')\gamma_\times(\theta')\rangle \tag{2.73}$$

$$= \int_0^\infty \frac{{\rm d}\ell\,\ell}{2\pi} P_\kappa(\ell)J_{0,4}(\ell\theta). \tag{2.74}$$

J_i is the i-th order Bessel function of the first kind. The shear correlation functions $\xi_\pm$ are estimators of the 3D dark matter distribution, weighted by the lensing kernel; γ_t is the tangential shear around foreground galaxies, providing a probe of the dark matter, but only around foreground galaxies and is, as such, also sensitive to r; $\omega(\theta)$ is the estimator of the 3D galaxy distribution, weighted by

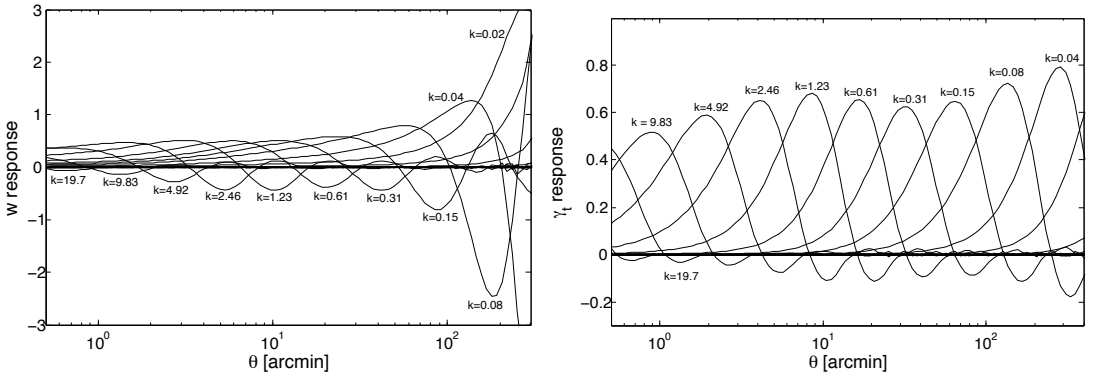

Figure 2.8 *w and γ_t response, defined as $w(k \pm \Delta k)/w(k)$ and $\gamma_t(k \pm \Delta k)/\gamma_t(k)$, shown respectively in (a) and (b). This shows the relation between θ and k. The quoted k values correspond to the centre of the $k-$bins, defined in Equation* (2.75)*. As described in the text, this decomposition changes with cosmology and redshift distributions, as well as galaxy bias, set to $b = r = 1$. Per Figure the sum of the curves adds up to 1. Note the more localised behaviour of γ_t as a result of the J_2 filtering versus J_0 in w.*

the PDF of foreground galaxies.

Once the correlation functions are measured, we can distinguish between the two main approaches that I investigate in this thesis to measure galaxy bias parameters. The first relates observables to the different components in the definitions of b and r, see Section 2.3.2, so that the ratios provide the desired outcome. In the second approach, see Section 2.3.5, functions of $b(k, z)$ and $r(k, z)$ are fit to the lensing estimators. The caveat in measuring galaxy bias parameters directly from the real-space lensing estimators stems from the non-trivial relation between angular scales θ and Fourier scales k, which also differs per estimator. To show this, consider a binning in k where the lower k-value for each bin is given by

$$k_{\rm low}(n) = 10^{-4} \times 2^n \ {\rm Mpc}^{-1}\, h, \tag{2.75}$$

where the index n runs from 0 to ∞ and the upper k-value is $k_{\rm up} = k_{\rm low}(n + 1)$. For each $k-$bin we set the power spectrum to 0 for all $k-$values outside of the bin and calculate the estimators $w(\theta)$ and $\gamma_t(\theta)$. Figure 2.8 shows the resulting contributions of each $k-$bin to the estimators, after dividing by the (non-biased) theory predictions. Note that the result is sensitive to the adopted cosmology and redshift distributions, for which we used WMAP5 with a Smith et al. (2003) power spectrum and CFHTLenS redshift distributions with medians of 0.31 and 0.88 for the fore- and background, respectively.

The Figures 2.8 show how angular scales relate to wavenumbers, revealing the

different nature of w and γ_t. For example, a measure of γ_t at 30 arcmin is dominated by the power spectrum at $k \sim 0.3$ with significant contributions from $0.8 < k < 0.1$. The Figures are also interesting from the point of view of covariances. The mixing of k-modes will be reflected in the correlation between θ bins. Hence, the data points of projected clustering $w(\theta)$ are much more correlated compared to those of $\gamma_t(\theta)$. For extracting the growth rate from RSD, we are interesting in scales of $k \lesssim 0.5$, hence $\theta \gtrsim 20$ arcmin.

In the presence of a highly non-linear bias, for example with a k^2 term, high $k-$modes will contribute considerably to $w(\theta)$, since $w(\theta) \propto b^2$, so that the galaxy power spectrum at $k \sim 20$ will affect angular scales of $1 \gtrsim \theta \gtrsim 10$. At those k scales the power spectrum is poorly understood. This is worrisome in light of current modelling accuracies of the non-linear power spectrum (Harnois-Déraps et al., 2014; Takahashi et al., 2012). On the scales where models diverge, the bias measurements in this thesis are uncertain. However, the estimators also cover the quasi-linear regime and current and future surveys progress deeper and deeper into the linear regime where theoretical modelling is accurate.

2.3.2 Ratios of Estimators

In the previous section it was shown that the lensing and clustering correlation functions, referred to as the raw estimators, probe different scales for a given angular scale, due to the different orders of the Bessel functions, see Equations (2.69)-(2.74). Note however, that ξ_+ and ω both filter their corresponding power spectrum with J_0. Taking the square root of their ratio, we have

$$\sqrt{\frac{\omega(\theta)}{\xi_+(\theta)}} = \left(\frac{\int_0^\infty \frac{\mathrm{d}\ell\,\ell}{2\pi} P_n(\ell) J_0(\ell\theta)}{\int_0^\infty \frac{\mathrm{d}\ell\,\ell}{2\pi} P_\kappa(\ell) J_0(\ell\theta)} \right)^{1/2} \tag{2.76}$$

$$\simeq b(\theta) \times \left(\frac{\int_0^\infty \frac{\mathrm{d}\ell\,\ell}{2\pi} \int_0^\infty dw \left(\frac{p_f(w)}{f_K(w)}\right)^2 P_m\left(\frac{\ell}{f_K(w)}, w\right) J_0(\ell\theta)}{\int_0^\infty \frac{\mathrm{d}\ell\,\ell}{2\pi} \int_0^\infty \mathrm{d}w \left(\frac{W(w)}{f_K(w)}\right)^2 P_m\left(\frac{\ell}{f_K(w)}; w\right) J_0(\ell\theta)} \right)^{1/2} \tag{2.77}$$

Hence,

$$b = f_\theta \times \sqrt{\frac{\omega(\theta)}{\xi_+(\theta)}}, \tag{2.78}$$

where the function f_θ takes into account the difference between lensing kernel eq. (2.59) and p_f, as well as the difference in the amplitudes of the power spectra,

Equations (2.66) and (2.68), that is

$$f_\theta = \sqrt{\frac{\xi_+(\theta)}{\omega(\theta)}}\Bigg|_{\mathrm{b=r=1}}. \tag{2.79}$$

This method will only be exact in case where the bias is linear and time independent. A change in the bias over a small range of k scales, will affect all angular scales, see Figure 2.8. Also, the measured values cannot be too noisy as otherwise the ratio is poorly behaved. Consider for example a division by zero in large scales (Jullo et al., 2012). Furthermore, J_0 is a low pass filter, such that for a given θ, small l contribute predominantly. Perhaps the most important disadvantage, however, is that there is no similar method for obtaining $r(\theta)$, since $P_{\kappa n}(\propto br)$ is filtered by J_2.

2.3.3 Aperture Galaxy Bias

Several definitions of galaxy bias have been introduced due to the variety of ways in which we can describe density fields. This has resulted in a bias in terms of a smoothing scale R, the wave number k when taking the power spectrum, and comoving separation s in the case where we look at correlation functions. In this section yet another definition is introduced, the aperture galaxy bias, which is a clever combination of the previous definitions. It is based on the aperture mass, introduced in Section 1.2.5. The aperture method filters the convergence and number density fields with the same filter, so that their auto- and cross-correlation functions probe the same k scales for given angular separations.

By filtering the galaxy number density and convergence with the same filter U (which is compensated so that it obeys $\int \mathrm{d}x\, xU(x) = 0$), we can measure estimators of the variance of the dark matter and galaxy fields, including the covariance for an estimate of r. The idea was set out by Schneider et al. (1998) and uses a circular averaging of the shear field proposed by Kaiser (1995), called the aperture mass statistic, generalised by Schneider (1996), and discussed in the previous chapter (Section 1.2.5) where we introduced

$$M_{ap}(\theta_{ap}, \boldsymbol{\theta}) = \frac{1}{\theta_{ap}^2} \int \mathrm{d}^2\boldsymbol{\theta}' U\left(\frac{|\boldsymbol{\theta}' - \boldsymbol{\theta}|}{\theta_{ap}}\right) \kappa(\boldsymbol{\theta}'). \tag{2.80}$$

The aperture statistic performs a conversion from κ to M_{ap}, as illustrated in Figure 2.9, which shows M_{ap} for different smoothing sizes θ_{ap}. $M_{ap}(\theta_{ap})$ can

be measured from the shear correlation function $\xi_{\pm}$. To measure galaxy bias parameters, Schneider et al. (1998) proposed to convert δn to N_{ap}, the aperture count, using the same filter U

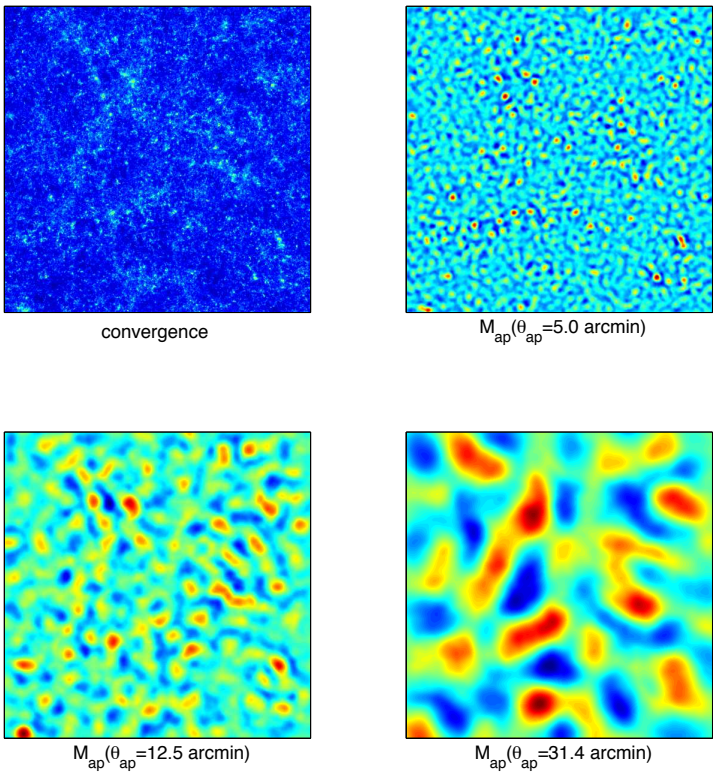

Figure 2.9 *The filtering of the convergence field, applied to a $z = 2$ clone realisation. The top left panel shows the convergence field, the remaining three Figures show M_{ap} for different smoothing sizes θ_{ap}.*

$$N_{ap}(\boldsymbol{\theta}, \theta_{ap}) = \frac{1}{\theta_{ap}^2} \int \mathrm{d}^2\theta' U\left(\frac{|\boldsymbol{\theta} - \boldsymbol{\theta}'|}{\theta_{ap}}\right) \delta n(\boldsymbol{\theta}') \tag{2.81}$$

In the naive approach that follows it is assumed that M_{ap} is proportional to δ_m like N_{ap} is to δ_g, which is only exact when the bias is scale- and time-independent, $b = b^{\mathrm{lin}}$,

$$\delta n(\boldsymbol{\theta}) = \int_0^\infty \mathrm{d}w\, p_f(w) b(f_K(w)\boldsymbol{\theta}, w) \delta_m(f_K(w)\boldsymbol{\theta}, w), \tag{2.82}$$

$$\approx b \int_0^\infty \mathrm{d}w\, p_f(w) \delta_m(f_K(w)\boldsymbol{\theta}, w). \tag{2.83}$$

In this approximation, the galaxy bias parameters can be defined from the covariances of the filtered fields M_{ap} and N_{ap}, similar to (2.8) and (2.9) (Hoekstra

et al., 2002)

$$b(\theta_{ap}) = f_b(\theta_{ap})\sqrt{\frac{\langle N_{ap}^2(\theta_{ap})\rangle}{\langle M_{ap}^2(\theta_{ap})\rangle}} \tag{2.84}$$

$$r(\theta_{ap}) = f_r(\theta_{ap})\frac{\langle M_{ap}(\theta_{ap})N_{ap}(\theta_{ap})\rangle}{\sqrt{\langle M_{ap}^2(\theta_{ap})\rangle\langle M_{ap}^2(\theta_{ap})\rangle}}, \tag{2.85}$$

where the functions $f_b(\theta_{ap})$ and $f_r(\theta_{ap})$ account for the difference in volume probed by M_{ap} and N_{ap}

$$f_b(\theta_{ap}) = \sqrt{\frac{\langle M_{ap}^2(\theta_{ap})\rangle}{\langle N_{ap}^2(\theta_{ap})\rangle}}\bigg|_{\mathrm{b=r=1}} \tag{2.86}$$

$$f_r(\theta_{ap}) = \frac{\sqrt{\langle M_{ap}^2(\theta_{ap})\rangle\langle M_{ap}^2(\theta_{ap})\rangle}}{\langle M_{ap}(\theta_{ap})N_{ap}(\theta_{ap})\rangle}\bigg|_{\mathrm{b=r=1}}. \tag{2.87}$$

To calculate f_b and f_r we need theoretical descriptions of the aperture covariances. The autocorrelation function of M_{ap} is calculated by Schneider et al. (1998) as follows

$$\langle M_{\mathrm{ap}}^2(\theta_{ap})\rangle = \int \mathrm{d}^2\theta' U(\theta') \int \mathrm{d}^2\varphi U(\varphi)\langle\kappa(\boldsymbol{\theta'})\kappa(\boldsymbol{\varphi})\rangle \tag{2.88}$$

$$= \int \mathrm{d}^2\theta' U(\theta') \int \mathrm{d}^2\varphi U(\varphi) \int \frac{\mathrm{d}^2 l}{(2\pi)^2} \mathrm{e}^{i\boldsymbol{l}\cdot(\boldsymbol{\theta'}-\boldsymbol{\varphi})} P_\kappa(l) \tag{2.89}$$

$$= 2\pi \int_0^\infty \mathrm{d}l l P_\kappa(l) \left(\int_0^\theta \mathrm{d}\varphi\varphi U(\varphi) J_0(l\varphi)\right)^2, \tag{2.90}$$

The variance of N_{ap} and covariance of M_{ap} and N_{ap} is found similarly. If we define $I(\theta l) = \int_0^\theta \mathrm{d}\varphi\varphi U(\varphi) J_0(l\varphi)$, they can be written as

$$\langle M_{ap}^2(\theta_{\mathrm{ap}})\rangle = 2\pi \int_0^\infty \mathrm{d}\ell\, \ell P_\kappa(\ell) I^2(\ell\theta) \tag{2.91}$$

$$\langle N_{ap}^2(\theta_{\mathrm{ap}})\rangle = 2\pi \int_0^\infty \mathrm{d}\ell\, \ell P_n(\ell) I^2(\ell\theta) \tag{2.92}$$

$$\langle M_{ap}N_{ap}(\theta_{\mathrm{ap}})\rangle = 2\pi \int_0^\infty \mathrm{d}\ell\, \ell P_{\kappa n}(\ell) I^2(\ell\theta) \tag{2.93}$$

Equations (2.84) and (2.85) rely on $b(k)$ and $r(k)$ to vary slowly with time and

scale

$$\langle N_{ap}^2(\theta_{ap})\rangle \approx \langle N_{ap}^2(\theta_{ap})\rangle|_{b=1} \times b^2(\theta_{ap}) \tag{2.94}$$

$$\langle M_{ap}N_{ap}(\theta_{ap})\rangle \approx \langle M_{ap}M_{ap}(\theta_{ap})\rangle|_{b=r=1} \times b(\theta_{ap})\, r(\theta_{ap}) \tag{2.95}$$

By taking ratios one can rearrange for $b(\theta_{ap})$ and $r(\theta_{ap})$ to give Equations (2.84) and (2.85).

In practice, the aperture statistics are derived from integrals over the raw estimators

$$\langle M_{ap}^2(\theta_{\rm ap})\rangle = \frac{1}{2}\int_0^\infty {\rm d}x\, x\big[\xi_+(x\theta_{ap})T_+(x) + \xi_-(x\theta_{ap})T_-(x)\big] \tag{2.96}$$

$$\langle N_{ap}^2(\theta_{\rm ap})\rangle = \int_0^\infty {\rm d}x\, x\, \omega(x\theta_{\rm ap})T_+(x) \tag{2.97}$$

$$\langle M_{ap}N_{ap}(\theta_{\rm ap})\rangle = \int_0^\infty {\rm d}x\, x\, \langle\gamma_t\rangle(x\theta_{\rm ap})F(x), \tag{2.98}$$

where the functions $T_\pm$ and F are given by

$$T_\pm(x) = (2\pi)^2 \int_0^\infty {\rm d}s\, s\, I^2(s)J_{0,4}(sx), \tag{2.99}$$

$$F(x) = (2\pi)^2 \int_0^\infty {\rm d}s\, s\, I^2(s)J_2(sx). \tag{2.100}$$

The filter function suggested by Schneider et al. (1998) is

$$U(\theta) = \frac{9}{\pi\theta_{\rm ap}^2}\left[1 - \left(\frac{\theta}{\theta_{\rm ap}}\right)^2\right]\left[\frac{1}{3} - \left(\frac{\theta}{\theta_{\rm ap}}\right)^2\right]. \tag{2.101}$$

With this choice of filter function $I(\ell\theta)$ is given by

$$I(\ell\theta) = \frac{12}{\pi(l\theta)^2}J_4(l\theta), \tag{2.102}$$

Note that as I is a narrow-band filter, a single θ_{ap} mode can be related to an angular wavenumber $\ell \sim 4.25/\theta_{ap}$, which Bartelmann and Schneider (1999) found by writing the filter function as a Dirac delta function

$$J^2(x) \approx \frac{512}{1155\pi^3}\delta_D(x - \frac{693\pi}{512}) \approx 1.43 \times 10^{-2}\delta_D(x - 4.25), \tag{2.103}$$

motivated by the peaked form of the filter function. With $z_{\rm eff}$ the mean redshift

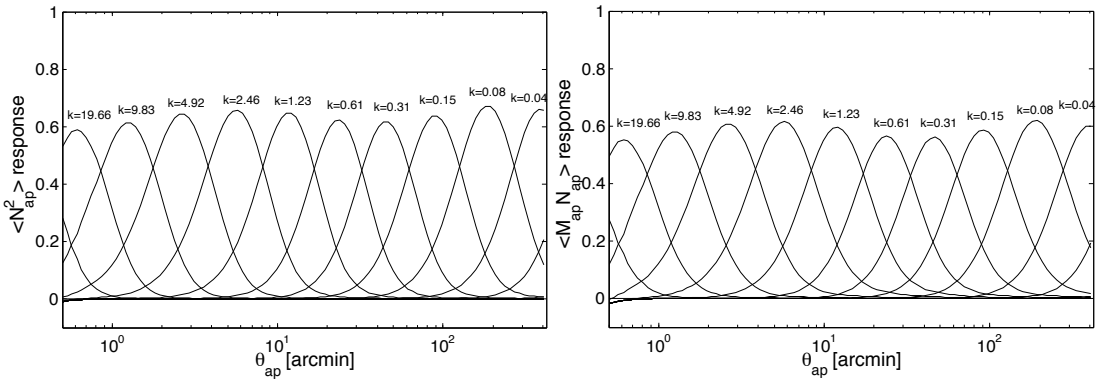

Figure 2.10 *$\langle N_{ap}^2 \rangle$ and $\langle M_{ap} N_{ap} \rangle$ response to different k-scales, as in Figure 2.8. The same conditions were applied as in Figure 2.8.*

of the foreground distribution, it is convenient to define the effective wavenumber $k_{\rm ap}$ and effective physical scale $R_{\rm ap}$ probed as

$$k_{\rm ap} = \frac{4.25}{\theta_{\rm ap} f_K(w(z_{\rm eff}))} \tag{2.104}$$

$$R_{\rm ap} = \frac{2\pi}{k_{\rm ap}} \approx 1.48\, \theta_{\rm ap} f_K(w(z_{\rm eff})), \tag{2.105}$$

noting that the correct way to think about $k_{\rm ap}$ and $R_{\rm ap}$ is in terms of distributions, of which details are determined by the adopted filter function. Figure 2.10 shows the transformation from a binning in Fourier space, given by Equation (2.75), to a binning in θ_{ap}. This shows that the conversions in Equation (2.104) are approximate, since θ_{ap} scales contain contributions from multiple $k-$bins.

The integral constraint introduces a bias in the projected angular clustering $\omega(\theta)$ which can be understood from the sensitivity of the mean galaxy density to the considered volume, explained in more detail in Section 3.2.1. As a result of the finite nature of the compensated filter function, the aperture count variance $\langle N_{\rm ap}^2(\theta_{\rm ap}) \rangle$ is insensitive to the integral constraint.

The aperture statistics in Equations (2.96)-(2.98) are biased at small and large scales, due to the broadness of the filter function. Hence the range over which θ_{ap} can be related to physical scales, see Equation (2.104), should be carefully examined, see Kilbinger et al. (2013). The upper limit on θ_{ap} is given by the finite survey size. The lower limit on θ_{ap} results from the determination of galaxy ellipticities, which for any method is limited by galaxy sizes. For example, CFHTLenS used a lower limit of $\theta_{ap} = 5.5$ arcmin in the determination of cosmological parameters from the aperture statistics (Kilbinger et al., 2013).

2.3.4 Time and scale-dependent Aperture Bias

In order to separate b and r from the power spectra and write the parameters of interest outside the integrals, e.g. Equations (2.82) and (2.83), the aperture bias method assumes small scale- and time-dependence of the bias parameters. The integrals run over redshift (for projection) and angular wavenumber (for the Fourier to real space conversion). In this section, I assess how accurate this approximation is.

Theory

From the Dirac delta function approximation in (2.103) Hoekstra et al. (2002) found expressions for the weighted (in time and scale) averages of the bias parameters

$$\langle b^2\rangle(\theta_{\rm ap}) \approx \frac{\int_0^\infty {\rm d}w\, h_b(w,\theta_{\rm ap}) b^2\left(\frac{4.25}{\theta_{\rm ap} f_K(w)}, w\right)}{\int_0^\infty {\rm d}w\, h_b(w,\theta_{\rm ap})} \tag{2.106}$$

$$\langle r\rangle(\theta_{\rm ap}) \approx \frac{\int_0^\infty {\rm d}w\, h_r(w,\theta_{\rm ap}) r\left(\frac{4.25}{\theta_{\rm ap} f_K(w)}, w\right)}{\int_0^\infty {\rm d}w\, h_r(w,\theta_{\rm ap})} \tag{2.107}$$

where the functions h_b and h_r are given by

$$h_b(\theta_{\rm ap}, w) = 2\pi \left(\frac{p_f(w)}{f_K(w)}\right)^2 \int_0^\infty {\rm d}\ell\, \ell\, P_m\left(\frac{\ell}{f_K(w)\theta_{\rm ap}}, w\right) J^2(\ell\theta_{ap}) \tag{2.108}$$

$$h_r(\theta_{\rm ap}, w) = 2\pi \frac{p_f(w) W(w)}{(f_K(w))^2} \int_0^\infty {\rm d}\ell\, \ell\, P_m\left(\frac{\ell}{f_K(w)\theta_{\rm ap}}, w\right) J^2(\ell\theta_{ap}) \tag{2.109}$$

The fudge factors f_b and f_r (Equations (2.86) and (2.87), respectively) account for the difference in volume probed. The correction becomes stronger and more angular-dependent when the lensing kernel peaks at a different redshift to the foreground distribution. In the presence of time-dependent bias, which is expected from a variety of reasons, see Section 2.1.2, this can mean that γ_t is sensitive to a slightly different cross-correlation coefficient and galaxy bias than those we are interested in, the bias parameters of the foreground galaxy sample.

As an example, we can write the cross-correlation coefficient in terms of the

measured bias parameters

$$r_{\rm measured} = \frac{b_{gm}}{b_g} \times r_{\rm true} \tag{2.110}$$

where b_{gm} is the bias measured from $P_{gm} = b_{gm} r P_m$, while b_g is the bias in $P_g = b_g^2 P_m$. Normally, $b_{gm} = b_g$. However, b_{gm} is the bias weighted by the lensing kernel times foreground $n(z)$, and b_g is the bias weighted by just the foreground $n(z)$. Therefore, $b_{gm}/b_g = 1$ is only exact if the lensing kernel and foreground $n(z)$ overlap. Therefore, some discrepancy between $r_{\rm measured}$ and $r_{\rm true}$ is expected in the presence of time-dependent bias and an offset between the peaks of the lensing kernel and foreground $n(z)$. Note that a narrower foreground $n(z)$ makes sure that $b_{gm} \simeq b_g$, because the time is more limited over which b can vary. With a narrow foreground $n(z)$, the lensing kernel may well peak at a redshift where there are no lenses, so that the product with the foreground $n(z)$ does not contribute.

Results

We test the impact of a nonlinear time-dependent galaxy bias on the measurement of r using the aperture method by looking at the WiggleZ and BOSS samples with RCSLenS in the background. WiggleZ has a much broader $n(z)$ compared to BOSS, as shown in Figure 2.11. Therefore, bias time-dependence affects $r(\theta_{ap})$ of the full WiggleZ sample much more than that of BOSS, see Figure 2.12, where the true galaxy bias is given by $b = (1+z)b_0$ with $b_0 = 1$, while the measurement assumes $b = 1$. The effect from time-dependence is more significant for BOSS, but much less compared to WiggleZ.

How well the aperture bias model recovers the true cross-correlation coefficient is shown in Figure 2.13, where for the $r(k)$ model we choose a functional form motivated by observations of $r \sim 0.5$ (e.g. Simon et al., 2007) and the fact that $r \to 1$ with decreasing k. A smooth transition from $r \sim 0.5$ to 1 is provided by the following function

$$r(k) = [\tan^{-1}(-k) + \pi]/\pi, \tag{2.111}$$

The bias model of Cole et al. (2005) describes simulations well and is employed

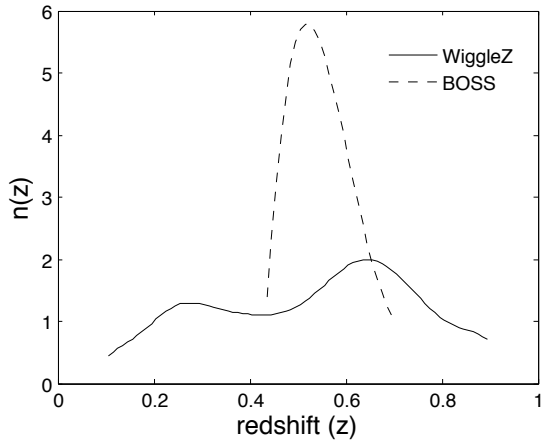

Figure 2.11 *The redshift distributions of WiggleZ and BOSS.*

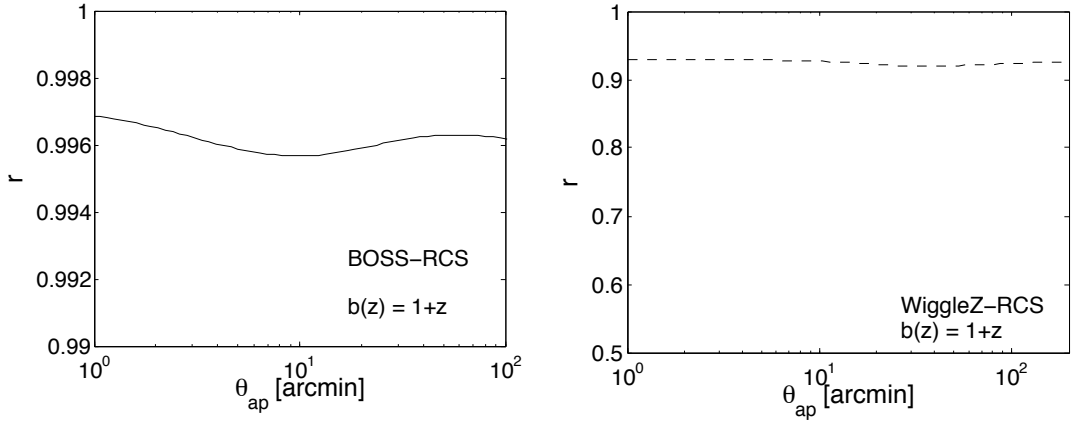

Figure 2.12 *The cross-correlation coefficient $r(\theta_{ap})$ for BOSS (a) and WiggleZ (b) with RCSLenS as the source distribution in the presence of a time-dependent bias $b(z) = (1+z)b_0$ with $b_0 = 1$.*

here

$$b(k) = b_1 \sqrt{\frac{1 + C_1 k^2}{1 + C_2 k}}, \tag{2.112}$$

where b_1, C_1, and C_2 are free parameters, see Section 2.3.5 for more details of this model. The aperture cross-correlation coefficient is a weighted quantity, see Equation 2.106, resulting in a discrepancy between input model $r(k)$, black solid line, and the recovered value, and is also slightly affected by $b(k, z)$. Fig. 2.13 shows that, in the presence of time- and scale-dependence, a few percent discrepancy between true and measured $r(\theta_{ap})$ is inherent to the aperture method. The Cole et al. (2005) model, Equation (2.112), was used with $[b_1, C_1, C_2] = [1.2, 7, 1.4]$. The resulting $b(k)$ was further multiplied with $1 + z$ to include time-dependence. CFHTLenS redshift distributions were used for this figure,

see Section 5.3.

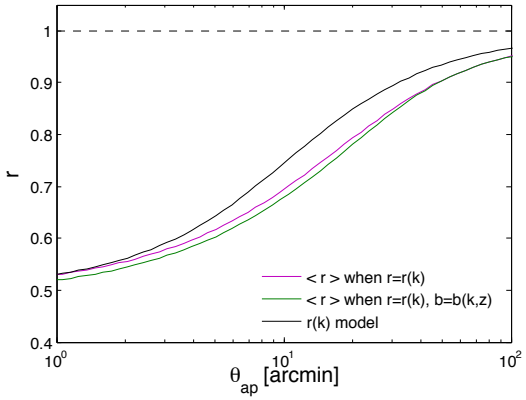

Figure 2.13 *The cross-correlation coefficient as measured by the aperture galaxy bias method in the presence of scale-dependence in r (magenta line) and when we, in addition, include scale- and time-dependence in the bias (green line). The input model for r(k) is shown by the black solid line. See Equations* (2.111) *and* (2.112) *for the models of scale-dependence.*

Fig. 2.14 summarises the bias in the aperture method from the assumption of a scale independent bias when the bias is in fact scale and time-dependent. Again the model in Equation (2.112) was used for $b(k)$, $b(z)$ was given by $b(z) = 1 + z$ and time- and scale-dependence combined was given by $b(k, z) = b(k)b(z)$. The redshift distributions correspond to CFHTLenS' fore- and background samples, discussed in 5.3. The legend in the top left panel is for all panels.

The top two panels show b (left) and r (right) measured by the aperture galaxy bias method when the true underlying galaxy bias is time-dependent, given by $b(z) = (1 + z)b_0$, with $b_0 = 1$. The dashed line is the average galaxy bias, weighted by the redshift distribution of foreground galaxies. The solid lines show the recovery of the aperture method.

The middle two panels show the recovery of a scale-dependent bias for the aperture method, shown for 3 different values of the C_1 parameter in Equation (2.112), while b_1 and C_2 were fixed to $[b_1, C_2] = [1.2, 1.4]$. With increasing scale-dependence the discrepancy is worse. For the bias model, the input model with $C_1 = 7$ (green line in middle left plot) would be better fit by $C_1 \simeq 10.84$ for data in 7 logarithmic bins from 4 to 60 arcminutes, and keeping b_1 fixed, otherwise the best fit values would be $[b_1, C_1] = [1.33, 8.63]$. Also note that r is affected at the 1% level.

The lower panels include time-dependence by multiplying $b(z) = (1 + z)b_0$

with $b(k)$, showing that including time-dependence does not lead to significant discrepancies, although for broader foreground distributions this will become more important.

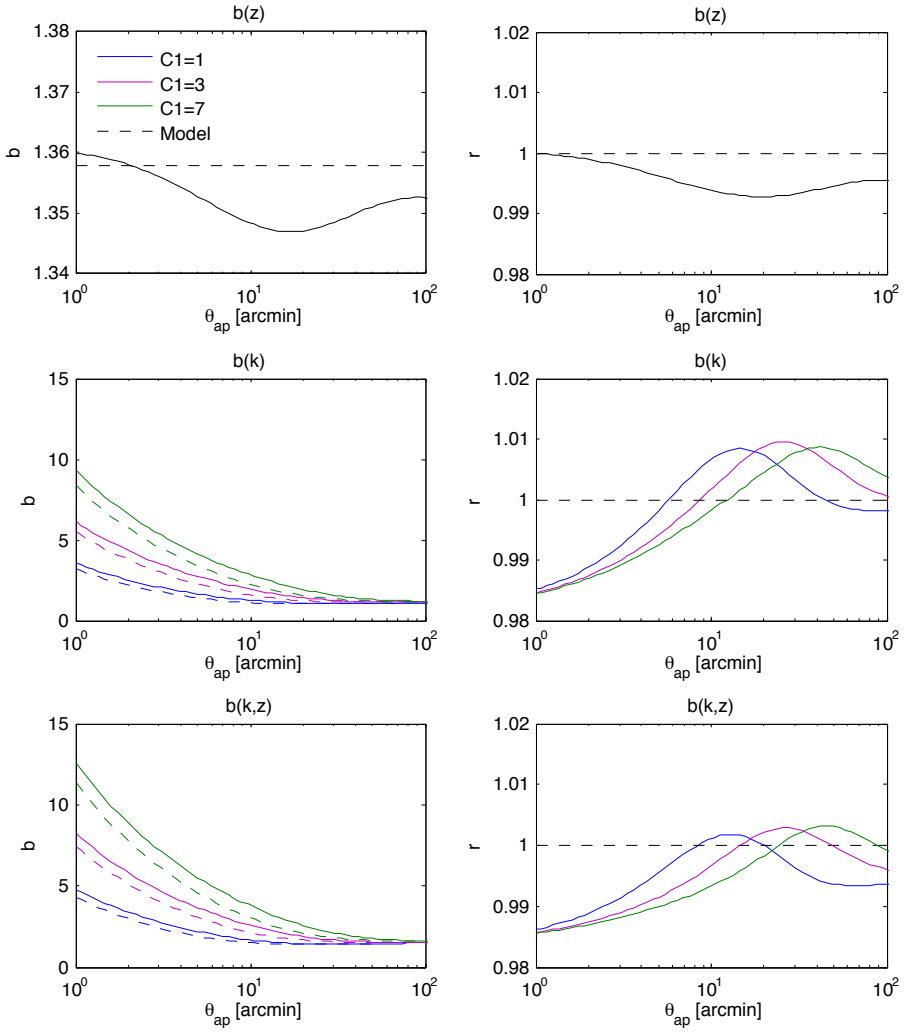

Figure 2.14 *An overview of the recovery of the galaxy bias parameters b (left) and r (right) by the aperture method when the galaxy bias is nonlinear and/or time-dependent. The legend in the top left panel serves for all panels, where C_1 is a scale-dependence parameter in Equation (2.112). The dashed lines show the input model, the solid lines the aperture method recovery. Top panels show the effect of time-dependence (the model is here the weighted average of $b(z)$). In the middle panels the bias is scale-dependent, and the lower panels show the combined effect.*

Conclusion

The aperture statistic provides a method to measure $b(\theta_{ap})$ and $r(\theta_{ap})$, but, as shown in this analysis, they are difficult to interpret; they were defined similar to

$b(R)$ and $r(R)$, are theoretically described by weighted versions of $b(k)$ and $r(k)$, and are measured with correlation functions like $b(s)$ and $r(s)$. All studies using the aperture mass statistic measure a slightly low cross-correlation coefficient, even in the quasi-linear regime where RSD studies assume $r = 1$. This could in part be attributed to scale- and time-dependence. Based on the results in this section, the effects are, however, not strong enough to attribute the $r < 1$ observations solely to the inaccuracy that were revealed in this analysis.

In addition to the low $r(\theta_{ap})$ values measured in the literature, it has also been found to exceed unity at small scales, which may in part be explained by taking ratios of noisy quantities. This additional complication is addressed in Chapter 3, where it is shown that, with present day number densities and survey areas, further offsets of $\sim 1\%$ can be expected. It is, however, worth measuring these parameters for the samples available in this thesis, see Chapter 4, noting that they are not easily translated to $b(k)$ and $r(k)$, as $5 - 10\%$ offsets can be expected, depending on the scale- and time-dependence of the galaxy bias parameters.

2.3.5 Fitting Formulae

Improving our understanding of galaxy bias not only improves the accuracy of cosmological constraints from galaxy surveys, but also opens up a wealth of information about the observed galaxy distribution. The nature of galaxy bias is linked to galaxy formation, which implies that the functional in Equation (2.2) is not easily condensed into a set of parameters that can be constrained. However, several attempts have been made, both from simulations and theory.

In this thesis, galaxy bias is studied with the lensing and clustering estimators (w, γ_t, and $\xi_\pm$), which requires models or a binning in wavenumber k and redshift z, see for example Simon (2012). Given the complexity of galaxy bias and the accuracy of current surveys, there is a trade-off between number of free parameters and the restrictiveness of the model. That is, with lots of parameters we increase flexibility but decrease constraining power, while with fewer parameters we run the risk of having a poor description of the galaxy bias. In this section I will review some simple bias models $b(k)$ and decide whether they are good candidates to be used in fitting models to lensing and clustering data.

Scale-dependence from discrete tracers

Schulz and White (2006) derive a scale-dependent bias model from the consideration that dark matter particles cluster within haloes, the 1-halo term, and that the haloes themselves cluster, the 2-halo term. This configuration of dark matter clustering is traced by galaxies, but being discrete tracers, the 1-halo term of the galaxy power spectrum is shifted by a different amount than the 2-halo term galaxy power spectrum, causing a scale-dependence in the galaxy bias beyond non-linear scales.

$$b(k) = b_1^{\mathrm{SW}} \sqrt{1 + \frac{b_2^{\mathrm{SW}}}{P_m(k,z)}}, \tag{2.113}$$

where b_1^{SW} and b_2^{SW} are free parameters. The model is only accurate for $0.001 < k < 0.1$ and is in principle a linear shot noise model, where the parameter b_2^{SW} depends on how galaxies populate dark matter haloes (often assumed to be Poissonian). A similar model, but with an extra free parameter, can be found in Seo and Eisenstein (2005) equation 1.

The model is intended to describe the effects of shot noise on the scale-dependence of the bias. It does not include all the complex processes that lead to additional scale-dependence. Hence, it may not provide a good fit to the lensing and clustering data.

N-body fitting formula

The (Cole et al., 2005) model, given in Equation (2.112), has no physical motivation but describes N-body simulations well. It is better behaved at small scales compared to the (Schulz and White, 2006) model, but involves an extra parameter. One way of dealing with this extra free parameter is to use halo model catalogues to predict either one of them. Based on this Cole et al. (2005) argue C_2 to be less sensitive to the galaxy population so that b_1 and C_1 are the free parameters. A disadvantage of fixing C_2 is that C_1 with non-zero C_2 cannot account for a linear bias. The current datasets are only just becoming sufficiently large to distinguish a linear from a non-linear bias. Hence, the assumption of scale-dependence is quite strong from an observational perspective. Figure 2.15 shows a fit of the model with nonzero C_2 to a linear bias. This shows that C_2 cannot cancel the scale-dependence. However, by comparing the minimum χ^2 of a linear model and that of a non-linear model, detection of scale-dependence may

or may not be concluded.

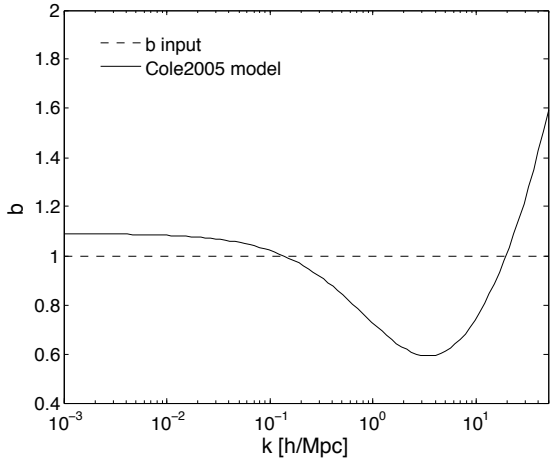

Figure 2.15 *The solid line is the attempt of the model in Equation* (2.112) *to recover a linear bias when setting* $C_2 = 1.4$*. The best fit values are* $b_1 = 1.09$ *and* $C_1 = 0.0601$*, and* k *was bounded as* $0.001 < k < 50$*.*

Renormalised bias parameters

Several authors predict the galaxy power spectrum from the local galaxy bias model of Equation (2.3) and perturbation theory. The density fluctuation field at some redshift is expanded as

$$\delta_m(\mathbf{k}, z) = \delta_m^{(1)}(\mathbf{k}, z) + \delta_m^{(2)}(\mathbf{k}, z) + \delta_m^{(3)}(\mathbf{k}, z) + \cdots . \tag{2.114}$$

According to perturbation theory, the nth order matter contrast can be found from the linear field $\delta_m^{(1)}$, the growth Equation (1.13) and knowledge of how different Fourier modes are coupled as a result of non-linear clustering

$$\delta_m^{(n)}(\mathbf{k}, z) = D^n(z) \int d^3\mathbf{q_1} \cdots d^3\mathbf{q_1} \delta_m^{(1)}(\mathbf{q_1}) \cdots \delta_m^{(1)}(\mathbf{q_n}) \tag{2.115}$$

$$\times F_n(\mathbf{q}_1, \cdots, \mathbf{q}) \delta_D^3 \left(\mathbf{k} - \sum_i \mathbf{q_i} \right), \tag{2.116}$$

where F_n is the mode-coupling kernel. The second order standard mode coupling kernel is given by

$$F_2(\mathbf{q_1}, \mathbf{q_2}) = \frac{5}{7} + \frac{1}{2} \frac{\mathbf{q_1} \cdot \mathbf{q_2}}{q_1 q_2} \left(\frac{q_1}{q_2} + \frac{q_2}{q_2} \right) + \frac{2}{7} \left(\frac{\mathbf{q_1} \cdot \mathbf{q_2}}{q_1 q_2} \right)^2 \tag{2.117}$$

Heavens et al. (1998) renormalised the bias parameters by first expanding the galaxy density as

$$\rho_g = \rho_0 + \rho_0'\delta + \frac{1}{2}\rho_0''\delta^2 + \frac{1}{6}\rho_0'''\delta^3 + \epsilon + \mathcal{O}(\delta^4), \tag{2.118}$$

and then applying the perturbation theory formalism, from which it can be shown that

$$P_{gm}(k) = b_1 P_{mm}(k) + 2b_2 A(k), \tag{2.119}$$

$$P_{gg}(k) = b^2 P_{mm}(k) + 2b_1 b_2 A(k) + \frac{b_2^2}{2} B(k), \tag{2.120}$$

where

$$A(k) = \int \frac{d^3q}{(2\pi)^3} F_2(\mathbf{q}, \mathbf{k}-\mathbf{q}) P(q) P(|\mathbf{k}-\mathbf{q}|), \tag{2.121}$$

$$B(k) = \int \frac{d^3q}{(2\pi)^3} P(q) P(|\mathbf{k}-\mathbf{q}|), \tag{2.122}$$

(see also Baldauf et al. (2010); McDonald (2006); Nishizawa et al. (2013)). Although the model is physically motivated, it is by construction only accurate in the linear and quasi-linear regime. Also, the bias parameters b_1 and b_2 in here are renormalised, so although related to b_i in Equation (2.3), they have different meaning. There is no arbitrary smoothing scale involved as a result of the assumption in the peak-background split; the smoothing is large enough for the field to be Gaussian, hence is only valid at corresponding $k-$scales.

As was discussed in Section 2.1.3, several factors cause the local, quadratic bias expansion to be inaccurate. Even for the 2-point statistic very large smoothing scales of 30Mpc/h have to be applied in order to describe the bias sufficiently with this model (Manera and Gaztañaga, 2011).

Mandelbaum et al. (2013) have also measured b_1 and b_2 from the SDSS survey, using clustering and galaxy-galaxy lensing. Although they use the annular differential surface mass density (ADSD), also called ring statistic, and lack shear auto-correlations, this result will be interesting to compare to. Although the ring statistic excludes small scales where the model breaks down, the minimum scale used by Mandelbaum et al. (2013) of $R_0 = 4$Mpc is about an order of magnitude too low in order to be confident that no other mechanisms, such as nonlocal bias, affect the parameters constrained (Manera and Gaztañaga, 2011). The R_0 parameter does, however, allow them to exclude scales where results are likely to

be affected by stochasticity.

Nishizawa et al. (2013) provide a theoretical analysis of the dependence of b_1 and b_2 on halo mass, which they also compare to simulations, finding good agreement on large scales. Figure 2.16, taken from Nishizawa et al. (2013), shows b_1 and b_2 on the vertical axis as a function of halo mass on the horizontal axis. Clearly, this direct relation will become inaccurate in the presence of a more complicated bias relation, perhaps most notably stochasticity.

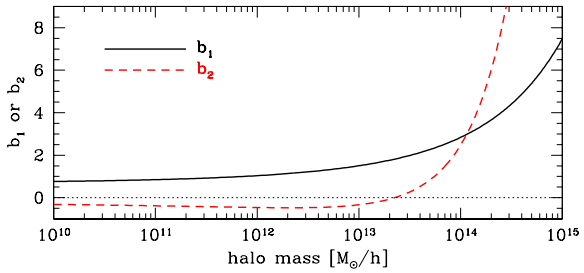

Figure 2.16 *This Figure is taken from Nishizawa et al. (2013) who calculated the dependence of the renormalised bias parameters b_1 and b_2 on halo mass. Hence, a measurement of b_1 and b_2 constrains the halo mass of the galaxy population, provided the second order bias model accurately describes the true galaxy bias of the survey.*

To conclude, using the renormalised bias parameters as a choice of fitting model has advantages:

- physically motivated,
- relation of parameters to halo mass,
- automatically includes redshift dependence,
- adopted in a previous publication (Mandelbaum et al., 2013).

These are set against the following disadvantages:

- the model is local and determinstic,
- the model is invalid at small scales.

The disadvantages can be partly dealt with. For example, by discarding small θ values, we can limit the fitting to (quasi-)linear scales. The minimum θ value can be varied in order to see if the results are still consistent.

Since both scale-dependence (determined by b_2) and stochasticity affect $r(k)$, the Equation (2.119) for P_{gm} is inaccurate in the presence of stochasticity. In order to test this in our analysis I advocate the use of an additional parameter $\mathcal{R}$ to allow for a stochastic component and nonzero higher order bias terms in P_{gm}. We therefore multiply P_{gm} by some function $\mathcal{R}(k)$, so that

$$P_{gm}(k) = \mathcal{R}(k)\left[b_1 P_{mm}(k) + 2b_2 A(k)\right], \tag{2.123}$$

where $\mathcal{R}(k)$ determines the change in $P_{gm}(k)$ as a result of nonzero stochastic and higher order terms. Similar to $r(k)$, the functional form of $\mathcal{R}$ is unknown and will depend on various factors, such as galaxy type. Noting that $P_{gm}(k) = b(k)r(k)P_{mm}(k)$, the set $[\mathcal{R}(k), b_1, b_2]$ is straightforwardly related to $r(k)$

$$r(k) = \mathcal{R}(k)\left(\frac{b_1 P_{mm}(k) + 2b_2 A(k)}{b(k)P_{mm}(k)}\right). \tag{2.124}$$

Although $R(k)$ is not a cross-correlation coefficient, when $r(k) = 1$, we have $\mathcal{R}(k) = 1$. In the fitting $\mathcal{R}$ can be set to a constant, allowing a three-parameter fit (b_1, b_2, and $\mathcal{R}$). If we find $\mathcal{R}$ to be consistent with $\mathcal{R} = 1$, then b_1 and b_2 are meaningful and can be related to halo mass through the formalism of Nishizawa et al. (2013).

Conclusion

With future surveys such as Euclid, the full matter power spectrum $P_m(k, z)$ can be measured directly from the data (Simon, 2012). The number of z and k bins is limited by the surveyed volume and selection function, and hence, for current surveys the S/N does not allow for fine k-binning, and we therefore need to make assumptions about $b(k)$ and $r(k)$.

Although the aperture mass statistic does not recover the exact scale-dependence of bias parameters, it can be used to construct a functional form. The advantage is that this will provide a good fit to the data and it is free from assumptions on how b and r vary with scale, as this comes solely from the data. However, scale-dependence in the aperture bias parameters is dominated by noise, see Chapter 3.

The Schulz and White (2006) model is only accurate at large scales, beyond the sensitivity of lensing measurements. Although the Cole et al. (2005) model is

accurate at smaller scales than the Schulz and White (2006) model, it makes a strong assumption about scale-dependence in the case of fixing C_2. Furthermore, both models only predict P_g, while for P_{gm} the cross-correlation coefficient is required. Therefore, these models are not suitable for the lensing analysis in Chapter 4.

We conclude that the most interesting model to constrain is the renormalised bias model, although an extension to incorporate stochasticity (and higher order nonlinear bias terms) is required if we are to use the raw lensing estimators, because angular separations mix physical scales, so that it is impossible to make a hard cut in real or Fourier space. The $\mathcal{R}$ parameter was introduced to solve this issue, from which we can also find the cross-correlation coefficient.

Chapter 3

Simulations and Method Testing

Since the first detections of galaxy-galaxy lensing (Brainerd et al., 1996; Fischer et al., 2000) and cosmic shear (Bacon et al., 2000; Kaiser et al., 2000; Van Waerbeke et al., 2000; Wittman et al., 2000) there have been huge advances in survey area, depth, quality, and understanding of systematics related to lensing, e.g. the Shear TEsting Program (STEP Heymans et al., 2006) and the GRavitational lEnsing Accuracy Testing project (GREAT Bridle, 2009). There have also been major advances in N-body simulations, which are crucial for accurate measurements of error covariance matrices.

In this chapter I measure error covariance matrices from lensing simulations, which will be used for galaxy bias measurements from CFHTLenS (Bonnett et al in prep.). The same techniques will be used for the error analysis in Chapter 4. Additionally, the simulations are used to test the galaxy bias methods discussed in Chapter 2.

3.1 Introduction

This thesis makes use of lensing simulations carried out by Harnois-Déraps et al. (2012) to estimate the covariance matrix for the galaxy bias measurements of Bonnett et al (in prep), as well as the measurements in Chapter 4. Ray-tracing simulations are computationally expensive dark matter N-body simulations through which the trajectories of photons are simulated, establishing the background shear field. By using the Born approximation, see section 1.2.5,

computation time can be significantly reduced allowing for more realisations. The overview here is based on Harnois-Déraps et al. (2012).

Multiple independent realisations of the Universe provide an estimate of cosmic variance, which is the uncertainty arising from the influence of the large scale structure on the measurement, so that a measurement at different parts of the sky have non-zero variance. Additional variance comes from intrinsic ellipticities, measurement error, the distribution of lenses and sources as a function of distance, and their number densities, all of which are included in the mock catalogues for this thesis. However, intrinsic alignments and the clustering of sources (Bernardeau, 1998) have not been taken into account, noting that the clone project will include all such systematics in the future (Harnois-Déraps et al., 2014).

In the real Universe we have one past light cone in which the observer and the light sources are causally connected. Because time is not constant throughout the volume, it is difficult to simulate this all at once. Therefore, the large modes that emanate from observer to earlier times are not easily modelled. Limber (1953) showed that these modes contribute little to the lensing statistics. For the clone simulations it was assumed that coherence in the shapes of galaxies occurs over maximum scales of a few times the size of the largest clusters, so that simulation box sizes of a few times $\sim 10^2$Mpc would be sufficient. The assumption proved to be a too optimistic interpretation of Limber's 1953 argument for the clone comoving box sizes of 147 Mpc/h, since the clones underestimate the lensing signal on large scales. Therefore, improved simulations are currently under construction by the same team, which we will use for future work, noting that this thesis makes use of the smaller simulations currently available.

The most reliable, albeit computationally expensive, way of simulating the lensing effect is to calculate, in 3 dimensions, the photon's geodesics. Due to the requirement of many realisations, the clone project has an alternative approach. Firstly, the output at a given redshift is used more than once by randomly rotating it, as well as shifting the origin, minimising the correlation between the resulting sub-volumes, which arises due to large scale structure growth across redshift slices. It was shown by Vale and White (2003) that a tiling-technique can offer almost identical results to the full 3D ray-tracing technique, while being less time consuming. The sub-volumes are collapsed into thin lenses, called tiles, of which the lensing effect is calculated in the assumption of the Born approximation, in which the lensing calculation involves only integration over the line of sight power

spectrum, not P_m over the photon's path, see also section 1.2.5.

The input cosmological model is based on the results from WMAP5 (Dunkley et al., 2009): $\Omega_\Lambda = 0.721$, $\Omega_m = 0.279$, $\Omega_b = 0.046$, $n_s = 0.96$, $\sigma_8 = 0.817$ and $h = 0.701$. The comoving volume of boxes at $z > 1$ is $V = 231.1^3(\mathrm{Mpc/h})^3$, and for $z < 1$ this is $V = 147.0^3(\mathrm{Mpc/h})^3$. There are 1024^2 pixels with a surface of 0.21^2 arcmin^2, yielding a total angular grid of $3.58^\circ \times 3.58^\circ$. With this set-up, the particle mass at $z > 1$, $m_p = 1.2759 \times 10^9 M_\odot$ and at $z < 1$, $m_p = 3.2837 \times 10^8 M_\odot$.

Compared to other lensing simulations, the clone focusses on small, rather than large scales. Both the Coyote Universe (Lawrence et al., 2010) and SUNGLASS (Kiessling et al., 2011) have less small scale accuracy for lensing. The clone realisations recover the projected power spectrum to high accuracy at an angular range of $0.5' \leq \theta \leq 40'$, independent of redshift. The lack in power of $< 10\%$ beyond 40 arcmin is the result of the small simulation box size and small scale accuracy is limited by the resolution. For the purpose of this thesis we neglect this boxsize effect, which results in a small underestimation of the errors on scales $\theta > 40'$.

The simulations allow us to test the methods for extracting galaxy bias parameters from weak lensing and clustering data, before applying them in Chapter 4 to WiggleZ, BOSS, and RCSLenS data. Section 3.2 describes the measurements of correlation functions and systematics, using the methods discussed in section 2.3, while section 3.3 describes the construction of the simulated source and lens catalogues. Results are shown in section 3.4 and discussed in 3.5.

3.2 Measurements of Correlation Functions

This section describes how to measure the lens position and source ellipticity auto- and cross-correlations, given in Equations (2.69) - (2.74).

3.2.1 Position-Position

The projected angular correlation function of galaxies $w(\theta)$ was introduced in section 2.3.1, and Equation 2.70 gives its relation to the power spectrum of galaxies and for small angles Limber's equation (Limber, 1953) provides an

accurate approximation to the real space correlation function from $w(\theta)$.

The clustering of galaxies is measured relative to a random field. This opens up a variety of possibilities to measure $w(\theta)$, perhaps the most simple of which is

$$1 + \xi = \langle DD \rangle / \langle RR \rangle \tag{3.1}$$

where DD and RR are data-data and random-random pair counts, respectively, in bins of $\theta + \delta\theta$. The $+1$ comes from the definition of an excess probability

$$dP = \rho_0^2 [1 + \xi(s)] \mathrm{d}V_1 \mathrm{d}V_2, \tag{3.2}$$

with ρ_0 the density of the field, and V_1 and V_2 the volume elements of the two objects (for projected clustering this is $dP = N(1 + w(\theta)\mathrm{d}\Omega$, with Ω the solid angle). A more robust approach is the widely used Landay-Szalay estimator (Landy and Szalay, 1993)

$$w(\theta) = \frac{\langle DD \rangle - 2\langle DR \rangle + \langle RR \rangle}{\langle RR \rangle}, \tag{3.3}$$

noting that the result should be insensitive to the method used for sufficiently large volumes (Hamilton, 1993).

The clustering on the sky has to satisfy the integral constraint

$$\int \int w(\theta) d\Omega^2 = 0, \tag{3.4}$$

where Ω is the area of the survey. Large scale modes on the order of the survey size and beyond are not included in the observed $w(\theta)$, leading to underestimation of the mean of the clustering.

The value of the integral constraint I_w is inversely proportional to the size of the survey. For the surveys used in this thesis, with values on the order of $I_w = 10^{-3}$ to $I_w = 10^{-2}$, it is important to take into account for the large scale modes, since $w(\theta)$ is on the order of I_w at $\theta = 100'$. Therefore, I_w is predicted from assumptions about the power spectrum to account for the fact that we describe the clustering theoretically from the viewpoint of infinite space, whereas the survey has a finite size. It can be estimated from the random catalogues as follows (Roche and Eales, 1999)

$$I_w = \frac{\sum_{i=1}^{N_\theta} \langle RR \rangle \, w_{\mathrm{model}}}{\sum_{i=1}^{N_\theta} \langle RR \rangle}, \tag{3.5}$$

with $w_{\rm model}$ predicted from theory (Equation 2.70).

3.2.2 Shear-Shear

The auto-correlation of the shear field is sensitive to the 3D matter distribution and it requires ellipticity measurements. Algorithms exist for extracting the ellipticity parameters e_1 and e_2 from imaged galaxies, for example Lensfit (Miller et al., 2013, and references therein). As discussed in section 1.2.5 the shear has two components, since the shapes are approximated by ellipses, giving two parameters per imaged galaxy. The parameters can be defined with respect to some coordinate frame

$$\begin{pmatrix} e_t \\ e_r \end{pmatrix} = \begin{pmatrix} \cos 2\phi & \sin 2\phi \\ -\sin 2\phi & \cos 2\phi \end{pmatrix} \begin{pmatrix} e_1 \\ e_2 \end{pmatrix} \tag{3.6}$$

with ϕ the angle between the (e_1, e_2)-frame and the (e_t, e_r)-frame. Performing this translation for all source galaxies, the shear correlations can be calculated

$$\xi_{tt}(\theta) = \frac{\sum_{ij}^{N_{\rm pair}} w_i w_j e_{t,i}(\boldsymbol{x_i}) e_{t,j}(\boldsymbol{x_j})}{\sum_{ij}^{N_{\rm pair}} w_i w_j} \tag{3.7}$$

$$\xi_{rr}(\theta) = \frac{\sum_{ij}^{N_{\rm pair}} w_i w_j e_{r,i}(\boldsymbol{x_i}) e_{r,j}(\boldsymbol{x_j})}{\sum_{ij}^{N_{\rm pair}} w_i w_j} \tag{3.8}$$

The sum and difference of ξ_{rr} and ξ_{tt} give ξ_+ and ξ_-, respectively

$$\xi_+(\theta) = \xi_{tt}(\theta) + \xi_{rr}(\theta) \tag{3.9}$$

$$\xi_-(\theta) = \xi_{tt}(\theta) - \xi_{rr}(\theta), \tag{3.10}$$

where $\theta = |\boldsymbol{x}_i - \boldsymbol{x}_j|$. It was shown in section 1.2.5 that the shear correlation functions can be written in terms of the convergence power spectrum, giving Equation (2.74).

3.2.3 Shear-Position

The tangential shear around foreground galaxies is sensitive to the dark matter, although only at the lens positions. It is calculated from the cross-correlation

between lens positions and background shear

$$\gamma_t(\theta) = \frac{\sum_i \sum_j w_i w_j e_{t,j}(\boldsymbol{x}_j)}{\sum_i \sum_j w_i w_j}. \tag{3.11}$$

3.2.4 Assessing Uncertainties

In this section I discuss several factors that contribute to the uncertainties in the correlation functions, and how to assess these. The number of pairs of galaxies or ellipticities increases with increasing angular separation θ. Hence, by averaging over larger areas the error on the mean becomes smaller. Because the fields are not random, owing to galaxy clustering of positions and potentially lensing systematics in the ellipticities, the variance scales nontrivially with bin size. However, by looking at the number of pairs within the bin, Poisson errors provide a reasonably accurate measure of the uncertainty from sampling a continuous density or shear field with a finite sample of lenses or sources (see equation 27 in Schneider et al. (2002a)). It is, however, not perfect, as the errors are correlated, which cannot be addressed with $\sqrt{N}$ error estimations.

A more robust error analysis is provided by jackknife or bootstrap resampling of the data. The jackknife repeatedly cuts out small parts of the data, calculates the correlations on the remainder, and measures the variances between the subsamples. Bootstrap is similar, but draws at random new datasets from the total sample, with repetition, so that the error bars are derived from the variance between those. The disadvantage of resampling techniques for astronomy is that it does not take into account cosmic variance: the number of Fourier modes in the survey volume is finite, and the correlation functions are affected by large scale density modes, which stretch beyond the survey volume. In this thesis we calculate errors from the variance between the independent clone realisations, which incorporates both shot noise and cosmic variance. The variance is then scaled to the survey area (Schneider et al., 2002a).

Shape Noise

An additional uncertainty arises from the intrinsic shapes of galaxies, that is, the almost random ellipticities in the absence of lensing. It decreases the signal to noise of lensing measurements, and is therefore referred to as shape noise. The

intrinsic ellipticity $e_{\rm int}$ and the shear γ both have two components, so can be written in complex form

$$e_{\rm int} = e_{\rm int,1} + i e_{\rm int,2} \tag{3.12}$$

$$\gamma = \gamma_{\rm lens,1} + i \gamma_{\rm lens,2}. \tag{3.13}$$

Then the combined ellipticity can be estimated as (Seitz and Schneider, 1997)

$$e = \frac{\gamma + e_{\rm int}}{1 + \gamma^* \ e_{\rm int}}, \tag{3.14}$$

where the asterisk denotes the complex conjugate. Including the measurement error n, the observed ellipticity can be written as

$$e_{\rm obs} = \gamma + e_{\rm int} + n \tag{3.15}$$

The variance of $e_{\rm int} + n$ was measured for CFHTLenS by Miller et al. (2013) to be $\mathrm{var}(e_{\rm int} + n) = \sigma_e^2 = (0.279)^2$, who also showed that the distribution is not exactly Gaussian. For the purpose of error estimations the Gaussian approximation suffices. In reality, the distribution of $e_{\rm int}$ is not perfectly random, since galaxies interact and evolve over time, leading to intrinsic alignments (e.g. Heavens et al., 2000).

Redshift Uncertainties

Redshifts for imaging surveys are usually derived from photometry, which is based on fitting spectral models to a limited number of filters, or colours (Hildebrandt et al., 2012, and references therein). The observed photometric redshift distribution may be an inaccurate representation, depending on the number and types of filters used. As a result of the highly varied nature of galaxies, it is not uncommon for the fitting procedure to confuse high and low redshift galaxies. This is called photo-z noise and often referred to as catastrophic errors.

Spectroscopic redshifts are more accurate, but difficult to obtain, whereas high number densities are required to study the small correlation of ellipticities due to lensing. Therefore, lensing has to resort to photometric redshifts, and more importantly, the systematics that arise from this.

Errors in distance estimations from the uncertainties in redshift can theoretically be modelled as a discrepancy between the observed and true redshift distribution. As an example, consider the distributions in Figure 3.1, where the dashed lines are broader versions of the solid lines. Fig. 3.2 considers a total of 4 scenarios of

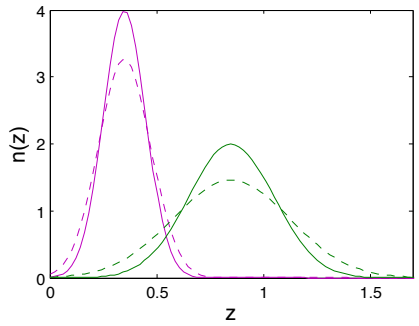

Figure 3.1 *Toy model redshift distributions to study uncertainties in redshift, which can be modelled as a broader or narrower observed versus true distribution. The magenta lines are the foreground distributions and green corresponds to the distribution of sources.*

redshift uncertainties, based on the redshift distributions in Figure 3.1. The offset as expected from redshift uncertainties in $b(\theta)$ from $\xi_{\pm}$ and w is calculated, also for the aperture galaxy bias parameters. The solid lines represent measurements where the observed distributions are broader, while the true distributions are narrower, see Figure 3.1, the dashed lines are the opposite case. The cyan lines only consider uncertainty in the background distribution. The magenta lines show the case where the foreground distribution of CFHTLenS is shifted by $\Delta z = 0.04$ to lower redshifts, while the background is as shown in Figure 3.5. To clarify, the scenarios can be summarised as

1. True distributions are narrow, observed distributions are broad
   (solid blue lines in Figure 3.2)

2. Observed distributions are narrow, true distributions are broad
   (dashed blue lines in Figure 3.2)

3. True distributions are narrow, observed foreground distribution is also narrow, observed background distribution is broad.
   (solid cyan lines in Figure 3.2)

4. Observed distributions are narrow, true foreground distribution is also narrow, true background distribution is broad.
   (dashed cyan lines in Figure 3.2)

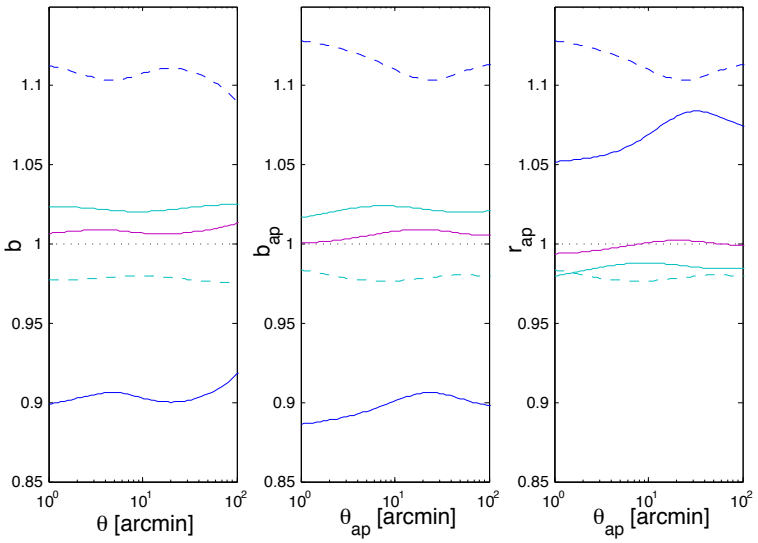

Figure 3.2 *The offsets, owing to redshift uncertainties, in galaxy bias parameters $b(\theta)$ from raw estimators, left panel, $b(\theta_{ap})$ in the middle panel, and $r(\theta_{ap})$ is shown to the right. The lines correspond to different scenarios described in the text and shown in Figure 3.1.*

The offsets in the galaxy bias parameters are significant for these cases. However, for CFHTLenS this would represent unrealistically large under- or over-estimations of the scatter in redshifts. Figure 8 of Hildebrandt et al. (2012) shows that the scatter in redshift is under control, but the so-called outliers which constitute a second, much smaller bump, causes a bias in the overall distributions of about $\Delta z = 0.04$ for the foreground distribution. This results in a small bias in the measurements of b on the order of 1% and is negligible for r, see the magenta lines in Figure 3.2.

A further redshift uncertainty comes from Redshift Space Distortions (RSD), discussed in section 1.2.4. Baldauf et al. (2010) showed that a small RSD correction factor needs to be applied to make sure the distances to the lenses as implied by the redshifts are correct. It should be noted that the analysis in there is based on Equation (2.32) under the assumptions that $r = 1$ and the contributions to the redshifts are described by linear theory. It will be interesting to repeat the analysis with a fingers-of-god model, as this will be significant at the scales probed by lensing.

Systematics and Lensing Biases

The clustering of sources and intrinsic galaxy alignments were mentioned as sources of systematic biases in the lensing results. Additionally, false lensing can arise when galaxy shapes are convolved with a non-spherical point spread function (PSF). Hence, it is important to know how the PSF behaves as a function of position in the image. A way to correct for this is to use the fact that on average the ellipticities e_1 and e_2 should be zero.

As was shown in section 1.2.5, in distorting the image of galaxies, lensing also magnifies and demagnifies their flux. Since surveys are flux limited, magnified galaxies are more likely to enter the survey than demagnified galaxies, altering the redshift distribution. This is magnification bias, and with ever improving data, cosmological parameter estimations from the galaxy power spectrum will have to take this into account (e.g. Duncan et al., 2014). Since more magnified galaxies than demagnified galaxies enter the survey sample (because of the flux limit and the slope of the number - magnitude relation), the population is more lensed, so that the theoretical prediction is slightly underestimated. This effect will become significant with next generation surveys (Schmidt et al., 2009).

Lensing systematics can be detected by measuring correlation functions which are designed to yield no lensing signal. In principle, lensing measures no B-modes and the difference between E- and B-modes is a rotation by $\pi/2$. Therefore, an interesting test is provided by $\gamma_\times$, the tangential shear around foreground galaxies after rotation of the source ellipticities by $\pi/2$. It is measured as

$$\gamma_\times(\theta) = \frac{\sum_i \sum_j w_i(\boldsymbol{x}_i) w_j e_{\times,j}(\boldsymbol{x}_j)}{\sum_i \sum_j w_i w_j}. \tag{3.16}$$

where $e_\times$ is defined as the shear rotated by 45° with respect to the line connecting the lens-source pair, hence $\gamma_\times$ should be zero in the absence of systematics. As discussed in section 1.2.5, E and B-modes can be separated with the aperture mass statistic, which also provides a useful test for systematics from measurement conditions and inaccurate modelling of the PSF. An alternative approach is to look at the star-galaxy cross correlation function $\langle \gamma \mathbf{e}^* \rangle$, where γ is the shear of the source, and $\mathbf{e}^*$ is the ellipticity of a star (or PSF since stars are point sources), see also Heymans et al. (2012). Observations for which $\langle \gamma \mathbf{e}^* \rangle$ is inconsistent with zero suffer from PSF contamination, leading to errors in the lensing measurement.

A small clustering systematic is worth noting here was well. In the presence of uncertainty on the positions of the galaxies, due to a broad PSF, or lensing deflection angles, the separations are on average increased by a small amount. If we randomly distort the positions of galaxies (for lensing deflection angles this is not realistic, as they are correlated) then the effect can be on the order of a percentage at small scales, but when separations become much larger than the uncertainty in the position, it is negligible. As was noted already in section 1.2.5, source clustering is, however, more worrisome and can lead to systematic errors (Schneider et al., 2002b).

Cosmological Framework

In this chapter as well as in 2.3.4 several causes of percentage level biases in the aperture bias method have come to light. It was argued by van Waerbeke (2000) that the method is relatively insensitive to the details of the matter power spectrum. However, a $\sim 10\%$ effect that was considered to be negligible in the year 2000 is critically important today, which we need to address.

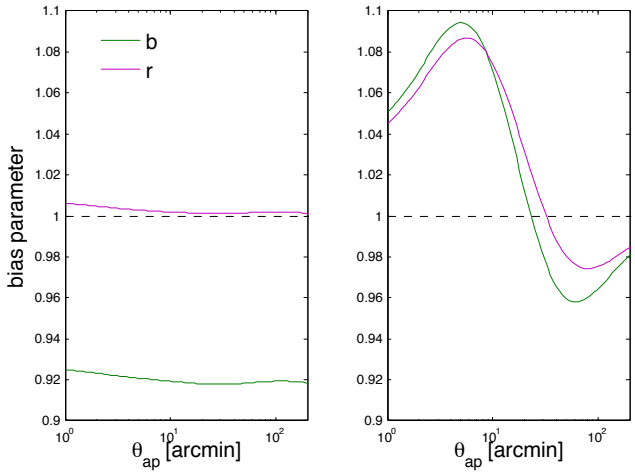

Figure 3.3 *Cosmological assumptions affect the bias parameters $b(\theta_{ap})$, green line, and $r(\theta_{ap})$, magenta line. In the left Figure, the assumed cosmology is WMAP with $\Omega_m = 0.279$, $H_0 = 701$ km $s^{-1}Mpc^{-1}$, and $\sigma_8 = 0.817$, and the true cosmology is given by Planck with $\Omega_m = 0.314$, $H_0 = 686$ km $s^{-1}Mpc^{-1}$, and $\sigma_8 = 0.834$. The left panel shows the effect of neglecting non-linear structure formation in the calibration factors.*

Consider the case where the aperture bias method assumes flat WMAP5 cosmology, as in the clones, with $\Omega_m = 0.279$, $H_0 = 70.1$km s^{-1}Mpc^{-1}, and $\sigma_8 = 0.817$, while the true underlying cosmology (that affects the measurements)

is given by Planck with $\Omega_m = 0.314$, $H_0 = 67.4$km s^{-1}Mpc^{-1}, and $\sigma_8 = 0.834$. The left panel of Figure 3.3 shows the result for unbiased matter tracers $b = r = 1$, showing a $\sim$ 10% error in $b(\theta_{ap})$, while $r(\theta_{ap})$ is almost insensitive to the cosmological framework. In addition to this, the right panel shows the galaxy bias measured under the assumption that the power spectrum is linear, while in reality it is given by Smith et al. (2003) halofit. Hence, accurate knowledge of the non-linear correction to the power spectrum is necessary: the linear assumption results in a scale-dependent bias within $\sim 10\%$ when neglecting nonlinear corrections.

Evidently, galaxy bias measurements are sensitive to the adopted cosmological framework. Ideally, galaxy bias and cosmology are constrained simultaneously.

3.3 Mock Data

This section describes the method to construct realistic shear data and the linearly biased foreground catalogues from the clones, described in section 3.1. Bonnett et al (in prep) measures $b(\theta_{ap})$ and $r(\theta_{ap})$ from the CFHTLenS samples, for which this thesis provides covariance matrices. Therefore, the samples are constructed to correspond to the work in Bonnett et al (in prep) and are given in table 3.1. The catalogues are based on the density output of the clones by

Table 3.1 *Mock Samples*

	b	n [arcmin^{-2}]	$z_{\rm med}$
early	2.0	0.58	0.33
late	1.0	0.80	0.33
all	1.2	1.56	0.33
background	n/a	5.73	0.86

inverse transform sampling of the 2-dimensional density field. In this technique one draws uniformly distributed numbers in the interval $[0, 1]$, which are then related to the distribution from which one wishes to sample (the density in this case), via the cumulative distribution. For example, if we wish to sample from a normal distribution $p_N(x)$ with mean $x = 0$, then if we randomly draw 0.5, the inverse transform method returns 0, because the integral from $x = -\infty$ to $x = 0$ (or the cumulative distribution at 0) is 0.5. By inverting the cumulative distribution random numbers are converted to a sample drawn from the probability distribution.

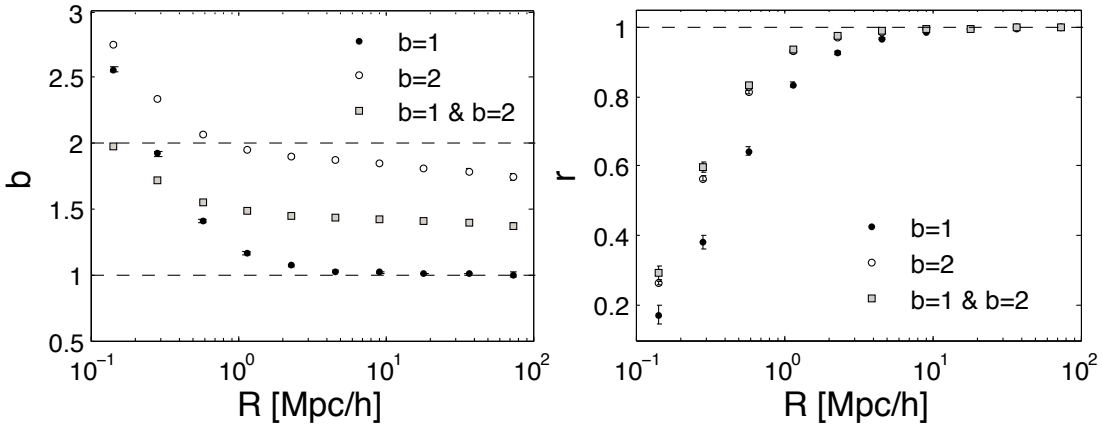

Figure 3.4 *The bias (a) and cross correlation coefficient (b) after sampling and biasing of the clone dark matter fields to yield approximately linearly biased samples. For this Figure, the redshift slices at $z = 0.344$ of the first 10 LOS were used for the means and the errors on them. Catalogues with number densities of 1 arcmin^{-2} were produced, with the combined sample (denoted $b = 1$ & $b = 2$) having twice the amount, hence the slightly better behaviour at smaller scales.*

Naively applying $b > 1$ to a δ_m field would result in negative density ρ_g in case the minimum value of the matter overdensity $\min(\delta_m)$ violates $b \times \min(\delta_m) \geq -1$. The solution is to either smooth the field sufficiently, or to apply the bias to ρ_m and imposing $\rho_g > 0$.

$$\delta_g = b\delta_m \tag{3.17}$$

$$\frac{\rho_g}{\bar{\rho}_g} - 1 = b\left(\frac{\rho_m}{\bar{\rho}_m} - 1\right) \tag{3.18}$$

$$\rho_g = b\bar{\rho}_g\left(\frac{\rho_m}{\bar{\rho}_m} + \frac{1}{b} - 1\right) \tag{3.19}$$

Setting all negative galaxy density values to $\rho_g = 0$ potentially clips ρ_g for $b > 1$, but has the advantage of optimal use of the small scale information. In this way biased catalogues were constructed, inevitably introducing some minor scale-dependence due to the clipping.

Figure 3.4 shows the galaxy bias parameters $b(R)$ and $r(R)$, given in Equation (2.8) and (2.9), for the sampling with the inverse transform method. For these figures the number density was set to 1 arcmin^2. The scale-dependence in both parameters is the result of shot noise and, for the $b \neq 1$ catalogues, clipping.

The lens and source distribution in redshift space that were used to sample galaxies from the clone simulations are shown in Figure 3.5. CFHTLenS

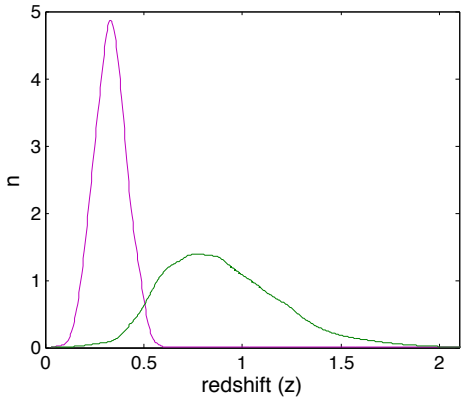

Figure 3.5 *The redshift distributions for this chapter are matched to CFHTLenS. The magenta line is the foreground (lens) distribution, the green line represents the background (source) distribution.*

subsamples were created corresponding to the work of Bonnett et al (in prep) of which details are given in Table 3.1.

The Clone Covariance Matrix and (Cross-)Correlation Functions

Covariance $\mathrm{cov}[X_i, X_j]$ between two variables X_i and X_j is defined as

$$\mathrm{cov}[X_i, X_j] = E[(X_i - \mu_i)(X_j - \mu_j)], \tag{3.20}$$

where μ is the mean of X and $E[x]$ is the expectation of x, or the sum of all possible values of x weighted by the probability distribution of x. Covariance between variables X and Y can also be written as σ_{XY}. The covariance matrix C is defined as

$$C = \begin{pmatrix} \sigma_X^2 & \sigma_{XY} \\ \sigma_{XY} & \sigma_Y^2 \end{pmatrix}, \tag{3.21}$$

which contains the knowledge of errors, including the correlation of errors.

In section 3.1 it was mentioned that the small box size of the clone simulations results in an underestimation of power at large scales, which affects the accuracy of the measurements, resulting in discrepancies. These are, however, only significant at large angular separations where the large scale modes contribute considerably to the estimators. Additionally, there is some minor small scale discrepancy due to the resolution of the simulations. Overall, this causes a slightly skewed power spectrum, which is not ideal if we are to provide a fair test for the methods with which to study galaxy bias.

The clone simulations are sufficiently accurate to estimate the covariance matrix, but the correlation functions do For the model testing we require use the covariance matrix to construct realistic mock measurements from theoretical predictions, to which correlated noise is applied as follows.

Uncorrelated noise is denoted $\boldsymbol{x}$, and obtained by drawing at random from a Gaussian of width $\sigma = 1$. Then the covariance of x is $C^x_{ij} = \langle x_i x_j \rangle = \delta_{ij}$. Now, we write the correlated data points as $y_k = B_{ki} x_i$. Then,

$$C^y_{km} = \langle y_k y_m \rangle = \langle B_{ki} x_i B_{mq} x_q \rangle \tag{3.22}$$

$$= B_{ki} B_{mq} \langle x_i x_q \rangle \tag{3.23}$$

$$= B_{ki} C_{iq} B^T_{qm} \tag{3.24}$$

$$C^y = B C^x B^T \tag{3.25}$$

As $C^x = \delta_{ij}$, then $C^y = BB^T$.

Going the opposite direction, we have a covariance matrix C^y that describes the correlated noise on data points $\boldsymbol{y}$.

1. Use Choleski Decomposition $C^y = LL^T$, where L is a lower triangular matrix.

2. Create vector of random numbers $\boldsymbol{x}$ drawn from a Gaussian with zero mean and unit variance.

3. Construct correlated noise $\boldsymbol{y} = L\boldsymbol{x}$

$$\begin{pmatrix} y_1 \\ y_2 \\ \vdots \end{pmatrix} = \begin{pmatrix} L_{11} & L_{12} & \cdots \\ L_{21} & L_{22} & \cdots \\ \vdots & \vdots & \ddots \end{pmatrix} \begin{pmatrix} x_1 \\ x_2 \\ \vdots \end{pmatrix} \tag{3.26}$$

4. Add $\boldsymbol{y}$ onto the theory curve T to get correlated data points.

$$T \rightarrow T + \boldsymbol{y} \tag{3.27}$$

We use this procedure to obtain mock realisations of the raw estimators, instead of using the means of the correlation functions as measured from the clones, as they are slightly affected by the box size and resolution.

Note that the Choleksy decomposition requires the covariance matrix to be Hermitian and positive definite. This is a problem in case of applying the formalism above to the aperture statistics, since they are derived from an integration over finely binned data, see Table 3.2. More specifically, the raw estimators from which the aperture statistics are calculated are measured in 1000 logarithmic θ bins, with $\theta_{\rm min} = 0.06'$ and $\theta_{\rm max} = 180'$. See Table 3.3 for the influence of the number of θ bins on the conversion, from which it can be concluded that a minimum of 100 bins is recommended.

With 1000 bins we have a 4000×4000 covariance matrix, for which it is impossible to perform the Cholesky decomposition. However, the off-diagonal part of the matrix is very noisy and small compared to the variances. Therefore, the covariance matrix of the raw estimators is approximated as diagonal when applying noise to the aperture statistics. That is, uncorrelated noise was added to the 1000 θ bins theory curves of the raw estimators to produce realistic aperture statistic realisations, while for the bias model fitting method we apply correlated noise, using the steps described above.

Table 3.2 *Estimators to Aperture Statistics*

Estimator		Aperture Statistic	Equation
$\xi_\pm(\theta)$	$\rightarrow$	$\langle M_{ap}^2 \rangle(\theta_{ap})$	(2.96)
$\gamma_t(\theta)$	$\rightarrow$	$\langle M_{ap} N_{ap} \rangle(\theta_{ap})$	(2.97)
$w(\theta)$	$\rightarrow$	$\langle N_{ap}^2 \rangle(\theta_{ap})$	(2.98)

Table 3.3 *Number of theta bins for conversion in Table 3.2. Input values were set to $b_{ap} = r_{ap} = 1$. No noise was applied, so that any deviation is solely due to too few θ bins.*

$N_{\rm bins}$	$b_{\rm ap}(4')$	$b_{\rm ap}(60')$	$r_{\rm ap}(4')$	$r_{\rm ap}(60')$
10	0.5916	0.9794	3.6975	0.3880
20	0.9788	0.9943	1.1655	0.9459
60	0.9999	1.0000	1.0026	1.0012
100	1.0000	1.0000	1.0001	0.9999
1000	1.0000	1.0000	1.0000	1.0000

3.4 Results

In this section results of the raw estimators and aperture statistics from the clone mock data are presented, using the methods described above. Theoretical

predictions are based on the same cosmological model adopted to construct the clones, see section 3.1, and the nonlinear corrections to the power spectrum are modelled with Smith et al. (2003) halofit.

3.4.1 Raw Estimators from the Clone Density and Shear Fields

Here results are presented of the raw estimators, w, γ_t, and $\xi_\pm$, measured directly from the clone output of simulated density and shear fields. The error on the mean is derived from the variance between the clone realisation and therefore correspond to a survey size of 12.85 deg^2.

Fig. 3.6 shows the clone results for the shear correlations $\xi_\pm$ as a function of angular separation θ for the CFHTLenS redshift distributions with a number density of sources of 5.7 arcmin^{-2}. With increasing θ the ξ_+ signal deviates more from the theoretical prediction. This is not the case for ξ_-, because θ values correspond to smaller physical scales, as can be understood from the J_4 Bessel function in Equation (2.74).

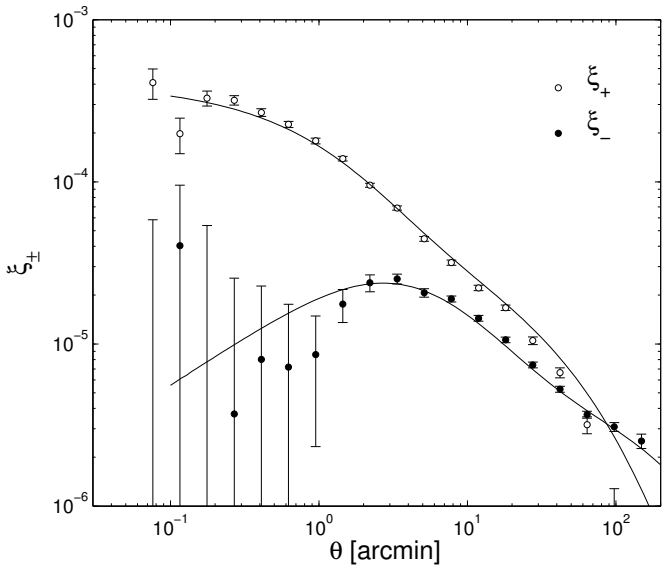

Figure 3.6 *The plus and minus component of the shear auto-correlation with radial galaxy distribution matched to the CFHTLenS background sample.*

Fig. 3.7 shows w, see section 3.2.1, for the samples in Table 3.1. The theory predictions incorporate the linear bias that was applied with Equation (3.19) to construct each sample. As was already noted and shown in Figure 3.4 the

linear bias is not recovered with exact precision, as a result of the clipping, which is evidently worse for higher bias. We use these catalogues only for estimating covariance matrices, for which the bias recovery is sufficiently accurate. The discrepancy here is in part also due to the skewed clone power spectrum, which can be seen from the result for the unbiased late sample, showing a similar discrepancy trend to the ξ_+ result in Figure 3.6, as expected from the J_0 filtering for both statistics.

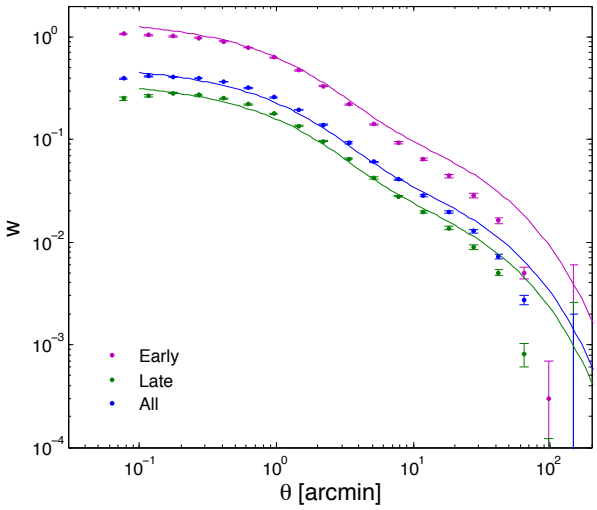

Figure 3.7 *The projected clustering of galaxies with radial galaxy distribution matched to the CFHTLenS foreground samples in Table 3.1.*

Fig. 3.8 shows the galaxy-galaxy lensing signal γ_t for the Late, Early, and All samples as measured directly from the 184 clone realisations. Discrepancies are again attributed to the skewed clone power spectrum as a result of the resolution at small scales and finite box size effects at large scales.

From the direct measurements on the clone mock data, shown in Figure 3.6, 3.7, and 3.8, we conclude that the method is sufficiently accurate for the purposes here: the construction of covariance matrices and the application of (correlated) noise to the theory curves to test the galaxy bias methods.

3.4.2 Raw and Aperture Statistics from Mock Data

The construction of mock data for testing purposes was described in Section 3.3. Correlated noise was estimated from the covariance matrix and applied to the theory curves, in order to provide unbiased tests of the aperture galaxy bias

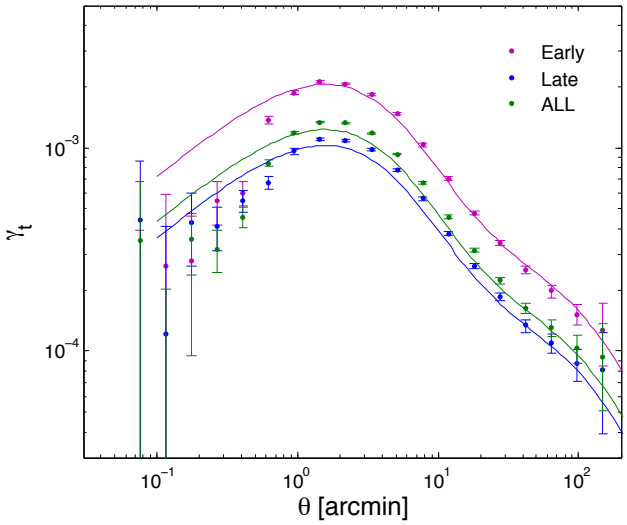

Figure 3.8 *The tangential shear around the clone foreground galaxies with CFHTLenS redshift probabilities for the lenses and sources.*

method, as well as the model fitting. The covariance matrix was scaled to the area of CFHTLenS, which is 154 deg^2, using $C_{\rm survey}/C_{\rm clone} = A_{\rm survey}/(N_{\rm LOS}A_{\rm clone})$.

For the model fitting approach, Section (2.3.5), we only use 7 logarithmically spaced θ bins per raw estimator. Figure 3.9 shows three independent measurements for w (top), γ_t (middle), and ξ_+ (bottom). By construction, the data (set to theory plus noise) is consistent with the theory predictions. It is interesting to see that "χ by eye" in the presence of correlated data can lead to wrong conclusions, which is especially evident for the ξ_+ results. Therefore, it is evident that the full covariance matrix needs to be taken into account when constraining models from the statistics.

Figure 3.10 shows an aperture statistics realisation, produced by using theory predictions for the raw estimators, with noise as calculated from the diagonal elements of the clone covariance matrix, which is very noisy for the finely binned raw estimators. The covariance matrix was scaled to a 154 deg^2 survey. For the error bars, 1000 realisations for the raw estimators were produced, after which they were converted to the aperture statistics. The variance between thus produced aperture statistics provides the estimate of the error on the mean.

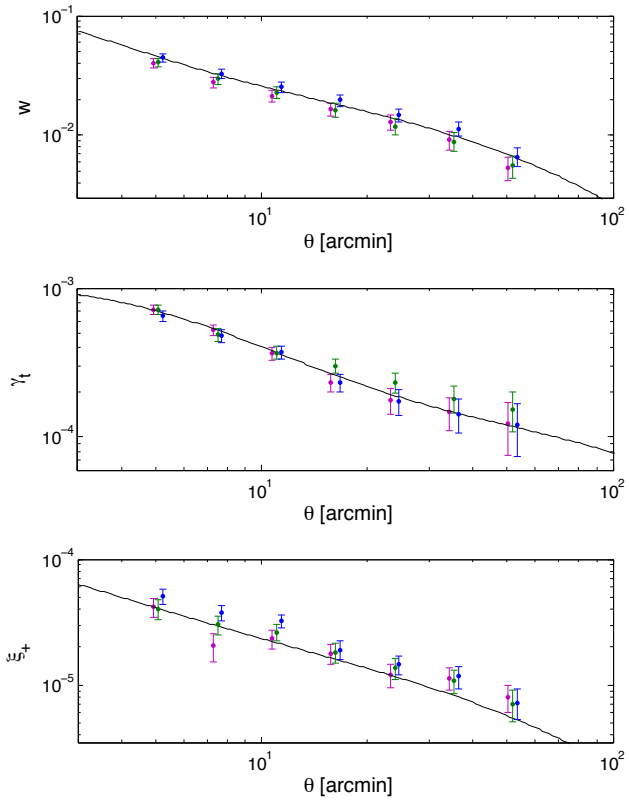

Figure 3.9 *Three realisations of the raw estimators ξ_+, γ_t, and w. The errors are estimated from the clone covariance matrix for a CFHTLenS like set-up without bias. The covariance matrix was scaled to correspond to a 154 square degree survey. Data points were set to theory predictions, after which correlated noise was applied.*

3.4.3 Galaxy Bias Results

This section shows results of galaxy bias measurements from (1) the ratio of w and ξ_+, the aperture bias method, and the model fitting technique. For all the results in this section the data was simulated from theory plus (correlated) noise, as described in the previous chapter, in order to provide unbiased tests of the methods. Also shown are results for mock subsamples of the CFHTLenS data.

Ratio of w and ξ_+

As discussed in Section 2.3.2, the bias can be estimated from the ratio of w and ξ_+ as a function angular separation θ. The disadvantages are clear: (1) the lack of a similar approach to measure r, (2) angular separations correspond to a wide range of physical scales as can be seen from the J_0 filtering of the power spectrum,

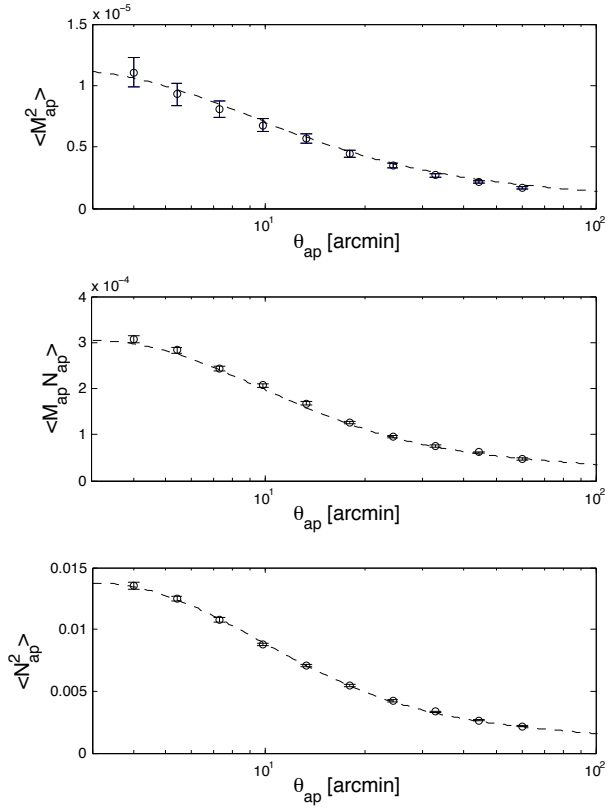

Figure 3.10 *A realisation of the aperture mass statistics. Error bars were calculated from the variance of 1000 noise realisations, which were derived from the Clone covariance matrix for a CFHTLenS like set-up without bias. The covariance matrix was scaled to correspond to a 154 square degree survey.*

see also Figure 2.8, (3) ratios of noisy quantities yield skewed distributions, and finally (4) time- and scale-dependence will bias the results. Nevertheless, the approach has the interesting advantage over the aperture bias method of not modifying the raw estimators.

The measurements of galaxy bias for the early, late, and all samples are presented in Figure 3.11. This Figure shows both the averages of 500 mock data sets, as well as one individual realisation per type of sub-sample, while the errorbars are derived from the variance between those. The covariance matrix was scaled to a 154 square degree survey. The offset due to noise is small and scales with the size of the error bar. The input bias is recovered well for all 3 samples.

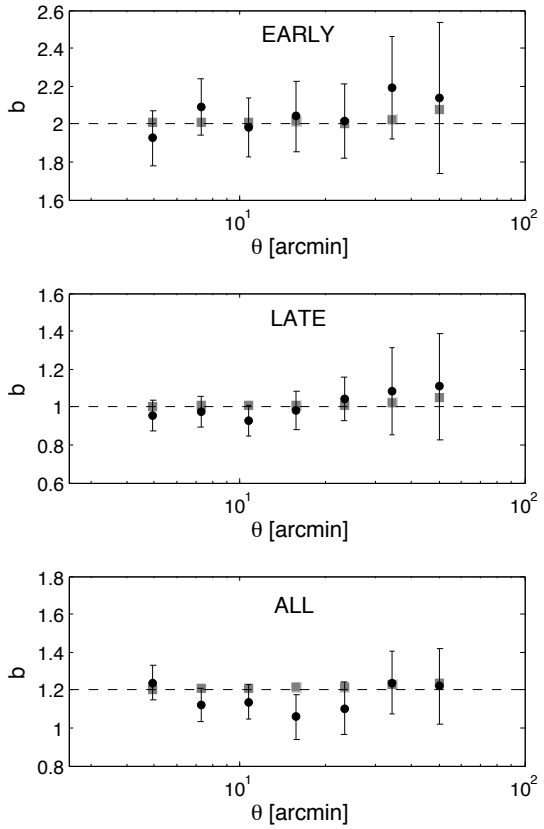

Figure 3.11 *The galaxy bias parameter $b(\theta)$ from the ratio of the raw estimators $w(\theta)$ and $\xi_+(\theta)$ showing both the mean (grey squares) of 500 noise realisations for a 154 deg^2 survey with CFHTLenS like set up, as well as 1 individual example (black points) for each foreground sample in Table 3.1.*

Ratios of Aperture Statistics

Fig. 3.12 shows constraints on the aperture galaxy bias, see Section 2.3.3, using the mock data (theory plus noise) in Table 3.1. The Figure presents $b(\theta_{ap})$ and $r(\theta_{ap})$ for the three samples, early (top), late (middle), and all (bottom). The grey data points correspond to the average of many realisations, while the black data points are from 1 realisation. This shows again that "χ-by-eye" should be avoided, since some of the single realisations falsely suggest scale-dependence, while this is the result of correlated data points. Also note that the scale-dependence due to noise is very similar for $b(\theta_{ap})$ and $r(\theta_{ap})$, which is attributed to noise in $\langle M_{ap}^2 \rangle$, which appears in the denominator of both bias parameters. The measurement is subject to a negligible bias in the mean introduced by taking ratios of noisy correlation functions, like in Section 3.4.3 for the ratio of w and ξ_+. Overall, the galaxy bias method recovers the linear galaxy bias parameters with good accuracy.

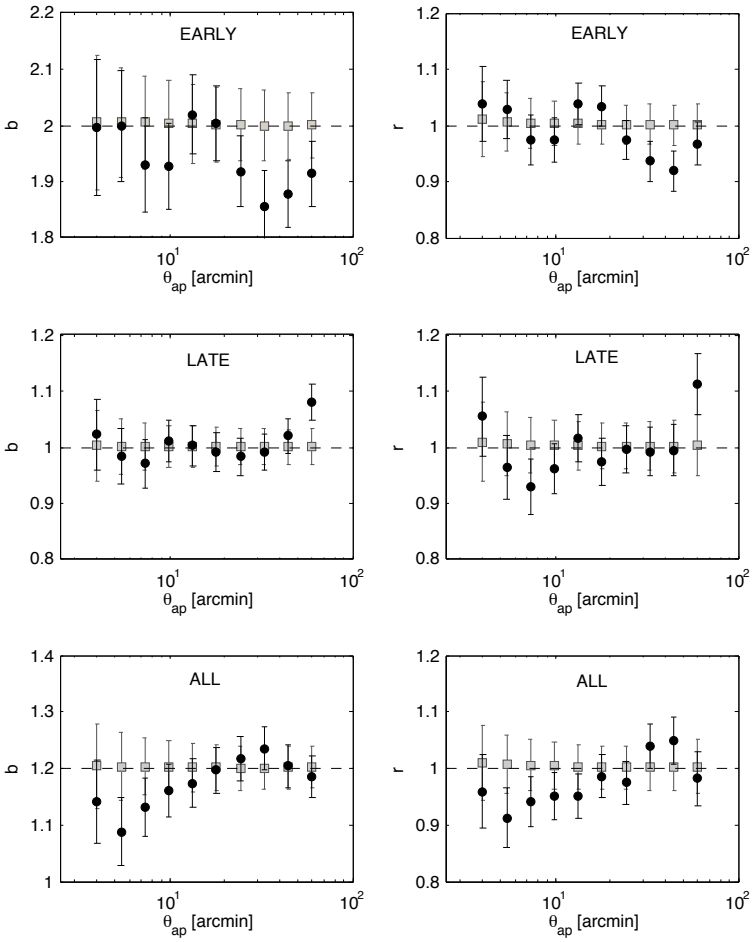

Figure 3.12 *The bias parameters b (left) and r (right) from the aperture statistics for the three samples in Table 3.1. The black data points are from 1 noise realisation, errors come from the variance between 2000 noise realisations, scaled to correspond to a survey of 154 deg^2. The means of the noise realisations are shown in grey, showing that the method recovers the linear bias parameters. However, the noise in b and r results in very similar scale-dependence, due to $\langle M_{ap}^2 \rangle$ in both denominators.*

It is worth investigating the offset expected from the ratio of estimators in the presence of noisy data. For example, for an estimator Z, defined as a ratio of two variables, say X and Y (like the bias parameters), we have

$$E(Z) = E\left(\frac{X}{Y}\right) \tag{3.28}$$

$$= E(X)E\left(\frac{1}{Y}\right) \tag{3.29}$$

$$\geq \frac{E(X)}{E(Y)}, \tag{3.30}$$

which follows from Jensen's inequality

$$\phi(E[X]) \leq E[\phi(X)], \tag{3.31}$$

for some convex function ϕ. The equality only occurs in the extreme case of $\sigma[Y] = 0$. I have done the following to test this. Create two vectors $X(t)$ and $Y(t)$ which have value 1 for all t, and t is a linear vector running from $t = 0$ to $t = 1$. Apply Gaussian noise to both X and Y with standard deviation $0.2\times(1-t)$. Then, 10^6 noise realisations were performed and for each realisation we calculate $Z = X/Y$, giving a measure of $Z = \langle X/Y \rangle$. In Figure 3.13 this is plotted against $Z = \langle X \rangle / \langle Y \rangle$, showing the behaviour expected from Equation 3.28, which also applies to the galaxy bias parameters when measured from ratios.

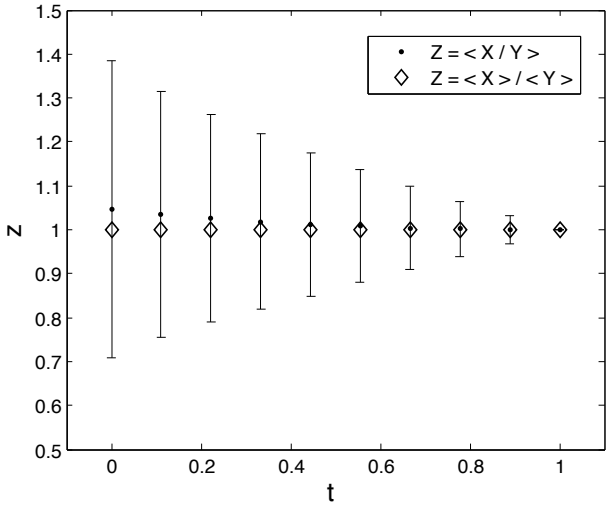

Figure 3.13 *The upward bias in Z from taking ratios of noisy quantities, see text for how this plot was constructed.*

Figure 3.14 shows the aperture galaxy bias parameters for different survey sizes. As expected from Equation (3.28), taking ratios results in an overestimation of the true input bias of $b = 1.2$. The systematic offset is amplified with increased noise, so smaller survey area. However, for the surveys in this thesis this systematic is negligible, noting that, for example, the galaxy bias constraints from the COSMOS survey (Jullo et al., 2012) will be slightly biased as a result of this systematic.

Figure 3.15 also shows the bias parameters from the aperture statistics, but for mock samples with scale dependent bias $b(k)$ given by the Cole et al. (2005) model, Equation (2.112), with $[b_1, C_1, C_2] = [1.2, 1.0, 1.4]$. We assume here that $b(k)$ does

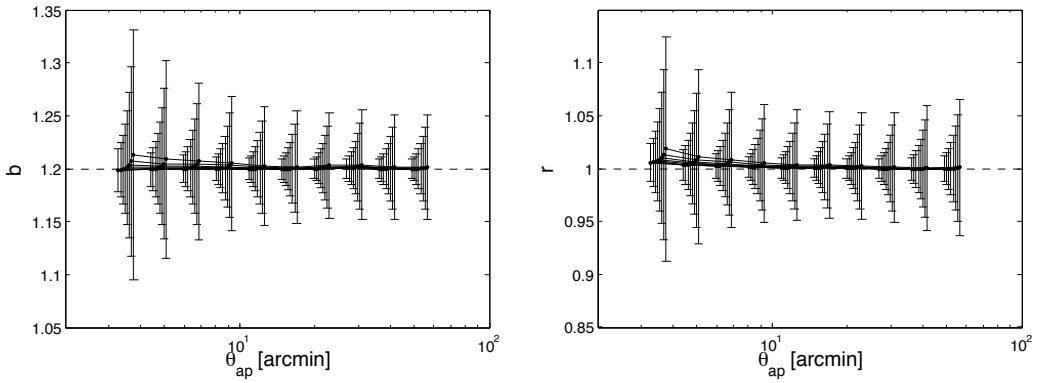

Figure 3.14 *The bias parameters from the aperture statistics, by taking the means of 1000 noise realisations for a range of survey areas, with the largest error bar corresponding to a 30 deg^2 survey and the smallest to the total clone area of 2.35×10^3 deg^2, in total showing data points for 10 logarithmically spaced areas. As expected from taking ratios of measurements, Equation* (3.28)*, data points with larger error bars are more biased. The CFHTLenS survey is sufficiently large for this effect to be negligible.*

not impact significantly on the covariance matrix, such that the covariance matrix can be approximated by $b = 1.2$ linear galaxy sample. The disagreement with the input model (dashed line) is due to the incorrect recovery of scale-dependence, discussed in Section 2.3.4.

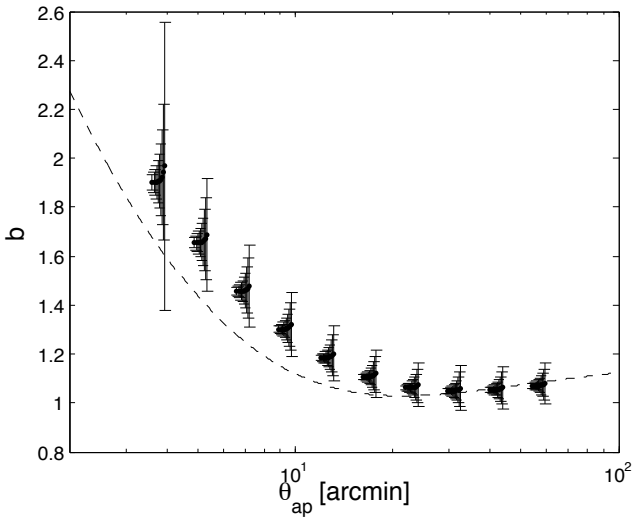

Figure 3.15 *Same as Figure 3.14 but only for $b(\theta_{ap})$ and with scale-dependence in the bias, given by the Cole et al. (2005) model with $[b_1, C_1, C_2] = [1.2, 1.0, 1.4]$. Deviations in r_{ap} are too small to be visible, see also Figure 2.14.*

Model Fitting

Model fitting does not suffer from taking ratios of noisy quantities and directly uses the raw estimators w, γ_t, and $\xi_\pm$. The galaxy bias parameters are measured directly as a function of k, which is desirable for RSD analyses, see Section 2.2, with the caveat of model assumptions. With next generation surveys, however, a binning in k and z space can discard the model assumptions. Section 2.3.5 discusses several galaxy bias models, concluding with a preference for the McDonald (2006) galaxy bias model. We include an additional parameter $\mathcal{R}$, see Equations (2.123) and (2.120), which show how the parameters of this model b_1, b_2, and $\mathcal{R}$ affect the cross - and galaxy power spectrum.

The θ-range that I use for the fitting is the same as in Figure 3.11. The parameters are constrained by minimising the χ^2 statistic

$$\chi^2 = (D - M)^T C^{-1} (D - M), \tag{3.32}$$

where D is the data vector, M the model vector with the parameters that we wish to constrain, and C is the covariance matrix. Note that I estimate the covariance matrix from a finite number of independent realisations. This measurement noise means that C^{-1} is a biased estimate of the inverse covariance matrix, as derived in Anderson (2013). The Anderson/Hartlap correction takes this into account (section 3.3.1 of Heymans et al., 2013, and references therein) and is included for the model fitting here and in the next chapter.

Fig. 3.16 shows b and r constraints for the mock CFHTLenS data in Table 3.1. For each sample 100 realisations are produced of which the best fit parameters are plotted, while the contours are the uncertainty for 1 realisation, centred around the average from the 100 plotted realisations. The contours represent 1σ and 2σ (68% and 95%) confidence levels, so $\sim$5 realisations are expected to lie outside the outer 2 σ contours for each sample in Figure 3.16.

The renormalised bias parameters have been measured before from lensing (Mandelbaum et al., 2013), albeit with a different method, the Υ statistic. Figure 3.17 shows the constraints on the renormalised bias parameters, including $\mathcal{R}$, from the ALL sample. This simulation shows that meaningful constraints can be achieved with the CFHTLenS data, although b_2 is the most uncertain parameter.

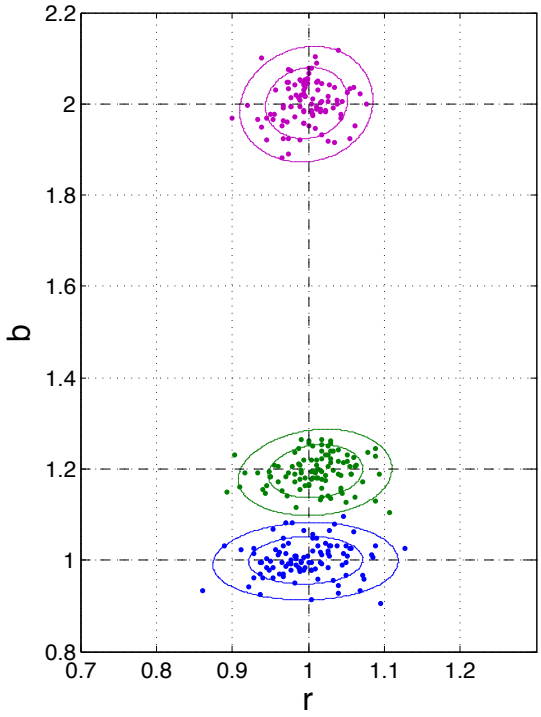

Figure 3.16 *Fit to b and r from 100 correlated noise realisations, shown as dots, with confidence regions corresponding to a 154 deg^2 survey.*

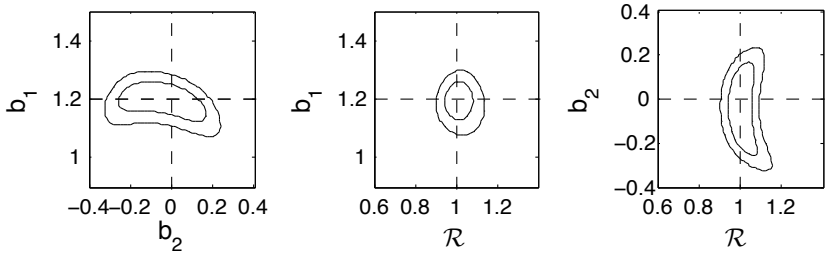

Figure 3.17 *Constraints on the renormalised bias parameters, see Section 2.3.5, including the parameter $\mathcal{R}$. Error regions correspond to the ALL sample, see Table 3.1, with parameters $[b_1, b_2, r] = [1.2, 0.0, 1.0]$, also shown as dashed lines in the Figures.*

3.5 Discussion and Conclusion

This chapter provides data independent covariance estimates for the work of Bonnett et al (in prep). Covariances were estimated from 184 independent realisations from the clone project Harnois-Déraps et al. (2012), noting that for future work larger simulations will be used (Harnois-Déraps et al., 2014). The techniques discussed here for measuring the covariance matrix for biased galaxy samples will also be used in the next chapter, where the techniques that were

tested here will be applied to same-sky surveys to measure the galaxy bias of WiggleZ and BOSS galaxies.

A technique was discussed from which to create unbiased mock realisations of the raw estimators, by applying correlated noise on the theoretical predictions. This enables powerful tests on the galaxy bias methods. The aperture galaxy bias method was found to accurately recover linear bias parameters, although data points were found to be very correlated, also between $b(\theta_{ap})$ and $r(\theta_{ap})$. Furthermore, for small surveys a systematic offset is expected from taking ratios. The main source of systematic is the inaccurate recovery of scale- and time-dependence, which was discussed in Section 2.3.4. Wrong assumptions on the cosmological framework also affect the aperture method, as was shown in Figure 3.3, noting that cosmological constraints from the CMB with Planck are very tight, also for σ_8, which is degenerate with the galaxy bias b.

Uncertainties were assessed in Section 3.2.4. The simulations provide an accurate estimate of the main sources of uncertainty: cosmic variance and shot noise, with the latter arising from intrinsic shape noise, lens and source number densities, and their redshift distributions. Some well-known biases were addressed, such as those from inaccurate PSF modelling, photo-z errors, intrinsic alignments, and source clustering.

The model fitting method measures $b(k)$ and $r(k)$ directly from the raw estimators and does not suffer from all the issues that affect the aperture method. The McDonald (2006) galaxy bias method is a theoretically motivated model and is accurately constraint with present data, see Figure 3.17, also with the extra parameter $\mathcal{R}$ to allow for more flexibility in the cross power spectrum P_{gm}.

The main motivation for measuring galaxy bias parameters is to aid galaxy cluster surveys in extracting cosmological parameters from RSD. Modelling of RSD is often performed in Fourier space (Blake et al., 2011). Since the model fitting yields estimates of $b(k)$ and $r(k)$ into the regime of RSD analysis, the model fitting with the McDonald (2006) galaxy bias model is our preferred choice.

Chapter 4

Measurements of Galaxy Bias

The dark matter distribution contains a wealth of information directly related to the physics of the Universe. With knowledge of how galaxies trace the underlying matter distribution, the clustering of galaxies becomes a key tool to probe cosmology.

A theoretical treatment of galaxy bias is complicated by hidden factors in galaxy formation, while observations are hindered by the fact that dark matter is only observable through its gravitational effect. Gravity can be studied with Weak Gravitational Lensing (WGL), Redshift Space Distortions (RSD), or the global expansion of the Universe. Indeed, powerful constraints on dark energy can be obtained by simultaneously analysing WGL, RSD, and the mapping of galaxies in space (Cai and Bernstein, 2012; Kirk et al., 2013).

This chapter presents an observational study of galaxy bias from measurements of clustering and lensing. The emphasis here is on the cosmological implications of galaxy bias when using galaxy surveys to measure the dark energy density. However, interest in galaxy bias is widespread, e.g. for understanding galaxy formation and the halo model (e.g Cacciato et al., 2012), and to probe inflation through non-gaussianity of the initial density field (e.g. Giannantonio et al., 2012).

First, the data is described in Section 4.1, then measurements of the cross-correlation statistics are measured in Section 4.2. The aperture statistics, introduced in Section 2.3.3, are presented in Section 4.2.5, and aperture galaxy bias results are shown in 4.3.1. Constraints on the renormalised galaxy bias model, introduced in Section 2.3.5, are presented in Section 4.3.2, followed by a

discussion in Section 4.4

4.1 Same-sky Surveys

A joint analysis of RSD and WGL requires same-sky surveys: a spectroscopic foreground sample and an imaged background distribution, both in the same region of the sky. Same-sky surveys are rare. In fact, there are currently only two large-area spectroscopic surveys which have significant overlap with a deep imaging survey. The spectroscopic samples are the Baryon Oscillations Spectroscopic Survey (BOSS) and the WiggleZ Dark Energy Survey (WiggleZ). The imaging survey with which they overlap is the Red Sequence Cluster Survey Lensing Survey (RCSLenS), a re-analysis of the Red Sequence Cluster Survey (RCS2) by the same LenS team who analysed CFHTLenS.

This chapter presents measurements of the galaxy bias of BOSS and WiggleZ, by comparing the galaxy clustering to the dark matter distribution, which is derived from the distortions in the shapes of RCSLenS galaxies. The foreground distributions probe different populations: while BOSS surveyed the distribution of Luminous Red Galaxies (LRGs), WiggleZ is a survey of blue emission-line galaxies. Both surveys continue to provide stringent constraints on the cosmological model, for which they rely on assumptions of a linear galaxy bias. With the use of WGL the bias parameters can, in principle, be found in a cosmologically independent way. In this section the three surveys are described.

4.1.1 BOSS Lenses

BOSS is designed to constrain cosmology by studying the imprint in the galaxy distribution from Baryon Acoustic Oscillations (BAO), which presents itself as a peak in the auto-correlation function or as wiggles in the power spectrum (see Section 1.2.4). If the galaxies are highly biased tracers of the matter field, the required number density is lower, since the bias is degenerate with clustering amplitude. In contrast to RSD, where the overall average bias is of interest, see Figure 2.7, with BAO the peak position is only affected if the galaxy bias is scale-dependent (e.g Coles and Erdogdu, 2007; Cresswell and Percival, 2009).

Although LRGs are typically passive elliptical galaxies with featureless spectra,

redshifts can be measured from strong continuum features, most notably the 4000 Å break. Together with the high bias of $b \sim 2$ (e.g. Tegmark et al., 2006) and the ability to efficiently find LRGs in photometric surveys (such as SDSS), LRGs are excellent targets for BAO studies. Furthermore, a high galaxy bias is preferred to make sure that transverse modes are not washed out by RSD, see Section 1.2.4 for more details. BOSS has been used to measure the growth rate from RSD to constrain cosmology (Samushia et al., 2013), finding results consistent with flat ΛCDM.

The Sloan Digital Sky Survey (SDSS) started drift-scanning the sky in 5 bands ($ugriz$) at the Apache Point Observatory, New Mexico, in 2000 and has made its data publicly available in increments, the latest of which is data release 10 (DR10). BOSS uses SDSS imaging for target selection and DR10 has measured redshifts of 859,322 galaxies as well as 166,300 quasars over 6,373 deg^2 of the sky. DR10 includes a low redshift sample (LOWZ) and a high redshift sample (CMASS). Eventually, BOSS will cover 10,000 deg^2, hence DR10 represents 64% of the completed area. Although the selection algorithms differ slightly, they target galaxies of very similar mass. For full details of the BOSS design see Dawson et al. (2013), and for the scope of DR10 see Ahn et al. (2014).

Previous Galaxy Bias Estimates for BOSS galaxies

Mandelbaum et al. (2013) have performed a model fit to SDSS galaxies by looking at clustering and galaxy-galaxy lensing from SDSS imaging, finding $b_1 \sim 2$ and $b_2 \sim 1$ for LRGs, where b_1 and b_2 correspond to the renormalised bias model, discussed in Section 2.3.5. In order to discuss the cosmological implications of the BAO peak, assumptions have to be made about the galaxy bias, see for example Anderson et al. (2012), which is achieved by comparing the clustering of galaxies to the theory prediction of dark matter clustering. Also, Sánchez et al. (2013) have studied the galaxy-galaxy lensing signal of CMASS to study the stellar and halo mass. They find the average mass for CMASS host halos to be $(2.3 \pm 0.1) \times 10^{13} h^{-1} M_\odot$, which is slightly lower than that of LRGs.

In Nuza et al. (2013) the galaxy bias is derived from a comparison between the correlation function of CMASS galaxies and that of the MultiDark simulation at the redshift of the galaxies, finding $b \sim 2.0$, with some indications of a scale- and time-dependent bias. The cosmological model was fixed to that of the MultiDark simulation, consistent with WMAP7. Note that scale-dependence affects the rate

at which the cross-correlation coefficient r rises to $r = 1$ at large scales, see Section 2.1.1. However, the BOSS cross-correlation coefficient has not been measured in the literature, despite its importance for cosmological constraints.

4.1.2 WiggleZ Lenses

Like BOSS, WiggleZ is a spectroscopic survey aimed at BAO, with important complementary cosmological constraints derived from RSD, among other probes. WiggleZ targets blue galaxies, which have lower mass (e.g Mandelbaum et al., 2006) and hence lower bias compared to LRGs, increasing the required number density for BAO studies. In addition to optical imaging, blue galaxies require ultraviolet (UV) imaging, which is impossible to observe from the ground. Despite this, there are interesting advantages: (1) blue galaxies have more prominent spectral features as a result of star formation, resulting in smaller redshift uncertainties, and (2) they can be thought of as field galaxies, tracing not merely clusters, but also the entire matter distribution, making their clustering properties less affected by non-linear effects. Although the BAO peak occurs around $\sim$ 100Mpc/h, the precise location is sensitive to the shape of the correlation function at small (non-linear) scales. Non-linear effects are also important for RSD analyses, because the linear prediction of the redshift space galaxy power spectrum, see Equation (1.47), is already inaccurate at $k > 0.02h$ Mpc^{-1} as a result of the assumption in Section 1.2.4 that the velocity field is generated under linear perturbation theory (Scoccimarro, 2004).

WiggleZ uses the Red Sequence Cluster Survey (RCS2; Gilbank et al., 2011), see also Section 4.1.3, SDSS, and the Galaxy Evolution Explorer (GALEX) for target selection and obtaining precise positions for fibre spectroscopy. GALEX is a retired UV satellite in operation from 2003 until 2013. A total of 238,770 spectra, observed with the AAOmega/2df spectrograph on the Anglo Australian Telescope (AAT), constitute the WiggleZ sample, covering $\sim$1000 deg^2. Full details on the survey strategy are described in Drinkwater et al. (2010).

Previous Galaxy Bias Estimates for WiggleZ galaxies

The WiggleZ galaxy bias is discussed in Marín et al. (2013), who use simulations to study the non-linearity of galaxy bias. They compare the 2- and 3-point correlation functions to the GiggleZ simulations (Poole et al., 2014) to fit for a

linear and non-linear bias, b_1 and b_2, respectively, noting that their parameters do not have the same meaning as those of the renormalised bias model, but correspond to the Press Schechter approach in Mo and White (1996). Their results are included here for reference in Figure 4.1, showing the linear bias b_1 and nonlinear bias b_2 as a function of redshift for three redshift cuts, as well as theoretical predictions from Scoccimarro et al. (2001), based on the halo model. Furthermore, Blake et al. (2011) utilised the sensitivity of RSD analyses on the cross-correlation coefficient, see also Section 2.2, to find $r(k) \sim 1$ for WiggleZ at scales $0.05 < k < 0.30$, marginalising over a linear bias b while fixing the growth rate to the ΛCDM prediction. The result comes from a technique that is very different compared to my weak lensing analysis that follows, so is interesting to compare with.

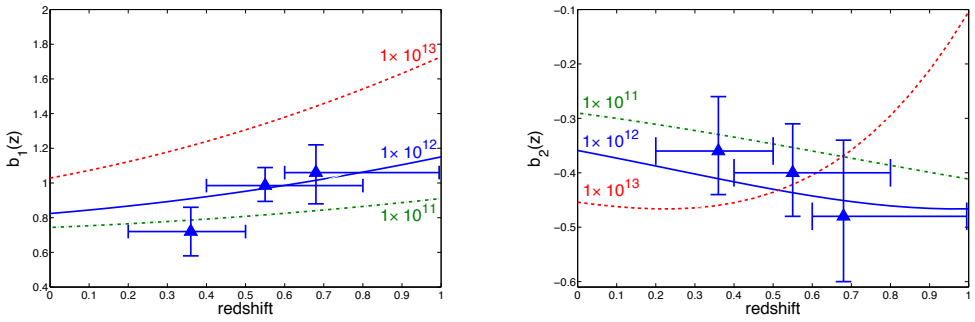

Figure 4.1 *Taken from Marín et al. (2013), who measured the linear bias b_1 (left) and non linear bias b_2 (right) from the 2- and 3-point correlation functions, as a function of redshift. Also shown are theoretical predictions for halos of masses $M_h = 10^{11}h^{-1}M_\odot$ (green dashed-dotted line), $M_h = 10^{12}h^{-1}M_\odot$ (blue solid line) and $M_h = 10^{13}h^{-1}M_\odot$ (red dashed line), noting that the halo mass of blue galaxies is more towards 10^{13} $h^{-1}M_\odot$ (e.g Velander et al., 2014).*

4.1.3 RCSLenS Sources

BOSS and WiggleZ have overlap with the Red Sequence Cluster Survey Lensing Survey (RCSLenS). RCSLenS images ~ 700 square degrees of the sky, measuring photometric redshifts for 400 deg^2 imaged in 4 bands out to $z \sim 2$. The same analysis tools were used as those developed for CFHTLenS[1].

The THELI tools are used for data reduction and are described in Erben et al.

[1]There are no RCSLenS publications at the time of writing this thesis. Information about the lensing part of the survey can be found online: http://www.rcslens.org/, while RCS2 is described in Gilbank et al. (2011).

(2013). RCSLenS uses all the data from the Red Sequence Cluster Survey 2 (RCS2), a project aimed at systematically searching the sky for clusters, employing the omnipresent red sequence in clusters to detect clusters of galaxies and measure their redshifts. The red sequence technique was proposed by Gladders and Yee (2000) and has established itself as a standard technique for galaxy cluster surveys alongside those based on bremsstrahlung radiation and the Sunyaev-Zeldovich effect, see also Chapter 6.

Photometric redshifts exist for only just over half the survey area. Therefore, we determine the redshift distribution by comparing RCS2 galaxies of the same magnitude to those of CFHTLenS, which has much higher number density and more accurate photometry due to the extra u-band. See Hildebrandt et al. (2012) for a complete description of the photometric redshift techniques.

Ellipticities were determined from Lensfit, a Bayesian model-fitting technique, see Miller et al. (2013). The PSF, which is an important source of systematic for ellipticity estimates, is taken into account by looking at multiple images of stars across the field. The model fitting method assumes galaxies are a sheared bulge plus disk, returning ellipticity parameters e_1 and e_2 for each source along with an inverse-variance weight, see also Equation (3.15).

Fig. 4.2 compares the redshift distributions of the same-sky surveys. In addition to the redshift distributions the lensing weight function is shown, see Equation (2.59). To aid visual comparison the distributions are not normalised to $\int_0^\infty n(z)dz = 1$, but their maxima are scaled to $n(z) = 1$. The LOWZ redshift distribution and RCSLenS weight function peak at a very similar position. However, for CMASS, RCSLenS would ideally be deeper. This is even more so for WiggleZ; Figure 4.2 shows that a large fraction of the WiggleZ lenses are behind the sources, contributing only noise in the galaxy-galaxy lensing signal.

4.2 Correlations and Cross-correlations from BOSS, WiggleZ, and RCSLenS

Here we show results for projected angular clustering $w(\theta)$, galaxy-galaxy lensing γ_t, and the shear autocorrelation function ξ_+, see Equations (2.69)-(2.74). The measurements of the (cross-)correlations were outlined in Section 3.2. Projected

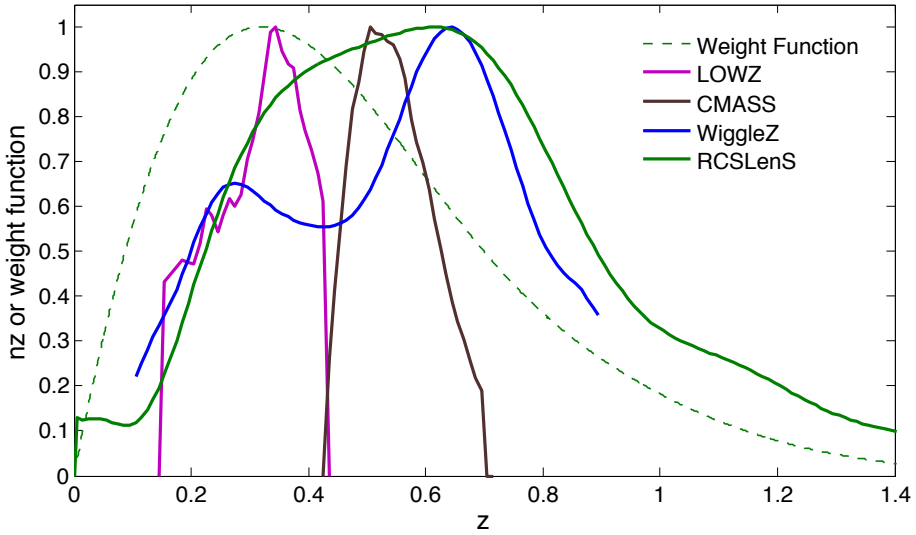

Figure 4.2 *Weight function and redshift distributions of RCSLenS compared to the foreground redshift distributions of BOSS-LOWZ, BOSS-CMASS and WiggleZ, which were normalised to have their maxima at* 1.

clustering is measured from the Landay-Szalay estimator, Equation (3.3) and also involves measuring the integral constraint, see Equation (3.5). Galaxy-galaxy lensing is an estimate of the matter around the lens galaxies and is estimated from cross-correlating the foreground positions (R.A and Dec.) with background shears (e_1 and e_2), see Equation (3.11). The shear autocorrelation function measures the full projected cosmological density field and is estimated from the background ellipticity parameters e_1 and e_2. Here we show binned results for all the estimators, noting that for the aperture statistic finely binned versions are required in order to perform the integrals in Equations (2.96)-(2.98).

Galaxy bias is dependent on galaxy mass, and hence on galaxy type and selection criteria. Since BOSS's LOWZ sample was constructed differently compared to the CMASS sample, they are treated separately. WiggleZ has a broad redshift range, allowing the same redshift limits as the LOWZ and CMASS samples, which is convenient for comparisons. The lensing kernel is poorly matched with the full WiggleZ redshift distribution, so is not analysed. Furthermore, the projected clustering signal $w(\theta)$ is low as a result of mixing many physical scales in angular separations. Table 4.1 lists the five different lens samples analysed in this section and their respective redshift ranges.

Covariance matrices were calculated in the same way as in Chapter 3. Mock realisations are produced by applying a bias of $b = 2$ and $b = 1$ for BOSS and

WiggleZ, respectively, and the number densities are adjusted to those of the real data, allowing mock measurements of w, γ_t, and $\xi_\pm$. In the future larger simulations will be used, since the Clone realisations are inaccurate beyond ~ 40 arcmin, as discussed in Chapter 3, see also Harnois-Déraps et al. (2014).

Table 4.1 *Data Samples*

Survey	Sub sample	Lower z limit	Upper z limit	I_w
BOSS	LOWZ	0.15	0.43	0.0145
BOSS	CMASS	0.43	0.70	0.0073
WiggleZ	LZ	0.15	0.43	0.0035
WiggleZ	HZ	0.43	0.70	0.0012

As discussed in Section 3.2.1 the measurement of $w(\theta)$ requires a small correction, known as the integral constraint I_w. This was calculated for each field separately and combined using area weighting. It requires a fiducial model of $w(\theta)$, and hence for the bias. The cosmological framework was based on the latest Planck flat ΛCDM constraints, see Table 1.1, and for the BOSS samples a constant bias was assumed of $b = 2$, whereas for WiggleZ $b = 1$ was adopted. The bias values are based on previous publications, discussed in the foregoing section. Table 4.1 lists I_w calculated for each field showing that it is a small correction for all surveys. Although it seems odd that, in our measurement of galaxy bias we need to assume a bias model, the correction is only marginally relevant at the largest angular separations. Note that, due to the finite nature of the filter function, the aperture galaxy bias method is insensitive to the integral constraint.

4.2.1 Shear Calibration

It was noted by Miller et al. (2013) that for CFTHTLenS the measured ellipticities have to calibrated. In addition to shape noise, the observed ellipticities are affected by measurement errors. Heymans et al. (2006) models the measurement error with the parameter m, so that

$$e^{\rm true} = (1 + m)e^{\rm obs}, \tag{4.1}$$

where m depends on galaxy size r and signal to noise $\nu_{\rm SN}$. It turns out that $\langle m \rangle \neq 0$, which introduces a systematic offset in the lensing correlation functions.

The value of the offset as a function of scale is the autocorrelation function of m

$$1 + K(\theta) = \frac{\sum w_i w_j [1 + m(\nu_{\mathrm{SN},i}, r_i)][1 + m(\nu_{\mathrm{SN},j}, r_j)]}{\sum w_i w_j}. \tag{4.2}$$

The shear auto-correlation functions are calibrated as follows

$$\xi_{\pm}^{\mathrm{cal}} = \frac{\xi_{\pm}}{1 + K(\theta)}, \tag{4.3}$$

and for galaxy-galaxy lensing the calibration is

$$1 + K_t(\theta) = \frac{\sum w_i [1 + m(\nu_{\mathrm{SN},i}, r_i)]}{\sum w_i}. \tag{4.4}$$

The calibrated γ_t^{cal} is [Blake et al 2014 (in prep)]

$$\gamma_t^{\mathrm{cal}} = \frac{\gamma_t}{1 + K_t(\theta)} \tag{4.5}$$

In what follows the superscript is dropped from the calibrated measurements. Blake et al 2014 (in prep) measured $1 + K_t(\theta)$ for RCS, finding it relatively insensitive to scale at a value of $1 + K_t(\theta) = 0.95$ and $1 + K(\theta)$ was found to be 0.90.

4.2.2 RCSLenS

In Figure 4.3 I present the shear correlation function measured from the RCSLenS Survey using only those fields that passed systematic tests, based on the requirement the star-galaxy cross-correlation function be consistent with zero (section 3.2 in Heymans et al., 2012). The area of the pass fields combined is $\sim$ 550 square degrees. The light grey circles in Figure 4.3 fields were included that failed the star-galaxy cross-correlation test (only $\sim$ 10% of the total area), showing its significance. Furthermore, ξ_+ is shown for those fields that have overlap with the spectroscopic surveys (squares for BOSS; circles for WiggleZ), found to be consistent with the full measurement as expected from homogeneity in both survey design and the Universe.

Theory predictions are also shown in Figure 4.3, based on ΛCDM cosmology and Smith et al. (2003) halofit, with Planck best fit parameters ($\Omega_m = 0.315, H_0 = 67.1, \Omega_\Lambda = 0.6825$) and three different values for σ_8: 0.5, 0.8344 (Planck best fit), and 1.0. The measurement of ξ_+ from all the pass fields is in good agreement with

$\sigma_8 = 0.8344$. Therefore, for the bias measurements we fix the cosmology to Planck constraints, noting that for a future work we let the cosmological parameters vary.

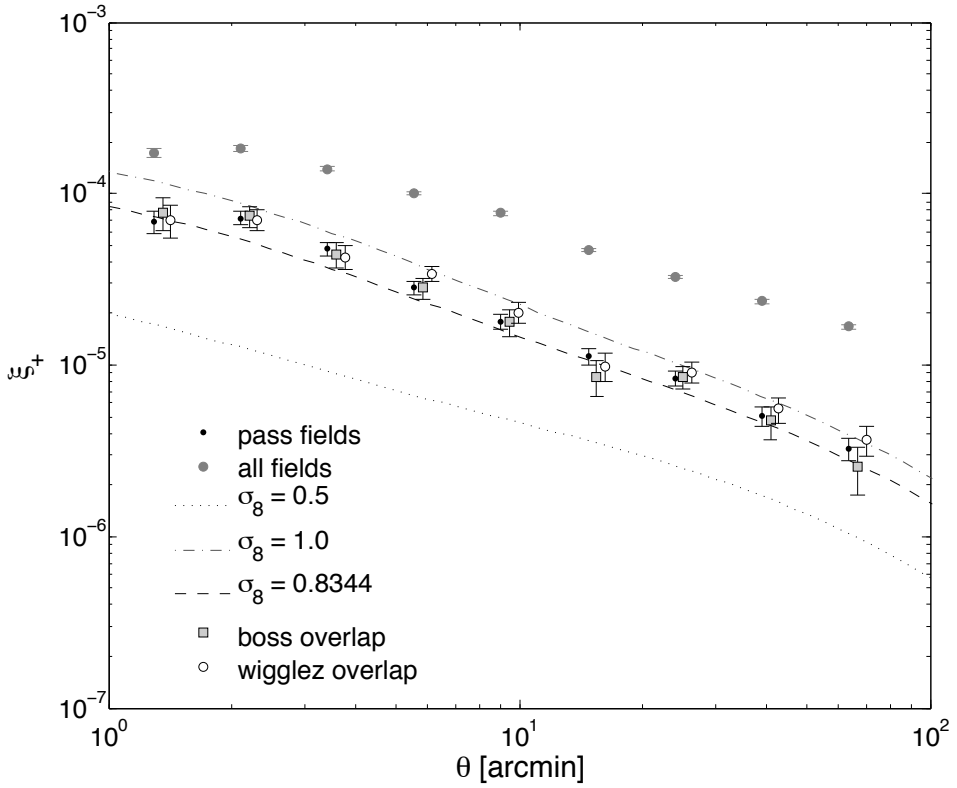

Figure 4.3 *The shear autocorrelation function ξ_+ from all the fields that passed systematic tests (black dots), and from all the fields (grey circles). Squares (circles) show ξ_+ from the pass fields that have overlap with BOSS (WiggleZ). Theory curves are shown based on Planck's ΛCDM best fit parameters, including $\sigma_8 = 0.5$ and $\sigma_8 = 1.0$.*

4.2.3 BOSS 2-Point Clustering: $w(\theta)$ and $\gamma_t(\theta)$.

The projected clustering w and galaxy-galaxy lensing γ_t of BOSS DR10 galaxies is presented in Figure 4.4. Also shown are Planck theory curves, to which a bias of $b = 2$ was applied and it is found to be consistent with the data on scales > 10 arcmin. For the theory curves, Smith et al. (2003) halofit was incorporated to model the small-scale clustering. The discrepancy at small scales is indicative of a scale-dependent bias, which is more pronounced for the LOWZ galaxies.

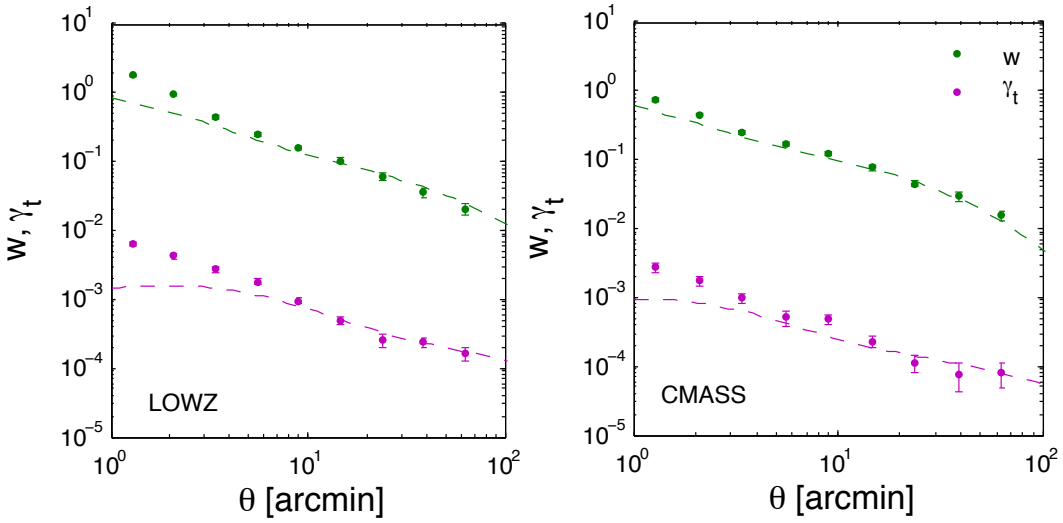

Figure 4.4 *Projected clustering w and galaxy-galaxy lensing γ_t of the LOWZ (left) and CMASS (right) samples. Also shown are ΛCDM theory predictions.*

4.2.4 WiggleZ 2-Point Clustering: $w(\theta)$ and $\gamma_t(\theta)$.

The tangential shear γ_t around the LZ and HZ galaxies as well as their projected clustering is shown in Figure 4.5. This can be compared to the theoretical predictions for a galaxy sample with $b = r = 1$. The clustering of galaxies seems slightly larger compared to the Planck prediction, especially for the higher redshift sample, is suggestive of galaxy bias evolution. The galaxy-galaxy lensing signal is low for both samples, which could be the result of a low cross-correlation coefficient, since $w(\theta)$ indicates $b > 1$.

Fig. 4.6 shows w and γ_t for the WiggleZ sample without redshift cuts, that is, the ALL sample. The projected angular clustering amplitude of a sample with a broad redshift distribution is lower, since more physical scales are mixed per angular separation. The negative signal at large scales is attributed to shot noise in combination with the low signal. At large scales γ_t agrees well with the $b = r = 1$ theory curve.

The broad $n(z)$ makes it difficult to interpret the signals, since time-dependence of the galaxy bias appears as scale-dependence. This is different for w and γ_t, as can be understood from Figure 2.8 where it was shown that θ corresponds differently to physical scales for w and γ_t. By using all the WiggleZ galaxies shot noise is suppressed, leading to smaller errors at small scales. However, the signal of $w(\theta)$ for samples with broader $n(z)$ is weaker. This is easy to see from the

extreme case of a survey with infinite depth: projecting all objects onto the 2D sky would result in white noise, hence $w(\theta) = 0$.

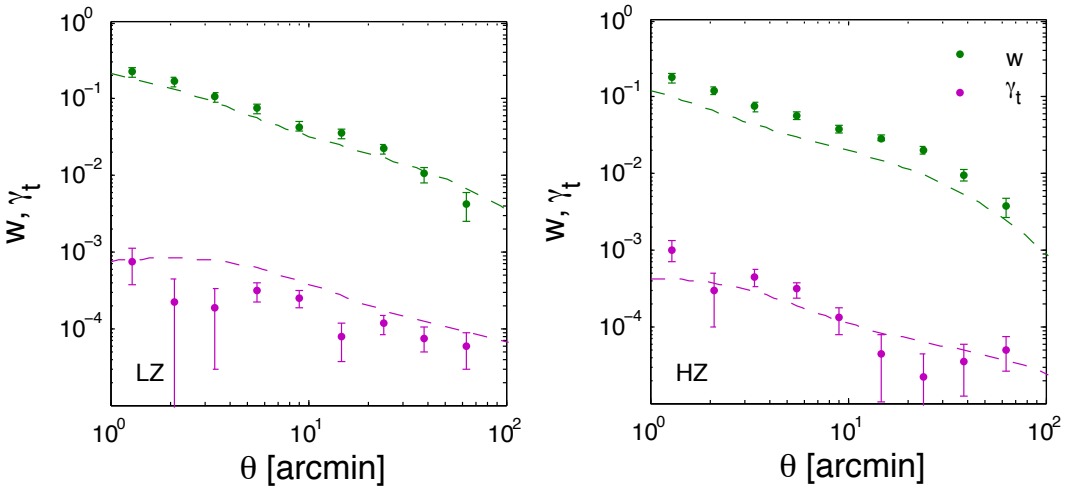

Figure 4.5 *Projected clustering w and galaxy-galaxy lensing γ_t of the WiggleZ LZ (left) and WiggleZ HZ (right) samples, defined in Table 4.1.*

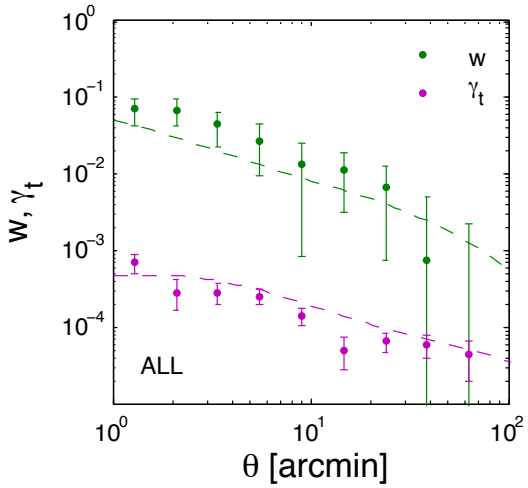

Figure 4.6 *Projected clustering w and galaxy-galaxy lensing γ_t of WiggleZ without redshift cuts (ALL sample in Table 4.1).*

4.2.5 Aperture Statistics

Section 2.3.3 discusses the aperture bias method. The lensing and clustering statistics are modified in order to enable the extraction of bias parameters from ratios of estimators. The conversions $\xi_\pm$ to $\langle M_{ap}^2 \rangle$, w to $\langle N_{ap}^2 \rangle$, and γ_t to $\langle M_{ap} N_{ap} \rangle$, are given in Equations (2.96), (2.97), and (2.98), respectively. For the integrations

we use finely binned raw estimators: 1000 θ bins from $\theta = 0.15'$ to $\theta = 200'$. The translation from θ_{ap} to k can be approximated with Equation (2.104). This is plotted for the WiggleZ and BOSS samples in Figure 4.7, where it can be shown that for the low redshift samples (LOWZ and LZ) an angular scale corresponds to larger physical scales, compared to the higher redshift samples. RSD analyses use k values as high as $\sim 0.4h$ Mpc^{-1} (e.g. Blake et al., 2011), which corresponds to $\theta_{ap} \simeq 18'$ for the high redshift samples, and to $\theta_{ap} \simeq 30'$ for the low redshift samples.

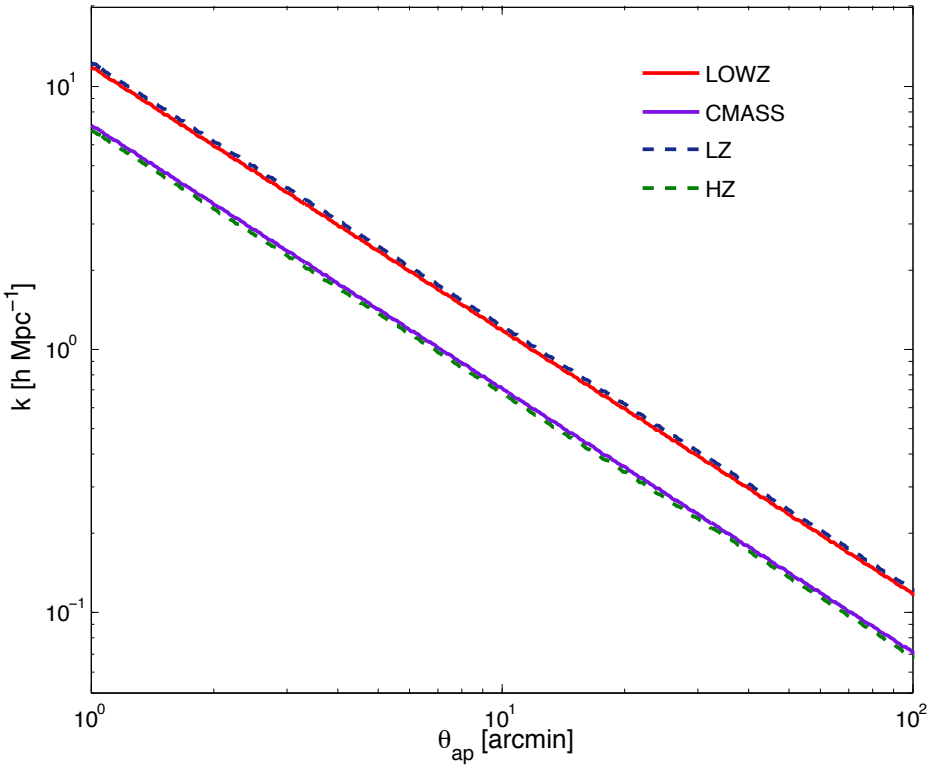

Figure 4.7 *The conversion from θ_{ap} to k scales for the samples in Table 3.1, approximated by Equation* (2.104)*. It shows that the aperture statistics, which are measured up to $\theta_{ap} = 100'$ here, probe into the quasi linear regime.*

Fig. 4.8 shows the measured aperture mass variance $\langle M_{ap}^2 \rangle$ from the RCSLenS survey. The analysis of the full survey can be compared to the result measured from the survey area restricted to the BOSS overlap (red data points) and WiggleZ overlap (blue data points). The signal is consistent for different area selections, since the data is taken to the same depth across all fields with the same seeing. Since ξ_+ (or $\langle M_{ap}^2 \rangle$) constrains cosmology it is not required to overlap with the spectroscopic surveys, hence data from the full RCSLenS survey is used to reduce noise. The same applies to $w(\theta)$, but for the purpose of this

thesis only the overlapping regions are used. This will be updated in a future analysis.

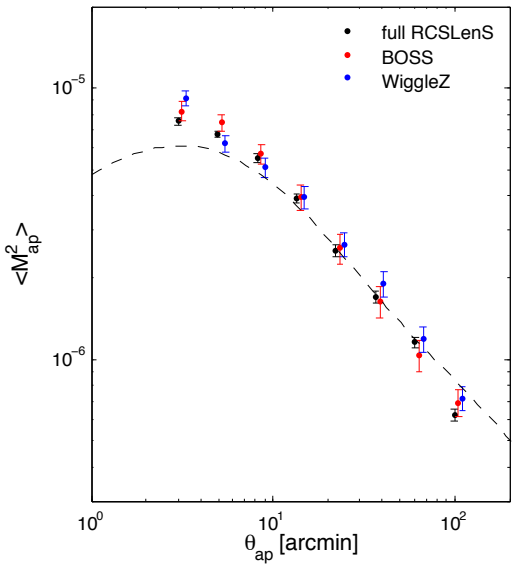

Figure 4.8 *The aperture mass autocorrelation function from RCSLenS, also showing the result from using only the fields with BOSS and WiggleZ overlap, offset by factors of 1.05. Error bars were derived from 184 LOS of the clone simulations with an RCSLenS set up. The dashed line represents the theoretical prediction using Planck cosmology.*

The aperture count variance $\langle N_{ap}^2 \rangle$ and galaxy-mass cross-correlation $\langle M_{ap} N_{ap} \rangle$ for the LOWZ and CMASS samples are shown in Figure 4.9, along with theoretical predictions for a galaxy population with $b = 2$ and $r = 1$. The LOWZ result disagrees more with a linear bias than the CMASS data points.

Fig. 4.10 shows the aperture count variance $\langle N_{ap}^2 \rangle$ and galaxy-mass cross-correlation $\langle M_{ap} N_{ap} \rangle$ for the WiggleZ LZ and HZ samples. The data points can be compared to the theoretical predictions (dashed lines) for an unbiased galaxy sample. Similar galaxy bias features as those seen in Figure 4.5 are suggested here: first, galaxy bias evolution from a comparison between the LZ and HZ sample and, second, a low cross-correlation coefficient, especially for the LZ sample.

4.3 Galaxy Bias Measurements

In this section two methods are used to extract information about the galaxy bias properties of the BOSS and WiggleZ samples. The aperture method was introduced and thoroughly tested in Chapters 2 and 3. Several issues were

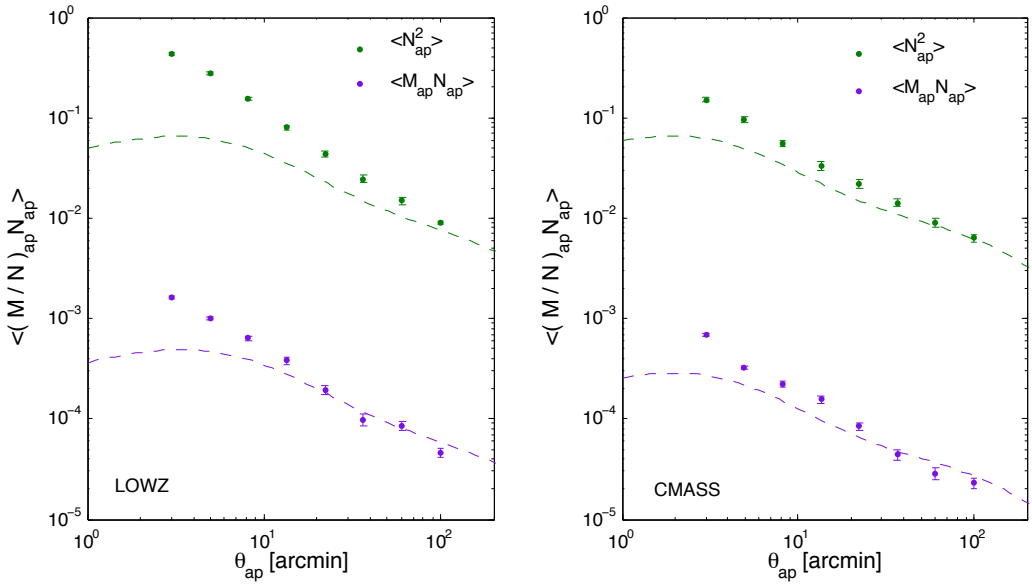

Figure 4.9 *The aperture statistics for the LOWZ (left) and CMASS (right) samples of BOSS. Theory curves assume $b = 2$ and $r = 1$.*

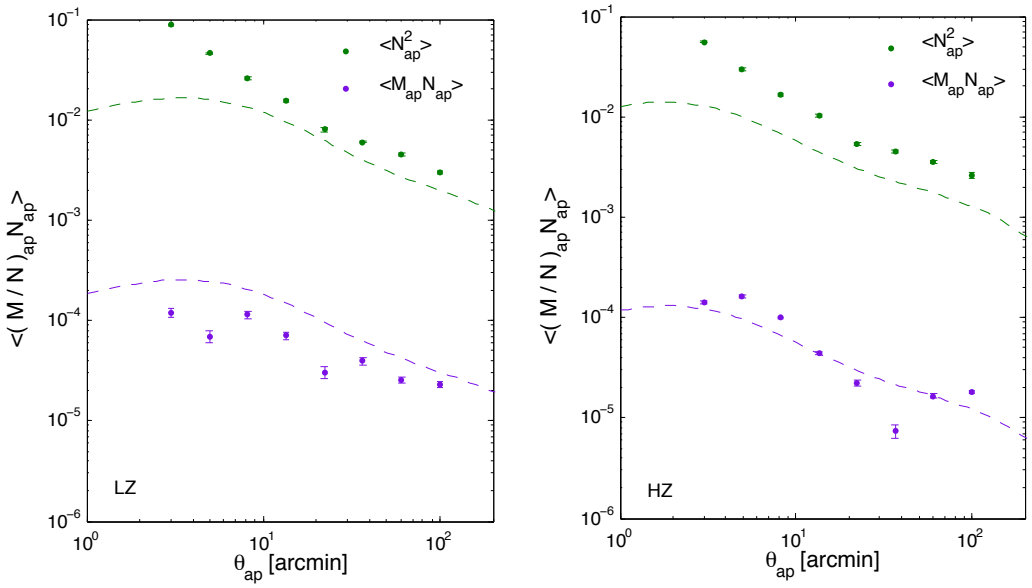

Figure 4.10 *The aperture statistics for the WiggleZ LZ (left) and HZ (right) samples. Theory curves assume $b = 1$ and $r = 1$.*

discussed, such as correlated data points, apparent scale-dependence from taking ratios, and issues regarding the recovery of the true time- and scale-dependence. The model fitting method does not modify the data and for RSD analyses it has the additional advantage of measuring $b(k)$ and $r(k)$ directly. This comes at a price: a choice of galaxy bias model is required. The renormalised galaxy bias model of McDonald (2006) is motivated in Section 2.3.5, where its

physical origin and previous use by Mandelbaum et al. (2013) were decisive considerations. Furthermore, in this analysis the model is given more flexibility with the addition of a parameter $\mathcal{R}$ to account for higher order nonlinear bias terms and stochasticity, in addition to b_1 and b_2 (see Equations (2.120) and (2.123) for the galaxy power spectrum P_{gg} and galaxy-matter cross power spectrum P_{gm}, respectively, for this galaxy bias model).

The raw estimators w, γ_t, and $\xi_\pm$ and aperture statistics $\langle N_{ap}^2 \rangle$, $\langle M_{ap} N_{ap} \rangle$, and $\langle M_{ap}^2 \rangle$ are first used to constrain $b(\theta_{ap})$ and $r(\theta_{ap})$, defined in Equations (2.84) and (2.85), respectively. We then look at the constraints on the McDonald (2006) galaxy bias model using the raw estimators.

4.3.1 Aperture Galaxy Bias Results

In this section galaxy bias results are presented for the aperture method, also used by Hoekstra et al. (2002), Simon et al. (2007), and Jullo et al. (2014), for the BOSS and WiggleZ samples. The calibration factors, Equation (2.86) and (2.87), were calculated under the assumption of flat ΛCDM and Planck best fit parameters in Table 1.1, including also the Smith et al. (2003) halofit formalism for the nonlinear power spectrum. Error bars were calculated from the clones (Harnois-Déraps et al., 2012), similar to the error estimations in Chapter 3. However, the lower number density and smaller depth compared to CFHTLenS in combination with the small clone area, which spans just 12.85 deg^2, often results in negative aperture statistics, causing complex bias parameters in a single clone LOS, when using the aperture bias ratio measurement. Therefore, the errors on the aperture galaxy bias parameters are calculated from error propagation as follows

$$\sigma_b = b(\theta_{ap}) \times \sqrt{\left(\frac{\sigma\left[\sqrt{\langle N_{ap}^2 \rangle}\right]}{\sqrt{\langle N_{ap}^2 \rangle}} \right)^2 + \left(\frac{\sigma\left[\sqrt{\langle M_{ap}^2 \rangle}\right]}{\sqrt{\langle M_{ap}^2 \rangle}} \right)^2}, \tag{4.6}$$

$$\sigma_r = r(\theta_{ap}) \times \sqrt{\left(\frac{\sigma\left[\langle M_{ap} N_{ap} \rangle\right]}{\langle M_{ap} N_{ap} \rangle} \right)^2 + \left(\frac{\sigma\left[\sqrt{\langle N_{ap}^2 \rangle}\right]}{\sqrt{\langle N_{ap}^2 \rangle}} \right)^2 + \left(\frac{\sigma\left[\sqrt{\langle M_{ap}^2 \rangle}\right]}{\sqrt{\langle M_{ap}^2 \rangle}} \right)^2}. \tag{4.7}$$

Here δx is the same as the standard deviation σ of the variable x, denoted σ_x. Note that error propagation neglects covariances between the individual aperture

statistics. In a future work larger simulations will be used, so that the errors may be estimated by taking the variance between $b(\theta_{ap})$ and between $r(\theta_{ap})$ measured for each realisation, as was done in Chapter 3. Chapter 3 showed that the measurements at different θ_{ap} values are heavily correlated. The aperture bias parameters are evaluated at 8 data points from $\theta_{ap} = 3$ to 100 arcmin.

The aperture galaxy bias results for BOSS are shown in Figure 4.11. The LOWZ sample shows prominent scale-dependence with $b(\theta_{ap} = 3') = 4.1 \pm 0.1$ and $b(\theta_{ap} = 100') = 2.2 \pm 0.1$. This may in part be due to the scale-dependence that arises from taking the ratio of noisy numbers, discussed in Section 3.4.3, but the feature is too strong to be solely explained in this way. The bias of the CMASS sample is very close to linear at $b = 2$, noting that nonlinearity is not well recovered by the aperture mass statistic, as discussed in Section 2.3.4. Furthermore, θ_{ap} for the LOWZ result corresponds to smaller physical scales (higher k), as can be seen from Figure 4.7. The cross-correlation coefficient $r(\theta_{ap})$ for the CMASS galaxies is consistent with $r = 1$ over the full range probed, but $r(\theta_{ap})$ for the LOWZ sample is lower at $\langle r(\theta_{ap}) \rangle = 0.9$, which may reflect the scale-dependence in $b(\theta_{ap})$. However, in light of the highly correlated data points, the measurement may in fact be consistent with perfect correlation, see Figure 3.12.

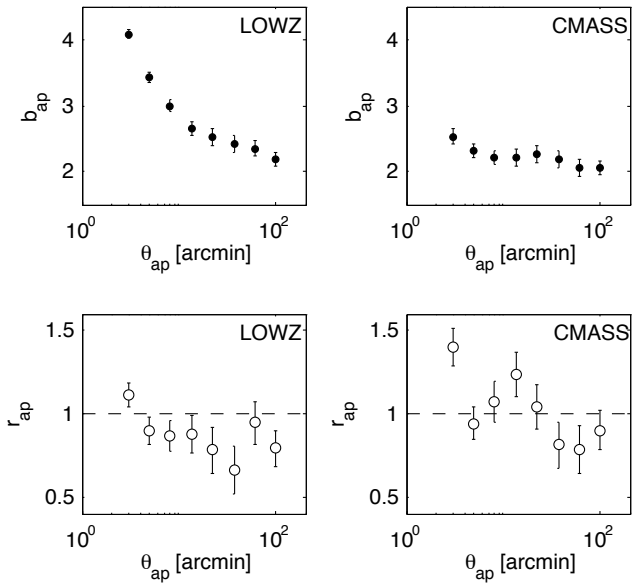

Figure 4.11 *The aperture galaxy bias results for BOSS, showing the aperture bias $b(\theta_{ap})$ (top) and aperture cross-correlation coefficient $r(\theta_{ap})$ (bottom), for LOWZ (left) and CMASS (right) BOSS galaxies.*

Fig. 4.12 shows the galaxy bias parameters for the WiggleZ samples, LZ (left), HZ (middle), and ALL (right). The scale-dependence in $b(\theta_{ap})$ for the LZ and HZ

samples is similar at small scales to the LOWZ result. The difference between $b(\theta_{ap} > 10')$ of the LZ and HZ samples is indicative of bias evolution (or selection effects). The cross-correlation coefficient $r(\theta_{ap})$ for the WiggleZ samples is lower compared to the LOWZ and CMASS results. WiggleZ galaxies trace lower mass haloes, resulting in less correlation between the shear field from RCSLenS and the positions of the lenses. Although $r(\theta_{ap})$ increases to $r(\theta_{ap}) = 1$ with increasing scale, as expected, the measurement shows strong stochasticity for WiggleZ galaxies.

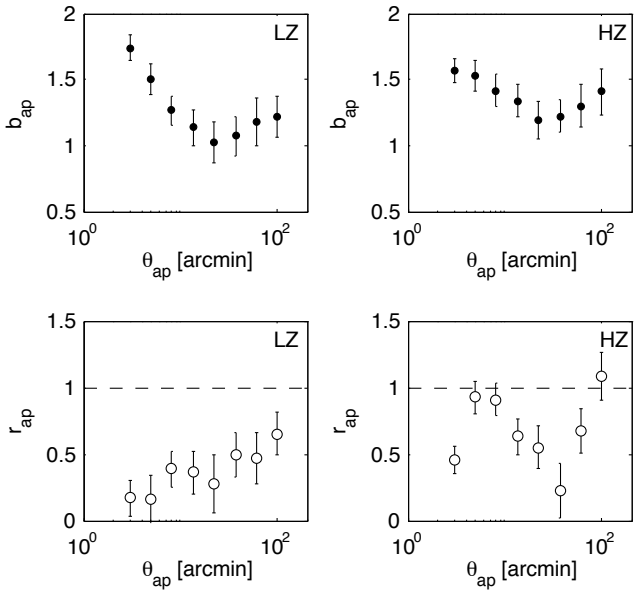

Figure 4.12 *The aperture galaxy bias results for WiggleZ.*

4.3.2 Galaxy Bias Model Fitting

In this section galaxy bias parameters are presented from a direct fit to the raw estimators w, γ_t, and ξ_+. In Section 2.3.5 I also discuss several bias fitting formulae, concluding with a preference for the renormalised bias parameters b_1, b_2. They were also measured by Mandelbaum et al. (2013) for the main SDSS sample and LRG subsamples, using the Υ ring statistic to exclude scales where the cross power spectrum P_{gm} is dominated by stochasticity. In Section 2.3.5 the parameter $\mathcal{R}$ was introduced, which will be constrained in the fitting procedure here.

The parameters are constrained by minimising the χ^2 statistic, Equation (3.32). The data vector D consists of ξ_+, $w(\theta)$, and γ_t, and the model vector M is varied

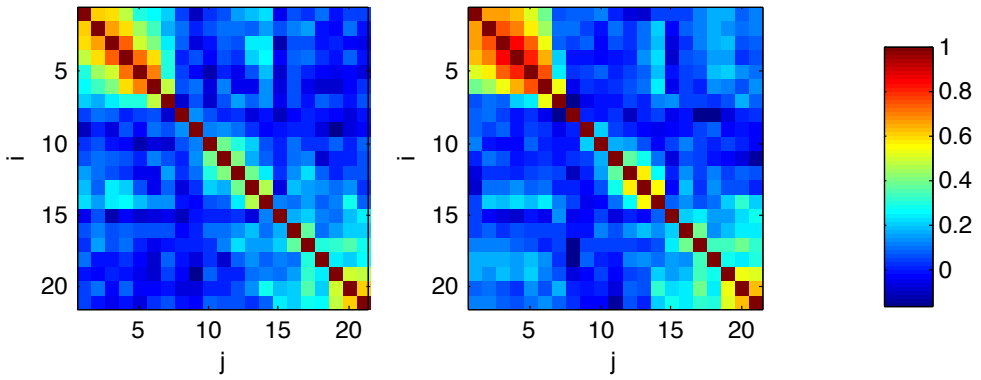

Figure 4.13 *The correlation matrices for the BOSS samples. To the left is LOWZ, to the right is CMASS.*

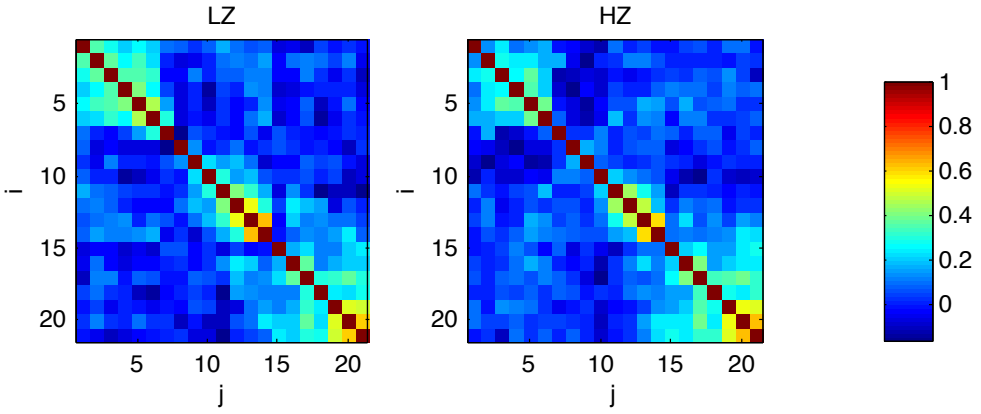

Figure 4.14 *The correlation matrices for the WiggleZ samples LZ (left) and HZ (middle) sample.*

with the fitting parameters b_1, b_2, and $\mathcal{R}$. The covariance matrix C, see Equation (3.21), is estimated from the clone simulations, as in Chapter 3. For future work larger simulations will be used to have a more accurate estimate of C on large scales ($\theta > 40'$). It is common to visualise C by using the correlation coefficient

$$\rho_{XY} = \frac{\sigma_{XY}}{\sigma_X \sigma_Y}. \tag{4.8}$$

Fig. 4.13 and Figure 4.14 show the correlation matrices for BOSS and WiggleZ, respectively. The top left 7 by 7 matrix shows the correlation between θ bins of w, the centre 7 by 7 matrix is γ_t, and the bottom right shows the correlation for ξ_+. The remaining cells show the correlations between estimators. The θ array consists of 7 logarithmically spaced bins from $\theta = 8$ to $\theta = 100$ arcmin (same for both).

Fig. 4.15, shows the 1σ and 2σ constraints for LOWZ (top panels) and CMASS (bottom panels) on the McDonald (2006) galaxy bias model. Of the measured raw estimators the small angular scales have high signal to noise, resulting in the small black contours, and the tight constraints for $8' < \theta < 100'$. Since the McDonald (2006) model is by design a large scale galaxy bias model, however, we also fit the parameters using $15' < \theta < 100'$, resulting in much larger uncertainties (filled contours), but focussing more on linear scales.

For both the LOWZ and CMASS samples the two fits using 2 different θ ranges are consistent. The LOWZ b_2 values are different, so that there is some indication for the requirement of higher order bias terms. For the $8' < \theta < 100'$ fit the value for b_2 is very similar to CMASS at $b_2 \simeq 0.5$, while b_1 is found to be slightly higher compared to CMASS. The range with higher minimum θ results in lower b_1 values for both BOSS samples, but more so for CMASS, although consistent with the $8' < \theta < 100'$ range.

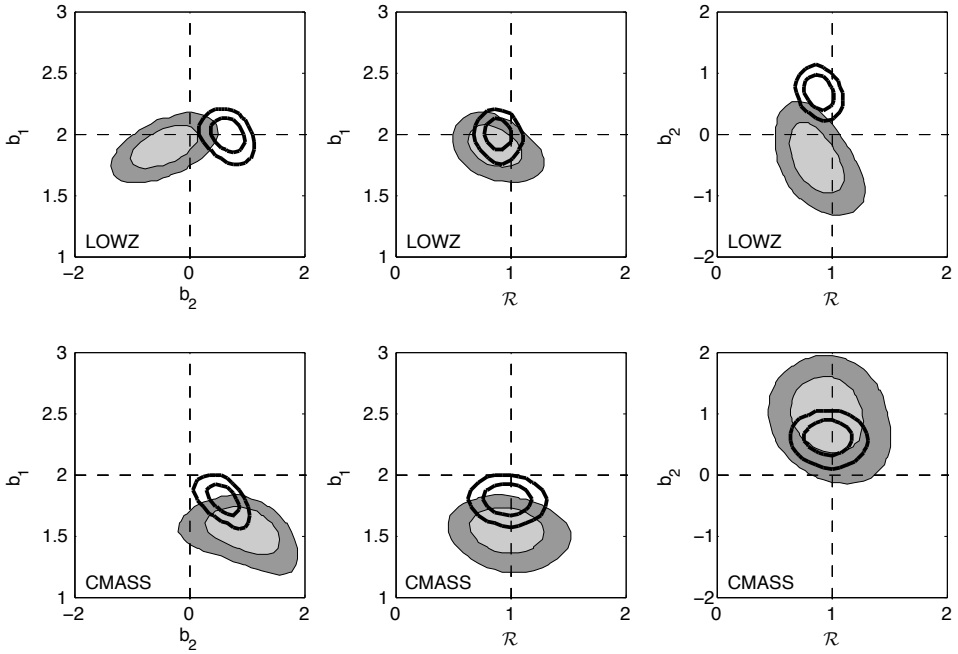

Figure 4.15 *Constraints on the McDonald (2006) galaxy bias model, including parameter $\mathcal{R}$, for LOWZ (top panels) and CMASS (bottom panels). The black contours are based on the measurement of raw estimators at $8' < \theta < 100'$, while the filled contours have $15' < \theta < 100'$.*

The 1σ and 2σ confidence contours for b_1, b_2, and $\mathcal{R}$ are shown in Figure 4.16 for the LZ (top panels) and HZ (lower panels) samples. The fits for the two θ ranges are found to be consistent.

The model is better constrained for the BOSS galaxies, which have higher signal to noise as a result of the higher bias. In particular, the uncertainty in b_2 is much larger for WiggleZ. The constraints for both samples are suggestive of significant stochasticity. As with the aperture method, the LZ sample has more stochasticity compared to the HZ sample. The LZ parameters are not well constrained when using $15' < \theta < 100'$. Bias evolution is indicated by the difference in b_1 for the two samples, which was also found with the aperture statistic.

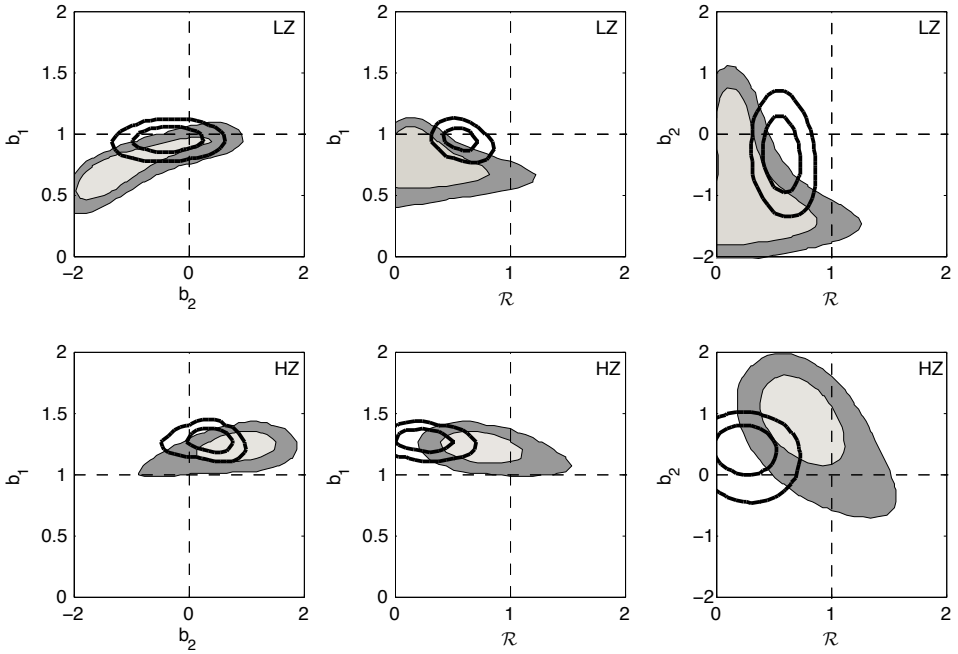

Figure 4.16 *Confidence contours (1 and 2 σ) of the renormalised bias parameters b_1, b_2, and $\mathcal{R}$ for the WiggleZ LZ and HZ samples (top and bottom panels, respectively). The black contours show the results from the $8' < \theta < 100'$ fit; the filled contours represent the fit for $15' < \theta < 100'$.*

4.4 Discussion and Conclusion

Galaxy bias results were shown for the spectroscopic samples BOSS and WiggleZ, by cross-correlating their positions with RCSLenS galaxies. Two methods were

employed: the aperture galaxy bias model, introduced in Section 2.3.3, and the McDonald (2006) galaxy bias model fitting, discussed in Section 2.3.5. Uncertainties were estimated from covariance matrices constructed independently from the data, using clone realisations. It was shown that the shear from RCSLenS is consistent with ΛCDM for Planck best fit cosmological parameters, after which cosmology was fixed for the galaxy bias results. For future work I will also marginalise over uncertainties in the cosmological framework, in addition to updating the clones with larger simulations to have more accurate covariance estimates.

4.4.1 Aperture Method versus Model Fitting

Overall very similar values were found by the two methods to extract galaxy bias parameters. The aperture bias method indicates a slightly higher bias b, compared to the model fitting. Only the low redshift samples (WiggleZ's LZ and BOSS' LOWZ) show prominent scale-dependence in $b(\theta_{ap})$, while the higher redshift samples have a more linear bias. This can be related to the fact that the bias is more strongly nonlinear at smaller physical scales, combined with the fact that the θ_{ap} range for the low redshift samples corresponds to smaller physical scales, see Figure 4.7.

Both the model fitting and the aperture bias constraints indicate more stochasticity for the WiggleZ samples, while the BOSS galaxy bias is consistent with a deterministic scenario. As was discussed in Section 2.1.1, a deterministic bias does not necessarily correspond to $r = 1$. This can be seen in Figure 4.17 where the cross-correlation coefficient is shown for different values of b_2. Note that the effect of $\mathcal{R}$ on the curves in Figure 4.17 is to scale $r(k)$ up or down, see Equation (2.123). For the WiggleZ LZ sample b_2 is consistent with zero and $\mathcal{R}$ is low, indicating that the increase to $r = 1$ with larger scales (lower k) is not well described by the McDonald (2006) bias model for this sample.

4.4.2 Comparison to Previous Results

The galaxy bias method was used for the first time by Hoekstra et al. (2002) to measure the galaxy bias of RCS galaxies, finding low $r(\theta_{ap})$ of ~ 0.6 and $b(\theta_{ap}) \simeq 1$. Simon et al. (2007) constrained the galaxy bias parameters from the

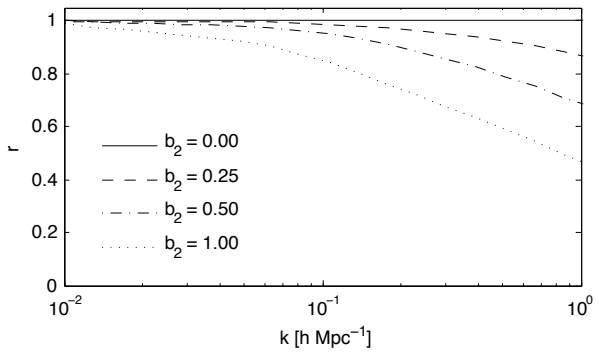

Figure 4.17 *The dependence of the cross-correlation coefficient, Equation* (2.17)*, on the parameter b_2 of the McDonald (2006) model. A redshift of $z = 0.5$ was assumed and we set $b_1 = 2$.*

Table 4.2 *McDonald (2006) model fitting results*

	BOSS LOWZ	BOSS CMASS	WiggleZ LZ	WiggleZ HZ
$8' < \theta < 100'$				
b_1	2.0 ± 0.1	1.8 ± 0.1	0.9 ± 0.1	1.3 ± 0.1
b_2	0.6 ± 0.2	0.6 ± 0.2	-0.4 ± 0.5	0.4 ± 0.4
$\mathcal{R}$	0.9 ± 0.1	1.0 ± 0.1	0.6 ± 0.2	0.3 ± 0.2
$15' < \theta < 100'$				
b_1	1.9 ± 0.2	1.6 ± 0.2	0.7 ± 0.3	1.2 ± 0.2
b_2	-0.4 ± 0.6	1.0 ± 0.6	-1.0 ± 0.7	0.9 ± 0.6
$\mathcal{R}$	0.8 ± 0.3	1.0 ± 0.3	0.2 ± 0.6	0.7 ± 0.4

the Garching-Bonn Deep Survey (GaBoDS), out to $\theta_{ap} = 20'$ to find a low $r(\theta_{ap})$ of around ~ 0.5, and $b(\theta_{ap}) \simeq 0.8$. Finally, Jullo et al. (2012) measured the galaxy bias parameters of the COSMOS survey, again out to $\theta_{ap} = 20'$, finding evidence for bias evolution in $b(\theta_{ap})$, while $r(\theta_{ap})$ was not well constrained (values ranging from 0 to 2 with large uncertainties).

The quality of the data for the results presented in this chapter allows us to extend the measurements out to larger scales compared to the previous aperture bias measurements. It is the first time that the method finds $r(\theta_{ap})$ to be consistent with unity, which I find with the BOSS galaxy samples. This may be related to the fact that all previous aperture bias methods have used lens samples with $b \sim 1$, while the tracers of more massive haloes will have better correlation with the total matter field, as measured by $\langle M_{ap} N_{ap} \rangle$.

By going out to larger scales with the aperture method we find some indication that the WiggleZ cross-correlation coefficient increases to $r = 1$. Also with the

model fitting, we find that for the HZ sample, when using $15' < \theta < 100'$ that the cross-correlation coefficient is consistent with $r = 1$. Blake et al. (2011) found $r(k)$ to be consistent with unity at scales used by their RSD analysis, averaging over all their redshift bins. The results presented here indicate that r is low for the LZ sample, even at large scales. The bias b is slightly higher compared to the results of Marín et al. (2013), see Figure 4.1, who find a linear bias of $b = 0.72 \pm 0.14$ at an effective redshift of $z_{\rm eff} = 0.35$, (the LZ sample has $\langle z \rangle = 0.3$ and we find $b_1 = 0.9 \pm 0.1$). They also find $b = 0.99 \pm 0.10$ at $z_{\rm eff} = 0.55$ (the HZ sample has $\langle z \rangle = 0.58$ for which the model fitting yields $b = 1.2 \pm 0.1$). However, the result of Marín et al. (2013) are based on a different technique, and given their evidence for scale-dependence and different scales probed, it is hard to conclude whether the results here are inconsistent, despite finding different values.

Fig. 4.18 shows constraints on the McDonald (2006) model from Mandelbaum et al. (2013). The LRG results (middle and lower panels) correspond roughly to the BOSS LOWZ sample, which colour cuts are similar for LRGs as well as probing similar redshifts. Mandelbaum et al. (2013) find for their lower redshift LRG sample $[b_1;\, b_2] = [2.07 \pm 0.05;\, 0.98^{+0.28}_{-0.24}]$ and for their higher redshift LRG sample $[b_1;\, b_2] = [2.26 \pm 0.06;\, 0.94^{+0.66}_{-0.54}]$. Mandelbaum et al. (2013) uses the Υ statistic, allowing the choice of a minimum scale of $R_0 = 2h^{-1}$Mpc, which correspond to $k = 2\pi/R_0 \sim 3.1h\mathrm{Mpc}^{-1}$. From Figure 2.8 it is clear that these k-scales correspond, at least for galaxy-galaxy lensing, more to the $8' < \theta < 100'$ than the $15' < \theta < 100'$ fit in this analysis. Indeed, when using the $8' < \theta < 100'$ range for fitting, the values for b_1 and b_2, see Table 4.2, are remarkably similar to the LRG constraints of Mandelbaum et al. (2013).

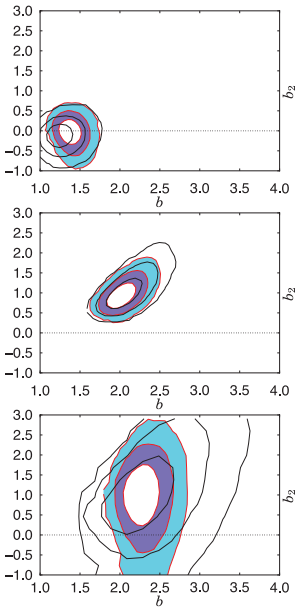

Figure 4.18 *Taken from Mandelbaum et al. (2013), showing constraints on the McDonald (2006) bias model from the* Υ *statistic for SDSS galaxy samples: Main L5 (top), LRGs at redshifts* $0.16 < z < 0.36$ *(middle), and LRGs at redshifts* $0.36 < z < 0.47$ *(bottom). The filled contours are based on jointly fitting all samples, and the solid black lines are the result of fitting for each sample separately.*

Chapter 5

Galaxy Bias From Density and Shear Fields

As a result of perturbations in the cosmological matter field the image of a galaxy is formed from a collection of deflected photons. Therefore, gravitational lensing is, by its very nature, a non-local effect. The shear field, sampled by background galaxies, is, however, directly related to the projected density field, allowing for mass reconstruction and, hence, a local comparison with the foreground galaxy field.

The galaxy bias parameters are defined as

$$b(R) \equiv \sqrt{\frac{\langle \delta_g^2 \rangle}{\langle \delta_m^2 \rangle}} \tag{5.1}$$

$$r(R) \equiv \frac{\langle \delta_g \delta_m \rangle}{\sqrt{\langle \delta_g^2 \rangle \langle \delta_m^2 \rangle}}, \tag{5.2}$$

where δ is the fractional overdensity, R is the smoothing scale, and the subscripts g and m denote galaxies and dark matter, respectively. These parameters have not been studied observationally as a result of the difficulty in obtaining a reliable estimate of δ_m. Chapter 2 describes several alternative galaxy bias techniques, which were tested and applied to data in chapters 3 and 4. In contrast to the methods described previously, a local comparison study measures a cross-correlation coefficient that is bounded between anti-correlation and perfect correlation $-1 < r(R) < 1$.

In this chapter I describe a concept study of local galaxy bias methods, for which I look at a more traditional approach as well as a new technique. In Section 5.1 previous galaxy dark matter comparisons are discussed. The methods are introduced in Section 5.2 and tested in Section 5.4 on mock data, described in Section 5.3.

5.1 Introduction

Mass reconstruction techniques, traditionally used for galaxy clusters, are becoming increasingly popular to map out the large-scale structure (Massey et al., 2007; Van Waerbeke et al., 2013), opening up the possibility to study galaxy bias locally.

The first local comparison of galaxies and dark matter was presented by Wilson et al. (2001). They compared the convergence field κ, derived from the source ellipticities, to that predicted from the galaxy number density κ_g. A peak was found to be present in both κ and κ_g, significant at 5.2 σ relative to a random distribution of galaxies, providing strong evidence that galaxies trace mass.

Fig. 5.1 is taken from Massey et al. (2007), which compares the mass reconstruction from the COSMOS survey to the projected number density of galaxies. The survey spans 1.64 deg^2 and is very deep with a broad lensing sensitivity that peaks at $z = 0.4$. They quote a cross-correlation coefficient of $r = 0.42$ for galaxies and dark matter, but without an uncertainty estimate or smoothing length[1], so it is not clear how to interpret this measurement. Massey et al. (2007) also imaged the 3D matter distribution with the idea of Taylor (2001), using distance information from the sources to relate the shear pattern to the 3D gravitational potential.

Van Waerbeke et al. (2013) present a much larger dark matter map of 154 deg^2 from CFHTLenS, see Figure 5.2, showing the convergence contours as well as the prediction of peaks in the map based on the foreground galaxy distribution, where the circle size is proportional to the peak height. Based on several maps like Figure 5.2 it is concluded that galaxies and mass are strongly correlated. An analysis like Wilson et al. (2001) would quantify the significance of this statement,

[1]The smoothing scale is not quoted but the angular resolution of 1.2′ and effective redshift of $z = 0.7$ indicate $R \approx 0.9$ Mpc.

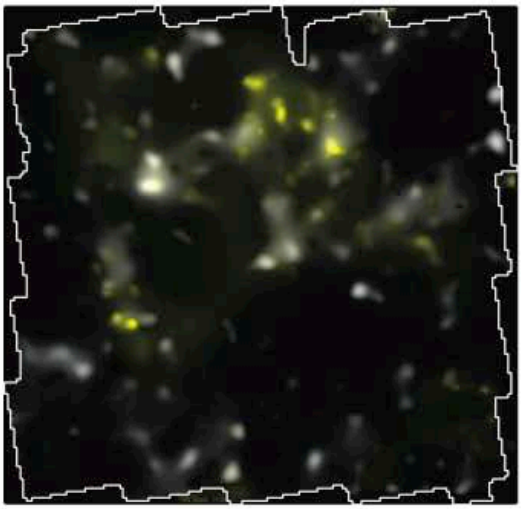

Figure 5.1 *Taken from Massey et al. (2007), showing a comparison between the convergence map (grey) and projected galaxy number density (yellow) from the COSMOS survey.*

without which it is difficult to read the visual comparisons[2].

Mass reconstruction of the large-scale structure is at an early stage, but has yielded encouraging results. With next generation surveys it will become an important tool for cosmology, providing detailed comparisons with structures in other wavelengths, such as those from the CMB and SZ or X-ray selected galaxy clusters, see Section 1.2. In this chapter I consider the possibility of using mass reconstruction for the purpose of measuring galaxy bias parameters $b(R)$ and $r(R)$.

5.2 Shear and Density Galaxy Bias Methods

In deriving the convergence field from the source ellipticities we obtain a noisy estimate of the convergence field $\kappa_{\rm obs}$, which can be written as

$$\kappa_{\rm obs} = \kappa_{\rm lensing} + \kappa_{\rm noise} \tag{5.3}$$

[2]The choice of contour colours in Figure 5.2 is such that the convergence becomes brighter with increasing density, whereas white is the colour of the galaxy peaks. For example, one of the highest convergence peaks at $[02^h14', -3°24']$ has no galaxy overdensity at the centre, while the colouring makes it appear as if there is.

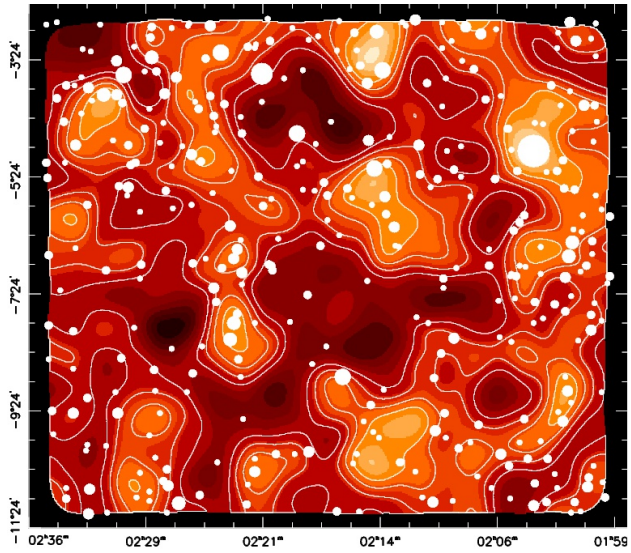

Figure 5.2 *Taken from Van Waerbeke et al. (2013), showing a comparison between the convergence map (contours) from CFHTLenS. Also shown are peaks in the convergence predicted from the galaxy overdensity, in an attempt to show the correlation between galaxies and matter.*

(e.g. Lombardi et al., 2002; Schmidt and Rozo, 2011; van Waerbeke, 2000) Intrinsic shape noise of background galaxies is the dominant contributor in $\kappa_{\rm noise}$ and contaminates $\kappa_{\rm obs}$. It has to be dealt with in order to separate out the lensing signal, so that reliable bias parameters can be obtained. The presence of holes in the data leads to further artificial structure in the convergence maps, but can be treated with a maximum likelihood analysis in which the gaps are taken into account (Bartelmann et al., 1996). Several algorithms for mass reconstruction have been developed, which have been shown to yield similar but still different outcomes (e.g. Jullo et al., 2014).

As well as considering galaxy bias from δ_g and the reconstructed δ_m field, an alternative method is proposed here, which deals with noise differently. Instead of deriving the matter distribution from the shapes of background galaxies, the shear pattern of background galaxies is predicted from the distribution of foreground galaxies. The galaxy bias parameters can then be cast in terms of the observed shear field together with its foreground prediction. Hence, this method does not modify the shear field, but instead transforms the galaxy number density. The steps are described below.

5.2.1 Shear-Density Transformations

Kaiser and Squires (1993) provide a formalism to relate density and shear fields. For the shear method, henceforth γ-method, the expected shear γ_g induced on background galaxies is calculated based on the spatial distribution of foreground galaxies. As a result of galaxy bias, γ_g is biased with respect to the true shear field γ_m. A comparison between γ_g and γ_m will provide information about galaxy bias, similar to the δ-method, which measures galaxy bias from δ_g and δ_m.

In cosmic weak lensing the 2D convergence is the averaged 3D density integrated over the source redshift probability function $p_b(z)$ from the observer out to infinity. Before predicting the biased shear field γ_m, we first need to predict the convergence based on the distribution of foreground galaxies. We give this quantity the symbol κ_g to distinguish it from the true convergence field and use the same relation between κ and δ_m, see Equation (1.73), to write

$$\kappa_g(\boldsymbol{\theta}) = \frac{3H_0^2\Omega_m}{2c^2}\int_0^\infty \mathrm{d}w g(w) f_K(w) \frac{\delta_g[f_K(w)\boldsymbol{\theta}, w]}{a(w)}, \tag{5.4}$$

where H_0 is the present day hubble constant, Ω_m the cosmic matter density, c the speed of light, w the comoving distance, f_K the comoving angular diameter distance, a the scale factor, and $g(w)$ is the lensing weight function, see Equation (1.72).

The 3D galaxy density information, required for κ_g, can be estimated from the projected 2D density field δ_g^{2D} and $p_f(z)$, the redshift distribution of the lenses, by substituting $\delta_g[f_K(w)\boldsymbol{\theta}, w]$ with $p_f(w)\delta_g^{\mathrm{2D}}(\boldsymbol{\theta})$ in Equation (5.4). Hence, the predicted convergence field κ_g is directly proportional to δ_g

$$\kappa_g(\boldsymbol{\theta}) = F_{\delta\kappa}\, \delta_g^{\mathrm{2D}}(\boldsymbol{\theta}), \tag{5.5}$$

where $F_{\delta\kappa}$ is defined as

$$F_{\delta\kappa} \equiv \frac{3H_0^2\Omega_m}{2c^2}\int_0^\infty \mathrm{d}w g(w) f_K(w) \frac{p_f(w)}{a(w)}. \tag{5.6}$$

The fake shear field γ_g is predicted from κ_g, such that, if galaxies are unbiased tracers of the total matter distribution, the shear prediction corresponds exactly with the observed shear field. The (biased) shear field γ_g can be predicted as

follows

$$\gamma_g(\theta) = \frac{1}{\pi}\int \mathcal{D}(\theta-\theta')\kappa_g(\theta')\mathrm{d}^2\theta' \tag{5.7}$$

$$= \frac{F_{\delta\kappa}}{\pi}\int \mathcal{D}(\theta-\theta')\delta_g^{2D}(\theta')\mathrm{d}^2\theta', \tag{5.8}$$

where the kernel $\mathcal{D}$ is given by

$$\mathcal{D}(x) = \frac{1}{(x^*)^2}. \tag{5.9}$$

The shear is a spin-2 field. We use the complex shear parameterisation

$$\gamma = \gamma_1 + \gamma_2 i = |\gamma|e^{2i\phi}, \tag{5.10}$$

where $|\gamma|$ is the amplitude and ϕ the orientation. The γ_g field can be regarded as a biased shear field, since it is calculated from the foreground galaxies, which are biased tracers of the matter density. Therefore, galaxy bias properties can be derived from comparing γ_g to the observed shear field, which will be discussed in Section 5.2.2.

The integral in 5.7 is difficult to solve as a result of the singularity induced by the kernel $\mathcal{D}(x)$. Therefore, the calculation of $\gamma_g(\theta)$ is performed in Fourier space, which is outlined in Kaiser and Squires (1993). The steps are as follows

1. Fourier transform κ_g to obtain $\hat{\kappa}_g$.
2. Calculate ellipticity parameters from the convergence (Kaiser and Squires, 1993)

$$\hat{\gamma}_1 = \frac{k_x^2 - k_y^2}{k^2} \times \hat{\kappa}_g \tag{5.11}$$

$$\hat{\gamma}_2 = \frac{2k_xk_y}{k^2} \times \hat{\kappa}_g, \tag{5.12}$$

   where k_x and k_y are the wavenumbers in the direction of x and y, respectively, and $k^2 = k_x^2 + k_y^2$.
3. Fourier transform $\hat{e}_i$ to obtain the ellipticity parameters γ_i (where $i = 1, 2$).

From Equations (5.11) and (5.12) it can be seen that the convergence field can be obtained from either γ_1 or γ_2. Kaiser and Squires (1993) propose the following

combination

$$\hat{\kappa} = -\frac{k_x^2 - k_y^2}{k^2}\hat{\gamma}_1 - \frac{2k_x k_y}{k^2}\hat{\gamma}_2, \tag{5.13}$$

making use of both γ_1 and γ_2.

5.2.2 Local Galaxy Bias Parameters

The two observables in this analysis are δ_g, the number density contrast of foreground galaxies, and γ_m,the shear field sampled by the source galaxies. With Equations (5.11) - (5.13) we can obtain estimates of δ_m and γ_g. Hence, galaxy bias can be measured from local comparisons of these quantities.

The galaxy bias parameters for the δ-method are given in Equations (5.1) and (5.2). The shear galaxy bias parameters of the γ-method are defined as

$$b(R) \equiv \sqrt{\frac{\langle|\gamma_g|^2\rangle}{\langle|\gamma_m|^2\rangle}} \tag{5.14}$$

$$r(R) \equiv \frac{\Re\left[\langle\gamma_m\gamma_g^*\rangle\right]}{\sqrt{\langle|\gamma_m|^2\rangle\langle|\gamma_g|^2\rangle}}, \tag{5.15}$$

similar to Equations (5.1) and (5.2). The numerator in Equation (5.15) was chosen to have real $r(R)$ from complex shear fields, while having $r_{AB} = r_{BA}$, since $\Re\left[\langle\gamma_m\gamma_g^*\rangle\right] = \Re\left[\langle\gamma_g\gamma_m^*\rangle\right]$. The smoothing length depends on the type of filter used, for which we choose a simple averaging over squares: first, the field is divided into square cells of size R, defined as the length of the square sides, and second, the average of the shear or density in the square cell gives $\gamma(R)$ or $\delta(R)$. Note that the shear field is a spin-2 vector field, unlike the scalar density field. In principle, however, the two methods should recover the same galaxy bias parameters.

5.3 Mock Data

Mock data was constructed from the clone project simulations, described in Section 3.1. The background galaxies were sampled from realisations at output $0.55 < z < 0.62$. The corresponding lensing kernel, see Equation (2.59), peaks at a redshift of $z = 0.3$. The distribution of foreground galaxies was constructed to

match the lensing kernel, see Figure 5.3. With this set-up cosmological corrections are not required. With real data, however, the observed shear pattern γ_m probes a different volume than that corresponding to the lenses. Therefore, the galaxy bias measurement involves cosmological calibration factors, similar to the aperture galaxy bias.

Since the predicted shear field γ_g is derived from the foreground galaxies δ_g, the uncertainty in γ_g depends on the number density of foreground galaxies δ_g. By selecting N galaxies at random from the smooth clone density field we study the influence of shot noise. The uncertainty in γ_m is dominated by the variance in the intrinsic (unlensed) shapes, see Section 3.2.4, which we simulate by adding Gaussian noise to the ellipticities of the mock shear field γ_m, using Equation (3.14) with ellipticity variance $\sigma_e^2 = (0.279)^2$, unless noted otherwise.

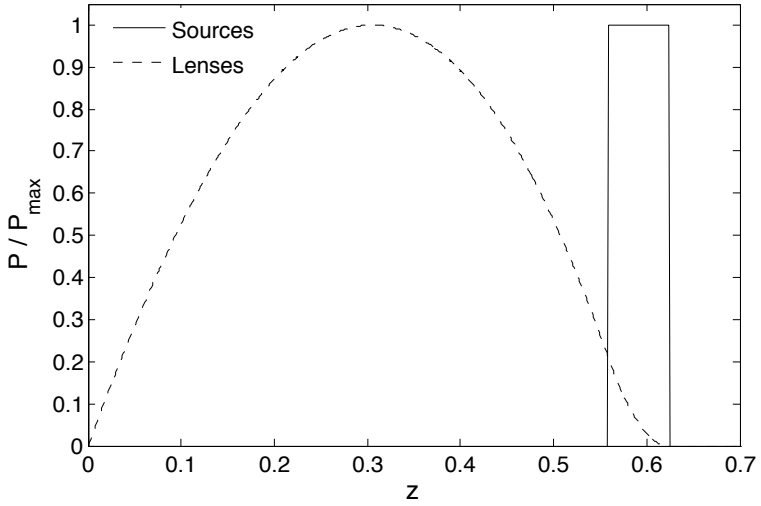

Figure 5.3 *The probability distribution of lenses and sources. The lens distribution was matched to the lensing kernel.*

The clone realisation area is 12.85 deg^2, which is too small for exact transformations between γ and δ fields, see Section 3.1. This is reflected in the nonzero means of the lensing and clustering fields, while in theory they should be zero. The standard deviations of the κ and γ fields are typically a factor of ~ 10 greater than the mean, which are on the order of $\sim 0.1 \times 10^{-2}$ for the κ and γ_m fields.

Furthermore, the simulation output of the clones is such that the shear and density fields cover the same area, whereas the shear field is sensitive to the density outside the provided box. Therefore, we do not have sufficient information to provide exact predictions of the shear fields from the clone κ output, and the same applies to the transformation from γ to κ.

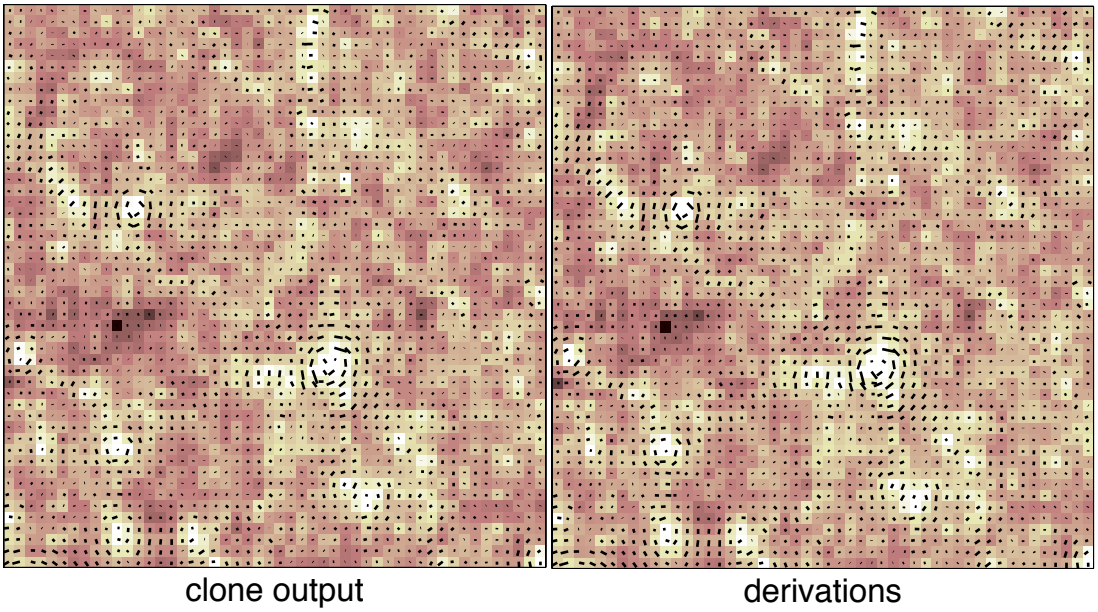

Figure 5.4 *Comparison of the clone γ_m and κ output (left) against the fields derived from the Kaiser and Squires (1993) method (right). The scalar κ field and spin-2 γ field to the left were derived from the γ and κ fields to the right, respectively. For plotting, the fields were smoothed by averaging over square cells of width 0.3 h^{-1} Mpc.*

The left panel of Figure 5.4 shows the γ_m and κ fields from clone realisation LOS18. The fields in the right panel were derived from the clone output in the left panel. The sticks show the spin-2 shear fields, which form circular patterns around overdensities with increased length. Careful inspection shows minor differences, which lead to significant offsets in the measurement of $b(R)$ from both methods. The cross-correlation coefficient is much closer to unity, since this quantity is not sensitive to an amplitude difference in the fields.

From the clone comparisons I conclude that the algorithm is working correctly, but that, in reality, larger fields will be required in order to include the influence of large-scale modes on the transformations. Van Waerbeke et al. (2013) also stressed the importance of large-scale shear patterns on the derivation of the convergence field. They argue that the COSMOS field, used by Massey et al. (2007), is too small for accurate mass reconstructions of the cosmological density field.

For the concept study it is undesirable to be affected by uncontrollable factors, which vary with every clone realisation. Therefore, mock shear fields are generated by transforming the clone density fields to shear fields using the Kaiser and Squires (1993) formalism. After applying shape noise to the new shear field

with $\sigma_e = 0.279$, see Equation (3.14) in Section 3.2.4, the result is treated as the observed shear field γ_m, instead of using the clone shear fields.

5.4 Results

In this section the δ-method and γ-method, described in Section 5.2, are applied to mock data, described in Section 5.3. The δ-method measures $b(R)$ and $r(R)$, see Equations (5.1) and (5.2), from δ_g and δ_m, obtained from the galaxy number density and the Kaiser and Squires (1993) formalism, respectively. With the γ-method we measure $b(R)$ and $r(R)$ from Equations (5.14) and (5.15), which quantify the relative difference of galaxy and dark matter distributions from a comparison of the observed shear pattern γ_m and the shear prediction γ_g, based on the foreground distribution of galaxies.

Figure 5.5 shows the inaccuracy in recovering bias parameters when comparing the clone output to the derived fields, such as those shown in Figure 5.4. I used 10 LOS for this figure, showing the mean and the error on the mean for b (left) and r (right). The numerator in the bias parameters is the transformed field (e.g. the right panel of Figure 5.4); the clone output is in the denominator (e.g. the left panel of Figure 5.4). For the lower panels of Figure 5.5 a mean correction was applied, $\gamma_{\rm new} = \gamma - \langle\gamma\rangle$ and $\delta_{\rm new} = \delta - \langle\delta\rangle$, improving the recovery of b and r significantly, but not completely. A possible cause for the remaining discrepancy at large-scales is the fact that the shear is affected by the density outside the box, which information is not provided. For the comparison in Figure 5.5 I discarded the outer 10% of the fields, which provided a marginal improvement. Henceforth, the mock shear observables γ_m are constructed by transforming the clone κ fields, instead of using the clone shear fields directly.

In Figure 5.6 the galaxy bias parameters from both methods are shown for a case where the number density of lenses is 13 arcmin^{-2}, and the intrinsic galaxy shapes have a variance of $\sigma_e^2 = (0.279)^2$. The number density of sources is set by the number of grid cells before smoothing, giving 20 arcmin^{-2}. Apart from redshift distributions and the higher source number density, this scenario corresponds to a CFHTLenS like survey. Error bars were derived from 10 noise realisations. The input galaxy bias was constructed from the second order bias model, given in Equation (2.6), with $b_1 = 0.8$ and $b_2 = 0.1$, shown as the dashed lines. The bias b is systematically too high but follows the scale-dependence of the input model.

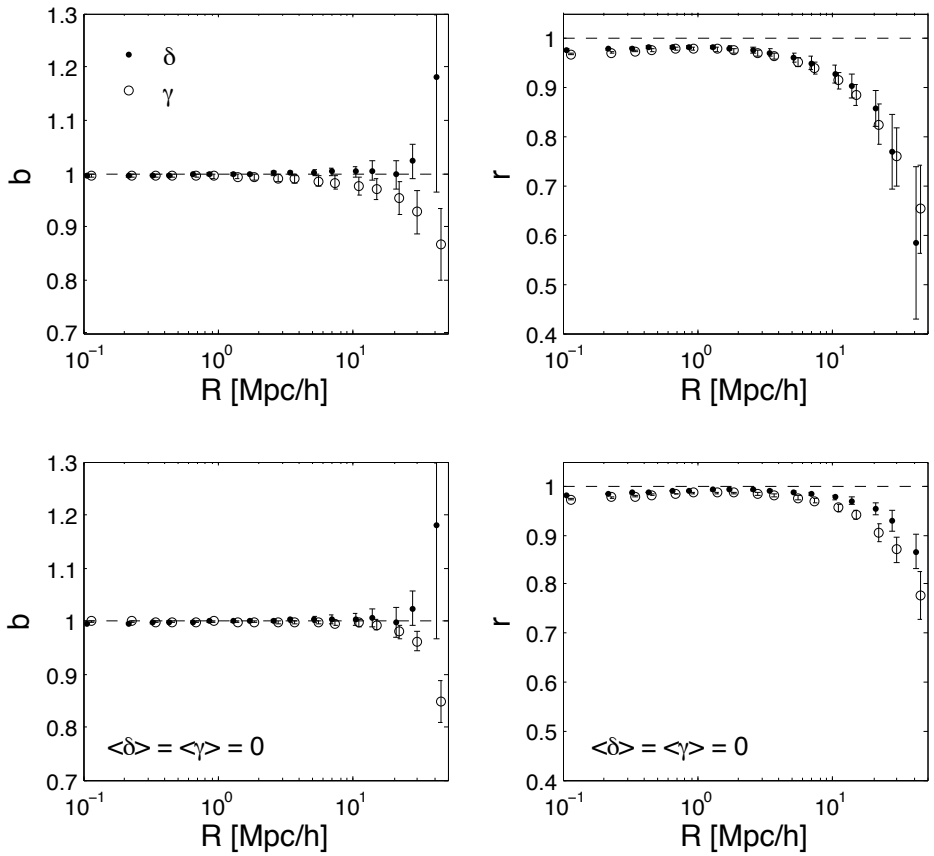

Figure 5.5 *The bias parameters b (left) and r (right) from the clones, using the δ-method (dots) and γ-method (open circles, offset for clarity). For the lower panels the shear and delta fields were modified to have zero mean.*

The disagreement with the input model r is less at larger smoothing lengths.

Intrinsic shape noise is the main challenge for the local galaxy bias methods. Figure 5.7 shows b and r from both methods as a function of intrinsic shape variance σ_e for a smoothing length of $R = 37$ Mpc/h. The mock configuration is the same as for Figure 5.6, except for the bias model, which is here $b = r = 1$. It is encouraging to see that shape noise cancels almost entirely for r at large smoothing lengths. However, the estimates of b are significantly affected by shape noise across all scales. The noise cannot simply be subtracted, since the exact noise field is unknown. However, simulations can calibrate the combined effect of shape noise and galaxy number densities.

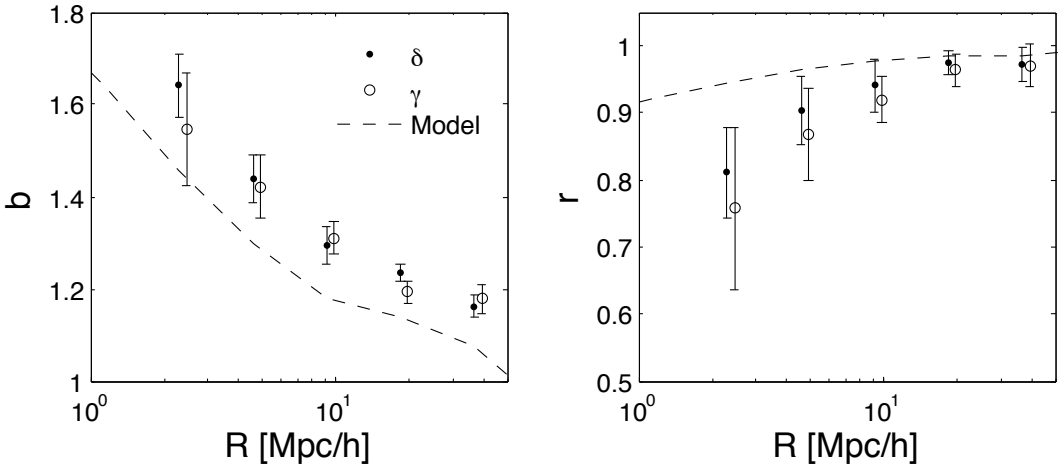

Figure 5.6 *Galaxy bias parameters b (left) and r (right) from the δ-method (dots) and γ-method (circles). A biased field was constructed from the second order bias expansion in Equation* (2.6) *with* $b_1 = 0.8$ *and* $b_2 = 0.1$*. The model line was constructed by applying the bias model to a clone dark matter field without any noise and measure* $b(R)$ *and* $r(R)$*. Error bars were derived from 50 mock realisations with CFHTLenS like properties: the lens (source) number density was set to 13 (20)* $arcmin^{-2}$ *and intrinsic shape noise was applied to the source ellipticities with* $\sigma_e = 0.279$*.*

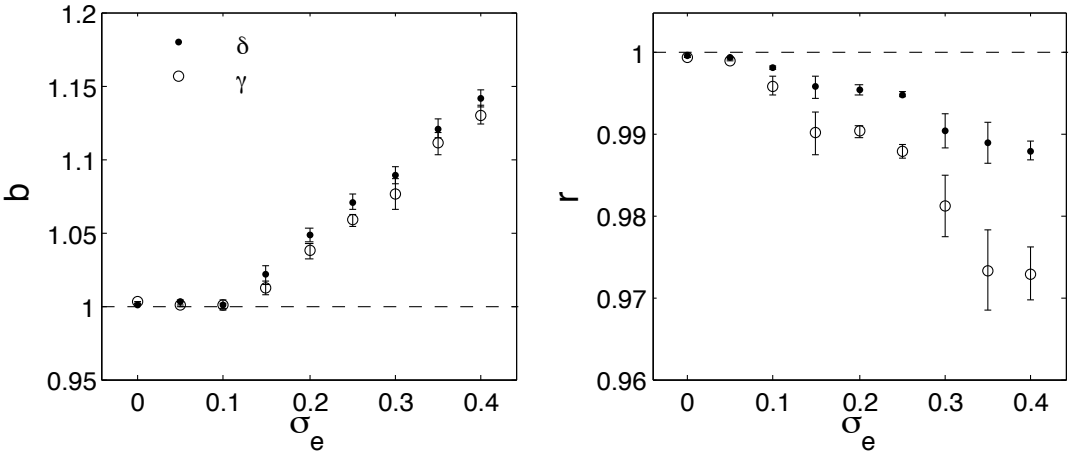

Figure 5.7 *The influence of intrinsic shape noise on the bias parameters b (left) and r (right). The bias was set to* $b = 1$*, and the smoothing length is* $R = 37h^{-1}Mpc$*. The data points are derived by taking the average of 10 mock realisations, also showing the error on the mean.*

5.5 Discussion and Conclusion

With future surveys mass reconstructions become sufficiently accurate to study galaxy bias from local comparisons. The large-scale distribution of dark matter

in space has been mapped by, most notably, Van Waerbeke et al. (2013), but the results were argued to be too noisy for studying galaxy bias properties.

In this chapter I have studied the possibility of obtaining local galaxy bias parameters from mass reconstruction and shear prediction, denoted δ-method and γ-method, respectively. In the δ-method the observed shear γ_m is used to estimate δ_m, which is compared to the fractional overdensity of galaxies δ_g. The γ-method compares the observed shear pattern γ_m to γ_g, the prediction of the shear based on δ_g. Since δ_g is subject to galaxy bias, the shear prediction is similarly biased, so that we can extract the galaxy bias parameters $b(R)$ and $r(R)$.

The choice of redshift distributions was such that no cosmological calibration factors were required. For real data cosmological corrections have to be calculated, similar to the aperture bias method. Apart from redshift distributions and the absence of masks in our analysis, a mock configuration similar to a CFHTLenS survey was tested. Intrinsic shape noise was found to be the dominant source of systematic, accounting for a $\sim 10\%$ positive offset in b. Although not ideal, this can be calibrated with mock surveys.

Although the two methods yield very similar results, shape noise introduces noticeable differences. From Figures 5.6 and 5.7 it can be seen that the galaxy bias b from the γ-method is slightly less affected by shape noise, while r from the δ method is better behaved. Since the δ-method and γ-method complement each other, no method is preferred.

The galaxy bias parameters were estimated from taking ratios of noisy quantities, which introduces a systematic offset, as was discussed in Section 3.4.3. This can be solved by constraining the difference in galaxy and dark matter fields by minimising the χ^2 statistic, Equation (3.32), using a model for the galaxy field, such as the local bias expansion (2.3). Furthermore, with a real survey a minimum χ^2 fitting or likelihood analysis is preferential, since it also takes into account masks.

Although r cannot be constrained in a similar way, it can be estimated by including higher order bias terms, see e.g. Equation (2.12), noting that this excludes the contribution from stochasticity. This does, however, allow us to investigate stochasticity by comparing r obtained from ratios against r inferred from a minimum χ^2 fit.

The possibility of investigating stochasticity is only one example of the many interesting galaxy bias properties that can be investigated with accurate transformations of δ and γ fields. For instance, this approach can be used to determine a density-dependent bias model, which is impossible with conventional methods based on 2-point statistics. Furthermore, the density and shear fields can be clipped (Simpson et al., 2011), suppressing the influence of rare high density peaks. We can also work in the opposite direction in order to investigate how correlated peaks in the galaxy and dark matter density are. Additionally, the density and shear fields can be Fourier transformed to measure galaxy bias parameters in terms of power spectra, allowing estimates of $b(k)$ and $r(k)$, defined in Equations (2.16) and (2.17). For future surveys, the analysis can in principle be performed in 3D space (Taylor, 2001). To conclude, a local study of galaxy bias requires high quality data, but would provide a wealth of information about galaxy formation and cosmological density fields.

Chapter 6

Evolution of the Galaxy Cluster X-Ray Luminosity Function

The focus of this thesis is on the relative distributions of galaxies and dark matter. Although in this chapter we again focus on the use of tracers to understand structure formation and evolution, it is based on X-ray selected galaxy clusters, quite different from the previous chapters.

I present measurements of the galaxy cluster X-ray Luminosity Function (XLF) from the Wide Angle ROSAT Pointed Survey (WARPS) and quantify its evolution. WARPS is a serendipitous survey of the central region of ROSAT pointed observations and was carried out in two phases (WARPS-I and WARPS-II). The results here are based on a final sample of 124 clusters, complete above a flux limit of 6.5×10^{-14} erg cm^{-2} s^{-1}, with members out to redshift $z \sim 1.05$, and a sky coverage of 70.9 deg^2. We find significant evidence for negative evolution of the XLF, which complements the majority of X-ray cluster surveys. To quantify the suggested evolution, we perform a maximum likelihood analysis and conclude that the evolution is driven by a decreasing number density of high luminosity clusters with redshift, while the bulk of the cluster population remains nearly unchanged out to redshift $z \approx 1.1$, as expected in a low density Universe. The results are found to be insensitive to a variety of sources of systematic uncertainty that affect the measurement of the XLF and determination of the survey selection function. We perform a Bayesian analysis of the XLF to fully account for uncertainties in the local XLF on the measured evolution, and find that the detected evolution remains significant at the 95% level. We observe a

significant excess of clusters in the WARPS at $0.1 < z < 0.3$ and $L_X \approx 2 \times 10^{43}$ erg s^{-1} compared with the reference low-redshift XLF, or our Bayesian fit to the WARPS data. We find that the excess cannot be explained by sample variance, or Eddington bias, and is unlikely to be due to problems with the survey selection function.

Part of the work presented here has already been published for the degree of MSc, supervised by Dr. Ben Maughan and Prof. Steve Phillipps, at the University of Bristol. However, substantial work was carried out during my time as a PhD student, in order for the work to reach a sufficient standard for publication. The work (Koens et al., 2013) is published in Monthly Notices of the Royal Astronomical Society: MNRAS (November 11, 2013) Vol. 435 3231-3242.

The publication, which was written and submitted during my time as a PhD student, is printed here in verbatim along with a detailed description of new versus old work for each section, see Table 6.1. It is sometimes difficult to divide between the two, since in many ways it was an improvement upon previous work, without having to write original scripts, only updates. Therefore I have added notes for clarification. In the table I regard anything as old in the case that the majority of the work was completed for the MSc degree, but use (✓) to account for significant update work and add notes to clarify. The research was mostly carried out by myself, but it should be noted it was done in collaboration with the full WARPS team. However, as lead author I was involved in the entire process that lead to the publication.

Table 6.1 *MSc versus PhD*

Section	MSc	PhD	Notes
1.	✓		
2.	✓	(✓)	REFLEX data included in Figure1 for publ.
3.	✓		
3.1	✓		
3.2	✓	(✓)	Fig. 5 updated with cosmological framework
3.3		✓	
4.		✓	
4.1		✓	4.1.3 is mainly by B. Maughan (2nd author) 4.1.4 is mainly by S. Phillipps (collaborator)
4.2		✓	
4.3		✓	
5.	(✓)	✓	Conclusions mostly based on PhD work
App.	✓	(✓)	Results updated with cosmological framework

6.1 Introduction

Evolutionary properties of gravitationally bound objects in the universe are described by models of structure formation. The currently favoured cosmology (flat ΛCDM) predicts little change in the abundance of galaxy clusters at late times when the energy density of the universe becomes dominated by Ω_Λ. The evolution of cluster abundance depends on the growth rate f, which is mainly sensitive to the mean cosmic matter density Ω_m as $f(z) \simeq \Omega_m(z)^\gamma$, where $\gamma \simeq 0.6$ in a Universe described by General Relativity (Linder, 2005).

Galaxy clusters, the largest objects to have decoupled from the Hubble expansion, are particularly interesting for studying these properties as a result of their X-ray brightness. The X-ray emission is the result of bremsstrahlung emitted by the hot intracluster medium ($10^7 - 10^8$K) which contributes more than 80% of the baryonic content of the cluster. Therefore, the mass of a cluster can be estimated from its luminosity with the use of scaling relations and some simplifying assumptions (Kaiser, 1986). The X-ray emitting gas has enabled cluster detections out to high redshift ($z \gtrsim 1$). Hence, X-ray galaxy cluster surveys potentially cover a significant portion of the evolution history of clusters and have high statistical completeness, thus providing the leverage to place tight

cosmological constraints (e.g. Borgani et al., 1999; Mantz et al., 2010; Schuecker et al., 2003; Vikhlinin et al., 2009).

Early predictions of evolution in the number density of clusters, e.g. Kaiser (1986), pointed towards strong positive evolution – an increase in the number density of clusters with redshift. This prediction assumes a matter power spectrum with a power-law form, and that the heating of gas is solely by adiabatic compression during the collapse of dark matter halos. The first opportunity to test these predictions came with the Einstein Medium Sensitivity Survey (EMSS Gioia et al., 1990b), which detected clusters out to $z \approx 0.8$. Contrary to the theoretical prediction, the first teams to test for evolution in the XLF found strong negative evolution (Edge et al., 1990; Gioia et al., 1990a; Henry et al., 1992). These controversial findings heated the debate and together with the launch of the ROSAT X-ray observatory gave rise to a flurry of attempts to measure evolution in the XLF, with some later analyses raising concerns over the Einstein results (e.g. Ellis and Jones, 2002).

ROSAT performed an all-sky survey which was used to construct large flux limited cluster samples, from which the local cluster XLF was accurately determined. There are three such surveys: the Brightest Cluster Sample (Ebeling et al., 2000, 1998), the ROSAT All-Sky Survey 1 Brightest Sample (De Grandi et al., 1999), and the ROSAT-ESO Flux-Limited X-ray (REFLEX) galaxy cluster survey (Böhringer et al., 2001). These local XLFs act as the crucial baseline for quantifying evolution in deeper surveys.

Once the ROSAT all-sky survey was completed the observatory remained available for pointed observations, which has resulted in an extensive archive of deep observations, providing the ingredients for many serendipitous X-ray cluster surveys. This includes the Wide Angle ROSAT Pointed Survey (Horner et al., 2008; Perlman et al., 2002; Scharf et al., 1997), the subject of this paper. Similar surveys that probe the X-ray universe out to high redshift include the ROSAT International X-ray/Optical Survey (RIXOS Castander et al., 1995; Mason et al., 2000), the ROSAT Deep Cluster Survey (RDCS Rosati et al., 1995, 1998), the Bright Serendipitous High-Redshift Archival ROSAT Cluster (BSHARC) Survey (Romer et al., 2000), the Massive Cluster Survey (MACS) (Ebeling et al., 2001), the Brera Multi-scale Wavelet ROSAT HRI (BMW-HRI) survey (Moretti et al., 2001; Panzera et al., 2003) ROSAT North Ecliptic Pole (NEP) Survey (Gioia et al., 2001; Henry et al., 2001), SSHARC (Burke et al., 2003), and the 160 Square Degree (160SD Mullis et al., 2003, 2004; Vikhlinin et al., 1998), extended

to the 400 Square Degree (400SD) survey (Burenin et al., 2007).

XMM-Newton archival data is also used for surveys based on serendipitous cluster detections. Currently in progress are the XMM Cluster Survey (XCS Mehrtens et al., 2012), the XMM-Newton Distant Cluster Project (XDCP Fassbender et al., 2011), and the XMM-Newton eXtra eXtra Large (XXL) Survey (Pierre et al., 2011). One serendipitous galaxy cluster survey is based on Chandra archival data and is part of the Chandra Multiwavelength Project (CHaMP Barkhouse et al., 2006).

The most recent determination of the XLF was performed by Mullis et al. (2004) using 201 clusters from the 160SD catalogue. This work found significant evidence for negative evolution of the XLF at the bright end. That is, the number density of high luminosity clusters was lower at $0.6 < z < 0.8$ than in the local Universe. Meanwhile Mantz et al. (2008) used the XLF of several ROSAT cluster surveys at $z < 0.5$ to measure the cluster mass function and hence constrain cosmological parameters.

In this paper we investigate the evolution of the XLF of a sample of 124 WARPS galaxy clusters detected above a flux limit of 6.5×10^{-14} erg cm^{-2} s^{-1} over a total area of 70.9 deg^2, and covering a wide redshift range ($0.02 < z < 1.10$). The survey design was outlined in Scharf et al. (1997) and the catalogues are presented in two separate papers: WARPS-I (Perlman et al., 2002) and WARPS-II (Horner et al., 2008). The evolution of the WARPS galaxy clusters has previously been investigated using phase-I of the survey. Jones et al. (1998) found no significant evolution in the $\log N - \log S$ relation from the WARPS-I sample and a preliminary measurement of the XLF (constructed when the survey was complete for $z < 0.85$) was also found to be consistent with no evolution (Jones et al., 2000).

This work represents a useful cross-check and extension of the Mullis et al. (2004) results. While the WARPS survey covers a smaller area, it is deeper; the 160SD XLF extends to $z \approx 0.7$. Importantly, while both surveys are drawn from ROSAT pointed observations, the cluster detection and confirmation strategies differ significantly, allowing us to assess the sensitivity of the evolution results to those factors.

The current paper is organised as follows: §2 briefly reviews the WARPS survey and the combined WARPS-I + WARPS-II sample. The selection function of the full survey is presented for the first time. In §3 the X-ray Luminosity function is presented for different redshift ranges. Subsequently, in §4 a maximum likelihood

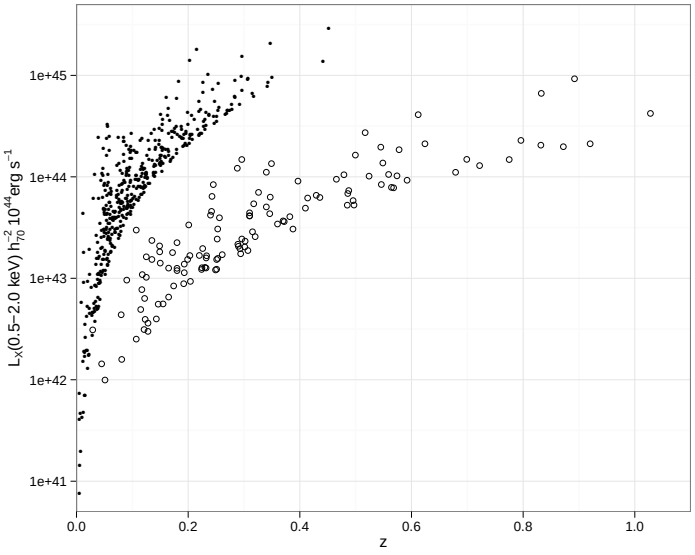

Figure 6.1 *The WARPS clusters (hollow points) as points in the L_X-z plane. Also plotted is the REFLEX sample (solid points), which provides the low-redshift reference XLF for this study (Böhringer et al., 2001).*

analysis robustly assesses evolution in the XLF. In §5 and §6 we discuss our results and summarise our conclusions. Throughout the paper errors are quoted at the 68% confidence level and a ΛCDM cosmology of $H_0 = 70\,h_{70}$ km s^{-1} Mpc^{-1}, $\Omega_m = 0.3$, and $\Omega_\Lambda = 0.7$, is adopted. All fluxes are corrected for absorption, and are quoted in the observer's frame $0.5 - 2$ keV band. Luminosities are converted to the rest frame $0.5 - 2$ keV band of each cluster.

6.2 The WARPS Cluster Sample

The survey is based entirely on serendipitous detections in ROSAT images from pointed observations with the Position Sensitive Proportional Counter (PSPC) instrument. Here we summarise the key facts and direct the reader to Scharf et al. (1997) for full details of the survey methodology.

PSPC fields were selected based on the following criteria. The fields are at a Galactic latitude of $|b| \geq 20°$, have exposure times of $t_{\rm exp} \geq 8$ks, are non-overlapping, and the original target is not a galaxy cluster or some other source such as a bright star that would hamper optical follow-up. Out of the ∼7000 fields in the HEASARC archive 381 satisfy the criteria.

Sources were detected with Voronoi Tessellation and Percolation (VTP) (Ebeling and Wiedenmann, 1993) in an annulus of inner radius 3 arcminutes and outer radius 15 arcminutes. VTP does not discriminate against shape or size and is particularly sensitive to sources of low surface brightness. WARPS has assessed the efficacy of VTP as a source detection algorithm by optically imaging all X-ray candidates in WARPS-I lacking counterparts on existing sky survey plates.

The completeness and efficiency of the VTP detection algorithm were established with simulations of azimuthally symmetrical clusters, inserted into PSPC fields.

The detected flux is extrapolated to infinite radius assuming a β profile. Although Chandra and XMM-Newton data have revealed significant substructure in cluster images up to $z \sim 1$, the relatively poor PSPC angular resolution means that the assumption of spherical symmetry is not expected to strongly affect the detection efficiency and flux estimation. This conclusion is supported by the good agreement between the WARPS and other ROSAT serendipitous surveys that used independent detection algorithms and selection functions (Horner et al., 2008, ; this work). Based on our simulations a statistically complete sample was defined, comprising 124 clusters above a conservative flux of 6.5×10^{-14} erg cm^{-2} s^{-1} (Horner et al., 2008) (145 sources were confirmed by WARPS).

For clusters in common, WARPS fluxes were found to be in reasonable agreement with those determined by other serendipitous ROSAT surveys (Horner et al., 2008). Spectroscopic redshifts were obtained for all clusters, with 2 or more concordant redshifts required to confirm a cluster. WARPS did not obtain near-infrared imaging of cluster candidates, placing an upper limit on the redshift out to which clusters can be detected. This limit is ~ 1.1, and the uncertainty arising from this is addressed in Section 6.4.1.

In combining WARPS-I and WARPS-II catalogues, it was found that background levels were missing for 1 WARPS-I field and 27 WARPS-II fields. The background level of each field is required in order to compute the selection function, and so these were remeasured from the archived PSPC data. The ROSAT PSPC data have been reprocessed since the cluster detection was performed, so we checked the background measurements for all WARPS-I fields using the currently available PSPC data against our original measurements. The new measurements were found to be $\sim 7\%$ lower on average, depending somewhat on the source detection algorithm used to exclude sources in each field. We thus renormalised the background measurements for the 28 missing fields in the combined WARPS

catalogue by this factor, for consistency with the data used for cluster detection. We investigated the impact of this systematic effect on the selection function, and found it to be insensitive to whether or not this background scaling was applied to the 28 missing fields. This is not surprising given the small magnitude of the correction and the small fraction of fields affected.

In Figure 6.1 the WARPS clusters are plotted in the luminosity-redshift plane. The fluxes of the clusters have been K-corrected to the cluster rest frame assuming an APEC thermal plasma model (Smith et al., 2001), for which we set the metallicity to 0.3 $Z_{\odot}$. The plasma temperature required for this conversion was estimated iteratively from the X-ray luminosity using the luminosity temperature scaling relation of Markevitch (1998), although the magnitude of the K-correction was insensitive to this choice.

The selection function for WARPS-I and WARPS-II combined is shown in Figure 6.2 and is based on 381 PSPC fields. The effective sky coverage for an object of given luminosity and extent is determined by the performance of VTP, the degrading PSF with off-axis angle, and the background levels and exposure times of the fields. The variance in the field properties of the survey alters the steepness of the decrease; e.g. if all the fields were the same, we expect a much more sudden drop from 100% to 0%. We find the curve for the full survey to be very similar to that for WARPS-I, figure 9 in Scharf et al. (1997).

6.3 The X-ray Luminosity Function

The X-ray Luminosity Function (XLF), conventionally given the symbol ϕ, is the comoving number density n of objects per luminosity interval:

$$\phi(L_{\rm X}, z) = \frac{{\rm d}n(L_{\rm X}, z)}{{\rm d}L_{\rm X}}. \tag{6.1}$$

The Schechter function (Schechter, 1976) is the canonical, parametric representation of the luminosity function:

$$\phi(L_{\rm X}, z){\rm d}L_{\rm X} = \phi^* \left(\frac{L_{\rm X}}{L^*_{\rm X}}\right)^{-\alpha} \exp\left(-\frac{L_{\rm X}}{L^*_{\rm X}}\right) \left(\frac{{\rm d}L_{\rm X}}{L^*_{\rm X}}\right), \tag{6.2}$$

where the parameter ϕ^* normalises the XLF, and α determines the steepness at $L_{\rm X} < L^*_{\rm X}$.

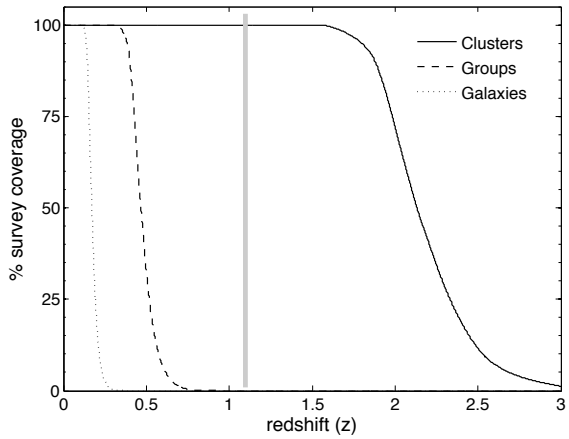

Figure 6.2 *Survey coverage for three classes of objects as a function of redshift. The objects are defined as: elliptical galaxies with* $L_X(0.5-2.0\ keV) = 1\times10^{42}$ *erg* s^{-1} *and effective core radius* $r_c = 50$ *kpc, groups with* $L_X(0.5-2.0\ keV) = 1\times10^{43}$ *erg* s^{-1} *and effective core radius* $r_c = 100$ *kpc, and clusters with* $L_X(0.5-2.0\ keV) = 5\times10^{44}$ *erg* s^{-1} *and effective core radius* $r_c = 250$ *kpc. The grey line represents the approximate upper redshift limit imposed by the lack of near infra-red follow-up of cluster candidates.*

The conventional method to compute the differential XLF is the $1/V_{\rm max}$ method (Avni and Bahcall, 1980; Schmidt, 1968), where $V_{\rm max}$ denotes the maximum co-moving volume, given by

$$V_{\rm max} = \int_{z_{\rm min}}^{z_{\rm max}} \Omega(f_{\rm X}, r_\theta) \frac{{\rm d}V(z)}{{\rm d}z} {\rm d}z, \tag{6.3}$$

where $\Omega(f_{\rm X}, r_\theta)$ is the sky coverage as a function of flux $f_{\rm X}(L_{\rm X}, z)$ and angular extent $r_\theta(r_c, z)$ (here r_c is the core radius of the cluster surface brightness distribution, conventionally parameterised with a β-model), and ${\rm d}V(z)/{\rm d}z$ is the differential, co-moving volume, which is strongly sensitive to the cosmological framework. The maximum co-moving volume is calculated for all N galaxy clusters. The XLF is then obtained by summing the corresponding density contributions per luminosity bin, that is

$$\phi(L_{{\rm X}_j}, z) = \frac{1}{\Delta L_{{\rm X}_j}} \sum_{i=0}^{N_j} \frac{1}{V_{{\rm max},i}}, \tag{6.4}$$

where the subscript j denotes the j-th bin. Due to the sensitivity to the choice of binning, the method is less ideal for quantifying evolution. However, it is a conventional way of presenting a sample of objects, so we include it here to allow easy comparisons with previous work.

Alternatively, Page and Carrera (2000) provide an estimate of ϕ, which expression is obtained by integrating (6.1) and noting that ϕ changes little compared to the survey volume element in the volume - luminosity plane, such that it can be taken out of the integral, giving

$$\phi(L_{\mathrm{X}_j}, z) = \frac{N_j}{\int_{L_{\mathrm{X,min}}}^{L_{\mathrm{X,max}}} \int_{z_{\mathrm{min}}}^{z_{\mathrm{max}}} \Omega(f_{\mathrm{X}}, r_\theta) \frac{\mathrm{d}V(z)}{\mathrm{d}z} \mathrm{d}z \mathrm{d}L_{\mathrm{X}}}, \tag{6.5}$$

where L_{X_j} is the bin centre and N_j is the number of clusters in the j-th bin.

We apply the method of Page and Carrera (2000) to account for the flux limit of the survey to effectively decrease the width of some of the bins, enhancing the XLF. The Page-Carrera estimator was also deployed by Mullis et al. (2004), who found a marginal increase at the faint end of the XLF compared to the V_{max} estimator. Our results were similarly insensitive to the choice of volume estimator; the uncertainties at the faint end of the XLF are dominated by those arising from small number statistics, the statistical error on f_X and the uncertainty on r_θ.

6.3.1 The WARPS XLF

In order to present the binned WARPS XLF, we divide the clusters according to their redshifts to study the local ($0.02 < z < 0.3$; 67 clusters), intermediate redshift ($0.3 < z < 0.6$; 44 clusters), and high redshift ($0.6 < z < 1.1$; 13 clusters) populations, similar to Mullis et al. (2004).

We apply the same L_{X} binning as Mullis et al. (2004) to allow for comparison. Poisson errors on the counts in each luminosity bin are provided by Gehrels (1986), which are much larger than the flux measurement errors.

Good knowledge of the local XLF is essential for studying its evolution and is provided with great accuracy by the ROSAT all-sky survey. The XLF of the local WARPS sample of 67 $0.02 < z < 0.3$ clusters is shown in Figure 6.3. The lower redshift limit is set to $z = 0.02$ below which many clusters become too extended relative to the size of the PSPC fields to be detected. Over this redshift range the WARPS XLF agrees remarkably well with the all-sky samples, represented by the REFLEX model in Figure 6.3.

There appears to be a high number density of clusters at $L_{\mathrm{X(0.5-2.0keV)}} \approx 1.5 \times 10^{43}$ erg s^{-1} compared to the Schechter function. We note that this feature is also

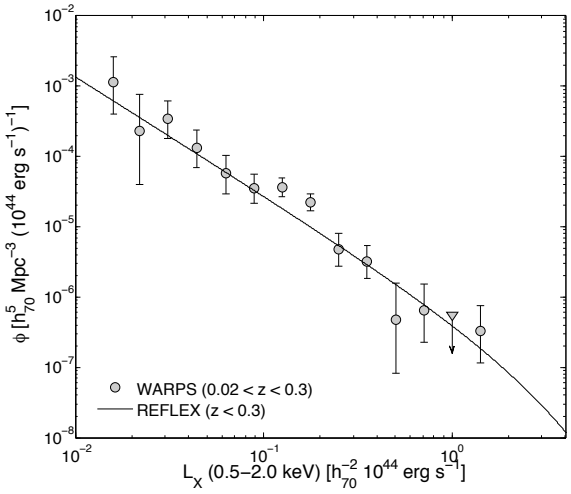

Figure 6.3 *The XLF from the local WARPS sample along with the best fit Schechter function of the REFLEX sample.*

present in the local XLF of the 160SD sample (Mullis et al., 2004, figure 4) We test the significance of this excess in section 6.3.2, and discuss possible interpretations in section 6.4.2.

In Figure 6.4 we show the intermediate and high redshift XLFs along with the local REFLEX Schechter function. The majority of data points of both the intermediate and high redshift XLF are slightly low compared to the local baseline. This is a first indication from the data of negative evolution. Whether this is significant will be addressed in the next section.

6.3.2 Expected Versus Observed Numbers

The expected number of objects in the luminosity-redshift plane is obtained by integrating equation (6.1)

$$N_{\rm exp} = \int_{L_{\rm X,min}}^{L_{\rm X,max}} \int_{z_{\rm min}}^{z_{\rm max}} \phi(L_{\rm X}, z)\Omega(f_{\rm X}, r_\theta)\frac{{\rm d}V(z)}{{\rm d}z}{\rm d}z{\rm d}L_{\rm X}. \qquad (6.6)$$

As mentioned in Section 6.3 the XLF changes little compared to the volume element. Hence we can predict the number of clusters for any of the WARPS subsets based on the local reference XLF $\phi_{\rm local}$, the observed XLF for the subset

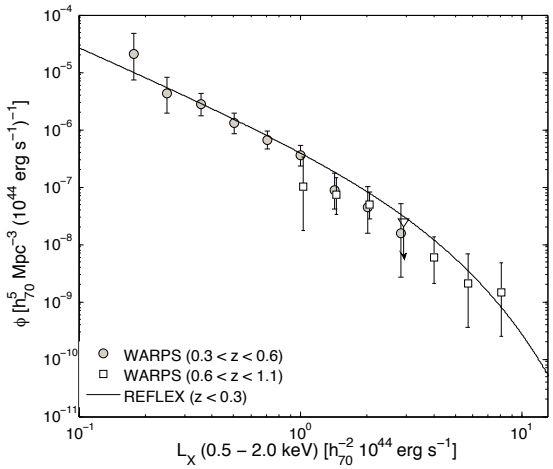

Figure 6.4 *The XLF from the intermediate and high redshift WARPS samples along with the best fit Schechter function of the REFLEX sample.*

$\phi_{\rm observed}$, and the number of clusters observed in that subset $N_{\rm observed}$:

$$N_{\rm exp} \approx N_{\rm observed} \times \frac{\phi_{\rm local}}{\phi_{\rm observed}}. \tag{6.7}$$

If the local reference XLF is a good description of the WARPS XLF, and there is no evolution, then $N_{\rm exp}$ should be consistent with $N_{\rm observed}$ for all subsets.

Using the REFLEX best fit Schechter function as the local reference, we compute the expected cluster numbers for each luminosity bin in each of the WARPS subsets. The results are plotted in figure 6.5. When integrated over the full range of luminosities, 60 clusters are expected from equation (6.7) for the low-z subset, instead of the 67 observed. For the intermediate-z subset, 67 are predicted instead of the 44 observed, and for the high redshift subset, the local relation predicts 36 clusters instead of the 13 that are observed. The differences for the low and intermediate redshift subsets are not strongly significant, but the lack of high-z clusters compared to the local prediction is significant at $> 4\sigma$, assuming Poisson errors on both numbers.

Figure 6.5 also illustrates the excess of clusters around $L_{\rm X(0.5-2.0keV)} \approx 1.5 \times 10^{43}$ erg s^{-1} in the low-z subset seen in figure 6.3. Over the two bins with excess counts, there are 28 clusters observed, while only 14 are predicted by the REFLEX XLF. This is a significant excess; the probability of observing $N > 27$ for a Poisson distribution with a mean of 14 is 6.4×10^{-4}. The same analysis was also applied to the larger low-z subset of the 160SD sample. According to Equation (6.7), the number of clusters predicted by the local REFLEX XLF over the two bins with

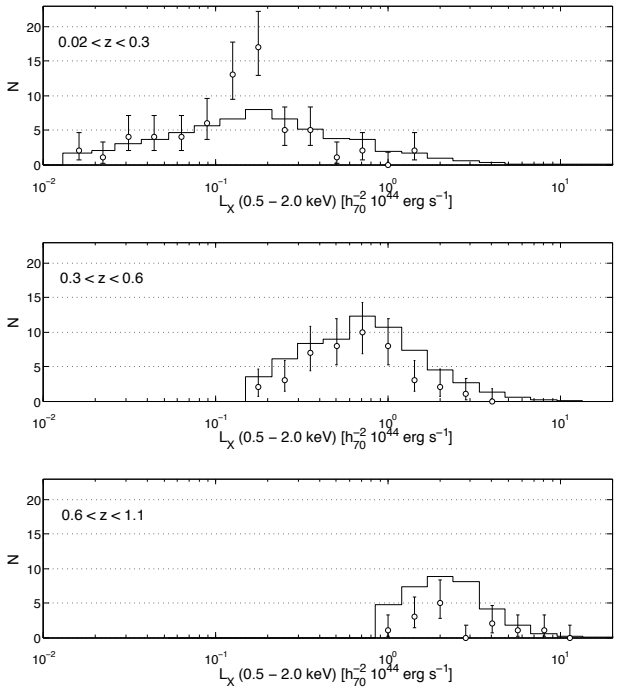

Figure 6.5 *Expected cluster numbers (solid line) versus observed (dots) per luminosity bin for the local, intermediate, and high redshift samples. The expected number of clusters is calculated per luminosity bin from Equation* (6.6).

excess counts for the 160SD sample is 18, significantly lower than the observed number of 40 clusters [$P(N > 39) = 5.3 \times 10^{-6}$ for a Poisson distribution with mean 18].

The number of clusters, N_{mod}, predicted by the REFLEX fit is uncertain due to the errors on the REFLEX Schecter function parameters. Assuming that the covariance in the REFLEX Schechter function parameters is similar to that found in our fit (section 4.1.3), then the resulting uncertainty on the REFLEX N_{mod} is estimated to be 26%. As the observed number counts are a Poissonian realisation of the model prediction, the probability of observing $\geqslant N_{\rm obs}$ clusters for a set of model parameters θ which predicts a number $N_{\rm mod}$ is

$$P(N_{\rm obs}|\theta) = \int P(\geqslant N_{obs}|N_{\rm mod})P(N_{\rm mod}|\theta)dN_{\rm mod}. \tag{6.8}$$

We model the first probability distribution as a Poisson distribution and the second as a Gaussian with mean 14 and standard deviation 3.7, which results in a probability of observing at least 28 clusters in this luminosity bump of 1%. The corresponding probability for the bump in the 160SD sample is 0.1%.

6.3.3 Evolving Schechter function

Here we deploy the maximum likelihood analysis first set out by Marshall et al. (1983), which fits an evolving Schechter function to the distribution of objects in luminosity redshift space. The treatment is free from arbitrary binning and with the generalisation of Mullis et al. (2004) accounts for flux uncertainties. We briefly summarise the method and apply it to the WARPS sample.

The XLF is characterised as an evolving Schechter function

$$\phi(L_{\rm X},z){\rm d}L_{\rm X} = \phi^*(z)\left[\frac{L_{\rm X}}{L^*_{\rm X}(z)}\right]^{-\alpha}\exp\left[-\frac{L_{\rm X}}{L^*_{\rm X}(z)}\right]\left[\frac{{\rm d}L_{\rm X}}{L^*_{\rm X}(z)}\right] \tag{6.9}$$

The parameters, except for α, are allowed to evolve as follows

$$\phi^*(z) = \phi^*_0\left[\frac{1+z}{1+z_0(L_{\rm X})}\right]^A, \tag{6.10}$$

$$L^*_{\rm X}(z) = L^*_{\rm X,0}\left[\frac{1+z}{1+z_0(L_{\rm X})}\right]^B, \tag{6.11}$$

where ϕ^*_0 and $L^*_{\rm X,0}$ are adopted from the local XLF. Due to the flux limit of the surveys, the median redshift z_0 increases with luminosity bin and is given by the local XLF. A deviation from $A = B = 0$ indicates evolution.

To be free from arbitrary binning, the luminosity redshift grid is chosen to be sufficiently fine for there to be either 1 or 0 clusters in each cell. We achieve this with ${\rm d}z = 0.01$ and ${\rm d}L_{\rm X} = 0.1\times10^{43}h^{-2}$ erg s^{-1} for the WARPS sample. In each cell the expected number of clusters is calculated

$$\lambda(L_{\rm X},z){\rm d}L_{\rm X}{\rm d}z = \phi(L_{\rm X},z)\Omega(f_{\rm X},r_\theta)\frac{{\rm d}V(z)}{{\rm d}z}{\rm d}L_{\rm X}{\rm d}z \tag{6.12}$$

The likelihood function $\mathcal{L}$ describes the joint probability of detecting 1 cluster at each occupied cell i and 0 in each empty cell j and is given by

$$\begin{aligned}\mathcal{L} = &\prod_i \lambda(L_{\rm X,i},z_i){\rm d}L_{\rm X}{\rm d}z\,\exp\left[-\lambda(L_{\rm X,i},z_i){\rm d}L_{\rm X}{\rm d}z\right]\\ &\times\prod_j\exp\left[-\lambda(L_{\rm X,i},z_i){\rm d}L_{\rm X}{\rm d}z\right],\end{aligned} \tag{6.13}$$

which makes use of the Poisson distribution and is valid when the number of expected clusters $\ll 1$ as expected for small cells. To account for the uncertainties

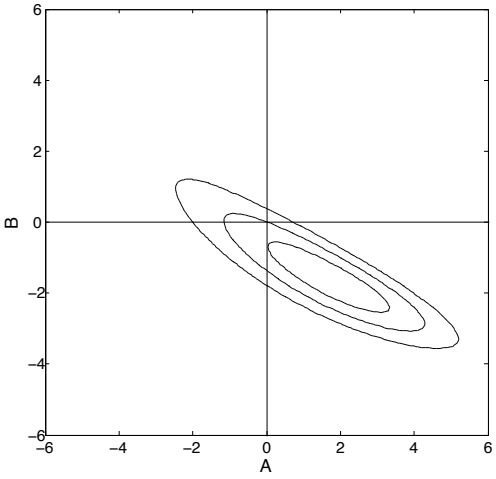

Figure 6.6 *Likelihood contours for the evolution parameters A and B, defined in Equations* (6.10) *and* (6.11)*, based on a comparison of the local REFLEX Schechter function and the complete WARPS distribution of clusters in luminosity redshift space. Contours show the* 1σ*,* 2σ*, and* 3σ *confidence limits.*

on the measured fluxes, we smooth the objects by a Gaussian in the luminosity direction, in the same way as in Mullis et al. (2004). The amount of smoothing is based on the 1σ flux errors. Redshift errors are not taken into account, since they are typically much smaller.

We calculate $\Delta S = S(A, B) - S(A_{\rm best}, B_{\rm best})$, where $S = -2 \ln \mathcal{L}$. In Figure 6.6 we plot contours of $\Delta S = 2.30$, 6.17, and 11.8, which correspond to the 1σ, 2σ, and 3σ confidence limits.

The contours for WARPS are shown in Figure 6.6, with evolution measured relative to the local XLF from REFLEX, for which we used all 124 WARPS clusters. We find evidence for negative evolution that is significant at 2σ, with $A = -1.88 \pm 0.62$ and $B = -1.76 \pm 0.53$. Stronger evidence for evolution was measured using only the WARPS clusters at $z > 0.3$. The same methodology was applied, and the resulting confidence contours on A and B are shown in Figure 6.7. The best fitting parameters for both samples are given in Table A.1.

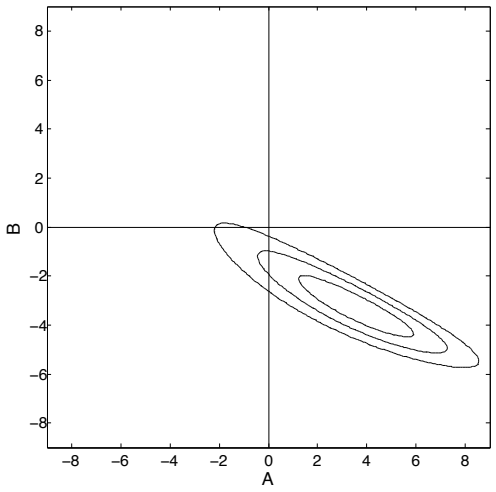

Figure 6.7 *Likelihood contours for the evolution parameters A and B, defined in Equations* (6.10) *and* (6.11)*, based on a comparison of the local REFLEX Schechter function and the $z > 0.3$ WARPS clusters. Contours show the 1σ, 2σ, and 3σ confidence limits.*

Dataset	redshift	ϕ^* $10^{-7}h_{70}^3\mathrm{Mpc}^{-3}$	α	L_X^* $10^{44}h_{70}^{-2}$
REFLEX	$z < 0.3$	2.94 ± 0.82	1.690 ± 0.045	2.64 ± 0.29
WARPS ML	$z > 0.02$	2.94	1.690	2.64
WARPS ML	$z > 0.3$	2.94	1.690	2.64
WARPS Bayesian	$z > 0.02$	3.68 ± 0.87	1.79 ± 0.04	2.59 ± 0.35
Dataset	redshift	A	B	
REFLEX	$z < 0.3$	-	-	
WARPS ML	$z > 0.02$	1.88 ± 0.62	-1.76 ± 0.53	
WARPS ML	$z > 0.3$	3.60 ± 0.95	-3.37 ± 0.56	
WARPS Bayesian	$z > 0.02$	-0.09 ± 1.19	-0.93 ± 0.58	

Table 6.2 *Best fitting XLF parameters. The REFLEX parameters are taken from (Böhringer et al., 2002), for a ΛCDM cosmology. The maximum likelihood (ML) fits assumed XLF shape parameters fixed at the REFLEX best fit values. The Bayesian fit used the REFLEX values as priors, as discussed in Section 6.4.1.*

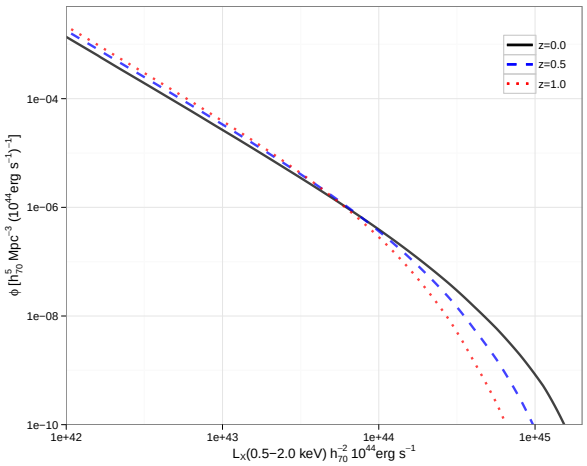

Figure 6.8 *Schechter functions with best-fitting evolution parameters from the maximum likelihood analysis to the full sample. The lines show the form of the Schechter function at redshifts 0, 0.5 and 1.*

6.4 Discussion

6.4.1 Evolution in the XLF

The comparison of expected and observed cluster number counts, and the maximum likelihood analysis of the unbinned cluster population both strongly support negative evolution of the XLF. The evolution in ϕ^* and L_X^* is degenerate, as is apparent in figure 6.6, but the net effect is significant, and consistent with a decrease in the number density of massive, high luminosity clusters with redshift, as expected in a ΛCDM hierarchical Universe. This is illustrated in Figure 6.8, which shows the best fitting evolution of the REFLEX $z = 0$ Schechter function.

In the maximum likelihood analysis of Section 6.3.3 we assume no evolution in the parameter α. Here we test whether this is justified by calculating ΔS for the parameter C defined as

$$\alpha(z) = \alpha_0 \left[\frac{1+z}{1+z_0(L_{\rm X})} \right]^C \tag{6.14}$$

and use our best fit parameters A and B from Section 6.3.3. We find $C_{\rm best} = 0.05 \pm 0.17$, and for $A = B = 0$ we have $C_{\rm best} = -0.05 \pm 0.17$. This is reassuring, since in the hierarchical picture of structure formation we expect evolution to occur at the bright end, whereas α determines the slope at fainter luminosities.

The negative evolution measured in the WARPS XLF is in very good agreement with that found for the 160SD (particularly for the $z > 0.3$ subset), and agrees qualitatively with previous measurements of negative evolution in the XLF (see figure 8 in Mullis et al., 2004). We note that the 160SD evolution was measured with respect to the BCS XLF, whereas we used the REFLEX XLF for our low-redshift baseline, so the agreement in evolution measures suggests that the choice of baseline does not strongly affect the measured evolution. The uncertainty on the local XLF and other systematics affecting the evolution measurements are discussed below.

Uncertainty on z_{max}

The upper redshift limit z_{max} for the high redshift sample is uncertain due to lack of near infra-red follow-up of cluster candidates. To our knowledge it is the first time this issue has been considered in the determination of the cluster XLF. The RDCS survey included near infra-red imaging which resulted in the successful detection of 4 clusters beyond redshift 1. However, these fall below the flux limit of their statistically complete sample, which has $z_{\mathrm{max}} = 0.83$. The detection and optical confirmation in WARPS of a cluster at $z = 1.028$ is consistent with our estimate of $z_{\mathrm{max}} \approx 1.1$, but the exact limit will depend on the characteristics of the galaxy populations and the photometric limits of the optical imaging for each cluster, so is not well defined.

As can be seen in Figure 6.2, for very luminous clusters the sky coverage of 100% is maintained well beyond the limit set by the optical observations. This means that the product $\Omega(f_{\mathrm{X}}, r_\theta) \times \frac{\mathrm{d}V(z)}{\mathrm{d}z}$ is nonzero in equation (6.5). Hence, an increase in z_{max} suppresses the XLF in those bins that represent sufficiently high X-ray luminosities. Although the influence of the choice of z_{max} on the XLF is suppressed by the flux limit, a too high value for z_{max} could falsely suggest negative evolution, whereas a too low value boosts the bright end towards the opposite conclusion.

We tested the robustness of the evolution measurement to z_{max} by reducing z_{max} to $z = 1$ and excluding the $z = 1.028$ cluster from the analysis. The contours in the $A - B$ plane were changed negligibly. This is a conservative approach, and shows our measured evolution is insensitive to the choice of z_{max}. If the effective z_{max} of the survey is actually larger than the assumed $z = 1.1$, then our non-detection of clusters beyond $z = 1.03$ would imply stronger evolution than that

measured here.

Cluster Surface Brightness

Although we refer to the statistically complete WARPS sample as "flux-limited", in practice it is the X-ray surface brightness and not the flux that determines whether or not a cluster is detected. To a first approximation, the surface brightness is related to the cluster flux by the core radius r_c, that sets the spatial scale of the surface brightness distribution. This then enters the XLF through the computation of the detection volumes of the clusters. Given the relatively large PSF of the PSPC at the off axis angles considered in WARPS, we do not expect our results to be sensitive to the choice of core radius, with the strongest effects expected at the faint end of the local XLF, which is most sensitive to uncertainties in the selection function.

For each WARPS cluster, a core radius was estimated from the PSPC data as the radius at which the surface brightness, fitted by a β-model with $\beta = 2/3$, is a factor $2^{1/\beta}$ lower than the central value. The uncertainties on the individual core radii are large, but the average r_c for WARPS is $\sim$ 100kpc, whereas Chandra observations of clusters show an average core radius of $\sim$ 150 kpc (Maughan et al., 2008).

A disadvantage of the Page-Carrera technique is that information about the core radius of the individual clusters is difficult to include. Thus when applying this technique, a fixed core radius of 102 kpc (average WARPS) was assumed for each cluster. However, using the $V_{\rm max}$ technique it was possible to investigate the effect of varying r_c. We found that the $V_{\rm max}$ technique yields nearly identical XLFs for a uniform core radius of 100 kpc (average WARPS), 150 kpc (average Chandra), and the individual core radii measured from the PSPC data.

Uncertainties on the Local XLF

In order to assess the impact of uncertainties on the form of the low redshift XLF on the measured evolution, we adopted a Bayesian approach to fitting the XLF. The posterior probability distribution for the set of model parameters $\theta = (\phi^*, L_X^*, \alpha, A, B)$ given the observed data $\mathbf{D}$ (the luminosity and redshift of each

cluster) is given in the normal way by

$$P(\theta|\mathbf{D}) \propto P(\mathbf{D}|\theta)\mathbf{P}(\theta). \tag{6.15}$$

Here the first term on the right is the likelihood function, and the second term is the prior probability distribution of the model parameters. This approach allows us to adopt the REFLEX low-z XLF parameters and their uncertainties as priors on ϕ^*, L_X^*, α, which can then be marginalised over. We adopt weak priors on A and B, simply assigning each a Gaussian distribution with mean zero, and standard deviation 100. We also generalise the likelihood expression from Equation (6.13) to include the statistical scatter of the measured luminosities. This accounts for the possibility that clusters that are nominally below the flux limit may be observed to be above the flux limit due to our noisy measurement of L_X (this is a source of Eddington bias and is discussed further below).

We divide the L_X, z parameter space into cells i, j with coordinates $(L_{X,i}, z_j)$ and widths $(dL_{X,i}, dz_j)$. As before, the XLF model predicts a number of clusters in cell i, j as

$$N_{\mathrm{mod},ij} = \lambda(L_{X,i}, z_j, \theta)\mathrm{d}L_{X,i}\mathrm{d}z_j. \tag{6.16}$$

However, the final number of clusters expected in cell i, j includes contributions from all of the other cells in the L_X direction, due to the noisy measurement of L_X. The contribution from a cell at $L_{X,k}, z_j$ to the number counts in a cell at $L_{X,i}, z_j$ is

$$N_{\mathrm{exp},ijk} = N_{\mathrm{mod},ik} P(L_{X,j}|L_{X,k}, \sigma_k) dL_{X,j} \tag{6.17}$$

The probability term here models the measurement noise on a cluster with "true" luminosity $L_{X,k}$ as a Gaussian with a mean $L_{X,k}$ and standard deviation σ_k. We model the increasing precision of the luminosity measurement with cluster flux by setting σ_k to be inversely proportional to the square root of the flux at $L_{X,k}, z_j$, as expected for measurements dominated by counting statistics. The constant of proportionality is set to give a 15% luminosity error at the flux limit, in agreement with the observed clusters.

The final expected number of clusters in cell $L_{X,i}, z_j$ is then

$$N_{\mathrm{exp},ij} = \sum_k N_{\mathrm{mod},ik} P(L_{X,j}|L_{X,k}, \sigma_k) dL_{X,j} \tag{6.18}$$

and the likelihood function is then

$$P(\mathbf{D}|\theta) = \prod_{ij} P(N_{\mathrm{obs},ij}|N_{\mathrm{exp},ij}). \tag{6.19}$$

The probability distribution of the number of observed clusters N_{obs} is Poissonian, and can be simplified as before in our working limit of one or zero observed clusters per cell.

The posterior probability distribution was analysed using the *Laplace's Demon* package Hall (2012) for the *R* statistical computing environment (R Development Core Team, 2012). An adaptive Metropolis Markov Chain Monte Carlo algorithm was used, and the resulting constraints on the model parameters are given in Table A.1. The Schechter function shape parameters are all consistent with the results from the REFLEX data alone, indicating that the WARPS data do not provide much extra information to constrain those parameters. The confidence contours for the evolution parameters are plotted in figure 6.9. As expected, marginalising over the uncertainties on the local XLF reduces the precision of the evolution measurements, though the presence of evolution (i.e. a difference from $A, B = (0, 0)$) is significant at more than 95%. This is the first time that evolution in the cluster XLF has included this source of uncertainty. The best fitting evolving Schechter function is compared with the low-redshift REFLEX Schechter function in figure 6.10.

The different evolution models are plotted in figure 6.11, which compares the number of clusters as a function of redshift predicted by the different model XLFs with that observed. The no-evolution REFLEX model clearly predicts more clusters than observed at $z > 0.6$. There is some tension between the $z > 0.3$ maximum likelihood fit and the Bayesian model, driven by the Bayesian model's accounting for the excess of WARPS clusters at $0.1 < z < 0.3$.

Cluster Correlation Function

We should also consider the likely contamination from any associated clusters that may lie on the line of sight to the sample cluster. Since the correlation function for clusters can be written as $\xi(r) = (r/r_0)^{-1.8}$, with the correlation length $r_0 \sim 20$ Mpc (e.g. Basilakos and Plionis, 2004; Moscardini et al., 2001), we can approximately integrate along the line of sight from, say, 2 Mpc (to represent the minimum possible separation) to ~ 150 Mpc (where the correlation

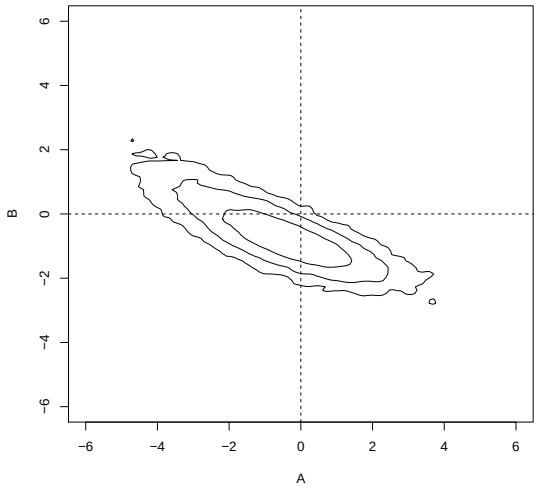

Figure 6.9 *Likelihood contours for the evolution parameters A and B, defined in Equations* (6.10) *and* (6.11)*, based on a Bayesian analysis and marginalising over the uncertainty on the shape parameters of the local XLF. Light grey contours show the constraints from the maximum likelihood analysis. Contours show the* 1σ*,* 2σ*, and* 3σ *confidence limits.*

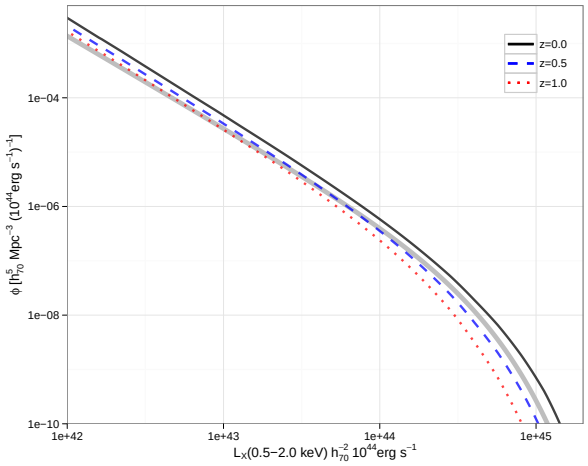

Figure 6.10 *Schechter functions with best-fitting evolution parameters from the Bayesian analysis. The lines show the form of the Schechter function at redshifts 0, 0.5 and 1, and the grey line shows the REFLEX Schechter function.*

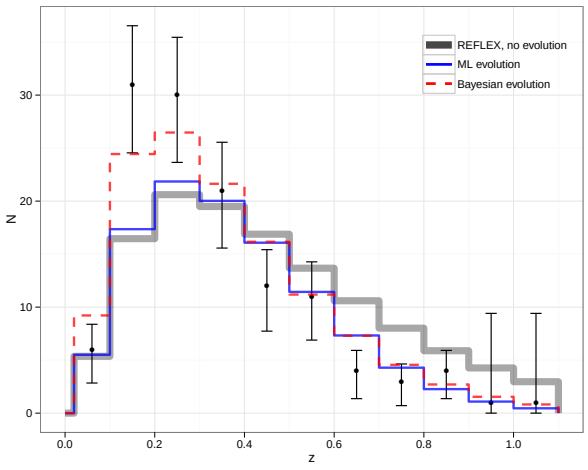

Figure 6.11 *The observed redshift distribution of the WARPS clusters is compared to the distribution predicted by different models for the XLF. Both the ML and Bayesian fits are to the full sample ($z > 0.02$). The error bars on the observed counts are computed according to Gehrels (1986).*

is negligible) to see that we expect close to twice as many clusters within this range as would be expected for an unclustered population. (We could alternatively integrate the two parameter $\xi(r_p, \pi)$ along $r_p = 0$ (e.g. Miller et al., 1999) to obtain essentially the same result). Taking a column of length ± 150 Mpc and radius 1 Mpc centred on a given cluster (i.e. a volume $\sim 10^3$ Mpc^3 and a density of clusters around 10^{-5} Mpc^{-3}, appropriate for rather small clusters with only 10-20 bright early type galaxies (see e.g. Koester et al., 2007), we evidently expect only $\sim 1\%$ contamination by 'clustered clusters'. Reasonable changes to any of the values used here, will only change this by a factor of a few. Indeed, if we are interested in contamination by large clusters (so that masses and fluxes are seriously affected), the number is around two orders of magnitude lower still.

6.4.2 Excess Number Density in Low-z XLF

Figures 6.3, 6.5, and 6.11 show that the WARPS detects a significant excess of systems in the range $L_{\mathrm{X}(0.5-2.0\mathrm{keV})} = 1.0 - 2.0 \times 10^{43}$ erg s^{-1} and $0.1 < z < 0.3$ relative to the REFLEX Schechter function. These luminosities correspond to $\sim$ 2keV systems, so are poor clusters or galaxy groups. Interestingly, a significant excess is seen at the same luminosity range in the 160SD low-z XLF. In determining this excess, we have been comparing observed number counts to the best fitting model to the observed REFLEX XLF. It is worth considering

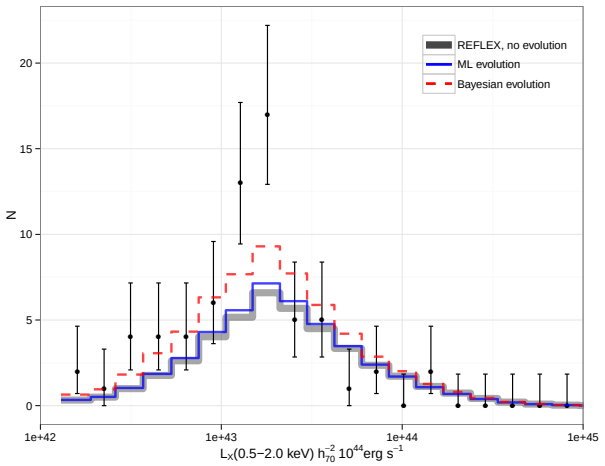

Figure 6.12 *The observed luminosity distribution of the WARPS clusters at $z < 0.3$ is compared to the distribution predicted by different models for the XLF. The error bars on the observed counts are computed according to Gehrels (1986).*

whether an excess is present in the REFLEX data, but inspection of figure 4 in (Mullis et al., 2004) shows that the REFLEX data are close to the best fitting Schechter function in this luminosity range. (note their figure is for $H_0 = 50$ km s^{-1} Mpc^{-1}).

The best-fitting Bayesian XLF model predicts a significantly larger number of clusters at $z < 0.3$ than the REFLEX model, as shown in figure 6.12. This somewhat reduces the significance of the excess clusters in the bump at $L_{\mathrm{X}(0.5-2.0\mathrm{keV})} = 1.0 - 2.0 \times 10^{43}$ erg s^{-1}. Marginalised over the uncertainties on the model parameters, the Bayesian model predicts 16.5 ± 3.7 clusters, compared with the 28 observed. The probability of observing at least 28 clusters in this luminosity bump of 2%. There is thus suggestive evidence that a real excess remains, and we now consider possible factors that could contribute to this.

Could the excess be simply a result of sample (cosmic) variance? The survey areas of WARPS and 160SD are much smaller than REFLEX, but the volumes surveyed are still significant. The clusters in the bump feature occupy the redshift range $0.1 < z < 0.3$ and the volume surveyed by WARPS in this redshift range is $\sim 10^7 h_{70}^3$ Mpc^3. This volume is larger than the volumes in which sample variance is expected to be significant for galaxy surveys (Driver and Robotham, 2010). For cluster surveys, Hu and Kravtsov (2003) provide analytical approximations to compute the relative contributions of Poisson noise and sample variance. Approximating the WARPS as a volume-limited survey

with a mass threshold of $10^{14} M_{\odot}$ at $z = 0.2$, the effects of Poisson noise and sample variance are approximately equal, with Poisson noise dominating at higher redshifts, and sample variance dominating at lower redshifts. This indicates that sample variance could be responsible for the excess cluster counts in the WARPS. However, it is more difficult for sample variance to explain the coincident, stronger, excess seen in the same part of the L, z plane in the 160SD survey. Only 40% of the WARPS fields and 35% of the WARPS clusters are in common with 160SD. If the excess were due to sample variance, then the addition of extra, independent, fields should result in regression to the mean, not increased significance of the excess as observed. We thus conclude it is unlikely that the excess seen in both surveys is due to sample variance, and investigate other possibilities.

The three dimensional distribution of the clusters in the luminosity and redshift range of the excess were examined, but there was no evidence for clustering in volume, so the excess is not caused by a superstructure of clusters. This is expected, since the selected fields are scattered across a large fraction of the sky.

A further possibility to explain the excess numbers is contamination in the detected flux from unresolved X-ray point sources, for example low luminosity Active Galactic Nuclei (AGN). Such contamination was removed where possible, but not all contaminating sources are resolved in the ROSAT PSPC images. Hence, some residual contamination is expected, enhancing the estimated cluster luminosities. Detailed modelling of the AGN population is beyond the scope of this paper, but this contamination would differ from the scatter models discussed above, as the effect is purely additive. Some mass or redshift dependence of the AGN contamination may be required to manifest the localised excess of clusters in the L_X, z plane.

Finally, we consider if selection bias may be responsible for the excess clusters seen in this region of the L_X, z plane. This is plausible, given that the excess is close to the flux limit in the region of the L_X, z plane where the WARPS is most sensitive (see Figure 6.1). Eddington bias enhances cluster number counts when scatter is present in the luminosities of the population. The slope of the XLF means that for a given flux limit, there are more clusters below the flux limit that may scatter into the sample than above the flux limit that may scatter out of the sample. There are two sources of scatter that may be important: statistical scatter due to the counting statistics on the L_X measurement, and intrinsic scatter in the cluster population. Our Bayesian analysis allows us to

investigate each of these sources of scatter in turn, by modifying the model for the population scatter in Equation (6.18).

Note that if the population scatter is constant with L_X and z, then a bias is present at all redshifts and luminosities, and increases towards higher luminosities due to the steepening of the XLF, so would not produce a localised excess in the L_x, z plane. However, the statistical scatter decreases with increasing L_X, as $\sim \sqrt{N}$ errors decrease above the flux limit, and increase below it. This gives rise to a bias that is strongest near the flux limit, with counting statistics allowing clusters nominally too faint for the sample to appear above the flux limit, so could plausibly contribute to the observed excess. However, the typical measurement error on luminosities close to the flux limit is $\approx 15\%$, and even modelling the increasing flux scatter below the flux limit, the bias due to this source of scatter was found to contribute < 1 additional cluster in the regions of the excess, compared to models with no scatter. We note however, that our model for the scaling of the statistical scatter with flux is simplistic – the measurement errors also depend on the exposure time and background level in the source field. Modelling this for clusters below the flux limit would require extensive simulations and is beyond the scope of this work.

The intrinsic scatter in luminosity of the cluster population is known to be significant, and if this varies with mass or redshift, it could result in a bias that contributed to a localised excess in number counts. The variation of cluster scatter with mass is not well measured, but there is evidence that the intrinsic luminosity scatter decreases above $z \approx 0.4$ (Maughan et al., 2007), albeit measured in a heterogeneous sample. We test the effect that evolving scatter could have on the measured XLF by replacing the scatter model in equation (6.18) with a lognormal distribution, with a standard deviation of 50% at $z < 0.45$, decreasing smoothly to 20% at $z > 0.55$ (Maughan et al., 2007). The effect of this evolving scatter is to increase the number of $z < 0.3$ clusters predicted by the Bayesian model by $\approx 10\%$, but this still leaves a significant excess of observed clusters at around $L_{\mathrm{X(0.5-2.0keV)}} = 1.0 - 2.0 \times 10^{43}$ erg s^{-1}.

Similarly, introducing an ad hoc model of intrinsic scatter which decreases from 90% to 20% at $L_{\mathrm{X(0.5-2.0keV)}} = 2.5 \times 10^{43}$ erg s^{-1} (designed to maximise the Eddington bias effect), only serves to increase the model prediction by 2.5 clusters in the bins contributing to the excess. When compared to the REFLEX XLF, the observed excess of WARPS clusters remains highly significant in the face of all bias contributions.

A luminosity of 2×10^{43} erg s^{-1} corresponds to a mass of $M_{200} \simeq 10^{14} M_{\odot}$, at the borderline between groups and clusters. It is possible that some feature of the cluster population in this region of the $L_{\rm X}, z$ plane enhances their detectability, by e.g. enhancing their surface brightness. This could result from, for instance, an enhanced AGN or cool core population, but the effects would need to be relatively localised in $L_{\rm X}$ and z. With the present data it is not possible to investigate this further, but with the arrival of new deep cluster surveys such as XXL or XCS, it should be possible to verify these results and extend the investigation.

Selection Function

The selection function was determined by calculating for each WARPS PSPC field the area fraction in which a source of given size and flux can be detected. The detection threshold was found by simulating clusters with a spherical β-profile. With more advanced X-ray telescopes it has become clear that clusters often exhibit significant substructure, which is not detected by ROSAT. Substructure was not simulated in determining the detection threshold, whereas this potentially affects the selection function and flux estimation. However, the angular resolution of PSPC images is relatively poor, so that the assumption of a spherical β-profile is not expected to significantly affect the results. WARPS is in good agreement with other surveys that were based on PSPC archival data with different survey design, indicating that the localised excess in the L_X, z-plane is not due to issues related to the selection function.

6.4.3 Sensitivity to High-Redshift Cool Core Clusters

Since the detection of clusters in X-ray surveys is driven by their surface brightness, the presence or absence of centrally peaked emission associated with a cool core may have a strong impact on the detection of a given cluster. There is some debate in the literature as to whether there are significant numbers of cool core clusters in the high-z ($z > 0.5$) Universe. Both Vikhlinin et al. (2007) and Santos et al. (2010) find a lack of high-z cool core clusters in the distant 400SD sample, but Santos et al. (2010) find evidence for moderate cool cores in high-z clusters detected in the WARPS and RDCS. They argue that the 400SD (and by extension 160SD) may have discarded high-z cool core clusters as being unresolved, but note that this does not imply incompleteness in the 400SD

providing the surface brightness dependence was modelled into the selection function.

The excellent agreement of the evolution in the XLF seen in the WARPS and 160SD at $z > 0.3$ despite their very different cluster detection algorithms implies that this is indeed the case, and that there are no significant problems with the selection function of either survey. We also note that the comparisons of clusters detected or missed by WARPS and 160SD in 157 common fields revealed no significant discrepancies, with differences being explained by the differing selection criteria (Horner et al., 2008).

6.5 Conclusions

We measured the evolution of the XLF out to $z \sim 1$ from the combined WARPS-I and WARPS-II surveys, finding significant evidence for negative evolution, in the sense of a reduction in the number density of massive luminous clusters with redshift. This is confirmed by comparing expected and observed numbers, and more convincingly by the maximum likelihood analysis. This is consistent with previous measurements of the evolution of the XLF, and the expectations of hierarchical structure formation in a ΛCDM Universe.

We investigate the sensitivity of these results to various sources of systematic uncertainty affecting the WARPS XLF and selection function. The results are not significantly affected by the modelling of the core radii of the clusters, the assumed upper redshift limit of the survey, or the technique used for estimating detection volumes for the clusters. The assumed value of $z_{\rm max} = 1.1$ is fairly conservative, as there is a cluster detected at $z = 1.05$ and many of the clusters would be detectable in X-rays to significantly higher redshift. Thus the true evolution could be somewhat stronger than we measure.

For the first time, we fully incorporate the uncertainties on the low-redshift XLF into a Bayesian analysis of the evolution, and find that while the precision of the measurements is reduced, evolution is still significant at the 95% level.

The good agreement of the measured evolution in the WARPS, 160SD and other surveys suggest that the result is not sensitive to the details of the cluster detection and follow-up strategy, and that the selection functions of both surveys are accurately modelled, including the effects of cool cores on the detectability of

clusters.

We identified a significant excess of $\sim$ 2keV systems at $z < 0.3$ observed in both the WARPS and 160SD surveys relative to the REFLEX XLF. A Bayesian fit to the WARPS data, which uses the REFLEX measurements as priors yields a model with slightly higher ϕ^* and α values than REFLEX, and reduces the excess. However, even with this model, and with including possible contributions from Eddington bias, the excess remains significant. The cause of the excess in not clear at present, although its presence in both the WARPS and 160SD argue against it being a result of a mis-calibrated selection function. New, more sensitive measurements of the XLF with surveys like XXL (Pierre et al., 2011) and XCS (Mehrtens et al., 2012) will provide better statistics for this part of the L_X, z plane, providing a means to address this question further.

Chapter 7

Conclusion

The relative distributions of galaxies and dark matter contain valuable information about galaxy formation and cosmology. Theoretical predictions of galaxy bias suffer from the poorly understood physics of galaxy formation. Therefore, galaxy bias is constrained in this thesis from galaxy clustering and gravitational lensing. In this chapter I provide an overview of the main outcomes and discuss their implications for cosmology.

7.1 Overview

7.1.1 Galaxies and Dark Matter in a Cosmological Context

The matter density field evolved under the influence of gravitational collapse from a nearly homogeneous state, as observed in the anisotropies of the cosmic microwave background, to the structure that we observe today. Dark matter is the dominant matter component, driving the dynamics of structure formation, which is directly linked to the expansion of the Universe. The baryonic density field in the dark matter potential wells contracts to form clusters of stars. As a result, these star clusters, or galaxies, trace the dark matter density field and contain a wealth of information about structure formation and the expansion of space.

The variance in the density field means that haloes collapse at different times, so that higher mass galaxies are formed earlier on in the Universe. This results in a

diverse population of galaxies, even in the case that all the galaxies follow the same evolutionary tracks. Although the evolution of galaxies arises in part from internal processes, it is further complicated by interactions, including mergers. This has given rise to an enormously diverse galaxy population, reflected by morphological classification diagrams. It was noted by Kaiser (1984), see also Chapter 2, that higher mass systems, such as the galaxy groups and clusters discussed in Chapter 6, are more biased as tracers of the total matter field. Hence, galaxy bias depends on mass, regardless of morphology, for which observational evidence was provided by Norberg et al. (2002).

Since the onset of modern cosmology, the distribution of galaxies in space has provided knowledge of structure formation and the dynamics of the Universe to ever increasing precision. Nowadays, galaxy surveys are digitalised, systematic mappings of the optical and infrared sky, after which selection algorithms separate stars from galaxies, resulting in catalogues of high statistical completeness. The imaged sky is then used by spectroscopic surveys, which provide reliable redshift estimates. By targeting galaxies which have prominent spectral features, such as the 4000Å break or star formation emission lines, the redshift uncertainties become sufficiently small, allowing to map their distribution in 3D space to reveal the cosmic web and study its properties. The choice of the targeted spectral feature is related to the type of galaxy observed, which affects the galaxy bias of the sample. Hence, galaxy bias can be thought of as a form of selection bias, and needs to be constrained for each galaxy survey in order to infer the dark matter field from the observed galaxies. At the same time, galaxy bias contains valuable information about how galaxies populate dark matter haloes, which is interesting from the perspective of galaxy formation.

Cosmological density fields can be described in several ways, most notably with the fractional overdensity δ as a function of position x, the power spectrum P as a function of wavenumber k, and the 2-point correlation function ξ as a function of comoving separation s, introduced in Equations (1.12), (1.18), and (1.23), respectively. Chapter 2 discusses how this leads to different definitions of galaxy bias, the most intuitive of which is based on fractional overdensities δ, giving the galaxy bias $b(R)$ and cross correlation coefficient $r(R)$, where R is a smoothing scale, see Equations (2.8) and (2.9), but we can also define bias in terms of Fourier modes $b(k)$, $r(k)$, or comoving separations $b(s)$, and $r(s)$, which have observational advantages.

Chapter 2 gives an overview of methods to measure galaxy bias. The most important are Weak Gravitational Lensing (WGL) and Redshift Space Distortions (RSD), introduced in Sections 1.2.4 and 1.2.5. Both techniques observe effects that are induced solely by the dark matter field: WGL looks at image distortions induced by the matter along the line of sight, while RSD looks at the velocities of galaxies induced by gravitational infall. The differences in how RSD and WGL are sensitive to gravity provide, when these two methods are combined, powerful constraints, see Section 1.2.5.

The discovery of accelerated expansion has led RSD to become a popular tool for constraining the growth rate f, defined in Equation (1.29), which is sensitive to the theory of gravity. Equation (2.30) shows the degeneracy of RSD measurements of f with galaxy bias parameters. Therefore, RSD as a probe of f relies heavily on knowledge of galaxy bias and Section 2.2 discusses systematic offsets in the measured growth rate under the assumption of simple galaxy bias scenarios. The cross correlation coefficient r is almost entirely degenerate with the measured growth rate, but is almost always assumed to be $r = 1$. This will be discussed further in Section 7.2.

7.1.2 Weak Lensing Analysis of Galaxy Bias

Overview of Methods

WGL is sensitive to the 3D matter power spectrum, which can be compared to the observed clustering of galaxies to detect galaxy bias. The lensing method that has become standard uses aperture statistics, see Section 2.3.3. The aperture method performs a filtering (with angular filter size θ_{ap}) of the raw estimators, w, γ_t, and $\xi_\pm$, see Equations (2.69)-(2.74), so that they probe the same physical scales, allowing for ratios of the statistics to measure $b(\theta_{ap})$ and $r(\theta_{ap})$, defined in Equations (2.84) and (2.85). Section 2.3.4 discusses how well galaxy bias parameters are recovered by this technique, with further tests in Chapter 3 on simulated lensing data, finding defects in the method in the case that galaxy bias parameters are scale- and time dependent. Furthermore, the data points for the aperture statistic are very correlated, leading to apparent scale dependence. There are advantages as well: the method is relatively insensitive to the shape of the power spectrum, shown in Section 3.2.4, and no integral constraint, see Equation (3.5), is required for the clustering of galaxies.

RSD modelling is often performed in Fourier space (e.g. Blake et al., 2011). Therefore, to aid RSD analyses with WGL observations, a galaxy bias method is preferred which constrains $b(k)$ and $r(k)$ directly from the data. The obvious disadvantage of this method is the necessity to choose a parametric form of the model bias. Galaxy bias models are discussed in Section 2.3.5, concluding with a preference for the McDonald galaxy bias model (McDonald, 2006). This model is physically motivated and was previously used for a WGL galaxy bias analysis to measure the galaxy bias of SDSS galaxies (Mandelbaum et al., 2013). In the model the galaxy power spectrum and galaxy-matter cross power spectrum are predicted from the matter power spectrum, the large scale bias b_1, and the scale dependence parameter b_2, see Equations (2.120) and (2.123), respectively. I introduced a third parameter $\mathcal{R}$ to give more flexibility to the model, for example, due to stochasticity or when higher order terms in Equation (2.3) are significant.

Finally, a method is introduced in Chapter 5 which is aimed at measuring parameters that are similar to $b(R)$ and $r(R)$, defined in terms of fractional overdensities δ. First, the background shear field is predicted from the foreground distribution of galaxies, after which galaxy bias parameters, defined in terms of shear fields, are measured and then related to the original $b(R)$ and $r(R)$ definitions. The method has the advantage of staying true to the definition of a cross correlation coefficient which is bounded between anti correlation $r = -1$ and perfect correlation $r = 1$. The technique requires high quality data, mainly a high background galaxy number density, in order suppress the noise from the intrinsic shapes of galaxies.

Galaxy Bias Measurements of BOSS and WiggleZ galaxies

The galaxy bias methods, described in Chapter 2 and tested on simulations in Chapter 3, were applied to same-sky surveys in Chapter 4, finding galaxy bias constraints for BOSS and WiggleZ galaxies, by cross correlating their clustering with RCSLenS shear. The two methods, the aperture galaxy bias and the model fitting, yielded similar results. Significant stochasticity was found for the WiggleZ sample, in particular for the lower redshift sub sample, for which I measured a rising cross correlation coefficient $r(\theta_{ap} = 3') = 0.2 \pm 0.2$ to $r(\theta_{ap} = 100') = 0.7 \pm 0.2$. BOSS galaxies follow a deterministic scenario within the uncertainties, finding $r(\theta_{ap})$ very close to unity. The aperture galaxy bias parameters are shown in Figure 4.11 and Figure 4.12; the model fitting results are presented in Figure

4.15 and Figure 4.16, for BOSS and WiggleZ respectively. The best fit values are quoted in Table 4.2. For the LOWZ sample I measured $b_1 = 2.0 \pm 0.1$ and $b_2 = 0.6 \pm 0.2$], consistent with the constraints from Mandelbaum et al. (2013) for LRG samples of SDSS.

7.2 Combining Weak Lensing and Redshift Space Distortions

As the Universe expands the matter density decreases, see Equation (1.13), and is reflected in the continuous increase in the distances between galaxies. Despite the accelerated expansion, which acts against structure formation, galaxies fall into overdense regions. This gravitational infall contributes to the observed redshifts of the galaxies, called Redshift Space Distortions (RSD). By mapping the clustering of galaxies, based on their (redshift-inferred) distances, along and perpendicular to the line of sight, a pattern can be observed, known as the butterfly diagram, see Figure 1.2. The extra contribution to the redshifts due to gravity only affects the distance components along the line of sight, causing this apparent clustering anisotropy. More structure growth means more anisotropy, so that information about the growth of structure and the expansion of the Universe can be derived from RSD.

The observed clustering pattern in Figure 1.2 depends on the growth rate f, but clearly also on galaxy bias. Section 2.2 describes how $b(k)$, $r(k)$, and f affect the redshift space power spectrum as a function of angle μ on the sky. It was concluded that $b(k)$ and $r(k)$ are both of great significance for measuring the growth rate f, so that false assumptions about galaxy bias leads to systematic offsets in RSD analyses.

The measured galaxy bias parameters of Chapter 4, summarised in Section 7.1.2, constrain $b(k)$ and $r(k)$, allowing us to assess the assumption of a linear bias, as was done in Section 2.2. RSD analyses suffer from small scale uncertainties in both the nonlinear power spectrum as well as virial motions inside galaxy clusters (the fingers-of-God effect), restricting the accuracy of the method to large scales. Therefore, scales probed by WGL have only small overlap with those used for RSD analyses, noting that the measurements here are on the largest scales yet for WGL.

7.2.1 Impact of the Measured Galaxy Bias on RSD Analyses of the Growth Rate

Provided the McDonald bias model is an accurate description of the true galaxy bias of the data, the model fitting provides a prediction of the galaxy bias at scales beyond what lensing is sensitive to. Therefore, we repeat the analysis in Section 2.2.1 to show the impact of the galaxy bias observations, Figure 4.15 and Figure 4.16, on the measured growth rate under the common assumption of a linear bias.

The McDonald bias model is in principle only accurate for very large scales, beyond the virial radius of galaxy clusters. Therefore, we use the best fit values from the $15' < \theta < 100'$ analysis of the galaxy samples in Table 4.1, noting that for a full analysis the uncertainties on the best fit values should be taken into account. By introducing $\mathcal{R}$ it was shown that the WiggleZ LZ galaxy bias is not well described at large scales by the McDonald bias model, since, if it was, $\mathcal{R}$ would be consistent with unity (if $\mathcal{R} \neq 1$, $r(k = 0) \neq 1$, whereas $r(k = 0) = 1$ by definition). In order to include the LZ WiggleZ sample in the analysis here, we repeat the fitting without $\mathcal{R}$ to find $b_1 = 0.8 \pm 0.1$ and $b_2 = -0.5 \pm 0.4$. For LOWZ, CMASS, and WiggleZ HZ $\mathcal{R}$ was found to be consistent with unity, so that we predict $r(k)$ from their best fit b_1 and b_2 values, see Table 4.2.

Figure 7.1 shows the growth rate constraints for BOSS and WiggleZ, where we used the lensing results of this thesis. It was produced by fitting a Kaiser model with linear bias parameter to a Kaiser model with the constrained McDonald bias model. For full details of the fitting see Section 2.2.2. The power spectrum and growth rate were chosen to correspond to the effective redshift of the sample. We assume general relativity for the fiducial growth rate at the mean redshift of the galaxy sample, so that $f_{\rm fid} = \Omega_m[\langle z \rangle]^{0.55}$, represented by the + symbol. For each sample the uncertainty in the power spectrum is calculated from Equation (2.56). The growth rate is systematically underestimated for all the samples, which is attributed to the assumption of $r = 1$. In this analysis the WiggleZ results are more affected. The results rely heavily on how well the model, that I have constrained at smaller scales, describes the galaxy bias at large scales

The extraction of the growth rate from RSD is a complicated task, involving accurate modelling of not only the galaxy bias, but also the nonlinear power spectrum, the Fingers-of-God effect, and a recent study suggests the existence

of velocity bias for CMASS galaxies (Guo et al., 2014). For this analysis we assumed the linear Kaiser model. It is interesting to note that recent growth rate measurements generally underestimate the growth rate relative to Planck CMB predictions (e.g. Chuang et al., 2013) . In light of this, Figure 7.1 seems to indicate that this may in part be explained by the assumption of $r = 1$.

The systematic bias in the growth rate (at the level of $\sim 2\sigma$ for BOSS and $\sim 3\sigma$ for WiggleZ) requires significant effort to increase the maximum scales probed by WGL. Also, RSD analyses should marginalise over the cross correlation coefficient.

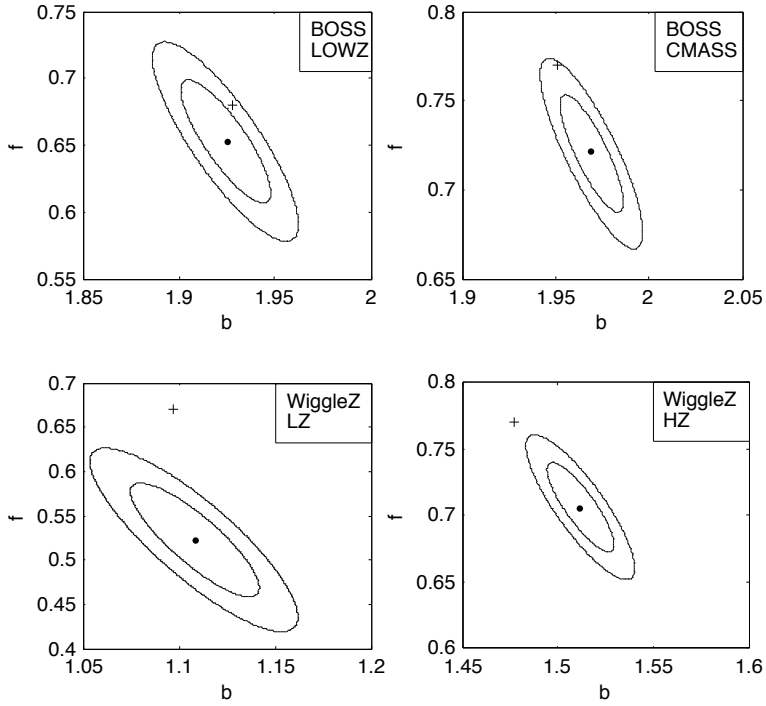

Figure 7.1 *1σ and 2σ confidence levels for the growth rate constraints of BOSS and WiggleZ under the assumption of linear bias. The true growth rate is represented by the $+$. The analysis is described in full detail in Section 2.2.1. The redshift of the samples are given in Table 4.1 and their galaxy bias constraints that were used for these Figures are quoted in Table 4.2. Errors were calculated from Equation* (2.56).

7.3 Outlook

Galaxy bias was introduced by Kaiser (1984) to bring the observed distribution of galaxy clusters in agreement with the $\Omega = 1$ Universe. The first observations

provided no signs for a nonlinear bias (e.g. Gaztanaga and Frieman, 1994; Verde et al., 2002) in the clustering of galaxies with respect to the CDM prediction. With improved data came the first detections of nonlinear bias (e.g. Gaztañaga et al., 2005; Hoekstra et al., 2002), supported by numerous papers that argued for nonlinear bias from theory (e.g. Babul and White, 1991; Borgani and Bonometto, 1990; Coles, 1993) and from theory applied to simulations (e.g. Mann et al., 1998).

Direct observations of galaxy bias remain sparse, which is not surprising in light of the difficulty in observing the dark matter distribution, since it can only be studied through its gravitational effects, for example via Weak Gravitational Lensing (WGL) and Redshift Space Distortions (RSD). However, the past decade has made cosmologists aware of the nontrivial relation between light and mass. This is perhaps unsurprising, giving the complex processes involved in galaxy formation, which theoretical descriptions remains uncertain. For example, the initial stellar mass function of galaxies is unknown as well as the exact role feedback processes play, whereas these are of fundamental importance in the formation of galaxies. Hence, the theoretical treatment of relating galaxy formation to galaxy bias has not reached a satisfactory state. Galaxy bias observations can also be used to investigate the halo model (Peacock and Smith, 2000), since the halo model predicts a relation between the bias at small and large scales (Simon et al, in prep).

Large imaging surveys with high number densities are upcoming (KiDS, DES, HSC, LSST, Euclid, AFTA, SKA). The plethora of possible dark energy scenarios puts pressure on all future galaxy redshift surveys to make optimal use of the data. Hence, the study of galaxy bias will remain important in its endeavour to relate astrophysical processes to the large scale distribution of galaxies and dark matter. The larger surveys push lensing measurements to larger scales where models are better understood. At the same time the growth rate becomes better constrained with larger surveys. To make use of the high quality small scale clustering signal, improvements are required in understanding nonlinear structure formation, the effect of baryons on the power spectrum, and modelling of the fingers of God effect. In order to interpret the high quality imaging data, methods for shape measurements as well as photometric redshifts need to be improved. The increase in survey size puts pressure on understanding systematics, as well as computation power in order to accurately determine the covariance matrix from many realisations of large N-body simulations.

New methods are explored to constrain galaxy bias, such as the clipping of the

density field to focus on large scale bias by reducing the effects of nonlinear physics (Simpson et al., 2011). This thesis presented a new method to measure galaxy bias from WGL in Chapter 5. The method requires high quality data, but opens up the possibility to study galaxy bias parameters locally. This will provide new insights in the galaxy bias relation, and it will be exciting to apply this technique to future surveys.

The results in this thesis show the success of gravitational lensing to map the relative distributions of galaxies and dark matter, out to large scales where gravity can reliably be constrained on cosmological scales. Although for many an inconvenient nuisance parameter, galaxy bias is the topic that relates the formation of galaxies to the properties of the Universe, and as such provides an exciting field to explore.

Appendix A

XLF Tables

For future reference we present tables of the binned X-ray Luminosity Function, see chapter 6. Per bin we also quote the number of observed clusters, their median redshift $\tilde{z}$, and their average X-ray luminosity $\overline{L}_{\rm X}$, see Table A.1. They were previously published in Koens et al. (2013).

Table A.1 *The X-ray Luminosity Function for the local, the intermediate redshift, and high redshift universe as measured by WARPS. Also shown are the observed number of clusters N_{obs}, their median redshift $\tilde{z}$, and their average luminosity $\overline{L}_X$.*

$L_{\rm X,centre}$ (0.5-2.0 keV) [h_{70}^{-2} 10^{44} erg s^{-1}]	ϕ [h_{70}^{5}Mpc^{-3} (10^{44}erg s^{-1})$^{-1}$]	$\phi^{+1\sigma}$ [h_{70}^{5}Mpc^{-3} (10^{44}erg s^{-1})$^{-1}$]	$\phi^{-1\sigma}$ [h_{70}^{5}Mpc^{-3} (10^{44}erg s^{-1})$^{-1}$]	$N_{\rm obs}$	$\tilde{z}$	$\overline{L}_{\rm X}$ (0.5-2.0 keV) [h_{70}^{-2} 10^{44} erg s^{-1}]
$0.02 < z < 0.3$						
0.011	2.26×10^{-3}	7.46×10^{-2}	3.91×10^{-4}	1	0.051	0.010
0.016	1.14×10^{-3}	2.64×10^{-2}	4.04×10^{-4}	2	0.063	0.015
0.022	2.33×10^{-4}	7.69×10^{-4}	4.03×10^{-3}	1	0.107	0.025
0.031	3.46×10^{-4}	6.20×10^{-4}	1.80×10^{-4}	4	0.125	0.032
0.044	1.33×10^{-4}	2.38×10^{-4}	6.94×10^{-5}	4	0.119	0.043
0.063	5.72×10^{-5}	1.02×10^{-4}	2.98×10^{-5}	4	0.151	0.060
0.089	3.53×10^{-5}	5.64×10^{-5}	2.13×10^{-5}	6	0.150	0.090
0.125	3.68×10^{-5}	5.01×10^{-5}	2.67×10^{-5}	13	0.193	0.125
0.177	2.25×10^{-5}	2.94×10^{-5}	1.71×10^{-5}	17	0.226	0.174
0.251	4.85×10^{-6}	8.13×10^{-6}	2.75×10^{-6}	5	0.252	0.233
0.355	3.24×10^{-6}	5.43×10^{-6}	1.84×10^{-6}	5	0.240	0.352
0.502	4.82×10^{-7}	1.59×10^{-6}	8.34×10^{-8}	1	0.242	0.457
0.710	6.51×10^{-7}	1.51×10^{-6}	2.30×10^{-7}	2	0.244	0.741
1.004	0	8.98×10^{-7}	0	0	*n.a.*	*n.a.*
1.420	3.25×10^{-7}	7.54×10^{-7}	1.15×10^{-7}	2	0.292	1.351
$0.3 < z < 0.6$						
0.177	2.07×10^{-5}	4.79×10^{-5}	7.31×10^{-6}	2	0.304	0.196
0.251	4.23×10^{-6}	8.35×10^{-6}	1.93×10^{-6}	3	0.315	0.259
0.355	2.78×10^{-6}	4.28×10^{-6}	1.75×10^{-6}	7	0.370	0.373
0.502	1.31×10^{-6}	1.96×10^{-6}	8.56×10^{-7}	8	0.378	0.507
0.710	6.68×10^{-7}	9.53×10^{-7}	4.60×10^{-7}	10	0.461	0.707
1.004	3.54×10^{-7}	5.29×10^{-7}	2.32×10^{-7}	8	0.502	1.006
1.420	8.94×10^{-8}	1.76×10^{-7}	4.08×10^{-8}	3	0.500	1.455
2.008	4.42×10^{-8}	1.02×10^{-7}	1.56×10^{-8}	2	0.561	1.909
2.840	1.56×10^{-8}	5.16×10^{-8}	2.71×10^{-9}	1	0.517	2.730
$0.6 < z < 1.1$						
1.004	1.01×10^{-7}	3.33×10^{-7}	1.74×10^{-8}	1	0.679	1.110
1.420	7.34×10^{-8}	1.45×10^{-7}	3.35×10^{-8}	3	0.722	1.421
2.008	4.87×10^{-8}	8.17×10^{-8}	2.77×10^{-8}	5	0.832	2.114
2.840	0	2.51×10^{-8}	0	0	*n.a.*	*n.a.*
4.016	5.88×10^{-9}	1.36×10^{-8}	2.08×10^{-9}	2	0.820	4.164
5.680	2.08×10^{-9}	6.86×10^{-9}	3.60×10^{-10}	1	0.833	6.655
8.032	1.47×10^{-9}	4.85×10^{-9}	2.54×10^{-10}	1	0.892	9.271

Bibliography

Ahn, C. P., R. Alexandroff, C. Allende Prieto, F. Anders, S. F. Anderson, T. Anderton, B. H. Andrews, É. Aubourg, S. Bailey, F. A. Bastien, and et al. "The Tenth Data Release of the Sloan Digital Sky Survey: First Spectroscopic Data from the SDSS-III Apache Point Observatory Galactic Evolution Experiment." *Astrophys. J. Supp.* (2014) 211: 17.

Alcock, C., and B. Paczynski. "An evolution free test for non-zero cosmological constant." *Nature* 281: (1979) 358.

Aldering, G., R. Knop, and P. Nugent. "The Rise Times of High- and Low-Redshift Type IA Supernovae Are Consistent." *Astron. J.* 119: (2000) 2110–2117.

Allen, S. W., R. W. Schmidt, and A. C. Fabian. "Cosmological constraints from the X-ray gas mass fraction in relaxed lensing clusters observed with Chandra." *Mon.Not.Roy.As.Soc.* 334: (2002) L11–L15.

Anderson, L., E. Aubourg, S. Bailey, D. Bizyaev, M. Blanton, A. S. Bolton, J. Brinkmann, J. R. Brownstein, A. Burden, A. J. Cuesta, L. A. N. da Costa, K. S. Dawson, R. de Putter, D. J. Eisenstein, J. E. Gunn, H. Guo, J.-C. Hamilton, P. Harding, S. Ho, K. Honscheid, E. Kazin, D. Kirkby, J.-P. Kneib, A. Labatie, C. Loomis, R. H. Lupton, E. Malanushenko, V. Malanushenko, R. Mandelbaum, M. Manera, C. Maraston, C. K. McBride, K. T. Mehta, O. Mena, F. Montesano, D. Muna, R. C. Nichol, S. E. Nuza, M. D. Olmstead, D. Oravetz, N. Padmanabhan, N. Palanque-Delabrouille, K. Pan, J. Parejko, I. Pâris, W. J. Percival, P. Petitjean, F. Prada, B. Reid, N. A. Roe, A. J. Ross, N. P. Ross, L. Samushia, A. G. Sánchez, D. J. Schlegel, D. P. Schneider, C. G. Scóccola, H.-J. Seo, E. S. Sheldon, A. Simmons, R. A. Skibba, M. A. Strauss, M. E. C. Swanson, D. Thomas, J. L. Tinker, R. Tojeiro, M. V. Magaña, L. Verde, C. Wagner, D. A. Wake, B. A. Weaver, D. H. Weinberg, M. White, X. Xu, C. Yèche, I. Zehavi, and G.-B. Zhao. "The clustering of galaxies in the SDSS-III Baryon Oscillation Spectroscopic Survey: baryon acoustic oscillations in the Data Release 9 spectroscopic galaxy sample." *Mon.Not.Roy.As.Soc.* 427: (2012) 3435–3467.

Anderson, T. W. "An Introduction to Multivariate Statistical Analysis." *Wiley* 108: (2013) 190.

Avni, Y., and J. N. Bahcall. "On the simultaneous analysis of several complete samples - The V/Vmax and Ve/Va variables, with applications to quasars." *Astrophys. J.* 235: (1980) 694–716.

Babul, A., and S. D. M. White. "Quasar-modulated galaxy clustering in a cold dark matter universe." *Mon.Not.Roy.As.Soc.* 253: (1991) 31P–34P.

Bacon, D. J., A. R. Refregier, and R. S. Ellis. "Detection of weak gravitational lensing by large-scale structure." *Mon.Not.Roy.As.Soc.* 318: (2000) 625–640.

Baldauf, T., R. E. Smith, U. Seljak, and R. Mandelbaum. "Algorithm for the direct reconstruction of the dark matter correlation function from weak lensing and galaxy clustering." *Phys. Rev. D* 81, (2010) 6: 063531.

Ballinger, W. E., J. A. Peacock, and A. F. Heavens. "Measuring the cosmological constant with redshift surveys." *Mon.Not.Roy.As.Soc.* 282: (1996) 877.

Bardeen, J. M., J. R. Bond, N. Kaiser, and A. S. Szalay. "The statistics of peaks of Gaussian random fields." *Astrophys. J.* 304: (1986) 15–61.

Barkhouse, W. A., P. J. Green, A. Vikhlinin, D.-W. Kim, D. Perley, R. Cameron, J. Silverman, A. Mossman, R. Burenin, B. T. Jannuzi, M. Kim, M. G. Smith, R. C. Smith, H. Tananbaum, and B. J. Wilkes. "ChaMP Serendipitous Galaxy Cluster Survey." *Astrophys. J.* 645: (2006) 955–976.

Bartelmann, M., R. Narayan, S. Seitz, and P. Schneider. "Maximum-likelihood Cluster Reconstruction." *Astrophys. J. Lett.* 464: (1996) L115.

Bartelmann, M., and P. Schneider. "Power spectrum from weak-shear data." *Astron. & Astrophys.* 345: (1999) 17–21.

Basilakos, S., and M. Plionis. "Modelling the two-point correlation function of galaxy clusters in the Sloan Digital Sky Survey." *Mon.Not.Roy.As.Soc.* 349: (2004) 882–888.

Bekenstein, J. D. "Relativistic gravitation theory for the modified Newtonian dynamics paradigm." *Phys. Rev. D* 70,(2004) 8: 083509.

Bernardeau, F. "The effects of source clustering on weak lensing statistics." *Astron. & Astrophys.* 338: (1998) 375–382.

Berry, C. P. L., and J. R. Gair. "Linearized f(R) gravity: Gravitational radiation and Solar System tests." *Phys. Rev. D* 83, (2011) 10: 104022.

Beutler, F., S. Saito, H.-J. Seo, J. Brinkmann, K. S. Dawson, D. J. Eisenstein, A. Font-Ribera, S. Ho, C. K. McBride, F. Montesano, W. J. Percival, A. J. Ross, N. P. Ross, L. Samushia, D. J. Schlegel, A. G. Sánchez, J. L. Tinker, and B. A. Weaver. "The clustering of galaxies in the SDSS-III Baryon Oscillation Spectroscopic Survey: Testing gravity with redshift-space distortions using the power spectrum multipoles." *ArXiv e-prints* 1312.4889 (2013).

Blake, C., I. K. Baldry, J. Bland-Hawthorn, L. Christodoulou, M. Colless, C. Conselice, S. P. Driver, A. M. Hopkins, J. Liske, J. Loveday, P. Norberg, J. A. Peacock, G. B. Poole, and A. S. G. Robotham. "Galaxy And Mass Assembly (GAMA): improved cosmic growth measurements using multiple tracers of large-scale structure." *Mon.Not.Roy.As.Soc.* 436: (2013) 3089–3105.

Blake, C., S. Brough, M. Colless, C. Contreras, W. Couch, S. Croom, T. Davis, M. J. Drinkwater, K. Forster, D. Gilbank, M. Gladders, K. Glazebrook, B. Jelliffe, R. J. Jurek, I.-H. Li, B. Madore, D. C. Martin, K. Pimbblet, G. B. Poole, M. Pracy, R. Sharp, E. Wisnioski, D. Woods, T. K. Wyder, and H. K. C. Yee. "The WiggleZ Dark Energy Survey: the growth rate of cosmic structure since redshift z=0.9." *Mon.Not.Roy.As.Soc.* 415: (2011) 2876–2891.

Blake, C., and K. Glazebrook. "Probing Dark Energy Using Baryonic Oscillations in the Galaxy Power Spectrum as a Cosmological Ruler." *Astrophys. J.* 594: (2003) 665–673.

Böhringer, H., C. A. Collins, L. Guzzo, P. Schuecker, W. Voges, D. M. Neumann, S. Schindler, G. Chincarini, S. De Grandi, R. G. Cruddace, A. C. Edge, T. H. Reiprich, and P. Shaver. "The ROSAT-ESO Flux-limited X-Ray (REFLEX) Galaxy Cluster Survey. IV. The X-Ray Luminosity Function." *Astrophys. J.* 566: (2002) 93–102.

Böhringer, H., P. Schuecker, L. Guzzo, C. A. Collins, W. Voges, S. Schindler, D. M. Neumann, R. G. Cruddace, S. De Grandi, G. Chincarini, A. C. Edge, H. T. MacGillivray, and P. Shaver. "The ROSAT-ESO flux limited X-ray (REFLEX) galaxy cluster survey. I. The construction of the cluster sample." *Astron. & Astrophys.* 369: (2001) 826–850.

Bonnett, C. "The Scale Dependent Galaxy Bias from CFHTLenS." In *American Astronomical Society Meeting Abstracts #219*. 2012, volume 219 of *American Astronomical Society Meeting Abstracts*, 130.08.

Borgani, S., and S. A. Bonometto. "Biased theories of galaxy formation with arbitrary threshold functions and background distribution." *Astrophys. J.* 348: (1990) 398–411.

Borgani, S., and L. Guzzo. "X-ray clusters of galaxies as tracers of structure in the Universe." *Nature* 409: (2001) 39–45.

Borgani, S., P. Rosati, P. Tozzi, and C. Norman. "Cosmological Constraints from the ROSAT Deep Cluster Survey." *Astrophys. J.* 517: (1999) 40–53.

Brainerd, T. G., R. D. Blandford, and I. Smail. "Weak Gravitational Lensing by Galaxies." *Astrophys. J.* 466: (1996) 623.

Branch, D., W. Romanishin, and E. Baron. "Statistical Connections between the Properties of Type IA Supernovae and the B-V Colors of Their Parent Galaxies, and the Value of H 0." *Astrophys. J.* 465: (1996) 73.

Bridle, S. "Handbook for the GREAT08 Challenge: An image analysis competition for cosmological lensing." *Annals of Applied Statistics* 3: (2009) 6–37.

Burenin, R. A., A. Vikhlinin, A. Hornstrup, H. Ebeling, H. Quintana, and A. Mescheryakov. "The 400 Square Degree ROSAT PSPC Galaxy Cluster Survey: Catalog and Statistical Calibration." *Astrophys. J. Supp.* 172: (2007) 561–582.

Burke, D. J., C. A. Collins, R. M. Sharples, A. K. Romer, and R. C. Nichol. "The Southern SHARC catalogue: a ROSAT survey for distant galaxy clusters." *Mon.Not.Roy.As.Soc.* 341: (2003) 1093–1108.

Cacciato, M., O. Lahav, F. C. van den Bosch, H. Hoekstra, and A. Dekel. "On combining galaxy clustering and weak lensing to unveil galaxy biasing via the halo model." *Mon.Not.Roy.As.Soc.* 426: (2012) 566–587.

Cai, Y.-C., and G. Bernstein. "Combining weak-lensing tomography and spectroscopic redshift surveys." *Mon.Not.Roy.As.Soc.* 422: (2012) 1045–1056.

Carroll, S. M., W. H. Press, and E. L. Turner. "The cosmological constant." *Annu. Rev. Astron. Astrophys.* 30: (1992) 499–542.

Castander, F. J., R. G. Bower, R. S. Ellis, A. Aragón-Salamanca, K. O. Mason, G. Hasinger, R. G. McMahon, F. J. Carrera, J. P. D. Mittaz, I. Pérez-Fournon, and H. J. Lehto. "Deficit of distant X-ray-emitting galaxy clusters and implications for cluster evolution." *Nature* 377: (1995) 39–41.

Chan, K. C., R. Scoccimarro, and R. K. Sheth. "Gravity and large-scale nonlocal bias." *Phys. Rev. D* 85, (2012) 8: 083509.

Chatrchyan, S., V. Khachatryan, A. M. Sirunyan, A. Tumasyan, W. Adam, E. Aguilo, T. Bergauer, M. Dragicevic, J. Erö, C. Fabjan, and et al. "Observation of a new boson at a mass of 125 GeV with the CMS experiment at the LHC." *Physics Letters B* 716: (2012) 30–61.

Chuang, C.-H., F. Prada, F. Beutler, D. J. Eisenstein, S. Escoffier, S. Ho, J.-P. Kneib, M. Manera, S. E. Nuza, D. J. Schlegel, D. P. Schneider, B. A. Weaver, J. R. Brownstein, K. S. Dawson, C. Maraston, and D. Thomas. "The clustering of galaxies in the SDSS-III Baryon Oscillation Spectroscopic Survey: single-probe measurements from CMASS and LOWZ anisotropic galaxy clustering." *ArXiv e-prints* 1312.4889 (2013).

Clifton, T., P. G. Ferreira, A. Padilla, and C. Skordis. "Modified gravity and cosmology." *Physics Reports* 513: (2012) 1–189.

Clowes, R. G., K. A. Harris, S. Raghunathan, L. E. Campusano, I. K. Söchting, and M. J. Graham. "A structure in the early Universe that exceeds the homogeneity scale of the R-W concordance cosmology." *Mon.Not.Roy.As.Soc.* 429: (2013) 2910–2916.

Cole, S., W. J. Percival, J. A. Peacock, P. Norberg, C. M. Baugh, C. S. Frenk, I. Baldry, J. Bland-Hawthorn, T. Bridges, R. Cannon, M. Colless, C. Collins, W. Couch, N. J. G. Cross, G. Dalton, V. R. Eke, R. De Propris, S. P. Driver, G. Efstathiou, R. S. Ellis, K. Glazebrook, C. Jackson, A. Jenkins, O. Lahav, I. Lewis, S. Lumsden, S. Maddox, D. Madgwick, B. A. Peterson, W. Sutherland, and K. Taylor. "The 2dF Galaxy Redshift Survey: power-spectrum analysis of the final data set and cosmological implications." *Mon.Not.Roy.As.Soc.* 362: (2005) 505–534.

Coles, P. "Galaxy formation with a local bias." *Mon.Not.Roy.As.Soc.* 262: (1993) 1065–1075.

Coles, P., and P. Erdogdu. "Scale dependent galaxy bias." *Journal of Cosmology and Astroparticle Physics* (1993) 10: 007.

Cooray, A., W. Hu, D. Huterer, and M. Joffre. "Measuring Angular Diameter Distances through Halo Clustering." *Astrophys. J. Lett.* 557: (2001) L7–L10.

Cresswell, J. G., and W. J. Percival. "Scale-dependent galaxy bias in the Sloan Digital Sky Survey as a function of luminosity and colour." *Mon.Not.Roy.As.Soc.* 392: (2009) 682–690.

Davis, M., G. Efstathiou, C. S. Frenk, and S. D. M. White. "The evolution of large-scale structure in a universe dominated by cold dark matter." *Astrophys. J.* 292: (1985) 371–394.

Davis, M., and M. J. Geller. "Galaxy Correlations as a Function of Morphological Type." *Astrophys. J.* 208: (1976) 13–19.

Dawson, K. S., D. J. Schlegel, C. P. Ahn, S. F. Anderson, É. Aubourg, S. Bailey, R. H. Barkhouser, J. E. Bautista, A. Beifiori, A. A. Berlind, V. Bhardwaj, D. Bizyaev, C. H. Blake, M. R. Blanton, M. Blomqvist, A. S. Bolton, A. Borde, J. Bovy, W. N. Brandt, H. Brewington, J. Brinkmann, P. J. Brown, J. R. Brownstein, K. Bundy, N. G. Busca, W. Carithers, A. R. Carnero, M. A. Carr, Y. Chen, J. Comparat, N. Connolly, F. Cope, R. A. C. Croft, A. J. Cuesta, L. N. da Costa, J. R. A. Davenport, T. Delubac, R. de Putter, S. Dhital, A. Ealet, G. L. Ebelke, D. J. Eisenstein, S. Escoffier, X. Fan, N. Filiz Ak, H. Finley, A. Font-Ribera, R. Génova-Santos, J. E. Gunn, H. Guo, D. Haggard, P. B. Hall, J.-C. Hamilton, B. Harris, D. W. Harris, S. Ho, D. W. Hogg, D. Holder, K. Honscheid, J. Huehnerhoff, B. Jordan, W. P. Jordan, G. Kauffmann, E. A. Kazin, D. Kirkby, M. A. Klaene, J.-P. Kneib, J.-M. Le Goff, K.-G. Lee, D. C. Long, C. P. Loomis, B. Lundgren, R. H. Lupton, M. A. G. Maia, M. Makler, E. Malanushenko, V. Malanushenko, R. Mandelbaum, M. Manera, C. Maraston, D. Margala, K. L. Masters, C. K. McBride, P. McDonald, I. D. McGreer, R. G. McMahon, O. Mena, J. Miralda-Escudé, A. D. Montero-Dorta, F. Montesano, D. Muna, A. D. Myers, T. Naugle, R. C. Nichol, P. Noterdaeme, S. E. Nuza, M. D. Olmstead, A. Oravetz, D. J. Oravetz, R. Owen, N. Padmanabhan, N. Palanque-Delabrouille, K. Pan, J. K. Parejko, I. Pâris, W. J. Percival, I. Pérez-Fournon, I. Pérez-Ràfols, P. Petitjean,

R. Pfaffenberger, J. Pforr, M. M. Pieri, F. Prada, A. M. Price-Whelan, M. J. Raddick, R. Rebolo, J. Rich, G. T. Richards, C. M. Rockosi, N. A. Roe, A. J. Ross, N. P. Ross, G. Rossi, J. A. Rubiño-Martin, L. Samushia, A. G. Sánchez, C. Sayres, S. J. Schmidt, D. P. Schneider, C. G. Scóccola, H.-J. Seo, A. Shelden, E. Sheldon, Y. Shen, Y. Shu, A. Slosar, S. A. Smee, S. A. Snedden, F. Stauffer, O. Steele, M. A. Strauss, A. Streblyanska, N. Suzuki, M. E. C. Swanson, T. Tal, M. Tanaka, D. Thomas, J. L. Tinker, R. Tojeiro, C. A. Tremonti, M. Vargas Magaña, L. Verde, M. Viel, D. A. Wake, M. Watson, B. A. Weaver, D. H. Weinberg, B. J. Weiner, A. A. West, M. White, W. M. Wood-Vasey, C. Yeche, I. Zehavi, G.-B. Zhao, and Z. Zheng. "The Baryon Oscillation Spectroscopic Survey of SDSS-III." *Astron. J.* (2013) 145: 10.

De Grandi, S., H. Böhringer, L. Guzzo, S. Molendi, G. Chincarini, C. Collins, R. Cruddace, D. Neumann, S. Schindler, P. Schuecker, and W. Voges. "A Flux-limited Sample of Bright Clusters of Galaxies from the Southern Part of the ROSAT All-Sky Survey: The Catalog and LOG N-LOG S." *Astrophys. J.* 514: (1999) 148–163.

de la Torre, S., L. Guzzo, J. A. Peacock, E. Branchini, A. Iovino, B. R. Granett, U. Abbas, C. Adami, S. Arnouts, J. Bel, M. Bolzonella, D. Bottini, A. Cappi, J. Coupon, O. Cucciati, I. Davidzon, G. De Lucia, A. Fritz, P. Franzetti, M. Fumana, B. Garilli, O. Ilbert, J. Krywult, V. Le Brun, O. Le Fèvre, D. Maccagni, K. Małek, F. Marulli, H. J. McCracken, L. Moscardini, L. Paioro, W. J. Percival, M. Polletta, A. Pollo, H. Schlagenhaufer, M. Scodeggio, L. A. M. Tasca, R. Tojeiro, D. Vergani, A. Zanichelli, A. Burden, C. Di Porto, A. Marchetti, C. Marinoni, Y. Mellier, P. Monaco, R. C. Nichol, S. Phleps, M. Wolk, and G. Zamorani. "The VIMOS Public Extragalactic Redshift Survey (VIPERS) . Galaxy clustering and redshift-space distortions in the first data release." *Astron. & Astrophys.* (2013) 557: A54.

Dekel, A., and O. Lahav. "Stochastic Nonlinear Galaxy Biasing." *Astrophys. J.* 520: (1999) 24–34.

Desjacques, V., D. Jeong, and F. Schmidt. "Accurate predictions for the scale-dependent galaxy bias from primordial non-Gaussianity." *Phys. Rev. D* 84, (2011) 6: 061301.

Drinkwater, M. J., R. J. Jurek, C. Blake, D. Woods, K. A. Pimbblet, K. Glazebrook, R. Sharp, M. B. Pracy, S. Brough, M. Colless, W. J. Couch, S. M. Croom, T. M. Davis, D. Forbes, K. Forster, D. G. Gilbank, M. Gladders, B. Jelliffe, N. Jones, I.-H. Li, B. Madore, D. C. Martin, G. B. Poole, T. Small, E. Wisnioski, T. Wyder, and H. K. C. Yee. "The WiggleZ Dark Energy Survey: survey design and first data release." *Mon.Not.Roy.As.Soc.* 401: (2010) 1429–1452.

Driver, S. P., and A. S. G. Robotham. "Quantifying cosmic variance." *Mon.Not.Roy.As.Soc.* 407: (2010) 2131–2140.

Duncan, C. A. J., B. Joachimi, A. F. Heavens, C. Heymans, and H. Hildebrandt. "On the complementarity of galaxy clustering with cosmic shear and flux magnification." *Mon.Not.Roy.As.Soc.* 437: (2014) 2471–2487.

Dunkley, J., E. Komatsu, M. R. Nolta, D. N. Spergel, D. Larson, G. Hinshaw, L. Page, C. L. Bennett, B. Gold, N. Jarosik, J. L. Weiland, M. Halpern, R. S. Hill, A. Kogut, M. Limon, S. S. Meyer, G. S. Tucker, E. Wollack, and E. L. Wright. "Five-Year Wilkinson Microwave Anisotropy Probe Observations: Likelihoods and Parameters from the WMAP Data." *Astrophys. J. Supp.* 180: (2009) 306–329.

Dvali, G., G. Gabadadze, and M. Porrati. "4D gravity on a brane in 5D Minkowski space." *Physics Letters B* 485: (2000) 208–214.

Ebeling, H., A. C. Edge, S. W. Allen, C. S. Crawford, A. C. Fabian, and J. P. Huchra. "The ROSAT Brightest Cluster Sample - IV. The extended sample." *Mon.Not.Roy.As.Soc.* 318: (2000) 333–340.

Ebeling, H., A. C. Edge, H. Bohringer, S. W. Allen, C. S. Crawford, A. C. Fabian, W. Voges, and J. P. Huchra. "The ROSAT Brightest Cluster Sample - I. The compilation of the sample and the cluster log N-log S distribution." *Mon.Not.Roy.As.Soc.* 301: (1998) 881–914.

Ebeling, H., A. C. Edge, and J. P. Henry. "MACS: A Quest for the Most Massive Galaxy Clusters in the Universe." *Astrophys. J.* 553: (2001) 668–676.

Ebeling, H., and G. Wiedenmann. "Detecting structure in two dimensions combining Voronoi tessellation and percolation." *Phys. Rev. D* 47: (1993) 704–710.

Edge, A. C., G. C. Stewart, A. C. Fabian, and K. A. Arnaud. "An X-Ray Flux-Limited Sample of Clusters of Galaxies - Evidence for Evolution of the Luminosity Function." *Mon.Not.Roy.As.Soc.* 245: (1990) 559.

Efstathiou, G., W. J. Sutherland, and S. J. Maddox. "The cosmological constant and cold dark matter." *Nature* 348: (1990) 705–707.

Einstein, A. "Die Grundlage der allgemeinen Relativitätstheorie." *Annalen der Physik* 354: (1916) 769–822.

Eisenstein, D. J., W. Hu, J. Silk, and A. S. Szalay. "Can Baryonic Features Produce the Observed 100 h^{-1} Mpc Clustering?" *Astrophys. J. Lett.* 494: (1998) L1–L4.

Eisenstein, D. J., I. Zehavi, D. W. Hogg, R. Scoccimarro, M. R. Blanton, R. C. Nichol, R. Scranton, H.-J. Seo, M. Tegmark, Z. Zheng, S. F. Anderson, J. Annis, N. Bahcall, J. Brinkmann, S. Burles, F. J. Castander, A. Connolly, I. Csabai, M. Doi, M. Fukugita, J. A. Frieman, K. Glazebrook, J. E. Gunn, J. S. Hendry, G. Hennessy, Z. Ivezić, S. Kent, G. R. Knapp, H. Lin, Y.-S. Loh, R. H. Lupton, B. Margon, T. A. McKay, A. Meiksin, J. A. Munn, A. Pope, M. W. Richmond,

D. Schlegel, D. P. Schneider, K. Shimasaku, C. Stoughton, M. A. Strauss, M. SubbaRao, A. S. Szalay, I. Szapudi, D. L. Tucker, B. Yanny, and D. G. York. "Detection of the Baryon Acoustic Peak in the Large-Scale Correlation Function of SDSS Luminous Red Galaxies." *Astrophys. J.* 633: (2005) 560–574.

Ellis, S. C., and L. R. Jones. "A reanalysis of the X-ray luminosities of clusters of galaxies with 0.3 z 0.6 in the EMSS sample." *Mon.Not.Roy.As.Soc.* 330: (2002) 631–641.

Erben, T., H. Hildebrandt, L. Miller, L. van Waerbeke, C. Heymans, H. Hoekstra, T. D. Kitching, Y. Mellier, J. Benjamin, C. Blake, C. Bonnett, O. Cordes, J. Coupon, L. Fu, R. Gavazzi, B. Gillis, E. Grocutt, S. D. J. Gwyn, K. Holhjem, M. J. Hudson, M. Kilbinger, K. Kuijken, M. Milkeraitis, B. T. P. Rowe, T. Schrabback, E. Semboloni, P. Simon, M. Smit, O. Toader, S. Vafaei, E. van Uitert, and M. Velander. "CFHTLenS: the Canada-France-Hawaii Telescope Lensing Survey - imaging data and catalogue products." *Mon.Not.Roy.As.Soc.* 433: (2013) 2545–2563.

Fassbender, R., H. Böhringer, A. Nastasi, R. Šuhada, M. Mühlegger, A. de Hoon, J. Kohnert, G. Lamer, J. J. Mohr, D. Pierini, G. W. Pratt, H. Quintana, P. Rosati, J. S. Santos, and A. D. Schwope. "The x-ray luminous galaxy cluster population at 0.9 z 1.6 as revealed by the XMM-Newton Distant Cluster Project." *New Journal of Physics* 13, (2011) 12: 125014.

Fischer, P., T. A. McKay, E. Sheldon, A. Connolly, A. Stebbins, J. A. Frieman, B. Jain, M. Joffre, D. Johnston, G. Bernstein, J. Annis, N. A. Bahcall, J. Brinkmann, M. A. Carr, I. Csabai, J. E. Gunn, G. S. Hennessy, R. B. Hindsley, C. Hull, Ž. Ivezić, G. R. Knapp, S. Limmongkol, R. H. Lupton, J. A. Munn, T. Nash, H. J. Newberg, R. Owen, J. R. Pier, C. M. Rockosi, D. P. Schneider, J. A. Smith, C. Stoughton, A. S. Szalay, G. P. Szokoly, A. R. Thakar, M. S. Vogeley, P. Waddell, D. H. Weinberg, D. G. York, and SDSS Collaboration. "Weak Lensing with Sloan Digital Sky Survey Commissioning Data: The Galaxy-Mass Correlation Function to 1 H^{-1} Mpc." *Astron. J.* 120: (2000) 1198–1208.

Friedmann, A. "Über die Krümmung des Raumes." *Zeitschrift fur Physik* 10: (1922) 377–386.

Frieman, J. A., and E. Gaztanaga. "The three-point function as a probe of models for large-scale structure." *Astrophys. J.* 425: (1994) 392–402.

Fry, J. N., and E. Gaztanaga. "Biasing and hierarchical statistics in large-scale structure." *Astrophys. J.* 413: (1993) 447–452.

Gaztañaga, E., P. Norberg, C. M. Baugh, and D. J. Croton. "Statistical analysis of galaxy surveys - II. The three-point galaxy correlation function measured from the 2dFGRS." *Mon.Not.Roy.As.Soc.* 364: (2005) 620–634.

Gaztanaga, E., and J. A. Frieman. "Bias and high-order galaxy correlation functions in the APM galaxy survey." *Astrophys. J. Lett.* 437: (1994) L13–L16.

Gehrels, N. "Confidence limits for small numbers of events in astrophysical data." *Astrophys. J.* 303: (1986) 336–346.

Giannantonio, T., C. Porciani, J. Carron, A. Amara, and A. Pillepich. "Constraining primordial non-Gaussianity with future galaxy surveys." *Mon.Not.Roy.As.Soc.* 422: (2012) 2854–2877.

Gilbank, D. G., M. D. Gladders, H. K. C. Yee, and B. C. Hsieh. "The Red-sequence Cluster Survey-2 (RCS-2): Survey Details and Photometric Catalog Construction." *Astron. J.* 141: 94.

Gioia, I. M., J. P. Henry, T. Maccacaro, S. L. Morris, J. T. Stocke, and A. Wolter. "The Extended Medium Sensitivity Survey distant cluster sample - X-ray cosmological evolution." *Astrophys. J. Lett.* 356: (1990a) L35–L38.

Gioia, I. M., J. P. Henry, C. R. Mullis, W. Voges, U. G. Briel, H. Böhringer, and J. P. Huchra. "Cluster Evolution in the ROSAT North Ecliptic Pole Survey." *Astrophys. J. Lett.* 553: (2001) L105–L108.

Gioia, I. M., T. Maccacaro, R. E. Schild, A. Wolter, J. T. Stocke, S. L. Morris, and J. P. Henry. "The Einstein Observatory Extended Medium-Sensitivity Survey. I - X-ray data and analysis." *Astrophys. J. Supp.* 72: (1990b) 567–619.

Gladders, M. D., and H. K. C. Yee. "A New Method For Galaxy Cluster Detection. I. The Algorithm." *Astron. J.* 120: (2000) 2148–2162.

Gunn, J. E. "On the Propagation of Light in Inhomogeneous Cosmologies. I. Mean Effects." *Astrophys. J.* 150: (1967) 737.

Guo, H., Z. Zheng, I. Zehavi, K. Dawson, R. A. Skibba, J. L. Tinker, D. H. Weinberg, M. White, and D. P. Schneider. "Velocity Bias from the Small Scale Clustering of SDSS-III BOSS Galaxies." *ArXiv e-prints* 1407.4811 (2014).

Guth, A. H. "Inflationary universe: A possible solution to the horizon and flatness problems." *Phys. Rev. D* 23: (1981) 347–356.

Guzik, J., and U. Seljak. "Galaxy-dark matter correlations applied to galaxy-galaxy lensing: predictions from the semi-analytic galaxy formation models." *Mon.Not.Roy.As.Soc.* 321: (2001) 439–449.

Hall, B. "LaplacesDemon: Complete Environment for Bayesian Inference." (2012). http://www.bayesian-inference.com/software

Hamilton, A. J. S. "Toward Better Ways to Measure the Galaxy Correlation Function." *Astrophys. J.* 417: (1993) 19.

Harnois-Déraps, J., S. Vafaei, and L. Van Waerbeke. "Gravitational lensing simulations - I. Covariance matrices and halo catalogues." *Mon.Not.Roy.As.Soc.* 426: (2012) 1262–1279.

Harnois-Déraps, J., L. van Waerbeke, M. Viola, and C. Heymans. "Baryons, Neutrinos, Feedback and Weak Gravitational Lensing." *ArXiv e-prints* 1407.4301. (2014)

Hatton, S., and S. Cole. "Modelling the redshift-space distortion of galaxy clustering." *Mon.Not.Roy.As.Soc.* 296: (1998) 10–20.

Heavens, A., A. Refregier, and C. Heymans. "Intrinsic correlation of galaxy shapes: implications for weak lensing measurements." *Mon.Not.Roy.As.Soc.* 319: (2000) 649–656.

Heavens, A. F., S. Matarrese, and L. Verde. "The non-linear redshift-space power spectrum of galaxies." *Mon.Not.Roy.As.Soc.* 301: (1998) 797–808.

Heitmann, K., M. White, C. Wagner, S. Habib, and D. Higdon. "The Coyote Universe. I. Precision Determination of the Nonlinear Matter Power Spectrum." *Astrophys. J.* 715: (2010) 104–121.

Henry, J. P., I. M. Gioia, T. Maccacaro, S. L. Morris, J. T. Stocke, and A. Wolter. "The extended medium sensitivity survey distant cluster sample - X-ray data and interpretation of the luminosity evolution." *Astrophys. J.* 386: (1992) 408–419.

Henry, J. P., I. M. Gioia, C. R. Mullis, W. Voges, U. G. Briel, H. Böhringer, and J. P. Huchra. "Overview of the ROSAT North Ecliptic Pole Survey." *Astrophys. J. Lett.* 553: (2001) L109–L113.

Heymans, C., M. Brown, A. Heavens, K. Meisenheimer, A. Taylor, and C. Wolf. "Weak lensing with COMBO-17: estimation and removal of intrinsic alignments." *Mon.Not.Roy.As.Soc.* 347: (2004) 895–908.

Heymans, C., E. Grocutt, A. Heavens, M. Kilbinger, T. D. Kitching, F. Simpson, J. Benjamin, T. Erben, H. Hildebrandt, H. Hoekstra, Y. Mellier, L. Miller, L. Van Waerbeke, M. L. Brown, J. Coupon, L. Fu, J. Harnois-Déraps, M. J. Hudson, K. Kuijken, B. Rowe, T. Schrabback, E. Semboloni, S. Vafaei, and M. Velander. "CFHTLenS tomographic weak lensing cosmological parameter constraints: Mitigating the impact of intrinsic galaxy alignments." *Mon.Not.Roy.As.Soc.* 432: (2013) 2433–2453.

Heymans, C., L. Van Waerbeke, D. Bacon, J. Berge, G. Bernstein, E. Bertin, S. Bridle, M. L. Brown, D. Clowe, H. Dahle, T. Erben, M. Gray, M. Hetterscheidt, H. Hoekstra, P. Hudelot, M. Jarvis, K. Kuijken, V. Margoniner, R. Massey, Y. Mellier, R. Nakajima, A. Refregier, J. Rhodes, T. Schrabback, and D. Wittman. "The Shear Testing Programme - I. Weak lensing analysis of simulated ground-based observations." *Mon.Not.Roy.As.Soc.* 368: (2006) 1323–1339.

Heymans, C., L. Van Waerbeke, L. Miller, T. Erben, H. Hildebrandt, H. Hoekstra, T. D. Kitching, Y. Mellier, P. Simon, C. Bonnett, J. Coupon, L. Fu, J. Harnois Déraps, M. J. Hudson, M. Kilbinger, K. Kuijken, B. Rowe, T. Schrabback, E. Semboloni, E. van Uitert, S. Vafaei, and M. Velander. "CFHTLenS: the Canada-France-Hawaii Telescope Lensing Survey." *Mon.Not.Roy.As.Soc.* 427: (2012) 146–166.

Hildebrandt, H., T. Erben, K. Kuijken, L. van Waerbeke, C. Heymans, J. Coupon, J. Benjamin, C. Bonnett, L. Fu, H. Hoekstra, T. D. Kitching, Y. Mellier, L. Miller, M. Velander, M. J. Hudson, B. T. P. Rowe, T. Schrabback, E. Semboloni, and N. Benítez. "CFHTLenS: improving the quality of photometric redshifts with precision photometry." *Mon.Not.Roy.As.Soc.* 421: (2012) 2355–2367.

Hoekstra, H., and B. Jain. "Weak Gravitational Lensing and Its Cosmological Applications." *Annual Review of Nuclear and Particle Science* 58: (2008) 99–123.

Hoekstra, H., L. van Waerbeke, M. D. Gladders, Y. Mellier, and H. K. C. Yee. "Weak Lensing Study of Galaxy Biasing." *Astrophys. J.* 577: (2002) 604–614.

Horner, D. J., E. S. Perlman, H. Ebeling, L. R. Jones, C. A. Scharf, G. Wegner, M. Malkan, and B. Maughan. "The WARPS Survey. VII. The WARPS-II Cluster Catalog." *Astrophys. J. Supp.* 176: (2008) 374–413.

Hu, W., and A. V. Kravtsov. "Sample Variance Considerations for Cluster Surveys." *Astrophys. J.* 584: (2003) 702–715.

Jackson, J. C., and M. Dodgson. "Deceleration without dark matter." *Mon.Not.Roy.As.Soc.* 285: (1997) 806–810.

Jones, L. R., H. Ebeling, C. Scharf, E. Perlman, D. Horner, B. Fairely, G. Wegner, and M. Malkan. "Evolution of the Cluster X-ray Luminosity Function from the WARPS Survey." In *Large Scale Structure in the X-ray Universe*, edited by M. Plionis, and I. Georgantopoulos. 2000, 35.

Jones, L. R., C. Scharf, H. Ebeling, E. Perlman, G. Wegner, M. Malkan, and D. Horner. "The WARPS Survey. II. The log N– log S Relation and the X-Ray Evolution of Low-Luminosity Clusters of Galaxies." *Astrophys. J.* 495: (1998) 100–114.

Jönsson, J., T. Dahlén, A. Goobar, C. Gunnarsson, E. Mörtsell, and K. Lee. "Lensing Magnification of Supernovae in the GOODS Fields." *Astrophys. J.* 639: (2006) 991–998.

Jullo, E., S. Pires, M. Jauzac, and J.-P. Kneib. "Weak lensing galaxy cluster field reconstruction." *Mon.Not.Roy.As.Soc.* 437: (2014) 3969–3979.

Jullo, E., J. Rhodes, A. Kiessling, J. E. Taylor, R. Massey, J. Berge, C. Schimd, J.-P. Kneib, and N. Scoville. "COSMOS: Stochastic Bias from Measurements of Weak Lensing and Galaxy Clustering." *Astrophys. J.* (2012) 750: 37.

Kaiser, N. "On the spatial correlations of Abell clusters." *Astrophys. J. Lett.* 284: (1984) L9–L12.

———. "Evolution and clustering of rich clusters." *Mon.Not.Roy.As.Soc.* 222: (1986) 323–345.

———. "Clustering in real space and in redshift space." *Mon.Not.Roy.As.Soc.* 227: (1987) 1–21.

———. "Nonlinear cluster lens reconstruction." *Astrophys. J. Lett.* 439: (1995) L1–L3.

Kaiser, N., and G. Squires. "Mapping the dark matter with weak gravitational lensing." *Astrophys. J.* 404: (1993) 441–450.

Kaiser, N., G. Wilson, and G. A. Luppino. "Large-Scale Cosmic Shear Measurements." *ArXiv Astrophysics e-prints* 0003338 (2000).

Kashlinsky, A., F. Atrio-Barandela, D. Kocevski, and H. Ebeling. "A Measurement of Large-Scale Peculiar Velocities of Clusters of Galaxies: Results and Cosmological Implications." *Astrophys. J. Lett.* 686: (2008) L49–L52.

Kereš, D., M. Vogelsberger, D. Sijacki, V. Springel, and L. Hernquist. "Moving-mesh cosmology: characteristics of galaxies and haloes." *Mon.Not.Roy.As.Soc.* 425: (2012) 2027–2048.

Kiessling, A., A. N. Taylor, and A. F. Heavens. "Simulating the effect of non-linear mode coupling in cosmological parameter estimation." *Mon.Not.Roy.As.Soc.* 416: (2011) 1045–1055.

Kilbinger, M., L. Fu, C. Heymans, F. Simpson, J. Benjamin, T. Erben, J. Harnois-Déraps, H. Hoekstra, H. Hildebrandt, T. D. Kitching, Y. Mellier, L. Miller, L. Van Waerbeke, K. Benabed, C. Bonnett, J. Coupon, M. J. Hudson, K. Kuijken, B. Rowe, T. Schrabback, E. Semboloni, S. Vafaei, and M. Velander. "CFHTLenS: combined probe cosmological model comparison using 2D weak gravitational lensing." *Mon.Not.Roy.As.Soc.* 430: (2013) 2200–2220.

Kim, A., A. Goobar, and S. Perlmutter. "A Generalized K Correction for Type IA Supernovae: Comparing R-band Photometry beyond z=0.2 with B, V, and R-band Nearby Photometry." *Pub. Astron. Soc. Pac.* 108: (1996) 190.

Kirk, D., O. Lahav, S. Bridle, S. Jouvel, F. B. Abdalla, and J. A. Frieman. "Optimising Spectroscopic and Photometric Galaxy Surveys: Same-sky Benefits for Dark Energy and Modified Gravity." *ArXiv e-prints* 1307.8062 (2013).

Klein, O. "Quantentheorie und fünfdimensionale Relativitätstheorie." *Zeitschrift fur Physik* 37: (1926) 895–906.

Koens, L. A., B. J. Maughan, L. R. Jones, H. Ebeling, D. J. Horner, E. S. Perlman, S. Phillipps, and C. A. Scharf. "The WARPS Survey - VIII. Evolution of the galaxy cluster X-ray Luminosity Function." *Mon.Not.Roy.As.Soc.* 435: (2013) 3231–3242.

Koester, B. P., T. A. McKay, J. Annis, R. H. Wechsler, A. Evrard, L. Bleem, M. Becker, D. Johnston, E. Sheldon, R. Nichol, C. Miller, R. Scranton, N. Bahcall, J. Barentine, H. Brewington, J. Brinkmann, M. Harvanek, S. Kleinman, J. Krzesinski, D. Long, A. Nitta, D. P. Schneider, S. Sneddin, W. Voges, and D. York. "A MaxBCG Catalog of 13,823 Galaxy Clusters from the Sloan Digital Sky Survey." *Astrophys. J.* 660: (2007) 239–255.

Kristian, J., and R. K. Sachs. "Observations in Cosmology." *Astrophys. J.* 143: (1966) 379.

Landy, S. D., and A. S. Szalay. "Bias and variance of angular correlation functions." *Astrophys. J.* 412: (1993) 64–71.

Lange, A. E., P. A. Ade, J. J. Bock, J. R. Bond, J. Borrill, A. Boscaleri, K. Coble, B. P. Crill, P. de Bernardis, P. Farese, P. Ferreira, K. Ganga, M. Giacometti, E. Hivon, V. V. Hristov, A. Iacoangeli, A. H. Jaffe, L. Martinis, S. Masi, P. D. Mauskopf, A. Melchiorri, T. Montroy, C. B. Netterfield, E. Pascale, F. Piacentini, D. Pogosyan, S. Prunet, S. Rao, G. Romeo, J. E. Ruhl, F. Scaramuzzi, and D. Sforna. "Cosmological parameters from the first results of Boomerang." *Phys. Rev. D* 63, (1993) 4: 042001.

Laureijs, R., J. Amiaux, S. Arduini, J. . Augueres, J. Brinchmann, R. Cole, M. Cropper, C. Dabin, L. Duvet, A. Ealet, and et al. "Euclid Definition Study Report." *ArXiv e-prints* 1110.3193 (2011).

Lawrence, E., K. Heitmann, M. White, D. Higdon, C. Wagner, S. Habib, and B. Williams. "The Coyote Universe. III. Simulation Suite and Precision Emulator for the Nonlinear Matter Power Spectrum." *Astrophys. J.* 713: (2010) 1322–1331.

Lehnert, M. D., N. P. H. Nesvadba, J.-G. Cuby, A. M. Swinbank, S. Morris, B. Clément, C. J. Evans, M. N. Bremer, and S. Basa. "Spectroscopic confirmation of a galaxy at redshift z = 8.6." *Nature* 467: (2010) 940–942.

Lemaître, G. "Expansion of the universe, A homogeneous universe of constant mass and increasing radius accounting for the radial velocity of extra-galactic nebulae." *Mon.Not.Roy.As.Soc.* 91: (1931) 483–490.

Lewis, A., and S. Bridle. "Cosmological parameters from CMB and other data: A Monte Carlo approach." *Phys. Rev. D* 66, (2002) 10: 103511.

Limber, D. N. "The Analysis of Counts of the Extragalactic Nebulae in Terms of a Fluctuating Density Field." *Astrophys. J.* 117: (1953) 134.

Linder, E. V. "Cosmic growth history and expansion history." *Phys. Rev. D* 72, (2005) 4: 043529.

Lindsay, S. N., M. J. Jarvis, M. G. Santos, M. J. I. Brown, S. M. Croom, S. P. Driver, A. M. Hopkins, J. Liske, J. Loveday, P. Norberg, and A. S. G. Robotham. "Galaxy and Mass Assembly: the evolution of bias in the radio source population." *Mon.Not.Roy.As.Soc.* 440: (2014) 1527–1541.

Lombardi, M., P. Schneider, and C. Morales-Merino. "The noise of cluster mass reconstructions from a source redshift distribution." *Astron. & Astrophys.* 382: (2002) 769–786.

Mandelbaum, R., U. Seljak, G. Kauffmann, C. M. Hirata, and J. Brinkmann. "Galaxy halo masses and satellite fractions from galaxy-galaxy lensing in the Sloan Digital Sky Survey: stellar mass, luminosity, morphology and environment dependencies." *Mon.Not.Roy.As.Soc.* 368: (2006) 715–731.

Mandelbaum, R., A. Slosar, T. Baldauf, U. Seljak, C. M. Hirata, R. Nakajima, R. Reyes, and R. E. Smith. "Cosmological parameter constraints from galaxy-galaxy lensing and galaxy clustering with the SDSS DR7." *Mon.Not.Roy.As.Soc.* 432: (2013) 1544–1575.

Manera, M., and E. Gaztañaga. "The local bias model in the large-scale halo distribution." *Mon.Not.Roy.As.Soc.* 415: (2011) 383–398.

Mann, R. G., J. A. Peacock, and A. F. Heavens. "Eulerian bias and the galaxy density field." *Mon.Not.Roy.As.Soc.* 293: (1998) 209.

Mantz, A., S. W. Allen, H. Ebeling, and D. Rapetti. "New constraints on dark energy from the observed growth of the most X-ray luminous galaxy clusters." *Mon.Not.Roy.As.Soc.* 387: (2008) 1179–1192.

Mantz, A., S. W. Allen, H. Ebeling, D. Rapetti, and A. Drlica-Wagner. "The observed growth of massive galaxy clusters - II. X-ray scaling relations." *Mon.Not.Roy.As.Soc.* 406: (2010) 1773–1795.

Marín, F. A., C. Blake, G. B. Poole, C. K. McBride, S. Brough, M. Colless, C. Contreras, W. Couch, D. J. Croton, S. Croom, T. Davis, M. J. Drinkwater, K. Forster, D. Gilbank, M. Gladders, K. Glazebrook, B. Jelliffe, R. J. Jurek, I.-h. Li, B. Madore, D. C. Martin, K. Pimbblet, M. Pracy, R. Sharp, E. Wisnioski, D. Woods, T. K. Wyder, and H. K. C. Yee. "The WiggleZ Dark Energy Survey: constraining galaxy bias and cosmic growth with three-point correlation functions." *Mon.Not.Roy.As.Soc.* 432: (2013) 2654–2668.

Markevitch, M. "The L_X-T Relation and Temperature Function for Nearby Clusters Revisited." *Astrophys. J.* 504: (1998) 27–34.

Markevitch, M., A. H. Gonzalez, D. Clowe, A. Vikhlinin, W. Forman, C. Jones, S. Murray, and W. Tucker. "Direct Constraints on the Dark Matter Self-Interaction Cross Section from the Merging Galaxy Cluster 1E 0657-56." *Astrophys. J.* 606: (2004) 819–824.

Marshall, H. L., H. Tananbaum, Y. Avni, and G. Zamorani. "Analysis of complete quasar samples to obtain parameters of luminosity and evolution functions." *Astrophys. J.* 269: (1983) 35–41.

Mason, K. O., F. J. Carrera, G. Hasinger, H. Andernach, A. Aragon-Salamanca, X. Barcons, R. Bower, W. N. Brandt, G. Branduardi-Raymont, J. Burgos-Martín, F. Cabrera-Guerra, R. Carballo, F. Castander, R. S. Ellis, J. I. González-Serrano, E. Martínez-González, J. M. Martín-Mirones, R. G. McMahon, J. P. D. Mittaz, K. L. Nicholson, M. J. Page, I. Pérez-Fournon, E. M. Puchnarewicz, E. Romero-Colmenero, A. D. Schwope, B. Vila, M. G. Watson, and D. Wonnacott. "The ROSAT International X-ray/Optical Survey (RIXOS): source catalogue." *Mon.Not.Roy.As.Soc.* 311: (2000) 456–484.

Massey, R., J. Rhodes, R. Ellis, N. Scoville, A. Leauthaud, A. Finoguenov, P. Capak, D. Bacon, H. Aussel, J.-P. Kneib, A. Koekemoer, H. McCracken, B. Mobasher, S. Pires, A. Refregier, S. Sasaki, J.-L. Starck, Y. Taniguchi, A. Taylor, and J. Taylor. "Dark matter maps reveal cosmic scaffolding." *Nature* 445: (2007) 286–290.

Matsubara, T. "Diagrammatic Methods in Statistics and Biasing in the Large-Scale Structure of the Universe." *Astrophys. J. Supp.* 101: (1995) 1.

Maughan, B. J., C. Jones, W. Forman, and L. Van Speybroeck. "Images, Structural Properties, and Metal Abundances of Galaxy Clusters Observed with Chandra ACIS-I at 0.1 z 1.3." *Astrophys. J. Supp.* 174: (2008) 117–135.

Maughan, B. J., C. Jones, L. R. Jones, and L. Van Speybroeck. "Deep XMM-Newton and Chandra Observations of Cl J1226.9+3332: A Detailed X-Ray Mass Analysis of a z = 0.89 Galaxy Cluster." *Astrophys. J.* 659: (2007) 1125–1137.

McDonald, P. "Clustering of dark matter tracers: Renormalizing the bias parameters." *Phys. Rev. D* 74, (2006) 10: 103512.

McDonald, P., and D. J. Eisenstein. "Dark energy and curvature from a future baryonic acoustic oscillation survey using the Lyman-α forest." *Phys. Rev. D* 76, (2007) 6: 063009.

McDonald, P., and U. Seljak. "How to evade the sample variance limit on measurements of redshift-space distortions." *Journal of Cosmology and Astroparticle Physics* 10: 007. (2009)

Mehrtens, N., A. K. Romer, M. Hilton, E. J. Lloyd-Davies, C. J. Miller, S. A. Stanford, M. Hosmer, B. Hoyle, C. A. Collins, A. R. Liddle, P. T. P. Viana, R. C. Nichol, J. P. Stott, E. N. Dubois, S. T. Kay, M. Sahlén, O. Young, C. J. Short, L. Christodoulou, W. A. Watson, M. Davidson, C. D. Harrison, L. Baruah, M. Smith, C. Burke, J. A. Mayers, P.-J. Deadman, P. J. Rooney, E. M. Edmondson, M. West, H. C. Campbell, A. C. Edge, R. G. Mann, K. Sabirli, D. Wake, C. Benoist, L. da Costa, M. A. G. Maia, and R. Ogando.

"The XMM Cluster Survey: optical analysis methodology and the first data release." *Mon.Not.Roy.As.Soc.* 423: (2012) 1024–1052.

Meiksin, A., M. White, and J. A. Peacock. "Baryonic signatures in large-scale structure." *Mon.Not.Roy.As.Soc.* 304: (1999) 851–864.

Merloni, A., P. Predehl, W. Becker, H. Böhringer, T. Boller, H. Brunner, M. Brusa, K. Dennerl, M. Freyberg, P. Friedrich, A. Georgakakis, F. Haberl, G. Hasinger, N. Meidinger, J. Mohr, K. Nandra, A. Rau, T. H. Reiprich, J. Robrade, M. Salvato, A. Santangelo, M. Sasaki, A. Schwope, J. Wilms, and t. German eROSITA Consortium. "eROSITA Science Book: Mapping the Structure of the Energetic Universe." *ArXiv e-prints* 1209.3114 . (2012)

Milgrom, M. "A modification of the Newtonian dynamics as a possible alternative to the hidden mass hypothesis." *Astrophys. J.* 270: (1983) 365–370.

Miller, C. J., D. J. Batuski, K. A. Slinglend, and J. M. Hill. "Projection, Spatial Correlations, and Anisotropies in a Large and Complete Sample of Abell Clusters." *Astrophys. J.* 523: (1999) 492–505.

Miller, L., C. Heymans, T. D. Kitching, L. van Waerbeke, T. Erben, H. Hildebrandt, H. Hoekstra, Y. Mellier, B. T. P. Rowe, J. Coupon, J. P. Dietrich, L. Fu, J. Harnois-Déraps, M. J. Hudson, M. Kilbinger, K. Kuijken, T. Schrabback, E. Semboloni, S. Vafaei, and M. Velander. "Bayesian galaxy shape measurement for weak lensing surveys - III. Application to the Canada-France-Hawaii Telescope Lensing Survey." *Mon.Not.Roy.As.Soc.* 429: (2013) 2858–2880.

Mo, H. J., and S. D. M. White. "An analytic model for the spatial clustering of dark matter haloes." *Mon.Not.Roy.As.Soc.* 282: (1996) 347–361.

Moretti, A., L. Guzzo, S. Campana, S. Covino, D. Lazzati, M. Longhetti, E. Molinari, M. R. Panzera, G. Tagliaferri, and I. dell'Antonio. "The BMW Deep X-ray Cluster Survey." In *X-ray Astronomy 2000*, edited by R. Giacconi, S. Serio, and L. Stella. 2001, volume 234 of *Astronomical Society of the Pacific Conference Series*, 393. (2000)

Moscardini, L., S. Matarrese, and H. J. Mo. "Constraining cosmological parameters with the clustering properties of galaxy clusters in optical and X-ray bands." *Mon.Not.Roy.As.Soc.* 327: (2001) 422–434.

Mullis, C. R., B. R. McNamara, H. Quintana, A. Vikhlinin, J. P. Henry, I. M. Gioia, A. Hornstrup, W. Forman, and C. Jones. "The 160 Square Degree ROSAT Survey: The Revised Catalog of 201 Clusters with Spectroscopic Redshifts." *Astrophys. J.* 594: (2003) 154–171.

Mullis, C. R., A. Vikhlinin, J. P. Henry, W. Forman, I. M. Gioia, A. Hornstrup, C. Jones, B. R. McNamara, and H. Quintana. "Evolution of the Cluster X-Ray Luminosity Function." *Astrophys. J.* 607: (2004) 175–189.

Nishizawa, A. J., M. Takada, and T. Nishimichi. "Perturbation theory for the non-linear halo power spectrum: the renormalized bias and halo bias." *Mon.Not.Roy.As.Soc.* 433: (2013) 209–220.

Norberg, P., C. M. Baugh, E. Hawkins, S. Maddox, D. Madgwick, O. Lahav, S. Cole, C. S. Frenk, I. Baldry, J. Bland-Hawthorn, T. Bridges, R. Cannon, M. Colless, C. Collins, W. Couch, G. Dalton, R. De Propris, S. P. Driver, G. Efstathiou, R. S. Ellis, K. Glazebrook, C. Jackson, I. Lewis, S. Lumsden, J. A. Peacock, B. A. Peterson, W. Sutherland, and K. Taylor. "The 2dF Galaxy Redshift Survey: the dependence of galaxy clustering on luminosity and spectral type." *Mon.Not.Roy.As.Soc.* 332: (2002) 827–838.

Nuza, S. E., A. G. Sánchez, F. Prada, A. Klypin, D. J. Schlegel, S. Gottlöber, A. D. Montero-Dorta, M. Manera, C. K. McBride, A. J. Ross, R. Angulo, M. Blanton, A. Bolton, G. Favole, L. Samushia, F. Montesano, W. J. Percival, N. Padmanabhan, M. Steinmetz, J. Tinker, R. Skibba, D. P. Schneider, H. Guo, I. Zehavi, Z. Zheng, D. Bizyaev, O. Malanushenko, V. Malanushenko, A. E. Oravetz, D. J. Oravetz, and A. C. Shelden. "The clustering of galaxies at z 0.5 in the SDSS-III Data Release 9 BOSS-CMASS sample: a test for the ΛCDM cosmology." *Mon.Not.Roy.As.Soc.* 432: (2013) 743–760.

Page, M. J., and F. J. Carrera. "An improved method of constructing binned luminosity functions." *Mon.Not.Roy.As.Soc.* 311: (2000) 433–440.

Panzera, M. R., S. Campana, S. Covino, D. Lazzati, R. P. Mignani, A. Moretti, and G. Tagliaferri. "The Brera Multi-scale Wavelet ROSAT HRI source catalogue." *Astron. & Astrophys.* 399: (2003) 351–364.

Peacock, J. A., and S. J. Dodds. "Non-linear evolution of cosmological power spectra." *Mon.Not.Roy.As.Soc.* 280: (1996) L19–L26.

Peacock, J. A., and R. E. Smith. "Halo occupation numbers and galaxy bias." *Mon.Not.Roy.As.Soc.* 318: (2000) 1144–1156.

Peebles, P. J. E. *The large-scale structure of the universe.* Princeton University Press (1980).

Pen, U.-L. "Reconstructing Nonlinear Stochastic Bias from Velocity Space Distortions." *Astrophys. J.* 504: (1998) 601–606.

Perlman, E. S., D. J. Horner, L. R. Jones, C. A. Scharf, H. Ebeling, G. Wegner, and M. Malkan. "The WARPS Survey. VI. Galaxy Cluster and Source Identifications from Phase I." *Astrophys. J. Supp.* 140: (2002) 265–301.

Perlmutter, S., G. Aldering, G. Goldhaber, R. A. Knop, P. Nugent, P. G. Castro, S. Deustua, S. Fabbro, A. Goobar, D. E. Groom, I. M. Hook, A. G. Kim, M. Y. Kim, J. C. Lee, N. J. Nunes, R. Pain, C. R. Pennypacker, R. Quimby, C. Lidman, R. S. Ellis, M. Irwin, R. G. McMahon, P. Ruiz-Lapuente, N. Walton, B. Schaefer, B. J. Boyle, A. V. Filippenko, T. Matheson, A. S. Fruchter, N. Panagia, H. J. M. Newberg, W. J. Couch, and T. S. C.

Project. "Measurements of Ω and Λ from 42 High-Redshift Supernovae." *Astrophys. J.* 517: (1999) 565–586.

Pierre, M., F. Pacaud, J. B. Juin, J. B. Melin, P. Valageas, N. Clerc, and P. S. Corasaniti. "Precision cosmology with a wide area XMM cluster survey." *Mon.Not.Roy.As.Soc.* 414: (2011) 1732–1746.

Planck Collaboration, P. A. R. Ade, N. Aghanim, M. I. R. Alves, C. Armitage-Caplan, M. Arnaud, M. Ashdown, F. Atrio-Barandela, J. Aumont, H. Aussel, and et al. "Planck 2013 results. I. Overview of products and scientific results." *ArXiv e-prints* 1303.5062 (2013)

Planck Collaboration, P. A. R. Ade, N. Aghanim, C. Armitage-Caplan, M. Arnaud, M. Ashdown, F. Atrio-Barandela, J. Aumont, H. Aussel, C. Baccigalupi, and et al. "Planck 2013 results. XXIX. Planck catalogue of Sunyaev-Zeldovich sources." *ArXiv e-prints*. 1303.5076 (2013)

Planck Collaboration, P. A. R. Ade, N. Aghanim, C. Armitage-Caplan, M. Arnaud, M. Ashdown, F. Atrio-Barandela, J. Aumont, C. Baccigalupi, A. J. Banday, and et al. "Planck 2013 results. XVI. Cosmological parameters." *ArXiv e-prints* 1303.5089 (2013)

———. "Planck 2013 results. XX. Cosmology from Sunyaev-Zeldovich cluster counts." *ArXiv e-prints* 1303.5080 (2013)

Pollack, J. E., R. E. Smith, and C. Porciani. "Modelling large-scale halo bias using the bispectrum." *Mon.Not.Roy.As.Soc.* 420: (2012) 3469–3489.

Poole, G. B., C. Blake, F. A. Marin, C. Power, S. J. Mutch, D. J. Croton, M. Colless, W. Couch, M. J. Drinkwater, and K. Glazebrook. "The Gigaparsec WiggleZ Simulations: Characterising scale dependant bias and associated systematics in growth of structure measurements." *ArXiv e-prints* 1407.0390 (2014)

R Development Core Team. "R: A Language and Environment for Statistical Computing." http://www.r-project.org/ (2012) .

Randall, L., and R. Sundrum. "Large Mass Hierarchy from a Small Extra Dimension." *Physical Review Letters* 83: (1999) 3370–3373.

Rees, M. J., and D. W. Sciama. "Large-scale Density Inhomogeneities in the Universe." *Nature* 217: (1968) 511–516.

Riess, A. G., A. V. Filippenko, P. Challis, A. Clocchiatti, A. Diercks, P. M. Garnavich, R. L. Gilliland, C. J. Hogan, S. Jha, R. P. Kirshner, B. Leibundgut, M. M. Phillips, D. Reiss, B. P. Schmidt, R. A. Schommer, R. C. Smith, J. Spyromilio, C. Stubbs, N. B. Suntzeff, and J. Tonry. "Observational Evidence from Supernovae for an Accelerating Universe and a Cosmological Constant." *Astron. J.* 116: (1998) 1009–1038.

Roche, N., and S. A. Eales. "The angular correlation function and hierarchical moments of ˜70000 faint galaxies to R=23.5." *Mon.Not.Roy.As.Soc.* 307: (1999) 703–721.

Romer, A. K., R. C. Nichol, B. P. Holden, M. P. Ulmer, R. A. Pildis, A. J. Merrelli, C. Adami, D. J. Burke, C. A. Collins, A. J. Metevier, R. G. Kron, and K. Commons. "The Bright SHARC Survey: The Cluster Catalog." *Astrophys. J. Supp.* 126: (2000) 209–269.

Rosati, P., R. Della Ceca, R. Burg, C. Norman, and R. Giacconi. "A first determination of the surface density of galaxy clusters at very low x-ray fluxes." *Astrophys. J. Lett.* 445: (1995) L11–L14.

Rosati, P., R. Della Ceca, C. Norman, and R. Giacconi. "The ROSAT Deep Cluster Survey: The X-Ray Luminosity Function out to z = 0.8." *Astrophys. J. Lett.* 492: (1998) L21–L24.

Sachs, R. K., and A. M. Wolfe. "Perturbations of a Cosmological Model and Angular Variations of the Microwave Background." *Astrophys. J.* 147: (1967) 73.

Samushia, L., B. A. Reid, M. White, W. J. Percival, A. J. Cuesta, L. Lombriser, M. Manera, R. C. Nichol, D. P. Schneider, D. Bizyaev, H. Brewington, E. Malanushenko, V. Malanushenko, D. Oravetz, K. Pan, A. Simmons, A. Shelden, S. Snedden, J. L. Tinker, B. A. Weaver, D. G. York, and G.-B. Zhao. "The clustering of galaxies in the SDSS-III DR9 Baryon Oscillation Spectroscopic Survey: testing deviations from Λ and general relativity using anisotropic clustering of galaxies." *Mon.Not.Roy.As.Soc.* 429: (2013) 1514–1528.

Sánchez, A. G., E. A. Kazin, F. Beutler, C.-H. Chuang, A. J. Cuesta, D. J. Eisenstein, M. Manera, F. Montesano, R. C. Nichol, N. Padmanabhan, W. Percival, F. Prada, A. J. Ross, D. J. Schlegel, J. Tinker, R. Tojeiro, D. H. Weinberg, X. Xu, J. Brinkmann, J. R. Brownstein, D. P. Schneider, and D. Thomas. "The clustering of galaxies in the SDSS-III Baryon Oscillation Spectroscopic Survey: cosmological constraints from the full shape of the clustering wedges." *Mon.Not.Roy.As.Soc.* 433: (2013) 1202–1222.

Sandage, A. "The Change of Redshift and Apparent Luminosity of Galaxies due to the Deceleration of Selected Expanding Universes." *Astrophys. J.* 136: (1962) 319.

Santos, J. S., P. Tozzi, P. Rosati, and H. Böhringer. "The evolution of cool-core clusters." *Astron. & Astrophys.* 521: A64. (2010)

Sasaki, S. "A New Method to Estimate Cosmological Parameters Using the Baryon Fraction of Clusters of Galaxies." *Pub. of the Astron. Soc. of Japan* 48: (1996) L119–L122.

Sato, K. "First-order phase transition of a vacuum and the expansion of the Universe." *Mon.Not.Roy.As.Soc.* 195: (1981) 467–479.

Scharf, C. A., H. Ebeling, E. Perlman, M. Malkan, and G. Wegner. "The Wide-Angle ROSAT Pointed X-Ray Survey of Galaxies, Groups, and Clusters. I. Method and First Results." *Astrophys. J.* 477: (1997) 79–92.

Schechter, P. "An analytic expression for the luminosity function for galaxies." *Astrophys. J.* 203: (1976) 297–306.

Schmidt, F., and E. Rozo. "Weak-lensing Peak Finding: Estimators, Filters, and Biases." *Astrophys. J.* (2011) 735: 119.

Schmidt, F., E. Rozo, S. Dodelson, L. Hui, and E. Sheldon. "Lensing Bias in Cosmic Shear." *Astrophys. J.* 702: (2009) 593–602.

Schmidt, M. "Space Distribution and Luminosity Functions of Quasi-Stellar Radio Sources." *Astrophys. J.* 151: (1968) 393.

Schneider, P. "Detection of (dark) matter concentrations via weak gravitational lensing." *Mon.Not.Roy.As.Soc.* 283: (1996) 837–853.

Schneider, P., L. van Waerbeke, B. Jain, and G. Kruse. "A new measure for cosmic shear." *Mon.Not.Roy.As.Soc.* 296: (1998) 873–892.

Schneider, P., L. van Waerbeke, M. Kilbinger, and Y. Mellier. "Analysis of two-point statistics of cosmic shear. I. Estimators and covariances." *Astron. & Astrophys.* 396: (2002a) 1–19.

Schneider, P., L. van Waerbeke, and Y. Mellier. "B-modes in cosmic shear from source redshift clustering." *Astron. & Astrophys.* 389: (2002b) 729–741.

Schuecker, P., H. Böhringer, C. A. Collins, and L. Guzzo. "The REFLEX galaxy cluster survey. VII. Omega$_m$ and sigma$_8$ from cluster abundance and large-scale clustering." *Astron. & Astrophys.* 398: (2003) 867–877.

Schulz, A. E., and M. White. "Scale-dependent bias and the halo model." *Astroparticle Physics* 25: (2006) 172–177.

Scoccimarro, R. "Redshift-space distortions, pairwise velocities, and nonlinearities." *Phys. Rev. D* 70, (2004) 8: 083007.

Scoccimarro, R., R. K. Sheth, L. Hui, and B. Jain. "How Many Galaxies Fit in a Halo? Constraints on Galaxy Formation Efficiency from Spatial Clustering." *Astrophys. J.* 546: (2001) 20–34.

Seifert, M. D. "Stability of spherically symmetric solutions in modified theories of gravity." *Phys. Rev. D* 76, (2007) 6: 064002.

Seitz, C., and P. Schneider. "Steps towards nonlinear cluster inversion through gravitational distortions. III. Including a redshift distribution of the sources." *Astron. & Astrophys.* 318: (1997) 687–699.

Seljak, U., and M. Zaldarriaga. "A Line-of-Sight Integration Approach to Cosmic Microwave Background Anisotropies." *Astrophys. J.* 469: (1996) 437.

Seo, H.-J., and D. J. Eisenstein. "Baryonic Acoustic Oscillations in Simulated Galaxy Redshift Surveys." *Astrophys. J.* 633: (2005) 575–588.

Shanks, T., R. Fong, B. J. Boyle, and B. A. Peterson. "The spatial clustering of QSOs." *Mon.Not.Roy.As.Soc.* 227: (1987) 739–748.

Sherwin, B. D., J. Dunkley, S. Das, J. W. Appel, J. R. Bond, C. S. Carvalho, M. J. Devlin, R. Dünner, T. Essinger-Hileman, J. W. Fowler, A. Hajian, M. Halpern, M. Hasselfield, A. D. Hincks, R. Hlozek, J. P. Hughes, K. D. Irwin, J. Klein, A. Kosowsky, T. A. Marriage, D. Marsden, K. Moodley, F. Menanteau, M. D. Niemack, M. R. Nolta, L. A. Page, L. Parker, E. D. Reese, B. L. Schmitt, N. Sehgal, J. Sievers, D. N. Spergel, S. T. Staggs, D. S. Swetz, E. R. Switzer, R. Thornton, K. Visnjic, and E. Wollack. "Evidence for Dark Energy from the Cosmic Microwave Background Alone Using the Atacama Cosmology Telescope Lensing Measurements." *Physical Review Letters* 107, (2011) 2: 021302.

Simon, P. "Time evolution of the stochastic linear bias of interacting galaxies on linear scales." *Astron. & Astrophys.* 430: (2005) 827–842.

———. "Retrieving the three-dimensional matter power spectrum and galaxy biasing parameters from lensing tomography." *Astron. & Astrophys.* (2012) 543: A2.

Simon, P., M. Hetterscheidt, M. Schirmer, T. Erben, P. Schneider, C. Wolf, and K. Meisenheimer. "GaBoDS: The Garching-Bonn Deep Survey. VI. Probing galaxy bias using weak gravitational lensing." *Astron. & Astrophys.* 461: (2007) 861–879.

Simpson, F., C. Heymans, D. Parkinson, C. Blake, M. Kilbinger, J. Benjamin, T. Erben, H. Hildebrandt, H. Hoekstra, T. D. Kitching, Y. Mellier, L. Miller, L. Van Waerbeke, J. Coupon, L. Fu, J. Harnois-Déraps, M. J. Hudson, K. Kuijken, B. Rowe, T. Schrabback, E. Semboloni, S. Vafaei, and M. Velander. "CFHTLenS: testing the laws of gravity with tomographic weak lensing and redshift-space distortions." *Mon.Not.Roy.As.Soc.* 429: (2013) 2249–2263.

Simpson, F., J. B. James, A. F. Heavens, and C. Heymans. "Clipping the Cosmos: The Bias and Bispectrum of Large Scale Structure." *Physical Review Letters* 107, 27: 271301. (2011)

Smith, R. E., J. A. Peacock, A. Jenkins, S. D. M. White, C. S. Frenk, F. R. Pearce, P. A. Thomas, G. Efstathiou, and H. M. P. Couchman. "Stable clustering, the halo model and non-linear cosmological power spectra." *Mon.Not.Roy.As.Soc.* 341: (2003) 1311–1332.

Smith, R. K., N. S. Brickhouse, D. A. Liedahl, and J. C. Raymond. "Collisional Plasma Models with APEC/APED: Emission-Line Diagnostics of Hydrogen-like and Helium-like Ions." *Astrophys. J. Lett.* 556: (2001) L91–L95.

Smoot, G. F., C. L. Bennett, A. Kogut, E. L. Wright, J. Aymon, N. W. Boggess, E. S. Cheng, G. de Amici, S. Gulkis, M. G. Hauser, G. Hinshaw, P. D. Jackson, M. Janssen, E. Kaita, T. Kelsall, P. Keegstra, C. Lineweaver, K. Loewenstein, P. Lubin, J. Mather, S. S. Meyer, S. H. Moseley, T. Murdock, L. Rokke, R. F. Silverberg, L. Tenorio, R. Weiss, and D. T. Wilkinson. "Structure in the COBE differential microwave radiometer first-year maps." *Astrophys. J. Lett.* 396: (1992) L1–L5.

Spergel, D. N., L. Verde, H. V. Peiris, E. Komatsu, M. R. Nolta, C. L. Bennett, M. Halpern, G. Hinshaw, N. Jarosik, A. Kogut, M. Limon, S. S. Meyer, L. Page, G. S. Tucker, J. L. Weiland, E. Wollack, and E. L. Wright. "First-Year Wilkinson Microwave Anisotropy Probe (WMAP) Observations: Determination of Cosmological Parameters." *Astrophys. J. Supp.* 148: (2003) 175–194.

Takahashi, R., M. Sato, T. Nishimichi, A. Taruya, and M. Oguri. "Revising the Halofit Model for the Nonlinear Matter Power Spectrum." *Astrophys. J.* 761: 152. (2012)

Taylor, A. N. "Imaging the 3-D cosmological mass distribution with weak gravitational lensing." *ArXiv Astrophysics e-prints* 0111605 (2001)

Tegmark, M. "Measuring Cosmological Parameters with Galaxy Surveys." *Physical Review Letters* 79: (1997) 3806–3809.

Tegmark, M., D. J. Eisenstein, M. A. Strauss, D. H. Weinberg, M. R. Blanton, J. A. Frieman, M. Fukugita, J. E. Gunn, A. J. S. Hamilton, G. R. Knapp, R. C. Nichol, J. P. Ostriker, N. Padmanabhan, W. J. Percival, D. J. Schlegel, D. P. Schneider, R. Scoccimarro, U. Seljak, H.-J. Seo, M. Swanson, A. S. Szalay, M. S. Vogeley, J. Yoo, I. Zehavi, K. Abazajian, S. F. Anderson, J. Annis, N. A. Bahcall, B. Bassett, A. Berlind, J. Brinkmann, T. Budavari, F. Castander, A. Connolly, I. Csabai, M. Doi, D. P. Finkbeiner, B. Gillespie, K. Glazebrook, G. S. Hennessy, D. W. Hogg, Ž. Ivezić, B. Jain, D. Johnston, S. Kent, D. Q. Lamb, B. C. Lee, H. Lin, J. Loveday, R. H. Lupton, J. A. Munn, K. Pan, C. Park, J. Peoples, J. R. Pier, A. Pope, M. Richmond, C. Rockosi, R. Scranton, R. K. Sheth, A. Stebbins, C. Stoughton, I. Szapudi, D. L. Tucker, D. E. vanden Berk, B. Yanny, and D. G. York. "Cosmological constraints from the SDSS luminous red galaxies." *Phys. Rev. D* 74, 12: 123507. (2006)

Tegmark, M., and P. J. E. Peebles. "The Time Evolution of Bias." *Astrophys. J. Lett.* 500: (1998) L79–L82.

Vale, C., and M. White. "Simulating Weak Lensing by Large-Scale Structure." *Astrophys. J.* 592: (2003) 699–709.

van Waerbeke, L. "Noise properties of gravitational lens mass reconstruction." *Mon.Not.Roy.As.Soc.* 313: (2000) 524–532.

Van Waerbeke, L., J. Benjamin, T. Erben, C. Heymans, H. Hildebrandt, H. Hoekstra, T. D. Kitching, Y. Mellier, L. Miller, J. Coupon, J. Harnois-Déraps, L. Fu, M. Hudson, M. Kilbinger, K. Kuijken, B. Rowe, T. Schrabback, E. Semboloni, S. Vafaei, E. van Uitert, and M. Velander. "CFHTLenS: mapping the large-scale structure with gravitational lensing." *Mon.Not.Roy.As.Soc.* 433: (2013) 3373–3388.

Van Waerbeke, L., Y. Mellier, T. Erben, J. C. Cuillandre, F. Bernardeau, R. Maoli, E. Bertin, H. J. McCracken, O. Le Fèvre, B. Fort, M. Dantel-Fort, B. Jain, and P. Schneider. "Detection of correlated galaxy ellipticities from CFHT data: first evidence for gravitational lensing by large-scale structures." *Astron. & Astrophys.* 358: (2000) 30–44.

Velander, M., E. van Uitert, H. Hoekstra, J. Coupon, T. Erben, C. Heymans, H. Hildebrandt, T. D. Kitching, Y. Mellier, L. Miller, L. Van Waerbeke, C. Bonnett, L. Fu, S. Giodini, M. J. Hudson, K. Kuijken, B. Rowe, T. Schrabback, and E. Semboloni. "CFHTLenS: the relation between galaxy dark matter haloes and baryons from weak gravitational lensing." *Mon.Not.Roy.As.Soc.* 437: (2014) 2111–2136.

Verde, L., A. F. Heavens, W. J. Percival, S. Matarrese, C. M. Baugh, J. Bland-Hawthorn, T. Bridges, R. Cannon, S. Cole, M. Colless, C. Collins, W. Couch, G. Dalton, R. De Propris, S. P. Driver, G. Efstathiou, R. S. Ellis, C. S. Frenk, K. Glazebrook, C. Jackson, O. Lahav, I. Lewis, S. Lumsden, S. Maddox, D. Madgwick, P. Norberg, J. A. Peacock, B. A. Peterson, W. Sutherland, and K. Taylor. "The 2dF Galaxy Redshift Survey: the bias of galaxies and the density of the Universe." *Mon.Not.Roy.As.Soc.* 335: (2002) 432–440.

Vikhlinin, A., R. Burenin, W. R. Forman, C. Jones, A. Hornstrup, S. S. Murray, and H. Quintana. "Lack of Cooling Flow Clusters at z 0.5." In *Heating versus Cooling in Galaxies and Clusters of Galaxies*, edited by H. Böhringer, G. W. Pratt, A. Finoguenov, and P. Schuecker. 2007, 48.

Vikhlinin, A., A. V. Kravtsov, R. A. Burenin, H. Ebeling, W. R. Forman, A. Hornstrup, C. Jones, S. S. Murray, D. Nagai, H. Quintana, and A. Voevodkin. "Chandra Cluster Cosmology Project III: Cosmological Parameter Constraints." *Astrophys. J.* 692: (2009) 1060–1074.

Vikhlinin, A., B. R. McNamara, W. Forman, C. Jones, H. Quintana, and A. Hornstrup. "A Catalog of 200 Galaxy Clusters Serendipitously Detected in the ROSAT PSPC Pointed Observations." *Astrophys. J.* 502: (1998) 558–581.

Wands, D. "Brane-world Cosmology." In *A Century of Relativity Physics: ERE 2005*, edited by L. Mornas, and J. Diaz Alonso. 2006, volume 841 of *American Institute of Physics Conference Series*, 228–243. (2006)

Weinberg, D., D. Bard, K. Dawson, O. Dore, J. Frieman, K. Gebhardt, M. Levi, and J. Rhodes. "Facilities for Dark Energy Investigations." *ArXiv e-prints* 1309.5380 (2013)

Wiersma, R. P. C., J. Schaye, and B. D. Smith. "The effect of photoionization on the cooling rates of enriched, astrophysical plasmas." *Mon.Not.Roy.As.Soc.* 393: (2009) 99–107.

Wilson, G., N. Kaiser, and G. A. Luppino. "Mass and Light in the Universe." *Astrophys. J.* 556: (2001) 601–618.

Wittman, D. M., J. A. Tyson, D. Kirkman, I. Dell'Antonio, and G. Bernstein. "Detection of weak gravitational lensing distortions of distant galaxies by cosmic dark matter at large scales." *Nature* 405: (2000) 143–148.

Yoo, J., and U. Seljak. "Wide Angle Effects in Galaxy Surveys." *ArXiv e-prints* 1308.1093 (2013)

Yoo, J., and Y. Watanabe. "Theoretical Models of Dark Energy." *International Journal of Modern Physics D* (2012) 21: 1230002.

Zel'dovich, Y. B. "Gravitational instability: An approximate theory for large density perturbations." *Astron. & Astrophys.* 5: (1970) 84–89.

Zeldovich, Y. B. "A hypothesis, unifying the structure and the entropy of the Universe." *Mon.Not.Roy.As.Soc.* 160: (1972) 1P.

Zeldovich, Y. B., and R. A. Sunyaev. "The Interaction of Matter and Radiation in a Hot-Model Universe." *Astrophysics and Space Science* 4: (1969) 301–316.

Zwicky, F. "On the Red Shift of Spectral Lines through Interstellar Space." *Proceedings of the National Academy of Science* 15: (1929) 773–779.

———. "Die Rotverschiebung von extragalaktischen Nebeln." *Helvetica Physica Acta* 6: (1933) 110–127.

———. "On the Masses of Nebulae and of Clusters of Nebulae." *Astrophys. J.* 86: (1937) 217.